

5-1-2013

Forensic Signatures of Chemical Process History in Uranium Oxides

Jonathan Plaue
University of Nevada, Las Vegas

Follow this and additional works at: <https://digitalscholarship.unlv.edu/thesesdissertations>

 Part of the [Radiochemistry Commons](#)

Repository Citation

Plaue, Jonathan, "Forensic Signatures of Chemical Process History in Uranium Oxides" (2013). *UNLV Theses, Dissertations, Professional Papers, and Capstones*. 1873.
<http://dx.doi.org/10.34917/4478292>

This Dissertation is protected by copyright and/or related rights. It has been brought to you by Digital Scholarship@UNLV with permission from the rights-holder(s). You are free to use this Dissertation in any way that is permitted by the copyright and related rights legislation that applies to your use. For other uses you need to obtain permission from the rights-holder(s) directly, unless additional rights are indicated by a Creative Commons license in the record and/or on the work itself.

This Dissertation has been accepted for inclusion in UNLV Theses, Dissertations, Professional Papers, and Capstones by an authorized administrator of Digital Scholarship@UNLV. For more information, please contact digitalscholarship@unlv.edu.

FORENSIC SIGNATURES OF CHEMICAL PROCESS HISTORY IN URANIUM OXIDES

By

Jonathan William Plaue

Bachelor of Science
Massachusetts Institute of Technology
2001

Master of Science
Massachusetts Institute of Technology
2003

A dissertation submitted in partial fulfillment
of the requirements for the

Doctor of Philosophy in Radiochemistry

Department of Chemistry
College of Science
The Graduate College

University of Nevada, Las Vegas
May 2013



THE GRADUATE COLLEGE

We recommend the dissertation prepared under our supervision by

Jonathan Plaue

entitled

Forensic Signatures of Chemical Process History in Uranium Oxides

be accepted in partial fulfillment of the requirements for the degree of

Doctor of Philosophy in Radiochemistry

Department of Chemistry

Kenneth Czerwinski, Ph.D., Committee Chair

Ian Hutcheon, Ph.D., Committee Member

Julie Gostic, Ph.D., Committee Member

Gary Cerefice, Ph.D., Graduate College Representative

Tom Piechota, Ph.D., Interim Vice President for Research &
Dean of the Graduate College

May 2013

ABSTRACT

Forensic Signatures of Chemical Process History in Uranium Oxides

By

Jonathan William Plaue

Dr. Kenneth R. Czerwinski, Examination Committee Chair
Professor of Chemistry
Chair of the Department of Radiochemistry
University of Nevada, Las Vegas

This dissertation comprehensively explores and develops new tools for nuclear forensic science to facilitate the identification of chemical process history in uranium oxides. Nuclear forensics is an emerging discipline motivated by the need to prevent and combat malevolent acts involving nuclear and radiological materials. This dissertation examined process signatures in uranium oxide powders, precursors, and sintered fuel pellets.

Signatures were investigated on set of powder and pellet exemplars synthesized in the laboratory and a set of real-world samples with process information obtained from the literature or manufacturer. The examined techniques included morphology as revealed by scanning electron microscopy, near-infrared reflectance (NIR) spectroscopy, thermogravimetric analysis, powder x-ray diffraction, specific surface area, and oxygen isotope composition. Overall, this dissertation identified promising process signatures related to powder morphology, NIR, and thermogravimetric analysis. Additional results provide insights on the direction of future research in the area of process signatures.

Disclaimer: This work performed under the auspices of the U.S. Department of Energy by Lawrence Livermore National Laboratory under Contract DE-AC52-07NA27344. The views and opinions of the author expressed herein do not necessarily state or reflect those of the United States government, the Defense Nuclear Facilities Safety Board, or Lawrence Livermore National Security, LLC, and shall not be used for advertising or product endorsement purposes. [LLNL-TH-627332]

ACKNOWLEDGEMENTS

First, I would like to thank my advisor, Ken Czerwinski. Ken has inspired my interest and provided me with superb opportunities in the field of radiochemistry since I met him during a freshmen-advising seminar at the Massachusetts Institute of Technology in 1997. A key part of those opportunities was the arrangement to work with Dr. Ian Hutcheon at Lawrence Livermore National Laboratory (LLNL). Ian has been a great local advisor and it has been enriching to work with such an instrumental figure in the field of nuclear forensics.

I would like to thank all of my colleagues at LLNL and the University of Nevada, Las Vegas (UNLV) for their assistance. In particular, Bill Kerlin, Erick Johnstone, Ed Masoulf, Kerry Campbell, Bradley Childs, Trevor Lowe, and Julie Bertoia were critical in making my visits to UNLV productive. At LLNL, Kim Knight, Rich and Julie Gostic, Sarah Roberts, Dave Ruddle, Greg Klunder, Mike Kristo, and Mike Singleton could not have been more helpful.

I would also like to thank the Defense Nuclear Facilities Safety Board for their support of my doctoral degree and previous educational support as part of their Professional Development Program. This small agency has made a notable contribution to the nuclear expertise pipeline. Finally, I thank my inspiring wife, Amy, and phenomenal son, Andrew. This would not have been possible without your support and understanding.

TABLE OF CONTENTS

ABSTRACT.....	iii
ACKNOWLEDGEMENTS.....	v
LIST OF TABLES	ix
LIST OF FIGURES	x
Chapter 1 Introduction	1
1.1 Nuclear forensics—the world demands development of a new science	1
1.2 Process signatures are needed to expand nuclear forensics.....	2
1.3 A good place to start—process signatures in uranium oxides.....	4
1.4 Organization of this dissertation.....	6
Chapter 2 Pertinent background information	8
2.1 Overview of applicable nuclear fuel cycle chemistry.....	8
2.1.1 Wet processes.....	9
2.1.2 Dry processes	12
2.2 Oxygen isotope fractionation.....	15
2.3 Instrumentation and analytical methods.....	17
2.3.1 Scanning electron microscopy	18
2.3.2 Gas adsorption methods.....	20
2.3.3 Powder x-ray diffraction	22
2.3.4 Near-infrared reflectance spectroscopy	23
2.3.5 Oxygen isotope ratio measurements	24
Chapter 3 Method development and assessment of state-of-the-art quantitative image analysis for nuclear forensics.....	26
3.1 Basics of applied image analysis	26
3.2 Existing methods and standards for image analysis	27
3.3 Challenges with sample preparation and image analysis for discrete particles	31
3.4 Assessment of planar standards applicable to sintered grains	33
3.4.1 Comparison between automated and manual methods for planar features	38
3.4.2 Recommendations and treatment of error for analysis of planar grains...	42
3.5 Texture as a quantitative tool for image analysis	45
3.6 Discussion of alternatives to image analysis for morphological study	51
3.7 Suggested areas for further study.....	53
Chapter 4 Process signatures in uranium precipitates and oxide powders.....	55
4.1 Identification of processes likely to produce uranium oxides	56

4.2	Methods	59
4.2.1	Synthesis of uranium precipitates and oxide exemplars.....	60
4.2.2	Analytical Methods	62
4.2.3	Real-world samples.....	63
4.3	Results and Discussion	66
4.3.1	Thermogravimetric methods can distinguish uranyl precipitates.....	66
4.3.2	Specific surface area is not indicative of process history	68
4.3.3	Phase analysis by powder XRD	72
4.3.4	NIR can distinguish uranyl precipitates and identify oxides.....	75
4.4	Conclusions and suggested areas for further study.....	82
Chapter 5	Morphology as a signature in uranium precipitates and oxides	84
5.1	Literature suggests a link between process and morphology	84
5.2	Sample imaging and processing.....	86
5.3	Results and Discussion	87
5.3.1	SEM imagery reveals morphology characteristic to precipitation process	87
5.3.2	Quantitative image analysis using texture requires additional efforts	97
5.3.3	Morphological signatures driven by a pseudomorphic behavior in uranium	100
5.4	Conclusions and suggested areas for further study.....	110
Chapter 6	Process signatures in uranium oxide nuclear fuels	112
6.1	Identification of potential signature generating aspects of fuel manufacturing... ..	112
6.2	Evidence of morphological signatures in the literature.....	115
6.3	Methods	117
6.3.1	Process analysis of commercially produced fuel pellets	117
6.3.2	Synthesis of miniaturized fuel pellets in the laboratory.....	119
6.3.3	SEM imaging and image analysis	123
6.4	Results and discussion.....	123
6.4.1	Grain morphology is visually distinct, but quantitatively non-specific	124
6.4.2	Other pellet features of forensic interest.....	137
6.5	Conclusions and suggested areas for further study.....	147
Chapter 7	Insights into oxygen isotope ratios as a process signature	149
7.1	The premise of oxygen isotope fractionation as a geolocation signature.....	150
7.2	Approach to study the fate of oxygen from meteoric water in the fuel cycle	153
7.3	Methods	155
7.3.1	Analysis of real-world samples	155
7.3.2	Equilibrium oxygen isotope fractionation measurements	156
7.3.3	Synthesis approach to equilibrium	159
7.3.4	Measurement of oxygen isotopic ratios	160
7.4	Results and discussion.....	162

7.4.1	Oxygen isotope ratios of real-world samples poorly correlate with local waters	162
7.4.2	Experiments yield first equilibrium oxygen isotope fractionation data for U_3O_8 -air system	166
7.4.3	Equilibrium oxygen isotope fractionation for U_3O_8 -air fails to explain ratios in real-world samples	171
7.5	Conclusions and suggested areas for further study.....	175
Chapter 8	Summary of contributions	177
APPENDIX.....		181
REFERENCES.....		297
VITA.....		310

LIST OF TABLES

Table 3-1: Definitions of common morphological descriptors	28
Table 3-3: Comparison of values for morphological descriptors on the same sample set between Mama and manual analysis methods	41
Table 4-1: Summary of processes identified to likely result in uranium oxides.....	58
Table 4-2: Generalized reactions for the common precipitations of uranium from solution	59
Table 4-3: Summary of conditions used to synthesize uranium oxide exemplars	61
Table 4-4: Process history derived from the literature and phase analysis of several commercially produced uranium ore concentrates	65
Table 4-5: Thermogravimetric signatures for common uranyl precipitates	68
Table 4-6: Measured specific surface area values for laboratory-derived exemplars	69
Table 4-7: Measured specific surface areas for selected real-world samples.....	70
Table 4-8: Summary of literature sources used in Figure 4-4	71
Table 4-9: Major phase composition of laboratory-derived exemplars by powder x-ray diffraction.....	74
Table 5-1: Qualitative descriptions of the morphological signatures associated with uranium precipitates.....	88
Table 5-2: Crystal properties for species relevant to persistence study	107
Table 6-1: Comparison by manufacturer of selected process parameters for commercial nuclear fuel pellets.....	118
Table 6-2: Measurements of morphological descriptors in pellets using ethylene stearate as a binder.....	131
Table 6-3: Measurements of morphological descriptors in pellets using aluminum stearate as a binder	132
Table 6-4: Measurements of morphological descriptors in pellets using zinc stearate as a binder	133
Table 6-5: Potential features of forensic interest observed on commercial fuel pellets	137
Table 7-1: Key chemical reactions governing the fate of oxygen isotope ratios from meteoric water in the nuclear fuel cycle	154
Table 7-2: Oxygen isotope ratios of real-world uranium oxides and nearby meteoric waters	163
Table 7-3: Oxygen isotope fractionation from U ₃ O ₈ – dry air partial exchange experiments	168
Table 7-4: Oxygen isotope fractionation resulting from the companion oxidation of UO ₂ samples heated in dry air for 20 hours at 800 °C	168
Table 7-5: Oxygen isotope fractionation for direct-metal oxidation experiments	169
Table 7-6: Limited kinetic study of oxygen isotope exchange in U ₃ O ₈ at 800°C	174

LIST OF FIGURES

Figure 2-1: Common dry process reactors for production of uranium dioxide: Integrated Dry Route (top), Direct Conversion Fluid Bed (middle), General Electric Company's gas flame (bottom).....	13
Figure 2-2: Schematic of oxygen isotope fractionation processes associated with the environmental water cycle..	17
Figure 2-3: Simplified diagram of a scanning electron microscope (top) and associated electron beam interactions with a sample (bottom).....	19
Figure 2-4: Simplified diagram of a specific surface area analyzer. Image from [56].	21
Figure 2-5: Illustration of Bragg's law (top) and simplified diagram of a powder x-ray diffractometer (bottom)	23
Figure 2-6: Image (top) and simplified one-line diagram (bottom) of the High Vacuum Fluorination System at Lawrence Livermore National Laboratory.....	25
Figure 3-1: Illustration of the thresholding and segmentation process for image analysis of an uranium dioxide fuel pellet specimen	27
Figure 3-3: Challenges encountered with the preparation of discrete particle samples.	32
Figure 3-4: Challenges encountered with imaging and analysis of planar features	34
Figure 3-5: Comparison of morphological descriptors for the MRS-3 standard between different scanning electron microscopes	36
Figure 3-6: Comparison between manual and automated image analysis techniques for a uranium dioxide fuel pellet specimen; example of 1 of 10 compared images	38
Figure 3-7: Comparison of distributions for grain area and Feret diameter between Mama and manually traced methods.....	40
Figure 3-8: Examination of the number of grains required to properly characterize a sample. Note that values for most descriptors stabilize after 500 measurements.	44
Figure 3-9: Example of visual textures displayed by different stainless steels used by Bharati to classify samples by quality	46
Figure 3-10: Representative secondary electron images used to select a magnification of 50,000 X for texture measurements.....	48
Figure 3-11: Secondary electron images of uranium precipitates used to determine the optimal user-defined values for scale and step size in texture measurements.....	50
Figure 3-12: Study on the variation of texture within a single sample of uranium oxide	51
Figure 4-1: Common chemical forms of uranium in the fuel cycles.....	57
Figure 4-2: Images of powdered aqueous uranium precipitates heated to 85 °C	66
Figure 4-3: Thermogravimetric and differential scanning calorimetry traces for uranyl precipitates.	67
Figure 4-4: Literature values for the specific surface area of uranium dioxide as a function of temperature and production process.....	71
Figure 4-5: Complete set of NIR spectra for laboratory-derived exemplars as a function of temperature and resulting chemical phase	76

Figure 4-6: Comparison of NIR spectra for laboratory-derived precipitates heated to 85 °C (top) and 750 °C (bottom) for detector region 1	79
Figure 4-7: Comparison of NIR spectra for laboratory-derived exemplars and real-world samples.....	81
Figure 5-1: Morphology as a function of temperature for the exemplars derived from volatile precipitants: ammonium hydroxide (left), hydrogen peroxide (middle), and ammonium carbonate (right).	89
Figure 5-2: Morphology as a function of temperature for the exemplars derived from non-volatile precipitants: magnesia (left) and sodium hydroxide (right).....	90
Figure 5-3: Comparison of secondary electron images of uranium oxides derived from precipitation with ammonium hydroxide.....	93
Figure 5-4: Comparison of secondary electron images of uranium oxides derived from precipitation with hydrogen peroxide	94
Figure 5-5: Comparison of secondary electron images of uranium oxides derived from precipitation with magnesia	95
Figure 5-6: Comparison of secondary electron images of uranium oxides derived from precipitation with sodium hydroxide	96
Figure 5-7: Comparison of secondary electron images of uranium oxides derived from precipitation with ammonium carbonate	97
Figure 5-8: Pattern spectra analysis of uranium precipitants heated to 85 °C	99
Figure 5-9: Principal component analysis scores plot of texture values for laboratory-derived exemplars and real-world samples presented in Figures 5-3 to 5-6.....	100
Figure 5-10: Demonstration of the utility of pseudomorphic transitions in the comparison of uranium oxides produced at 600 °C resulting from precipitation with ammonium carbonate (top), ammonia (middle), and hydrogen peroxide (bottom)	102
Figure 5-11: Secondary electron images of ammonium uranyl carbonate and resulting uranium oxides demonstrating persistence in morphology	105
Figure 5-12: Powder x-ray diffraction patterns for morphology persistence study under reducing (4 % hydrogen in argon) conditions (top) and air (bottom).	106
Figure 5-13: Examples of pseudomorphic transitions in other uranium bearing compounds	109
Figure 6-1: Summary flow sheet of common processes for the manufacture of uranium dioxide nuclear fuel.	115
Figure 6-2: Secondary electron images of the UO ₂ precursor powders : (a) precipitation with ammonium hydroxide, (b) store purchased, (c) precipitation with hydrogen peroxide, and (d) precipitation with ammonium carbonate.....	120
Figure 6-3: Time at temperature profile for sintering miniaturized fuel pellets.....	122
Figure 6-4: Examples of three commercial nuclear fuel pellets (top left) and two miniature pellets synthesized in the laboratory (bottom right).....	124
Figure 6-5: Density of laboratory-derived fuel pellets as a function of precursor oxide type and binder.....	125

Figure 6-6: Backscattered electron images representative of each of the laboratory-derived fuel pellets. Scale bar is 30 μm for all images.....	126
Figure 6-7: Cumulative distribution curves for maximum Feret size as a function of precursor UO_2 and binder.	128
Figure 6-8: Variation of median grain area (top) and aspect ratio (bottom) as a function of binder and precursor UO_2 powder..	130
Figure 6-9: Examples of grain morphologies in two fuel pellets types from Manufacturer A (left), B (middle), and C (right).....	134
Figure 6-10: Morphological descriptor measurements for commercial pellets from three manufacturers: distribution of grain area (top), sample of variation in grain area within a pellet type (middle), and aspect ratio (bottom).....	136
Figure 6-11: Alumina surface features resulting from the use of aluminum stearate as binder observed in pellets from Manufacturer C (a–c) and a laboratory-derived pellet replicating the feature	139
Figure 6-12: Additional alumina features observed in pellets from Manufacturer C: inside a surface pore (top), at triple points (middle), and within a mid-volume pore exposed through pellet sectioning (bottom).....	140
Figure 6-13: Unique features observed on pellets from Manufacturer A: sand-like surface debris (top) and aluminum-rich grain eruptions (bottom).....	142
Figure 6-14: Grain surface textures found on commercial pellets: stepped (top) and ripples (bottom).....	143
Figure 6-15: Unexplained surface features found on commercial pellets: bumps (top) and dimples (bottom).....	144
Figure 6-16: Other unexplained features found on commercial pellets: micrograin areas (top) and ring pores (bottom).....	145
Figure 6-17: Molybdenum features observed on commercial fuel pellets.	147
Figure 7-1: Global variation of $\delta^{18}\text{O}$ in meteoric waters as modeled by Bowen [182] ..	151
Figure 7-2: Compilation of available oxygen isotope fractionation data for uranium mineral–water system as a function of temperature by Fayek [5]..	152
Figure 7-3: Experimental configuration for partial exchange experiments in a controlled-atmosphere tube furnace with a set of companion samples in gold foil thimbles.....	158
Figure 7-4: Secondary electron images of the U_3O_8 powders utilized in companion equilibrium fractionation experiments.....	159
Figure 7-5: Experimental configuration for direct metal oxidation oxygen isotope fractionation experiments; furnace boat with gold foil thimble containing initial acid cleaned uranium metal (left) and resulting U_3O_8 sample after exposure to air at elevated temperature (right).....	161
Figure 7-6: Comparison of oxygen isotope fractionation in samples of anthropogenic U_3O_8 with the nearest monitored source of meteoric water.....	165
Figure 7-7: Partial exchange experiment plots as a function of temperature for U_3O_8 –dry air system.....	167
Figure 7-8: Observed oxygen isotope fractionation for real-world samples as a function of temperature as compared to the measured equilibrium for the U_3O_8 – air system. .	172

Chapter 1 Introduction

This chapter discusses the background and motivation for this research and provides the reader with an overview of the contents of this dissertation. Discussions include a review of the origins of nuclear forensics, the nature of process signatures, and the rationale for performing research with uranium oxides.

1.1 Nuclear forensics—the world demands development of a new science

The consequences resulting from the detonation of a nuclear explosive device are so grave that the international community has recently coalesced to promote the development and application of the best scientific and engineering capabilities toward a new technical discipline termed “nuclear forensics.” While there a number of definitions in use for nuclear forensics, a broadly accepted definition originated from the *Joint Working Group of the American Physical Society and the American Association for the Advancement of Science* [1], which defined nuclear forensics as:

The technical means by which nuclear materials, whether intercepted intact, or retrieved from post-explosion debris, are characterized (as to composition, physical condition, age, provenance, history) and interpreted (as to provenance, industrial history, and implications for nuclear device design).

Internationally, the Communiqués resulting from the Nuclear Security Summits of 2010 and 2012 [2][3] each formally recognized and endorsed the need for nuclear forensics. In the United States, the Congress passed the *Nuclear Forensics and*

Attribution Act of 2010 [4]. In one of six findings in the Act, Congress succinctly captured the key objectives for this fledgling discipline:

A robust and well-known capability to identify the source of nuclear or radiological material intended for or used in an act of terror could also deter prospective proliferators. Furthermore, the threat of effective attribution could compel improved security at material storage facilities, preventing the unwitting transfer of nuclear or radiological materials.

In essence, this finding indicates that effective nuclear forensics provides decision makers with information necessary to react to unanticipated events involving nuclear materials that are outside of regulatory control. The nature of these events may range from the interdiction of smuggled nuclear material or nuclear device (so-called pre-detonation forensics) to the analysis of debris resulting from the detonation of a nuclear explosive device (post-detonation forensics). Decision makers' reactions may include a desire for attribution (declare who did it), elimination (declare who did not do it), prosecution (legally prove who did it), and retribution (attack who did it)[5][6] [7]. Further, the sense of Congress captured the views of several authors [8][9][10] who suggested that nuclear forensics has potential value as a deterrent to non-nation state actors or nations that choose to aid such groups in nuclear terrorism.

1.2 Process signatures are needed to expand nuclear forensics

Findings in nuclear forensics result from the characterization and interpretation of physical and chemical information from the nuclear material—this information is commonly termed a “signature.” Development of signatures began with the advent of

nuclear forensics in the early 1990's following the dissolution of the Soviet Union and an associated increase in the incidence of illicit trafficking in nuclear materials. Formative groups in this new discipline at the Lawrence Livermore National Laboratory (LLNL) [11][12] and the European Commission's Institute for Transuranium Elements [13][14] applied fundamental techniques from the fields of radiochemistry and geochemistry to develop signatures.

Initially, signatures focused on utilizing the isotopic and elemental composition of the radioactive material to ascertain the origin, age, and production date of the material. The utility of signatures broadened with the application of more techniques adapted from radiochemistry and geochemistry. For example, Keegan [15] and Varga [16] demonstrated the ability to utilize trace element concentrations and isotope ratios to identify the provenance of uranium ore concentrates.

Kristo and Tumey [17] recently provided a case study on the attribution of uranium ore concentrate as part of their assessment of the state of nuclear forensics. The case study noted a desire to identify the type of milling and mining operations associated with the sample. The authors further noted that a predictive approach to attribution (as opposed to a comparative approach leveraging databases), requires identification of signatures indicative of sought-after findings (e.g, processing method) and that research in such predictive signatures is "sorely lacking."

This dissertation aims to contribute to the expansion of signatures indicative of chemical processing history—termed "process signatures" in this study. For example, process signatures might include characteristics that enable a forensic scientist to

determine the types of reagents, process conditions (e.g., pH, temperature, concentrations, etc), or physical manipulation methods associated with nuclear materials. In essence, process signatures contribute to answering the question—how was this radioactive material manufactured?

Process signatures represent an underdeveloped area in nuclear forensics, though research is beginning to emerge. For instance, Hastings [18] examined characteristics of uranium oxides produced through different methods and Varga [19] used infrared spectroscopy to classify uranium ore concentrates based on precipitation chemistry. Researchers have amassed a considerable amount of information on the nuclear fuel cycle during the past 70 years. While not explicitly derived for forensics applications, this information can illuminate valuable signatures and guide research efforts. Consequently, each chapter reviews general fuel cycle research applicable to the particular investigation.

1.3 A good place to start—process signatures in uranium oxides

Upon first inspection, uranium oxides—particularly in the form of uranium ore concentrate or nuclear fuel pellets—do not appear to be a threatening material worthy of significant study for process signature development. Uranium in most isotopic compositions has a relatively low radiotoxicity and therefore poses little danger as a component of a radioactive dispersal device or “dirty bomb”. Fuel pellets, in particular, are robust ceramics that required significant effort to disperse. Despite these points, there are several compelling reasons to research process signatures in uranium oxides, which are summarized below.

First, uranium oxides and fuel pellets are the most common forms of interdicted nuclear materials. According to the International Atomic Energy Agency's Illicit Trafficking Database, some isotopic mixture of uranium or thorium was involved in approximately 95 percent of the known smuggling incidents involving nuclear materials between 1993 and 2003 [20]. While trafficking in these materials presents relatively low direct risk, improved signatures may help to illuminate illicit trafficking activities for materials of greater concern.

Second, given the crucial role of uranium in the commercial and military nuclear fuel cycles, extensive research exists in the open literature, providing a tremendous asset to guide research. Furthermore, industry widely utilizes several common chemical processing techniques. However, the parameters used at each facility will likely vary resulting in a potentially fertile sample pool for investigation.

Third, an essential element of nuclear forensics is developing international collaborations and databases. Work on uranium, particularly uranium ore concentrates and other materials of natural isotopic composition, is less likely to be considered sensitive and therefore more likely amenable to cooperation. Establishing trust and demonstrating meaningful outcomes with insensitive materials may help facilitate further cooperation with more sensitive materials (e.g., HEU or plutonium).

Fourth, while uranium materials of natural or low-enriched isotopic compositions present low direct risk, improved signatures on these materials may yield insights into process signatures for higher risk materials (e.g., highly enriched uranium or plutonium). In particular, the chemical process behavior of uranium is unlikely to be

dependent on enrichment and many of the chemistries used for uranium processing are suitable for plutonium.

Finally, samples of uranium oxides are easier and safer to handle in the laboratory. The flexibility associated with working with uranium, as opposed to the glovebox operations required for other actinides, represents an important characteristic for initial research into process signatures.

1.4 Organization of this dissertation

Chapter 2 provides background information on the chemistry of applicable processes in the uranium fuel cycle, stable isotope fractionation processes and terminology, and the key instrumentation and methods. Each of the subsequent chapters presents the results of substantive experimental research grouped by topical area. The chapters are written in standalone manuscript form and include specific conclusions and suggested areas for further study. The topical areas for each chapter are as follows:

- Chapter 3 develops and assesses image analysis as an analytical technique.
- Chapter 4 systematically identifies the set of uranium precipitates and oxides most likely to be encountered in a nuclear forensics application, develops a set of samples for study, and characterizes the sample set for potential signatures indicative of chemical process history.
- Chapter 5 continues the study of uranium precipitates and oxides for signatures indicative of chemical process history with an exclusive focus on morphology.

- Chapter 6 examines uranium oxide nuclear fuel pellets for signatures indicative of chemical processing history.
- Chapter 7 examines the potential for stable oxygen isotope ratios in triuranium octoxide to provide a signature indicative of the geographic location of origin or chemical process.
- Chapter 8 summarizes the major contributions from this research and provides perspectives on areas for future study.

Chapter 2 Pertinent background information

This chapter provides pertinent background information to prepare the reader for the subsequent chapters. Background information is provided on the chemistry of applicable processes in the uranium fuel cycle, stable isotope fractionation processes and terminology, and the key instrumentation and methods used in this research. The material is to provide the reader with an adequate base of understanding for subsequent chapters and is not intended to be a comprehensive treatment of these topics.

2.1 Overview of applicable nuclear fuel cycle chemistry

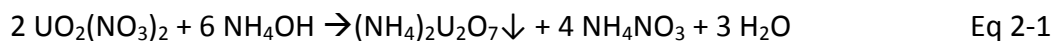
The fuel cycle for uranium can be broken into a number of steps in which uranium is: (1) chemically separated and concentrated from ore, (2) further refined into a chemically pure form, (3) converted into uranium hexafluoride and enriched in the isotope ^{235}U , and (4) reacted to oxide or metal for the manufacture of fuel for a nuclear reactor or explosive device. Many references provide comprehensive treatments on the chemistry of uranium in the nuclear fuel cycle [21][22][23][24]. This section provides a summary of common chemical processes associated with the precipitation processes—termed “wet” processes in the fuel manufacturing industry—used in steps 1, 2, and 4 for application in Chapter 4. This section also provides a summary of gas phase pyrohydrolysis reactions—termed “dry” processes—that are commercially utilized for the production of uranium dioxide for application in Chapter 6.

2.1.1 Wet processes

The separation of the uranyl ion from aqueous solutions through precipitation is a common step in the nuclear fuel cycle. Uranyl ions (UO_2^{2+}) form when uranium ore or other uranium-rich material (e.g., used nuclear fuel, scrap materials, etc) is dissolved in acid. The uranyl ion is then purified from other undesirable constituents through solvent extraction or ion exchange separation processes. The uranyl ion, in the form of uranyl difluoride, may also be produced in some fuel manufacturing processes through the introduction of uranium hexafluoride gas into aqueous solutions.

In all cases, uranyl ion is removed from aqueous solution through the introduction of reagent resulting in conditions favorable to precipitate uranium. There are five reagents commonly used for this process: (1) ammonium hydroxide (or ammonia gas), (2) hydrogen peroxide, (3) ammonium carbonate (or ammonia and carbon dioxide gases), (4) magnesia, and (5) sodium hydroxide. Each process is briefly reviewed below and will be applied further in Section 4.1.

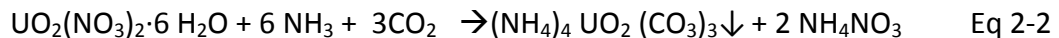
The most widely known precipitation route utilizes ammonia gas or ammonium hydroxide to precipitate uranium from solution according to the following equation:



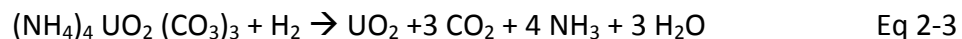
The precipitate is commonly referred to as ammonium diuranate (ADU), which is actually a mixture of ammonium and uranyl with varying ratios. The precipitate is physically separated from solution and rinsed prior to thermal oxidation or reduction to form triuranium octoxide (U_3O_8) or uranium dioxide (UO_2), respectively.

UO₂ derived from ADU typically results in a powder consisting of large agglomerates that require further attrition or granulation to create an acceptable flowing powder for nuclear fuel manufacturing. Several authors [25] [26] [27] have noted that variations in precipitation conditions resulted in differences in the ADU precipitate that, in turn, impacted the properties of the resulting UO₂. The ADU process has been widely used in United States and Australia.

The process utilizing ammonium carbonate was developed in Germany in the late 1970s by Nukem GmbH and the Reactor Brennelement/Kraftwerk Union [28]. The process involves precipitation through the introduction of gaseous ammonia and carbon dioxide as represented in the following reaction:

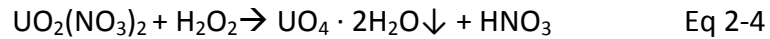


Alternatively, a solution of ammonium hydroxide and ammonium carbonate can be used. Mellah [29] determined this precipitation to be a second order reaction with an Arrhenius activation energy of 17.4 kJ/mol and k_2 of 0.31-0.437 L/mol min at 313 and 330 K. The precipitate, termed ammonium uranyl carbonate (AUC), is known to form large, easily filtered precipitates. Once filtered and washed, the precipitates are amenable to decomposition and reduction in a single step according the following reaction:



The resulting oxide is free-flowing and can be directly pressed into a high grade ceramic without additional pre-processing (e.g., granulation, binders, lubricants, etc). The AUC process has been employed in Germany, Sweden, South Korea and Argentina.

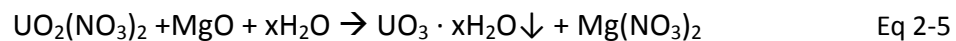
Another common process utilizes hydrogen peroxide. Peroxide reacts with uranyl to form the uranyl peroxide complex, which is insoluble in acidic conditions according to the following equation:



Peroxide precipitation is commonly utilized with in situ leaching operations, in part due to the ability of peroxide to solubilize uranyl under alkaline conditions [30][31].

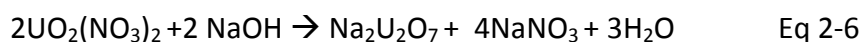
Peroxide precipitates tend to be very pure compared to the variety of metals that are co-precipitated under the hydroxide conditions associated with the four other processes discussed in the section.

Historically, magnesia was used as a cost effective reagent for precipitations associated with uranium ore milling and concentration [22]. Generally, magnesia forms hydroxide ions, which precipitate uranium as a hydrate oxide according to the following equation:



In practice, some magnesium is transferred with the solid precipitant phase, necessitating further purification steps prior to conversion or other operations sensitive to impurity.

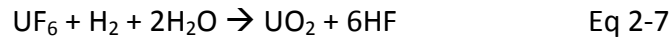
In some less common processes, particularly carbonate leaches, sodium hydroxide may be utilized [22][32]. The reaction can be generalized with the following equation:



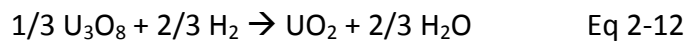
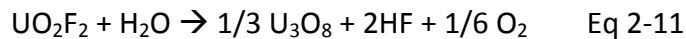
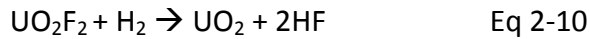
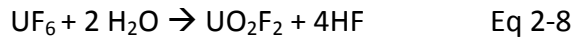
Use of sodium hydroxide also results in the precipitation of uranium hydroxide phases, similar to magnesia. In both cases, some sodium is transferred with the solid, usually necessitating additional purification steps.

2.1.2 Dry processes

In a dry process, uranium hexafluoride is sublimed to a gas, heated, and reacted in an atmosphere containing water vapor and hydrogen gas. All reactions are either gas-gas or solid-gas. The overall reaction, which results in the direct production of ceramic grade uranium dioxide, can be represented by:



This reaction is, in fact, a complicated series of parallel reactions better represented by:



There are three commercially prevalent forms of the dry process with the differences arising primarily from the choice in the design of the gas phase chemical reactor: (1) rotary kiln, (2) fluidized bed, and (3) gas flame. Figure 2-1 depicts a generalized schematic for each of the chemical reactors.

The rotary kiln method is represented by the Integrated Dry Route (IDR), which was developed by British Nuclear Fuels Limited [33] [34]. The IDR process involves a single-stage rotary kiln furnace providing three temperature zones ranging between

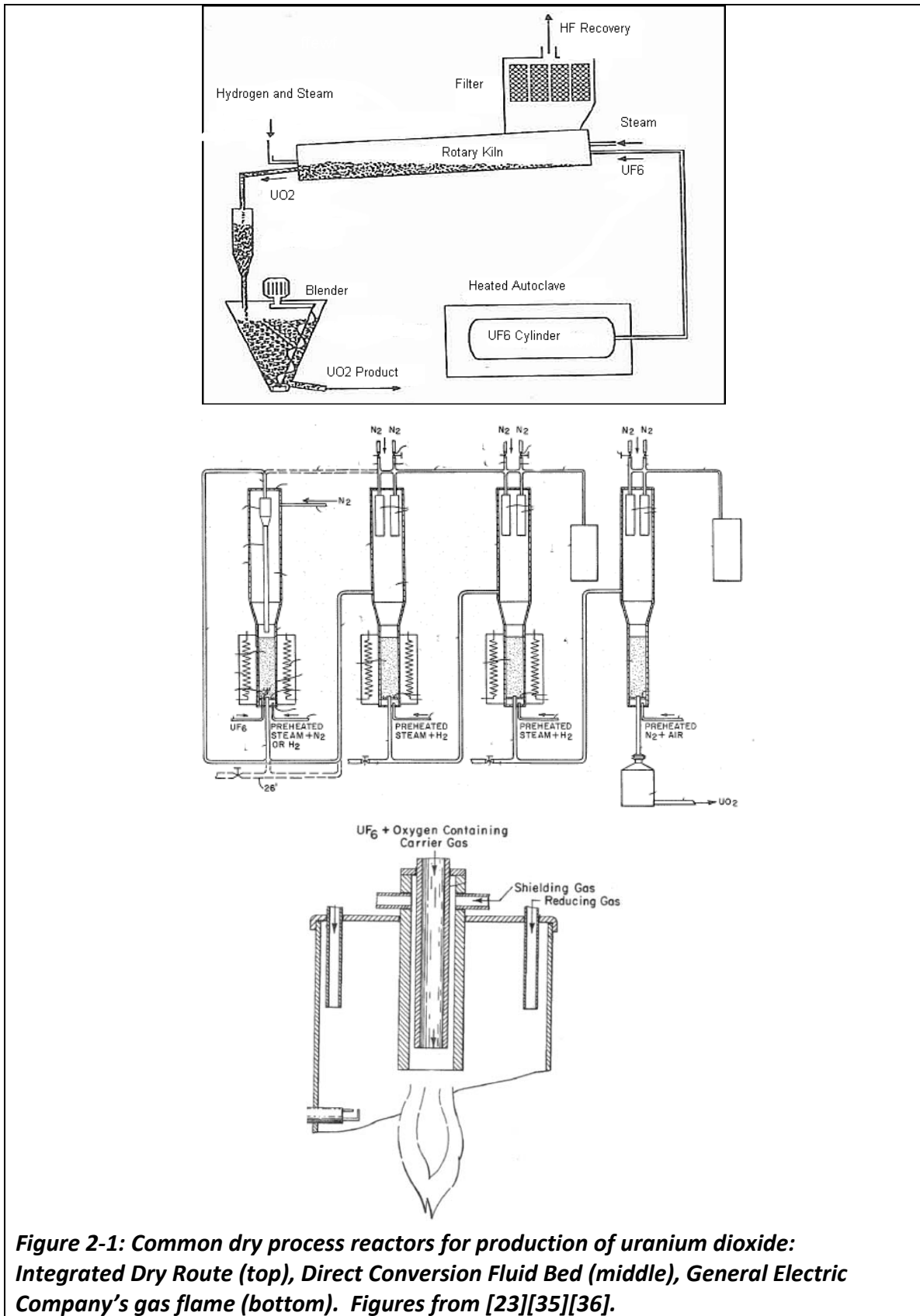


Figure 2-1: Common dry process reactors for production of uranium dioxide: Integrated Dry Route (top), Direct Conversion Fluid Bed (middle), General Electric Company's gas flame (bottom). Figures from [23][35][36].

600–800 °C [37]. Product reacts as it works its way through the rotating and baffled kiln. A similar process was patented by the French, with temperature zones ranging from 600–1200°C and the primary difference being an elevated initial reaction temperature of 850–900°C [38]. Manufacturers in the United Kingdom, France, and the United States have licensed IDR processes.

The fluidized bed methodology is represented by the Direct Conversion Fluid Bed (DCFB) process. DCFB was originally developed in the early 1960's at Argonne National Laboratory [39][40] and later commercially adopted by the Westinghouse Corporation [41][42] in the mid-1970s. Rather than a single reaction chamber, DCFB utilizes three to four fluidized bed reactors. In the first reactor, uranium hexafluoride is hydrolyzed with water to produce uranyl difluoride. Next, a hydrogen and steam flow is used to strip fluoride resulting in uranium dioxide. The product from the second reactor tends to have high fluorine levels, so a second exposure to steam and hydrogen is used to purify the uranium dioxide to reactor grade levels in a third reactor. Temperatures for the first reactor and the two defluorination reactors are typically in the range of 475–600 °C and 575–675 °C, respectively [43] If necessary, a fourth reactor is used to accurately control the oxidation state of the uranium (UO_{2+x}) through a heating step in a limited oxygen atmosphere. The DFCB process has been used in the United States and Sweden.

The gas flame methodology is represented by the General Electric Company's (GECO) gas flame reactor process [36]. Initial development work on gas flame technology was performed at Oak Ridge National Laboratory [44] [45]. The GECO process works through a single stage reduction and hydrolysis reaction within a flame

zone. The flame reaction temperature is in the range of 1300–1800 °C. In practice, flows rates include excess hydrogen and oxygen resulting in the production of water as a by-product of combustion. A second heat treatment step under hydrogen atmosphere near 1000 °C is often employed to reduce fluoride content in the final product. Considerable research and design effort has gone into the flame nozzle design to enable appropriate reactant mixing and prevent product buildup, facilitating a continuous process. Of note, the GECO process does not use water as a reactant, thus it is unlikely that the resulting product would be a candidate for geolocation based on the oxygen isotopic ratio of local process water, discussed in Chapter 7.

2.2 Oxygen isotope fractionation

Differences in the mass between isotopes can result in the fractionation—or preferential separation—of isotopes during chemical reactions through both kinetic and equilibrium processes. These fractionations are most pronounced in the stable isotopes of the light elements, such as oxygen. Consequently, the study and application of oxygen isotope fractionation is a cornerstone of geochemistry [46] [47].

Briefly, kinetic fractionation processes result from differences in kinetic energy derived from differences in molecular mass between molecules substituted with a heavier isotope. For example, at any given temperature, the velocity of H₂¹⁶O is 5.4 percent greater than H₂¹⁸O, which impacts a range of physicochemical behavior.

$$m_{18}v_{18}^2 = m_{20}v_{20}^2 \rightarrow \frac{v_{18}}{v_{20}} = \sqrt{\frac{m_{20}}{m_{18}}} = 1.054 \quad \text{Eq 2-13}$$

Equilibrium fractionation processes are driven by the quantum mechanical property known as zero-point energy—molecules containing the heavy isotope will have

a lower vibration frequency in the ground state than the molecule incorporating the light isotope. As a result, chemical bonds involving the heavier isotope are slightly less favored to react compared to the bonds involving the light isotope.

The geochemical community commonly utilizes a set of terms to describe stable isotope fractionation—these terms will be adopted in this study and are briefly summarized below to assist other disciplines. Oxygen isotopic fractionation is commonly expressed as a δ value, which is defined by the following equation:

$$\delta^{18}O = \left(\frac{\left[\frac{^{18}O}{^{16}O} \right]_{SMOW} - \left[\frac{^{18}O}{^{16}O} \right]_{Sample}}{\left[\frac{^{18}O}{^{16}O} \right]_{SMOW}} \right) \times 1000 \quad \text{Eq: 2-14}$$

where SMOW represents Standard Mean Oceanic Water with a $^{18}O/^{16}O$ taken as $2005.20 \pm 0.45 \times 10^{-6}$ [48] and the δ value is expressed in units of per mil (‰).

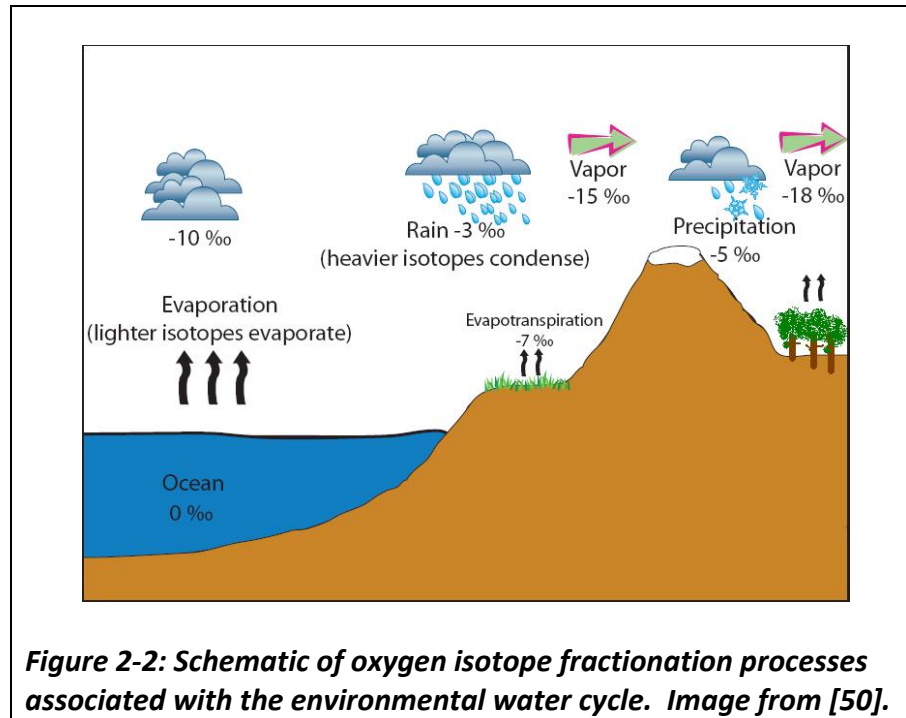
The fractionation between two substances A and B is expressed by a fractionation factor, termed α , defined by the following equation and equated to the δ unit for convenience:

$$\alpha_{A-B} = \frac{R_A}{R_B} = \frac{1000 + \delta_A}{1000 + \delta_B} \quad \text{Eq: 2-15}$$

where R is the ratio of $^{18}O/^{16}O$ in phases A and B.

The study of stable isotopes has yielded significant understanding in geochemistry for many decades and is now being applied to a wide range of forensic problems [49]. Fractionation of oxygen isotopes in water molecules through evaporation and condensation in the natural environment contributes to systematic variations in oxygen isotope ratios around the world (Figure 2-2). The potential to

exploit this phenomenon as a forensic tool for geolocation purposes is the subject of Chapter 7.



2.3 Instrumentation and analytical methods

This section provides an overview of the primary instrumentation and analytical methods used for this study. The intent is to provide the reader with a summary of the basic principles of the instrumentation, the basis for selecting the technique for nuclear forensic applications, a discussion of alternatives, and general aspects of sample preparation. Subsequent chapters provide specific details on the instrumentation and the precise methods applied in this dissertation.

2.3.1 Scanning electron microscopy

Scanning electron microscopy (SEM) is a versatile and commonly utilized form of microscopy that is well suited for the observation of topological and morphological

sample features on a nanometer to micrometer scale [51]. The SEM works by rastering electrons, generated through thermal and/or electrostatic means and focused into a beam using electromagnetic lenses, across an area of the sample (Figure 2-3). As the electrons interact with the sample, useful signals are generated as secondary electrons, backscattered electrons, and characteristic x-rays, which are detected and transformed into an image.

Secondary electron images provide excellent depth of field to aid in the study of morphological features. Backscattered electron images provide contrast as a function of the mean atomic number of the constituent atoms in the sample. Similarly, characteristic x-rays are emitted through the excitation of individual atoms and can be used for the semi-quantitative analysis of sample composition on the micrometer scale.

For SEM analysis, samples must be non-volatile to survive the vacuum environment and must be conductive to prevent charging by the electron beam. Non-conductive samples may be coated with a thin (typically a few tens of nanometers) layer of a conductive substance such as carbon, gold, or iridium. Powdered samples consisting of a fraction of a milligram are typically adhered to a specimen stub using conductive tape, adhesives, or set into epoxy resin and polished. Researchers must take significant care to ensure that the sample is adequately dispersed (discussed further in Chapter 3).

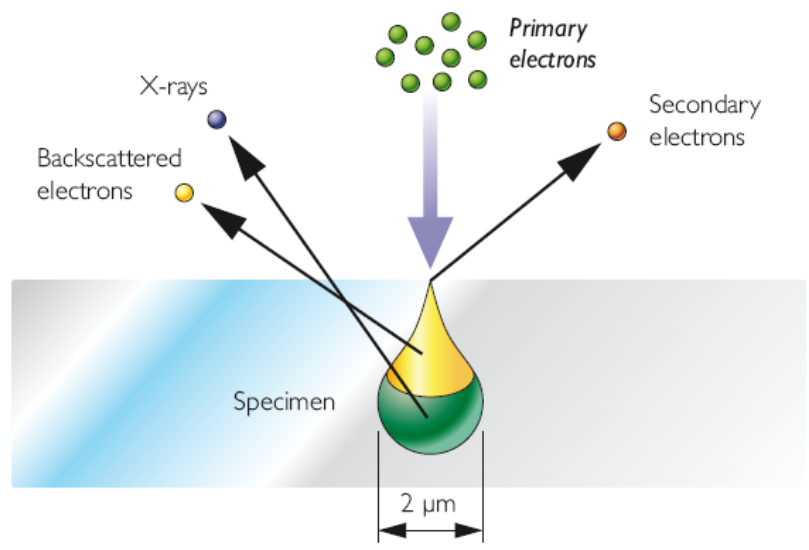
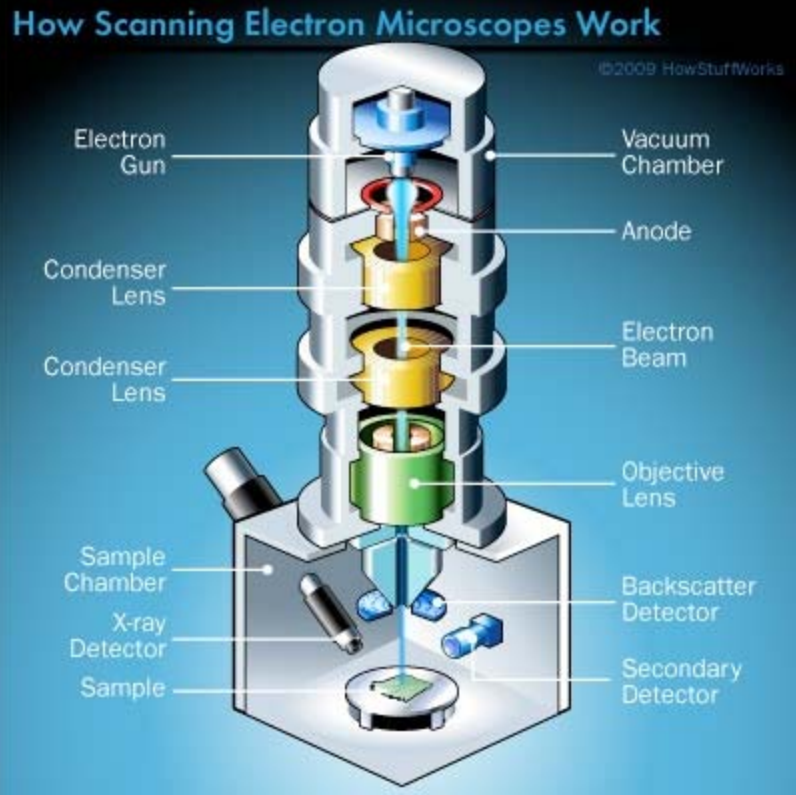


Figure 2-3: Simplified diagram of a scanning electron microscope (top) and associated electron beam interactions with a sample (bottom). Images from [52] and [53].

Alternatives to the SEM include optical microscopy, transmission electron microscopy, and laser scattering techniques. The SEM offers superior resolution

(typically at the nanometer range) and depth of field compared to optical microscopy, as well as simplified sample preparation compared to transmission electron microscopy. Laser scattering techniques offer a potentially viable alternative; however, these systems tend to provide results that are abstractions of the actual particle dimensions. A more thorough discussion of the tradeoffs on laser scattering is provided in Chapter 3.

2.3.2 Gas adsorption methods

The adsorption of gases to surfaces provides an important tool for the characterization of porous solids [54]. The best known application of this behavior is the methodology used to determine the specific surface area of a solid developed by Brauner, Emmett, and Teller (known as the BET method) [55]. The BET method extends the Langmuir equation, which relates the adsorption of a monolayer of gas molecules to a solid surface as a function of gas pressure and temperature, to a multilayer system.

Gas adsorption analyzers work through the introduction of a known quantity of adsorbate (typically nitrogen or krypton) into a sealed glass cell containing the sample under investigation (Figure 2-4). The cell is kept at liquid nitrogen temperature and changes in the system pressure are monitored as incremental doses of adsorbate are introduced into the system. The process continues at an incrementally increased initial pressure.

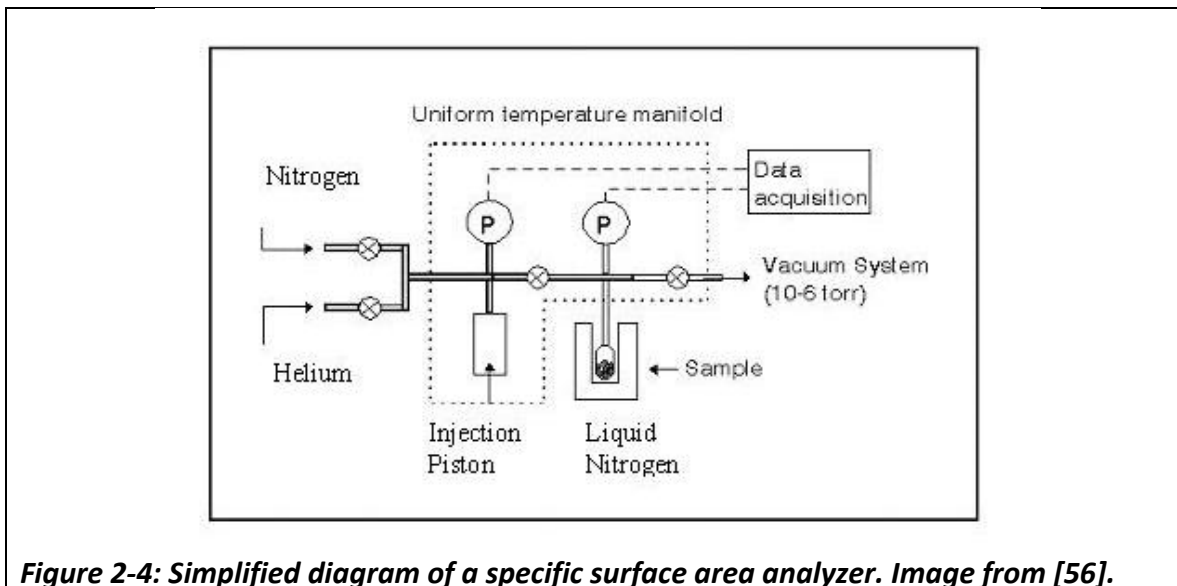


Figure 2-4: Simplified diagram of a specific surface area analyzer. Image from [56].

Preparation for BET analysis requires samples to be degassed—typically under elevated temperatures and vacuum, although some samples may be successfully degassed using a flowing inert gas. BET measurements are essentially non-destructive, other than the exposure to elevated and reduced temperatures for degassing and measurement, respectively. Most materials of interest to nuclear forensics will not be perturbed by these conditions and samples are easily retrieved for further chemical and physical analyses.

In theory, surface area measurements can be performed using any approach that provides quantitative information on sample morphology (e.g., SEM or laser methods). The tradeoffs with these alternatives include a potentially less representative measurement for heterogeneous powders due to the small sample size and lack of sample recovery.

2.3.3 Powder x-ray diffraction

Powder x-ray diffraction (XRD) is a powerful and common tool for the identification of solid crystalline phases. XRD works through the detection of x-rays diffracted from a primary x-ray beam incident to a thin layer of powder sample (Figure 2-5). The resulting diffraction pattern is governed by Bragg's law and is indicative of the compound or relative mixture of compounds in the sample. In this study, powder XRD will be applied for phase analysis; a straightforward application of the technology in which the diffraction pattern of the powder is compared to a standard, such as those maintained by the International Centre for Diffraction Data. There are no simple alternatives to powder XRD [57].

Samples for powder XRD analysis need to be distributed randomly, homogenous, and fine in particle size. These conditions are typically achieved by first grinding the powder and then applying it to the sample holder using a compatible liquid solvent. For radioactive materials, the samples are placed in either a sealed holder engineered for confinement or affixed using high x-ray transmittance materials.

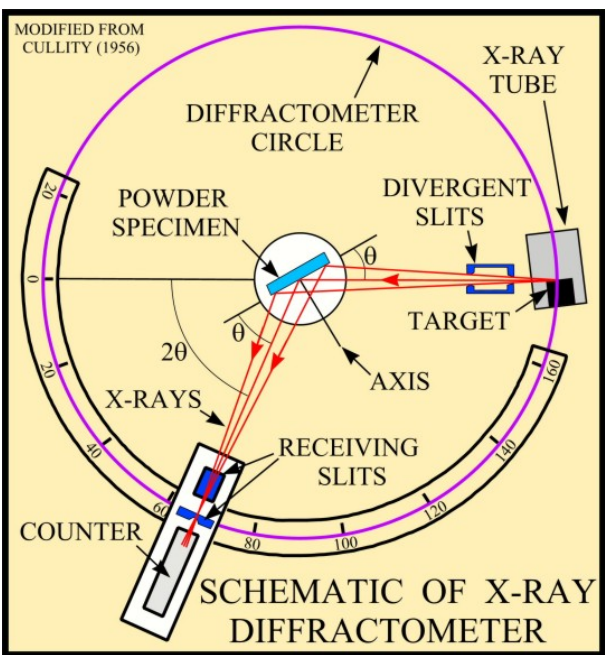
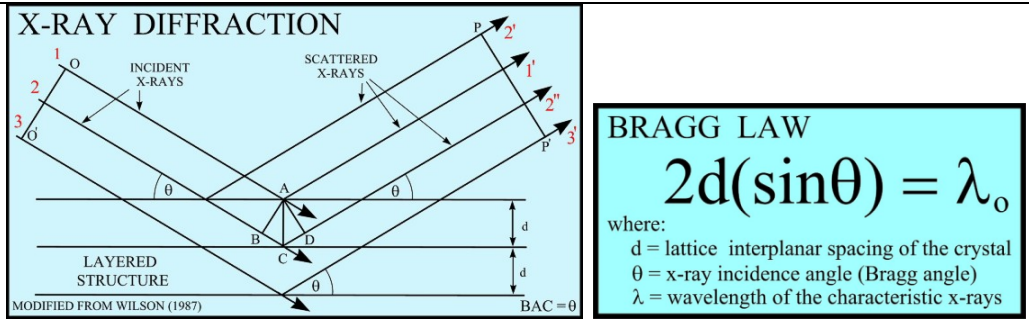


Figure 2-5: Illustration of Bragg's law (top) and simplified diagram of a powder x-ray diffractometer (bottom). Images from [58].

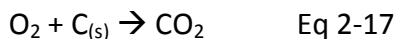
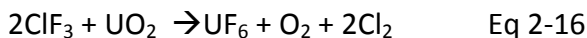
2.3.4 Near-infrared reflectance spectroscopy

Chapter 4 examines near-infrared reflectance (NIR) spectroscopy as a potential new technique in nuclear forensics. The NIR portion of the spectrum (about 800 to 2500 nm) is dominated by molecular overtone and combination bands, resulting in complex spectra that can be difficult to interpret directly and often require the use of multivariate methods [59]. In practice, the NIR technique requires an appropriate light source (commonly halogen), fiber optic cabling to transmit light to and from the sample,

and a detector. This equipment can be made very compact and ruggedized, resulting in a technique that is appropriate for measurements in the field. Furthermore, NIR is a non-contact technique, meaning that no sample preparation is required and anti-contamination precautions are minimized. In contrast, significant grinding and pellet processing procedures are required to obtain similar chemical information using a more traditional infrared spectroscopy device.

2.3.5 Oxygen isotope ratio measurements

Oxygen isotope ratios of uranium oxides were measured using the High Vacuum Fluorination System (HVFS) at the Lawrence Livermore National Laboratory (LLNL). The HVFS provides a one-of-a-kind capability within the Department of Energy's national laboratory system for oxygen isotope measurements in minerals and metal oxides of anthropogenic origin (Figure 2-6). The HVFS utilizes the oxidizing action of chlorine trifluoride (ClF_3) to quantitatively liberate oxygen gas from uranium oxides [60] [61]. The liberated gas is then reacted with carbon to form carbon dioxide, which is sealed into a glass ampoule and analyzed using a gas isotope ratio mass spectrometer for isotopic analysis. The overall process is represented by the following equations:



A companion technique to HVFS is secondary ion mass spectroscopy (SIMS). The accuracy of SIMS has been demonstrated on individual particles [62]; however, HVFS provides better accuracy for bulk samples (20–30 mg) that are potentially inhomogeneous.



High Vacuum Fluorination Line Simplified Piping Diagram
20-Aug-12

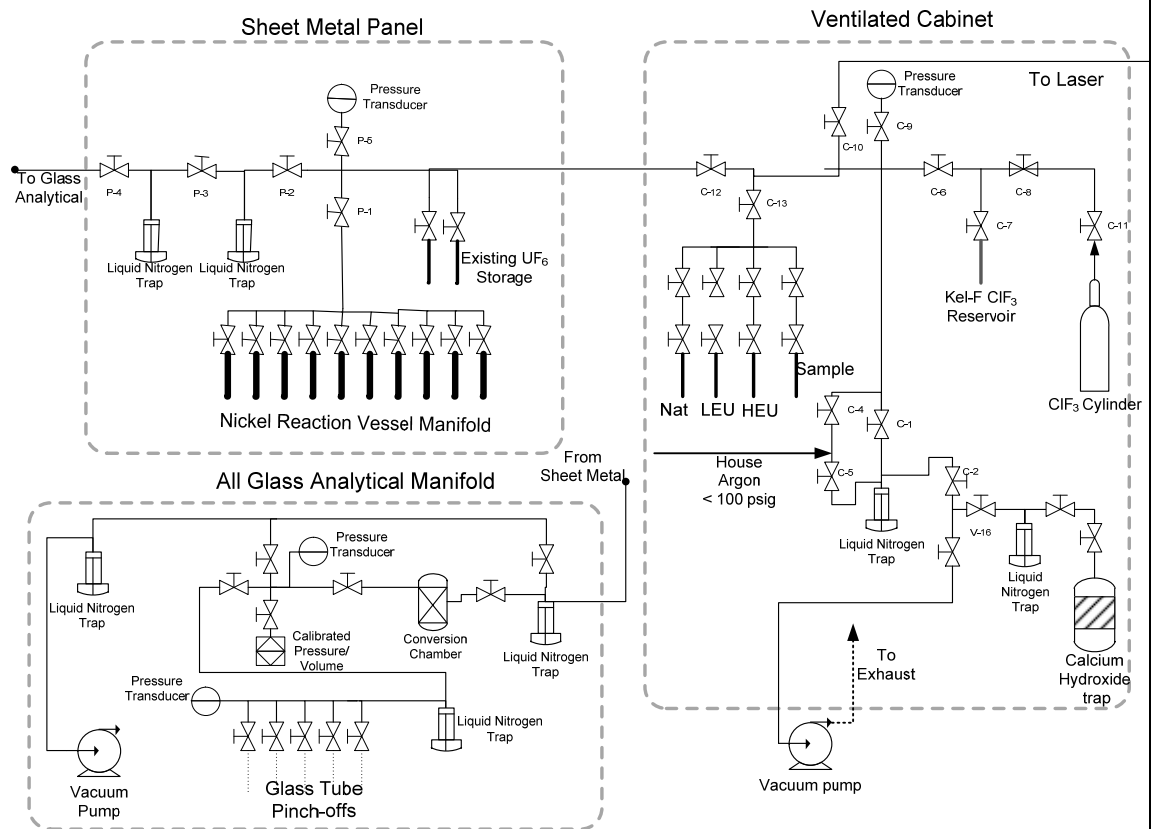


Figure 2-6: Image (top) and simplified one-line diagram (bottom) of the High Vacuum Fluorination System at Lawrence Livermore National Laboratory

Chapter 3 Method development and assessment of state-of-the-art quantitative image analysis for nuclear forensics

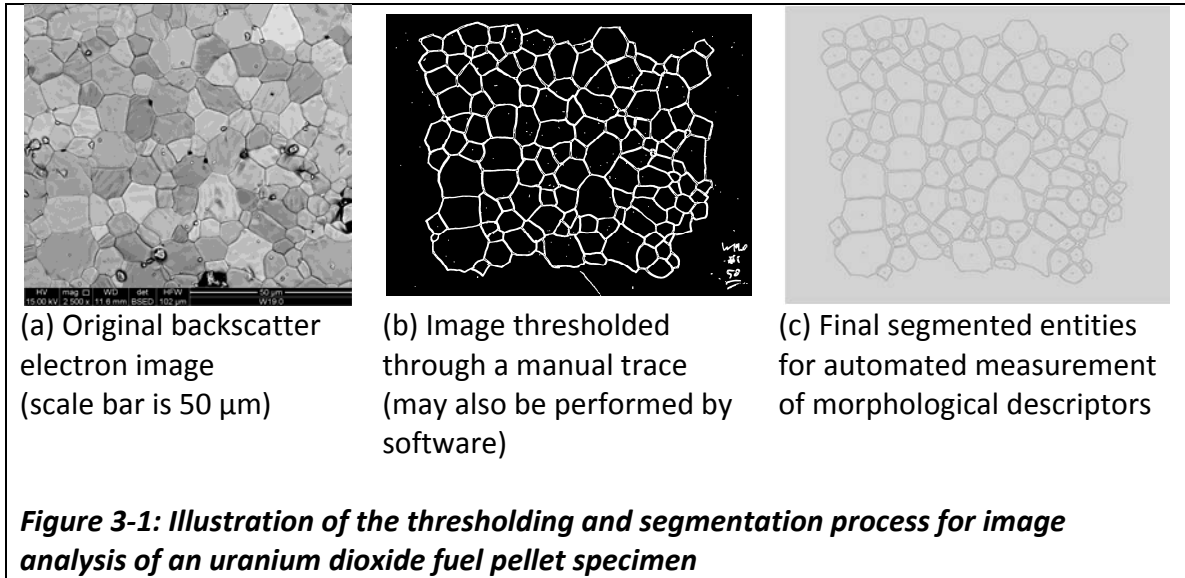
The objectives of this chapter are to assess available software tools used for quantitative image analysis assuming minimal development by the end-user and develop a recommended approach for examination of morphology as a signature in nuclear forensics. Quantitative image analysis is desired to strengthen the value of morphological signatures from simple qualitative comparisons of images. This study examined capabilities of image analysis for: (1) discrete particles, (2) planar grain structures in ceramics, and (3) textures of particle agglomerates.

3.1 Basics of applied image analysis

Image analysis is a technique where visual information is digitally transformed into numerical descriptors that can be used to quantitatively compare images. Image analysis is a growing field and its application to scanning electron microscopy (SEM) and optical microscopy are popular [63] [64], including use with ceramics [65]. An acquired image is transformed through thresholding and binary segmentation—processes that use various algorithms to identify lines or other connective features. Development of these algorithms is the subject of an entire field of computer science research and was not investigated beyond simple sensitivity studies to determine the most effective user defined values for a given algorithm with the uranium materials under study.

Figure 3-1 illustrates the thresholding and segmentation process for a fuel pellet. Once discrete units are segmented, measurements are made for various morphological descriptors. Unfortunately, many descriptors—a term used to describe aspects of an

image using mathematics—are used in the literature and universal definitions for descriptors do not exist, including those used by image analysis software packages.

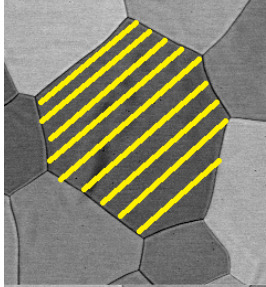
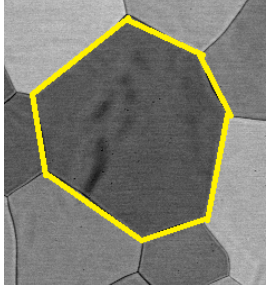
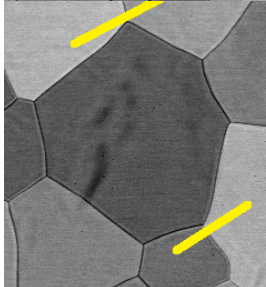
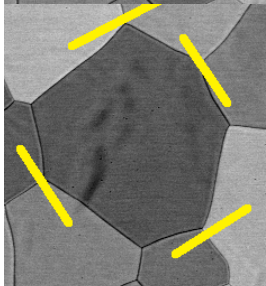
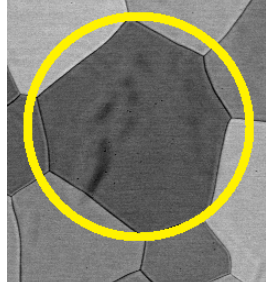


This work examined the ImageJ freeware developed by the National Institutes of Health [66] and the Morphological Assessment of Materials for Attribution (MAMA) software currently under development by the Los Alamos National Laboratory [67]. The descriptors examined in this work are defined in Table 3-1 and are consistent between the two software packages.

3.2 Existing methods and standards for image analysis

A survey of literature using image analysis to derive quantitative morphology of various samples revealed a general lack of standards, calibration, or other attempts to state the accuracy of the measured value compared to the real value. In most cases, researchers simply utilized the software output without any further verification. The application of image analysis to nuclear forensics necessitates a more robust approach that, at a minimum, provides an understanding of the sources and magnitudes of error.

Table 3-1: Definitions of common morphological descriptors

Descriptor	Definition	Example
Area	The number of pixels within an object converted into area	
Perimeter	The number of pixels around an object converted into distance	
Feret diameter	The distance between two parallel tangents of an object; typically reported as the maximum, but may also be specified for the minimum or average distances within the object. The Feret diameter is also commonly referred to as the caliper diameter.	
Aspect ratio	The distance of the major axis divided by the minor axis. Aspect ratio for a true circle is one.	
Circularity	A derived measure of the closeness to a true circle and is defined as $4\pi \text{ Area}/\text{Perimeter}^2$. Circularity for a true circle is one.	

As a result, the state of standardized methodologies, techniques, and supporting equipment was reviewed to gather best practices.

Historically, standardized methods for determining morphological characteristics of materials were crude. For example, ASTM [68] developed a standard for determining the average grain size in metals that included several simple methodologies such as visual comparison to reference grids and manual counts of grain boundaries intercepted by the diameter of a given circle size. This study judged the crudeness of these methods to potentially lose valuable forensic information and to incompletely leverage the advantages of improved quality and reduced imaging times offered by modern SEMs.

The International Standards Organization (ISO) developed a standard for the use of image analysis to determine particle size distributions applicable to static (as opposed to dynamic) images from both optical and SEM microscopy [69]. Although this standard focused on measurement of particle size, it was hoped that the approach could be adapted to the other relevant descriptors. However, a review of the standard revealed the lack of examination on the effects resulting from the user and the SEM-software system. In fact, ISO noted in numerous instances that parameters such as feature enhancement and thresholding depend on the imaging equipment and image analysis software. ISO recommends the use of either a certified standard graticule (a reference grid) or reference particles for development of calibration and distortion values to be reported with—but not actually used in the calculation of—particle size measurements. The ISO standard did not further address the effectiveness and accuracy of image analysis software algorithms.

This study found the commercial availability of morphological calibration standards for the SEM to be limited. Two products were identified and used for process development: (1) the Metrochip manufactured by MetroBoost, Santa Clara, California and (2) the MRS-3 measurement standard manufactured by Gellar MicroAnalytical Laboratory, Topsfield, Massachusetts. Both of these products provide high-contrast measurement features engineered for the SEM environment and are produced using semi-conductor manufacturing technologies.

As a result of this production method, neither manufacturer provides certified dimensions for most features. Instead, the Metrochip manufacturer claims traceability of the feature pitch (regular repetition, either edge to edge or center to center) with an accuracy at 100 ppm and a feature width at 10 %. The MRS-3 standard includes pitch patterns and planar arrays of circles and squares with a distribution of sizes. Unfortunately, the manufacturer reports measurements for these shape distributions as nominal, meaning that no absolute value can be given due to the level of uncertainty. Given the lack of availability of certified shape features, the nominal measurements were treated as the known values for this evaluation.

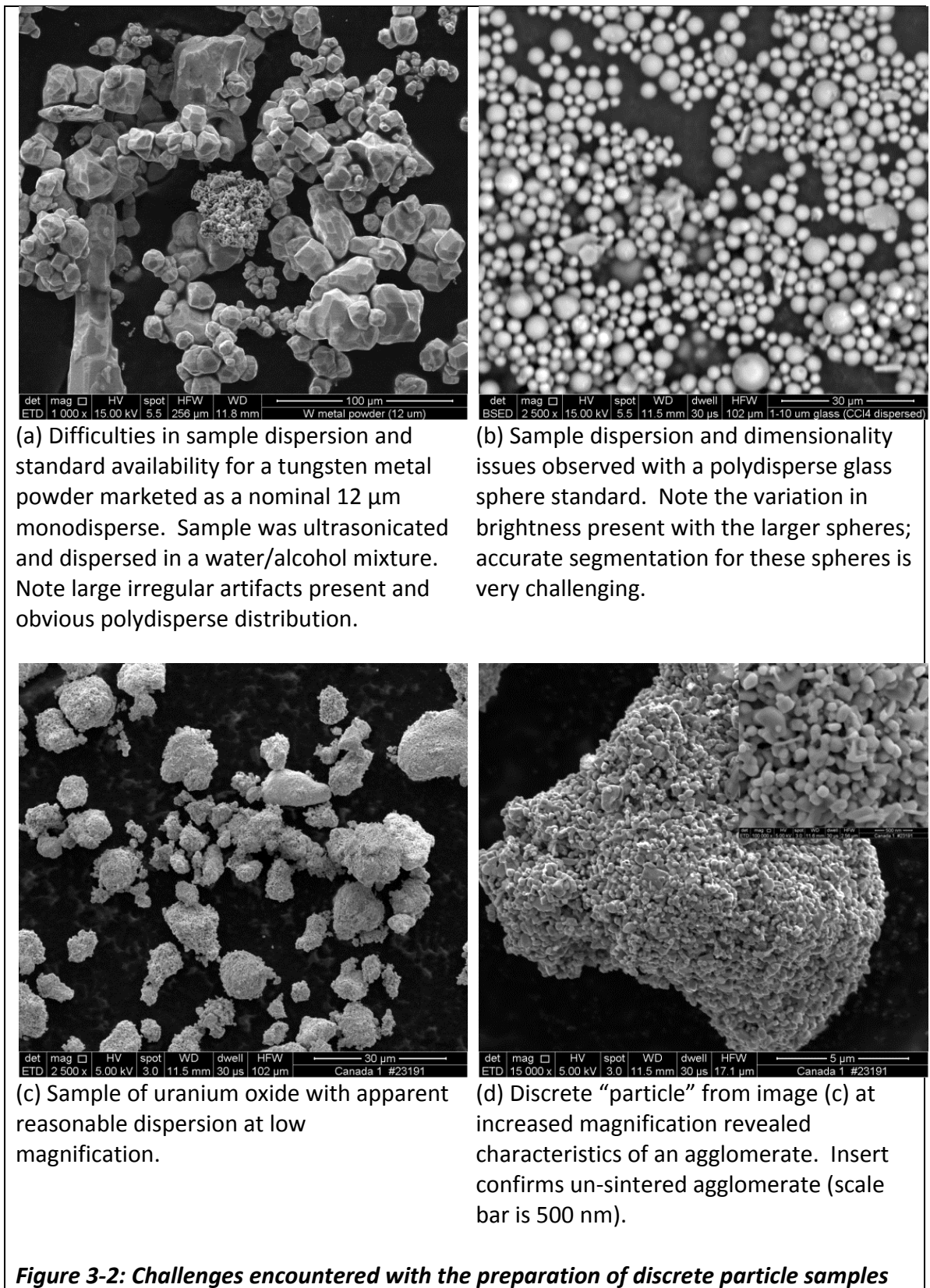
In theory, the use of a polydisperse particle standard would provide the best tool to assess the accuracy of the entire process from sampling, sample preparation and mounting, image capture, and image analysis. Several commercial vendors offer certified particle standards in monodisperse (defined as a distribution where 90 % of the particles are within 5 % of the median) or polydisperse (a wide distribution of sizes) varieties. The standards are typically made from glass, polystyrene, or metal and sold as

either dry powders or aqueous dispersions; however, neither type is explicitly designed for use in the SEM. Several types of particle standards were tested and the results are discussed below.

3.3 Challenges with sample preparation and image analysis for discrete particles

Testing various samples of discrete particles revealed concerns with sample dispersion, adequate standard availability, accurate segmenting (see Section 3.1) for particles with significant height, and agglomeration (Figure 3-2). Sample dispersion is a commonly encountered problem with image analysis, and while there are several recommended practices [69], an overall satisfactory method was not identified in this study. To improve dispersion, this study examined the use of ultrasonication, liquid dispersion with a variety of solvents and surfactants, and multiple direct transfers. In particular, samples with reasonable dispersion at lower magnifications revealed the presence of agglomerates for uranium oxide samples (Figure 3-2 c and d) when examined at higher magnifications. In such agglomerates, it is extremely difficult to discern the boundaries of a distinct grain.

This study also found the particle standards currently available to be problematic. Tungsten metal was explored to simulate the density of uranium materials, but the material received was obviously not monodispersed and included numerous, large irregular forms. Examination of available polystyrene or glass polydispersed sphere standards revealed non-spherical debris, and an additional issue with particle dimensionality. In an SEM image, the height of a particle can result in differences in the brightness of the signal (i.e., shadowing) across the exposed face.



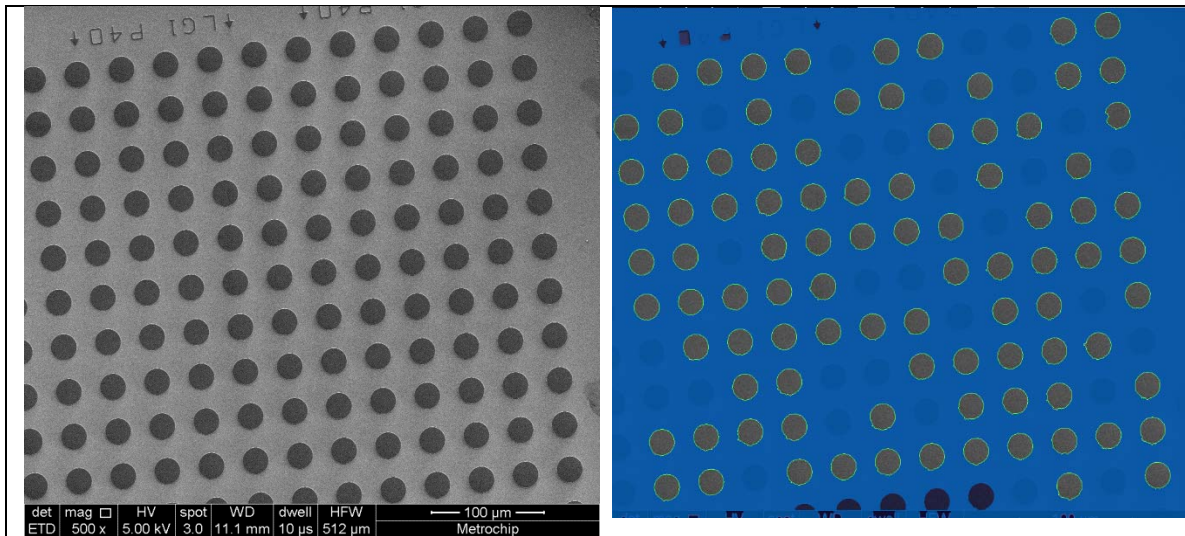
This difference in brightness created a significant impediment for the software to segment correctly the entire area of the sphere, since many of the segmentation algorithms are based on the detection of gradients in brightness.

Based on these observations, sample preparation techniques and image analysis technologies were determined to be insufficiently mature to proceed with accurate analysis of the morphologies of discrete uranium particles. Development and assessment efforts then focused on the utility of image analysis techniques for planar features, such as the ceramic sintered grain structure of a uranium dioxide fuel pellet. These types of materials do not require dispersion of the sample, thereby simplifying the process to imaging and subsequent software analysis.

3.4 Assessment of planar standards applicable to sintered grains

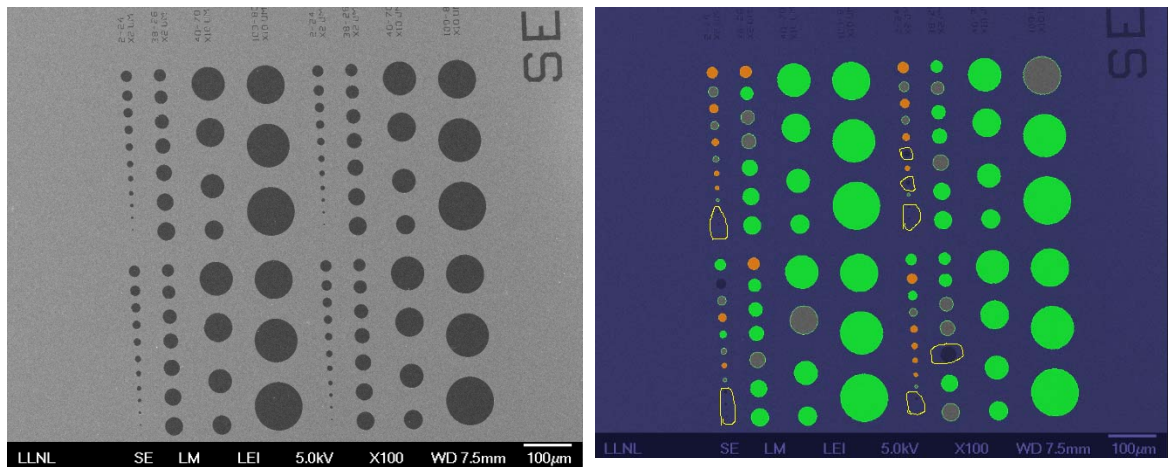
The Metrochip and MRS-3 standards were utilized to assess the efficacy of the imaging and automated software analysis process for planar features. Figure 3-3 demonstrates two of the primary issues encountered. First, the MAMA software experienced difficulty correctly identifying and segmenting the disk test features of the standard. Features examined included various sizes of disks, squares, and grids. Rates for missed features ranged from about 15 to 35 percent, depending on the feature type and size. It should be noted that the MAMA software allows users to manually correct missed features; however, the segmentation must be performed using an imprecise mouse interface and can be time consuming for complex samples.

Similar issues were encountered during limited testing using ImageJ on these test images. For both programs, adjustments to the image could be made to improve



(a) Original secondary electron image of a planar array of disks from the Metrochip.

(b) Segmented image of (a) revealed 25 percent of the disks were missed by the software. Note also the ragged edges apparent on some of the disks.



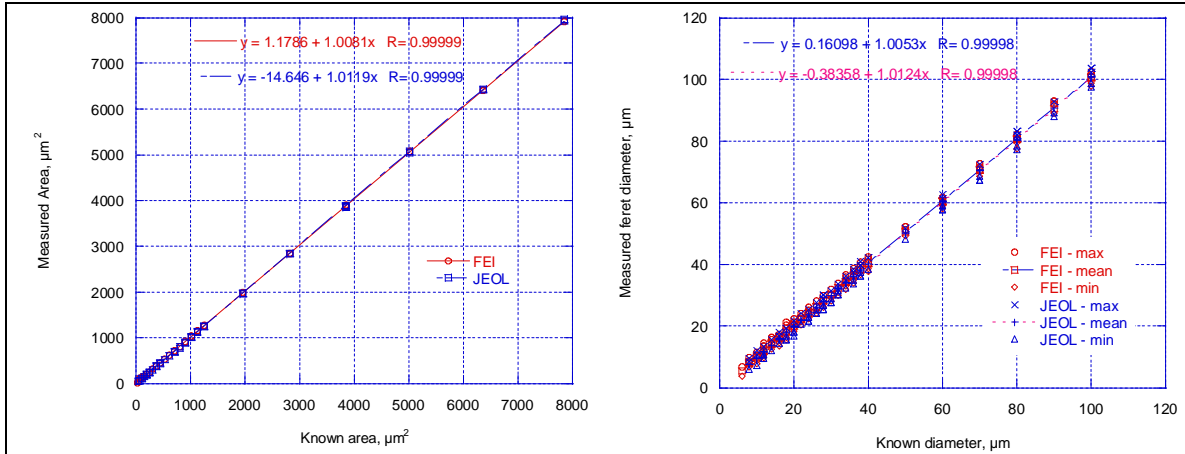
(c) Original secondary electron image of four sets of size distributed disks from the MRS-3 standard. Image acquired using the JEOL instrument.

(d) Segmented image of (c) revealed missing disks circled in yellow, as well as size and spatial variation in distortion. Shaded circles represent disks with circularity values of about 0.80-0.90 (green), 0.90-0.95 (grey), and 0.95-1.05 (orange).

Figure 3-3: Challenges encountered with imaging and analysis of planar features

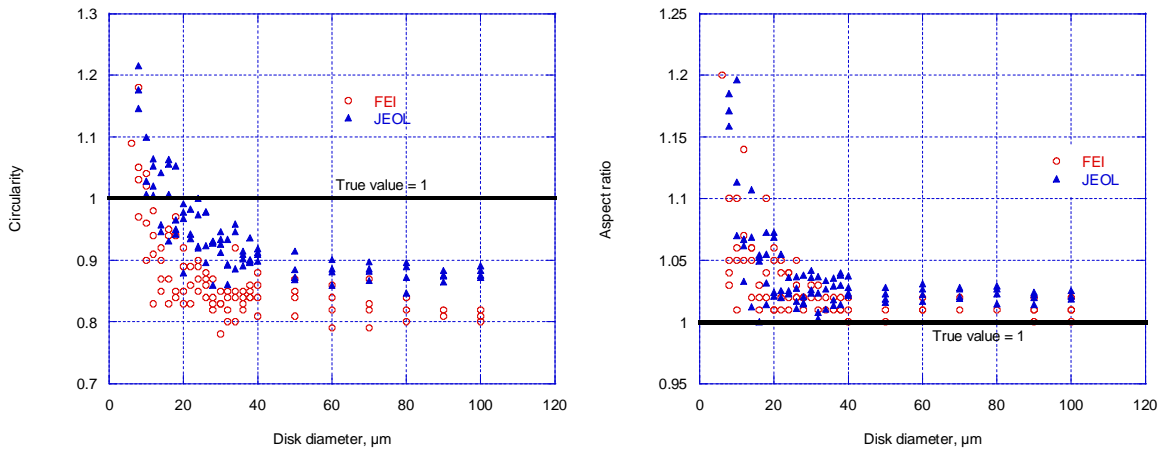
segmentation. However, these adjustments depended on the image under scrutiny and would not reproducibly result in the same effects when applied to different images. The use of such adjustments also raised the potential to increase bias introduced by the researcher.

The MRS-3 standard provided four sets of size distributed disks (Figure 3-3-4 c and d). This configuration allowed for the examination of measurement accuracy and reproducibility as a function of feature size and spatial location within the field of view. This evaluation also added a comparison between two SEM instruments (FEI and JEOL). Images from the FEI utilized the manufacturer's software algorithms for adjustment of image contrast, focus, and stigmatism. A skilled operator adjusted focus, contrast, and stigmatism for the images obtained from the JEOL. Results for selected morphological descriptors compared between SEM instruments revealed differences between each instrument (Figure 3-4).



(a) Area measurements were consistent between instruments and accurate to better than 2 percent across the range of sizes.

(b) Feret diameter measurements were consistent between instruments and accurate to within 1 percent for the mean and about 7 percent for the maximum and minimum values across the range of sizes.



(c) Circularity measurements were less accurate and varied considerably with disk size and instrument.

(d) Aspect ratio measurements were accurate to within better than 5 percent for both instruments when the feature size was at least 2 percent of the width of field of view.

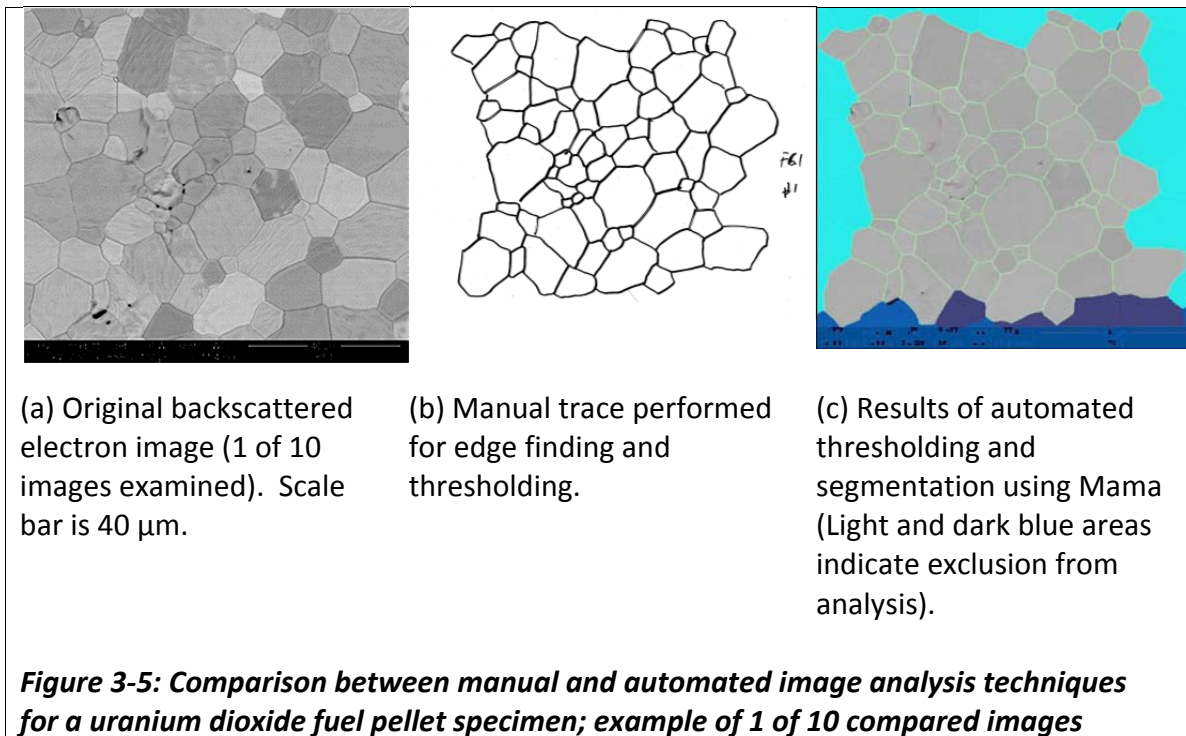
Figure 3-4: Comparison of morphological descriptors for the MRS-3 standard between different scanning electron microscopes

Conclusions resulting from these observations on the planar feature references included the following:

- Difficulties with segmentation were observed for images produced from both SEM instruments, particularly for smaller features. A limited size range would need to be established to enable reliable measurements
- Accuracy improved considerably for features with dimensions greater than about 2 percent of the width of the field of view
- Area measurements were accurate to better than 2 percent and consistent between instruments, likely because area provides the most signal per feature thereby minimizing error
- Feret diameters were accurate to 1 percent for the mean and about 7 percent for the maximum or minimum values—this error may have resulted from either ragged segmentation or distortions as function of spatial location in the field of view
- For description of feature shape, aspect ratio provided a more accurate and consistent measurement than circularity—error in the circularity measurements likely resulted from the perimeter established by a ragged segmentation

3.4.1 Comparison between automated and manual methods for planar features

The results of testing using planar standards indicated weaknesses in the accuracy of the segmentation processes and the need for human intervention to make corrections. Subsequently, in order to gauge the accuracy of the segmentation process a comparison was performed between an entirely manual process and the use of the MAMA software aided with manual correction. The objectives of the comparison were to: (1) ascertain whether the observed distributions of morphological descriptors were consistent, considering both methods relied on an element of human intervention, and (2) determine the most effective means of characterizing and reporting the distributions for use in nuclear forensic applications.



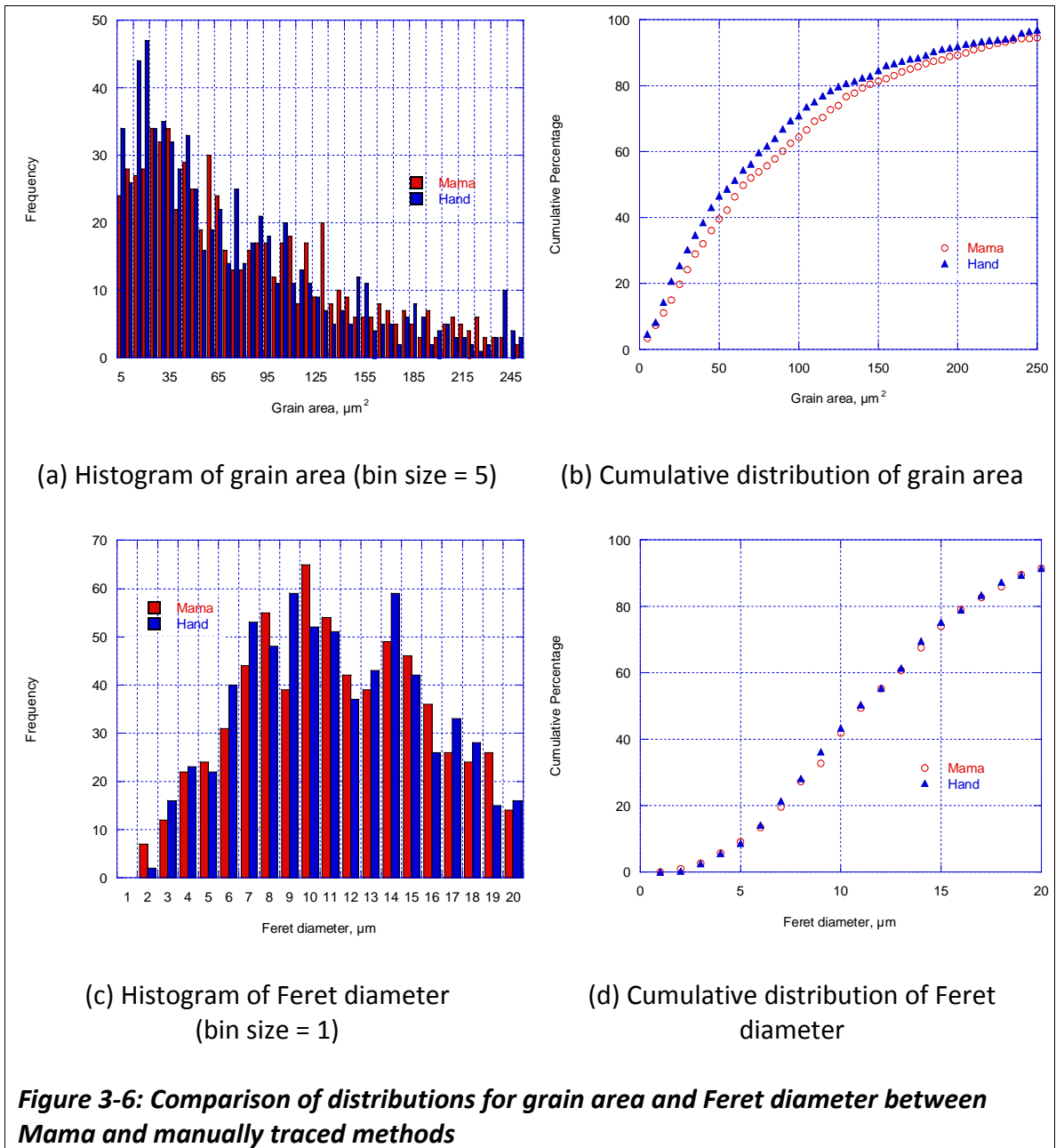
The comparison examined 10 images of a single uranium dioxide fuel pellet (Figure 3-5). For the manual method, grains were traced to perform edge finding, the

images scanned, and then analyzed using the ImageJ software. For the MAMA method, the original backscatter electron image was processed and then manual adjustments were performed to capture missed or incorrectly segmented grains. As anticipated, significant efficiencies were realized using MAMA with a process rate of less than 5 minutes per image as compared to about 20 minutes per image for the manual trace method.

Data for each of the five morphological descriptors previously discussed were collected. Data on particle size characteristics are often displayed using frequency histograms or cumulative distributions curves [70]. Figure 3-6 presents histograms and cumulative distribution curves for grain size area and Feret diameter. Note the total grain counts were 715 and 726 for the MAMA and manual methods, respectively. Alone, the observed difference of two percent in grain count suggested good consistency between the methods. Qualitative visual examination of the histograms also suggested good consistency; however, making such a visual comparison was significantly easier using the cumulative distribution curves. The use of cumulative distributions also provides the reader with immediate access to quantitative characteristics (e.g., median value). As a result, cumulative distribution curves were chosen to present all further comparisons of morphology data in this work.

This study also examined quantitative descriptions of distributions using several statistical approaches commonly used in particle analysis (Table 3-2). Data are presented as the values of the cumulative distribution at the 10th, 50th, and 90th percentiles (indicated as D_{xx}), as well as the derived term “Span”, defined as the difference between

D_{90} and D_{10} divided by D_{50} . These values provide direct, normalized values for comparison between samples without an inherent assumption in the shape of distribution. Data are also presented for the first four statistical moments—mean, variance, kurtosis, and skewness. The moments also provide measures of the shape of the data distribution, respectively the central tendency, spread, symmetry, and flatness.



The numerical comparisons in Table 3-2 suggest generally good agreement between the MAMA and manual methods. The difference between the measurements is generally less than 15 percent; however, the distributions for variance, kurtosis, and skewness are more substantial and explanations are not apparent. As an example of one of the exceptions, the difference on kurtosis for the Feret diameter measure was 10⁴ percent, despite differences of about 2 percent for the percentile measures and the mean. A visual comparison of the distributions (see Figure 3-6) further suggests strong agreement.

Table 3-2: Comparison of values for morphological descriptors on the same sample set between Mama (n =715) and manual analysis methods (n =726)

		D ₁₀	D ₅₀	D ₉₀	Span	Mean	Variance	Kurtosis	Skewness
Area, μm ²	Mama	13.2	65.9	203.7	2.9	91.0	6641.9	4.1	1.7
	Manual	11.5	57.8	183.5	3.0	79.7	5706.6	4.8	1.8
	Δ, %	14.6	14.1	11.0	2.9	14.3	16.4	14.6	7.5
Perimeter, μm	Mama	15.6	33.6	60.1	1.3	35.9	292.3	0.0	0.5
	Manual	15.0	31.9	57.1	1.3	34.1	275.3	0.5	0.7
	Δ, %	4.0	5.5	5.3	0.3	5.5	6.2	90.3	24.1
Feret Diameter, μm	Mama	5.2	11.2	19.1	1.2	11.9	36.4	28.1	2.8
	Manual	5.3	10.9	19.3	1.3	11.7	29.5	0.2	0.6
	Δ, %	2.6	2.5	0.6	2.4	2.0	23.5	15183.7	344.9
Circularity	Mama	0.6	0.7	0.8	0.2	0.7	0.0	5.9	-1.3
	Manual	0.6	0.7	0.8	0.2	0.7	0.0	3.2	-1.4
	Δ, %	5.8	3.7	3.0	10.2	4.3	5.8	81.8	8.4
Aspect Ratio	Mama	1.1	1.3	1.7	0.5	1.4	0.1	16.0	3.0
	Manual	1.1	1.4	2.0	0.6	1.5	0.2	6.1	2.1
	Δ, %	4.0	8.5	14.0	21.2	9.6	44.7	159.8	40.4

The testing with planar standards indicates that area, Feret diameter, and aspect ratio were the most accurate descriptors using image analysis. Given that some level of human intervention was required for both the manual and Mama methods, no reference point existed to gauge accuracy. Further, the differences between methods

for each of the five descriptors were similar, though the values for area were slightly higher than the other categories. As a result, no further information was gleaned from the comparison and the results from the planar testing were therefore applied in the recommendations below.

3.4.2 Recommendations and treatment of error for analysis of planar grains

The overall goal of this work is to make comparisons that can distinguish and classify samples of unknown origin against samples with known process pedigrees. In the examination of a given sample, two important sources of error and uncertainty can impact characterization: (1) sampling and imaging—how representative is the imaged sample of the true population and (2) measurement—for a measurement of a given morphological descriptor, how accurate is the value.

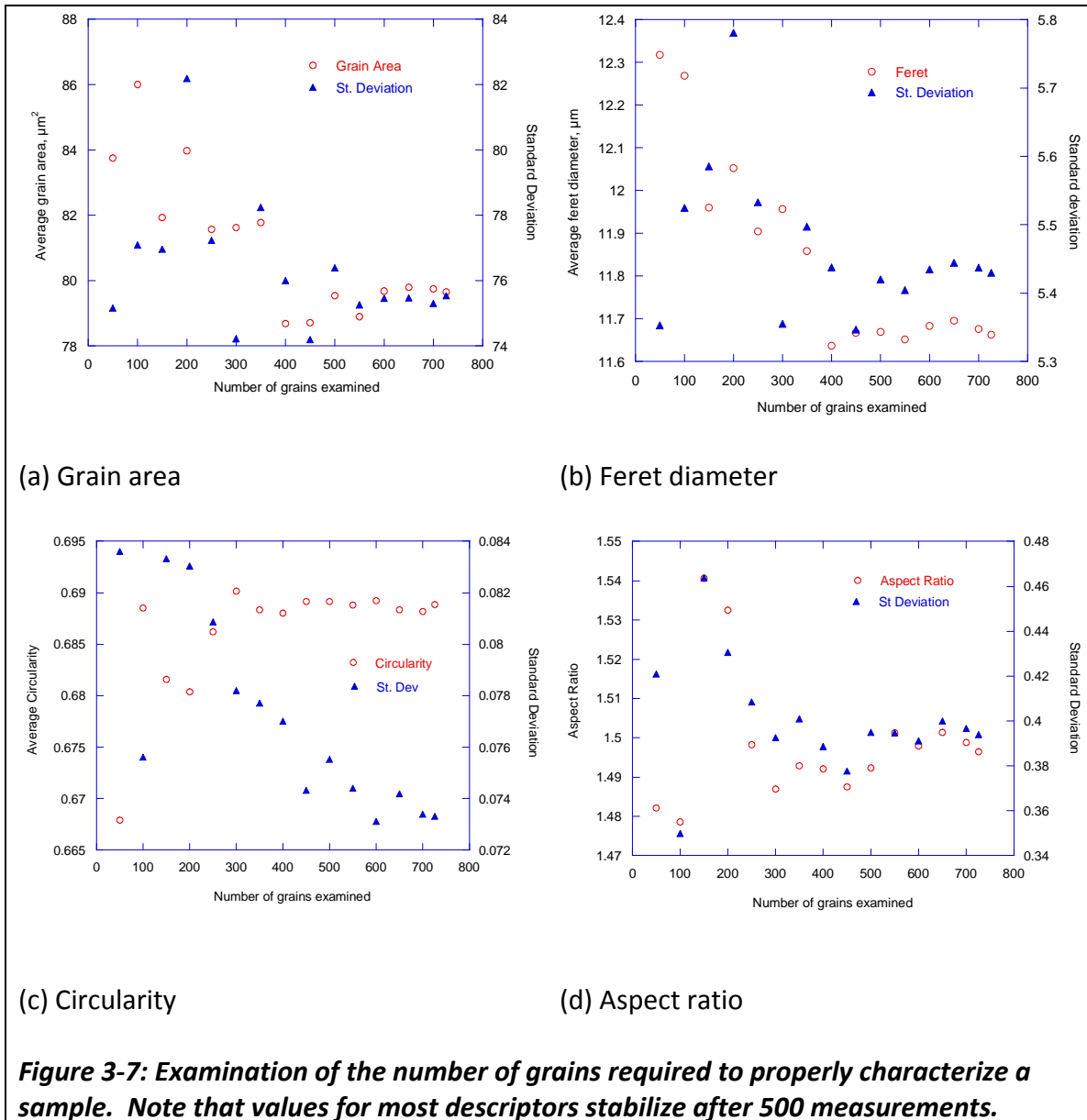
A discussion on the inaccuracies associated with the measurement of morphological descriptors was previously addressed (Sections 3.3 and 3.4). For comparison, the effect of sampling and imaging errors can largely be ignored if identical preparation and imaging methods are used. Nonetheless, the rigor required for forensic applications and the desire to generate large databases from multiple institutions using potentially different methodologies demands additional treatment to provide an overall error for the method.

Determining the error associated with imaging grains on the surface of a fuel pellet largely involves calculating the number of grains to be examined in order to make statistically valid statements. This inherently assumes that the population of grains is spatially homogenous (i.e., no localized differences in morphology).

Calculating the number of grains to be examined is a non-trivial problem. For perspective, a simple order of magnitude analysis indicated that a typical commercial fuel pellet requires about 9000 images, assuming a cross sectional area (0.9 cm diameter) is about $6.4 \times 10^7 \mu\text{m}^2$ with a mean grain area of about $100 \mu\text{m}^2$ at a field of view at 2500 X magnification (to facilitate manual correction during the segmentation process). Using these numbers, about 900 images would be necessary to directly measure 10 percent of the grain population of a single pellet. Given the time consuming manual intervention required to accurately segment grain images using current technology (> 5 minutes per image), this number represents an unrealistic task.

In the literature, Pons [63] recommended analysis of 80 to 100 particles for routine morphological analysis based upon a stability analysis of descriptors under investigation. The stability analysis examined the number of grain measurements required for the mean and standard deviation to plateau.

A sample fuel pellet was examined for the four descriptors under investigation in order to assess the number of grains needed to establish stable averages (Figure 3-7). The analysis revealed that values generally stabilized after the examination of about 500 grains. As a result, a minimum of 500 grains will be utilized in this work for forensic comparisons. However, a count of 500 grains represents a sample size of 0.07 percent of the grain population on a typical pellet face and additional quantification of error was desired. Using manual methods, analysis of 500 grains represents at least 45 minutes of work. Using automated methods with manual intervention, the necessary time is about 30 percent of the manual method, depending on the complexity of the sample.



Masuda and coworkers [71] [72] [73] performed an analytical estimation, and tested it using computer simulation, of the number of particles to be examined to determine the population mean with a stated error and confidence limit. This methodology was embraced in ISO Standard 13322-1:2004 [69]. The methodology assumed a log-normal distribution and required advance knowledge of the value of the geometric standard deviation. The assumption of a log-normal distribution may not

always be valid in nuclear forensic applications; however, there is considerable data to suggest that the log-normal distributions are common in man-made processes [70].

Likewise, the geometric standard deviations will not always be known ahead of time.

For the purposes of this evaluation, Masuda's methodology was applied to the pellet investigated in Figure 3-6 and Figure 3-7 in order to provide insights into the relative error and associated confidence for a measurement involving 500 grains. The principal equations from Appendix A of ISO 13322-1 are as follows:

$$\log n^* = -2 \log \delta + \log \omega$$
$$\omega = u^2 \alpha^2 \sigma^2 (2 c^2 \sigma^2 + 1)$$

where

n^* is the number of particles to be counted, taken as 500

δ is the relative error to be determined

u is a function of the desired confidence limit and provided by the standard

α is a constant associated with the process, taken as 2 by the standard

σ is the population standard deviation treated as $\ln \sigma_{\text{geo}}$ and found to be 0.44

c is a constant equal to $\beta + \alpha/2$, where β is 0 for distributions based on count

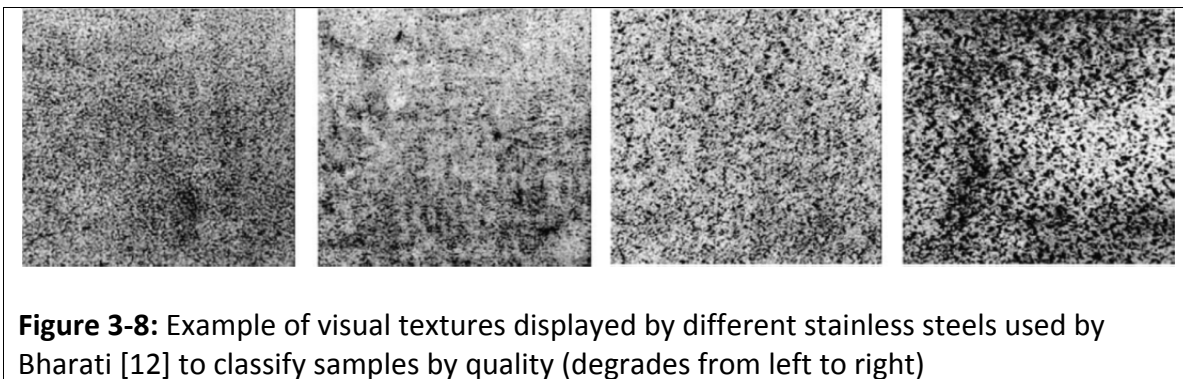
Using the value of u provided in the standard for 95 percent confidence, the relative error δ was found to be 0.19. Combining this sampling error with measurement errors previously determined (2 to 7 percent depending on the descriptor type) the overall error associated with the distribution of a given morphological descriptor for analysis of 500 grains was determined to be ± 0.20 with 95 percent confidence.

3.5 Texture as a quantitative tool for image analysis

Image analysis of textures is particularly useful when clearly defined grains are not present. As discussed previously, uranium materials have a propensity to

agglomerate, thus making texture analysis a prime candidate for sample classification in nuclear forensics.

The term “texture” connotes a qualitative description of the look and feel of a given surface. For example, in comparing road surfaces an asphalt pavement may be considered “smooth,” a gravel road “rough,” and a cobblestone pathway “bumpy.” These descriptions result from the periodicity, orientation, and variations in magnitudes of the observed surface features. Mathematics can be used in a similar manner to develop descriptions of visual textures. This science is the subject of considerable research in the fields of machine vision and image analysis. An example of visual textures used by Bharati et al [74] to demonstrate the use of texture to correctly classify samples of stainless steel based on quality is presented in Figure 3-9. Thorough background on the mathematics behind texture can be found in work by Tuceryan [75] and Soille [76] and will not be discussed in detail.



The texture analysis techniques investigated were those implemented within the MAMA software (version 0.9.6) available at the time of this study. The primary technique utilized is known as a pattern spectra or granulometric curve. These values

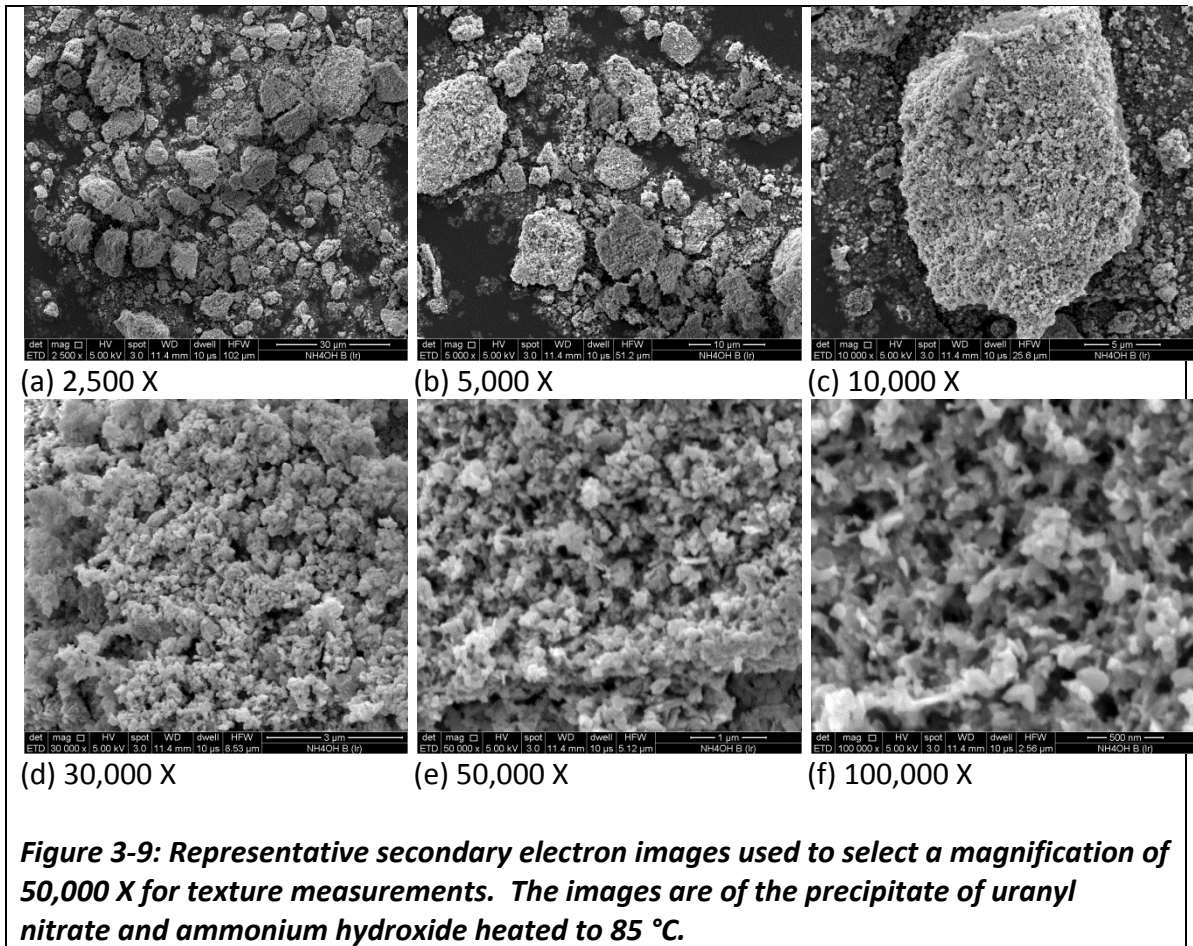
are generated through the comparison of a hypothetical structural element with a portion of the image—conceptually similar to applying a mathematical sieve to the image content, measuring what remains, changing the sieve size, and continuing onward. MAMA utilizes disks as the structural elements, which are then varied in both size and grey level to create the pattern spectra [67].

The second technique examined the spatial distribution of grey values in an image using an approach known as the gray-level co-occurrence matrix, first described by Haralick [77]. The MAMA software uses the gray-level co-occurrence implementation method developed by Connors [78], which results in outputs termed energy, entropy, difference moment, cluster shade, and cluster prominence. Each of these terms examines sets of pixels under different spatial relationships and provides values using the same size range and scale as the pattern spectra.

Although texture is now widely used in many image analysis applications, no reference materials or other standards currently exist to validate texture results. Consequently, the accuracy of the algorithms was assumed and efforts instead focused on applying and refining the existing texture tools for the uranium precipitates and oxides under examination. Application and refinement of the texture tool required the following: (1) selection of the magnification for examination of texture, (2) determination of the optimal user-defined parameters for the texture algorithms, and (3) identification of the error associated with method.

A qualitative visual comparison of the same uranium precipitate sample under a range of magnifications was used to select the optimal magnification for texture analysis

(Figure 3-9). The comparison suggested an optimum at a magnification of 50,000 X at which the field of view is entirely consumed with sample and the microstructure is clearly evident. Lower magnifications resulted in a reduced signal-to-noise ratio resulting from a field of view that includes significant background.



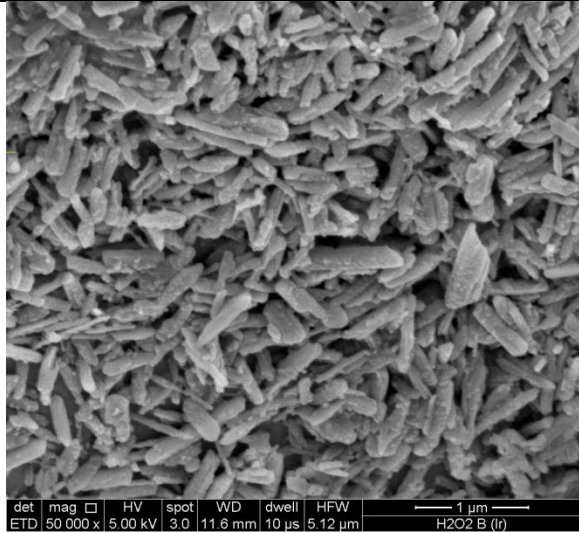
Higher magnifications also resulted in reduced signal-to-noise ratios and an increased fraction of the field of view occupied by vacant space in the microstructure.

The optimal values for the user-defined scale range and step size parameters were determined through the examination of four of the common uranium precipitates dried to 85 °C (Figure 3-10). In texture applications, scale is measured by the number of

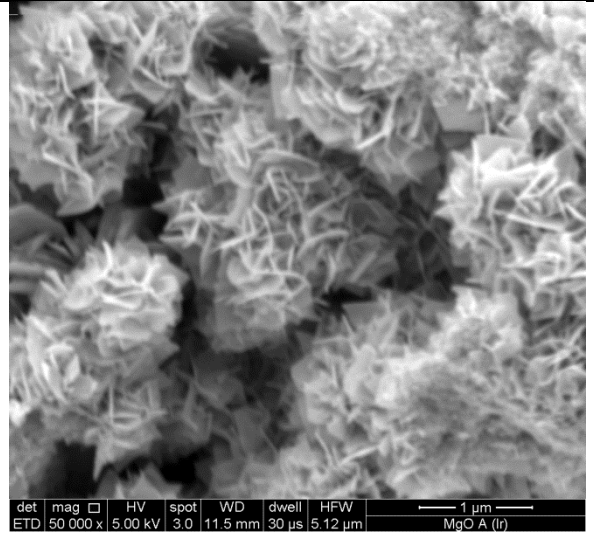
pixels, with the minimum scale representing the size of the texture feature and the maximum scale representing the distance between repeating features. The step size represents the number of measurements taken across the scale range. The scale ranges examined included minimums of 1, 5, and 10 pixels with corresponding maximums of 40, 60, and 80 and step sizes of 10 and 20 pixels. Image areas were manually selected when background or significant air gaps were evident, otherwise the entire image was measured. The scale range and step size that maximized the differences between each precipitate was determined to be scale range of 1 to 80 with a step size of 2.

The pattern spectra for hydrogen peroxide and ammonium hydroxide derived precipitates were similar despite distinct visual differences (Figure 3-11 a and c). This observation suggested that additional opportunities exist to refine or apply alternative texture algorithms to improve matching and classification concepts. However, such work is beyond the scope of this study.

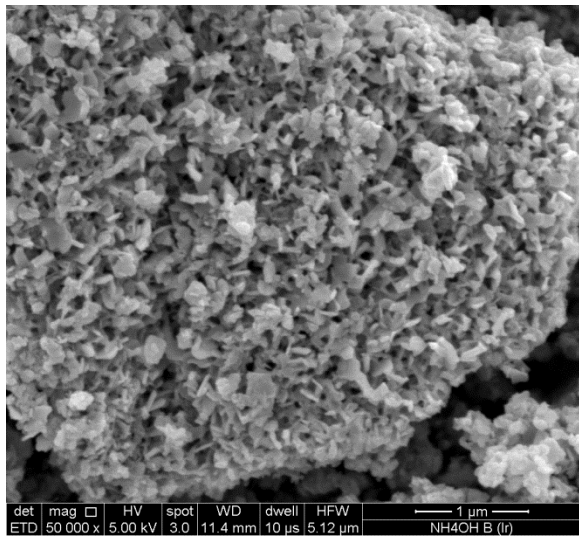
Next, pattern spectra for 10 images of the same material were compared to provide an indication of the variability within a sample and thus a measure of the sensitivity of the texture method (Figure 3-11). The variation of the pattern spectra for the 10 images was quantified by determining the coefficient of variation (ratio of the standard deviation to the mean) at each structural element size. Across the full-scale range of structural elements, the coefficient of variation averaged 0.13 with a variance of 0.01 (Figure 3-11). The significance of this sensitivity to distinguish uranium materials of different process origins will be explored in Chapter 5.



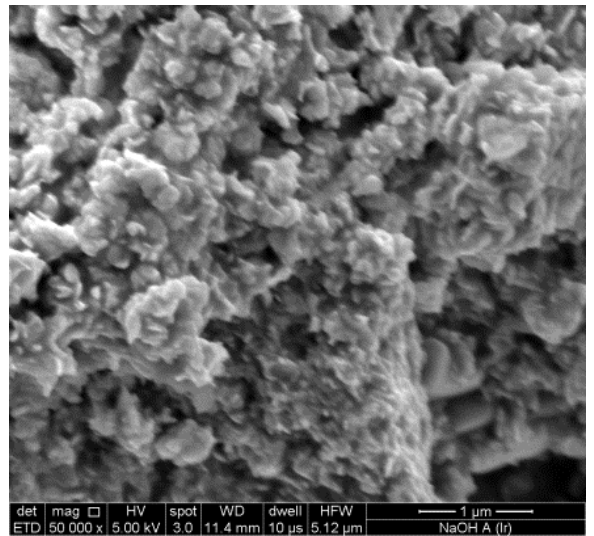
(a) Hydrogen peroxide



(b) Magnesia

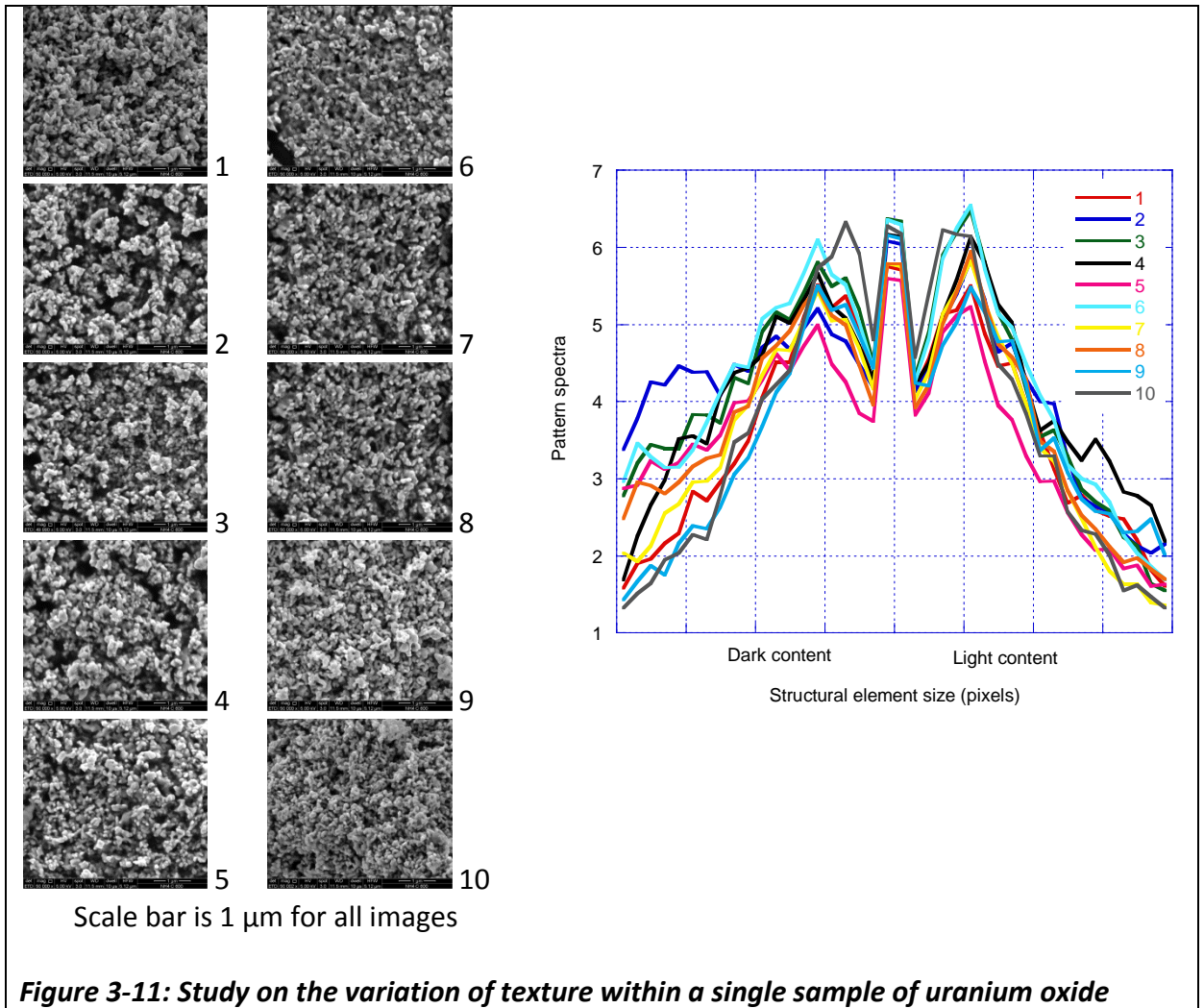


(c) Ammonium hydroxide



(d) Sodium hydroxide

Figure 3-10: Secondary electron images of uranium precipitates used to determine the optimal user-defined values for scale and step size in texture measurements.



3.6 Discussion of alternatives to image analysis for morphological study

Alternative particle characterization techniques to image analysis are widely described at the textbook level [70]; however, some discussion on their viability for nuclear forensic applications is warranted. Two techniques were further examined as part of this evaluation: (1) laser scattering methods, due to their popularity and (2) the electrical sensing zone method (also known as the Coulter counting method), due to the unique measurements offered by this technique.

In a laser scattering technique, the light scattering pattern of flowing, dispersed particles is measured and deconvoluted into a particle size distribution using one of several theoretical models (e.g., Fraunhofer or Mie) [70]. These models generally assume a spherical geometry and perform thousands of measurements on a given particle as it is continuously cycled through the measurement cell producing a distribution by volume, rather than number. For non-spherical particles, corrections can be applied to convert observed distribution into spherical equivalents; however, the scattering will depend on the particle's orientation during each measurement. Hence, a single non-spherical particle measured using laser scattering will result in a distribution of sizes. A good comparison between laser scattering and static image analysis methods is provided by Tinke [79].

Since the materials of interest in nuclear forensics are generally non-spherical, laser scattering was determined to be non-ideal because of the significant abstraction associated with the data. Other drawbacks to this method included typically large sample sizes (forensic applications may be limited to small quantities) and the common use of pressurized air as the dispersion medium (safety concerns with radioactive materials).

In the electrical sensing zone method, particles are suspended in a weak electrolyte and individually passed through an aperture with an applied electrical voltage. As each particle passes through the aperture, changes are detected in the impedance, which are correlated to the volume characteristics of the particle. As a

result, the electrical sensing zone technique provides number, volume, mass, and surface area size distributions in a single measurement.

Of particular interest to nuclear forensics, powders are dispersed in liquid, thereby alleviating the dispersion issues encountered in preparation of samples for microscopy, as well as offering improved confinement of radioactive contamination. Potential concerns with the method include a larger minimum detectable particle as compared to other methods (~100 versus 10 nm), and limitations on the size range that can be served by a given an aperture (typically ranges about 10 to 60 percent of the aperture size).

3.7 Suggested areas for further study

Based on the research performed during this assessment, the following recommendations are made for future work:

- The nuclear forensics community ought to develop morphology standards for use in SEM and associated image analysis processes. Comparisons across institutions and contributions to databases will be weakened without such standards.
- Additional focus is warranted on new sample preparation techniques. Adequate sample dispersion continues to be the Achilles heel for the application of image analysis to nuclear forensics.
- Image analysis software should be developed using better integration with the SEM hardware. Today, imaging is highly dependent on visual judgments made by the operator; however, the aspects of a good image determined by the human eye may not necessarily correspond to those aspects best utilized by algorithms.

- Alternative particle characterization technologies should be investigated that offer true measurements on individual particles that bypass the pitfalls of sample dispersion encountered with microscopy. The electrical sensing zone devices show particular promise for this purpose.

Chapter 4 Process signatures in uranium precipitates and oxide powders

The objectives of this chapter are to systematically identify the set of uranium precipitates and oxides most likely to be encountered in a nuclear forensics application, develop a set of samples for study, and characterize the sample set for potential signatures indicative of chemical process history. Examination of the chemical lifecycle of uranium revealed the prevalence of uranium oxides originating from the thermal treatment of precipitates from solutions of the uranyl ion during chemical separations.

Consequently, a set of reference uranium materials was synthesized in the laboratory using the commonly encountered aqueous precipitation reactions (Chapter 2). This set of laboratory-derived exemplars was characterized using the conventional techniques of powder x-ray diffraction (XRD), specific surface area, thermogravimetric methods, as well as the novel application of near-infrared reflectance (NIR) spectroscopy. Similar analyses were performed using a set of real-world samples, with process information obtained from the literature, to provide a comparison between materials synthesized in the laboratory and samples representative of actual industrial processes.

Results of this study indicate that powder XRD, thermogravimetric methods, and NIR spectroscopy can be used to properly identify uranium oxides and precipitates for the purposes of discerning their chemical process history. Furthermore, the development of NIR offers a new, potentially field-deployable forensic tool for rapid and non-destructive analysis. Specific surface area measurements were insufficient to distinguish process history. Overall, these techniques were unable to distinguish

identical compounds derived through different processes; however, morphology was found to be successful in this respect and is the subject of Chapter 5.

4.1 Identification of processes likely to produce uranium oxides

There are a variety of chemical processes that are utilized in the lifecycle of uranium [23][22][21] (See Chapter 2). These processes were systematically examined for common chemical forms, which reveal the prevalence of uranium oxides (UO_2 , U_3O_8 , and UO_3) (Figure 4-1). Uranium oxides serve both as an important process intermediate (e.g., a precursor to fluorination and a recycle form) and a final product form for application to nuclear fuel ceramics (i.e., UO_2) and storage (i.e., U_3O_8), due to their thermodynamic chemical stability.

Processes that produce uranium oxides (Table 4-1) can be grouped into three categories: (1) thermal oxidation of the products from precipitation reactions in aqueous systems used for elemental separation during ore concentration, chemical purification, or recycling, (2) solid phase thermal decomposition reactions, and (3) gas phase reactions associated with the direct conversion of uranium hexafluoride (UF_6) to uranium oxide. This study placed greater emphasis on the aqueous precipitation routes given their commonality in uranium ore concentration, refinement, and recycling processes. Selected dry processes, primarily direct oxidation of metal, nitrate, and fluorides, were examined as part of the study on morphology in Chapter 5. The study of oxides resulting from the gas phase reactions was impeded by the scarcity of available commercial samples and the complexities of reproducing these techniques in the laboratory.

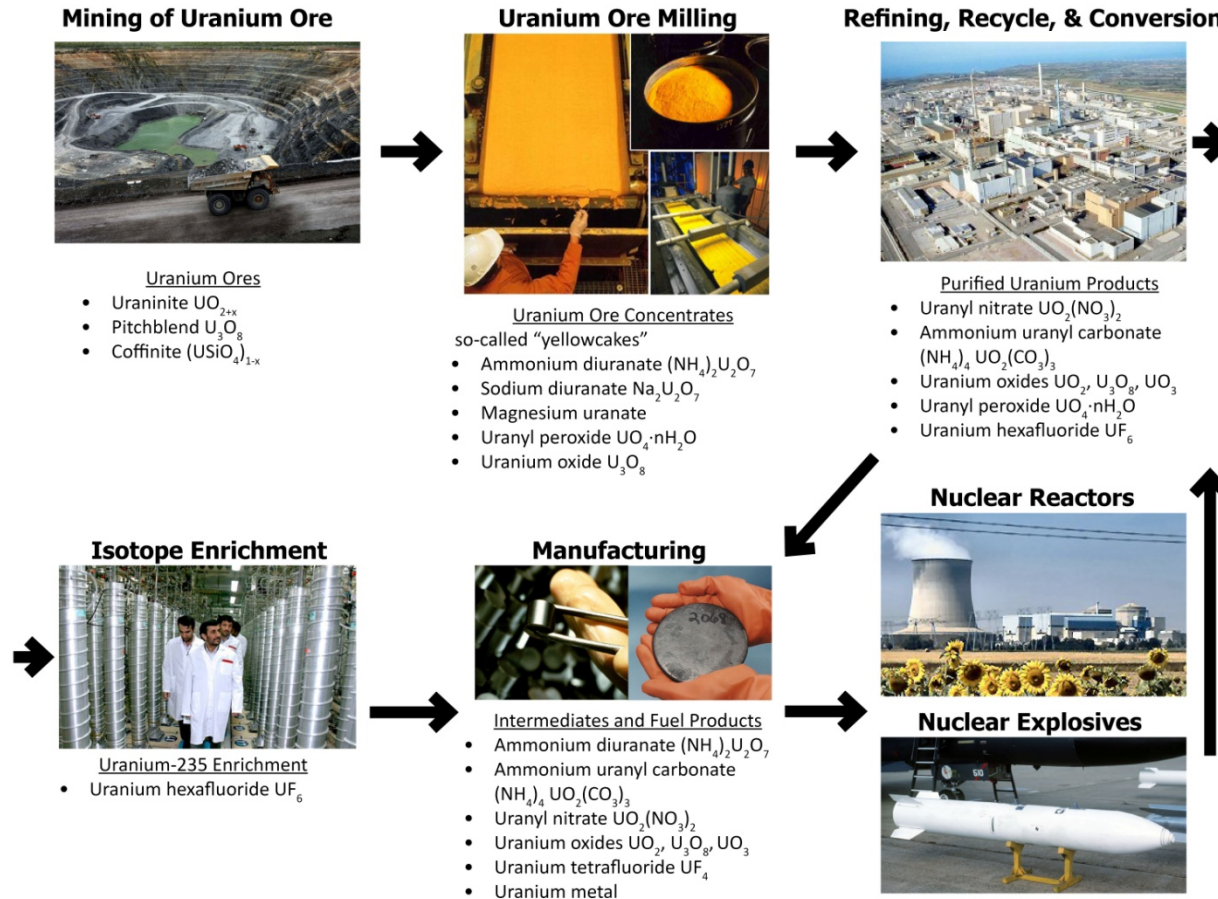


Figure 4-1: Common chemical forms of uranium in the fuel cycles. Images adapted from [80]–[86].

In commonly utilized aqueous processing schemes, whether for initial concentration from ore or purification activities associated with refining or recycling, uranium is generally precipitated from solution using one of five reagents (Table 4-2): (1) ammonium hydroxide (or ammonia gas), (2) hydrogen peroxide, (3) ammonium carbonate (or ammonia and carbon dioxide gases), (4) magnesia, or (5) sodium hydroxide (see Section 2.1.1) [23] [22] [24]. Following precipitation, samples are generally given a heat treatment to either dry or oxidize the material at temperatures typically ranging from 50 to 800 °C.

Table 4-1: Summary of processes identified to likely result in uranium oxides

Category	Process
Oxidation of precipitates used to produce uranium ore concentrates from mining operations	Ammonium hydroxide / ammonia gas Sodium hydroxide Magnesium oxide Hydrogen peroxide
Oxidation of precipitates in uranium purification processes (refining or recycling)	Ammonium hydroxide / ammonia gas Ammonium carbonate Hydrogen peroxide
Solid phase thermal reactions	Denitration of solutions and solids Direct oxidation of metal, hydrides, fluorides
Gas phase reactions	Direct flame reactions Pyrohydrolysis in a rotary kiln or fluidized bed reactor

This heat treatment will decompose the precipitate as a function of temperature depending on its chemistry. A list of generalized reactions (Table 4-2) provides the routes for various uranium oxide species formation. Of particular forensic interest, reactions 1–3 utilize organic precipitants that are susceptible to thermal decomposition and volatilization, while reactions 4 and 5 leave persistent Mg^{2+} and Na^+ ions. The

persistence of elevated concentrations of these ions in product oxides facilitates identification of these materials and their process history. As a result, this study placed greater emphasis on ascertaining whether process history could be discerned for oxides derived from the volatile precipitants.

Table 4-2: Generalized reactions for the commons precipitations of uranium from solution

Volatile	$2\text{UO}_2(\text{NO}_3)_2 + 6 \text{NH}_4\text{OH} \rightarrow (\text{NH}_4)_2\text{U}_2\text{O}_7 \downarrow + 4 \text{NH}_4\text{NO}_3 + 3 \text{H}_2\text{O}$	1
	$\text{UO}_2(\text{NO}_3)_2 + \text{H}_2\text{O}_2 \rightarrow \text{UO}_4 \cdot 2\text{H}_2\text{O} \downarrow + \text{HNO}_3$	2
	$\text{UO}_2(\text{NO}_3)_2 \cdot 6 \text{H}_2\text{O} + 6 \text{NH}_3 + 3\text{CO}_2 \rightarrow (\text{NH}_4)_4 \text{UO}_2 (\text{CO}_3)_3 \downarrow + 2 \text{NH}_4\text{NO}_3$	3
Persistent	$\text{UO}_2(\text{NO}_3)_2 + \text{MgO} + x\text{H}_2\text{O} \rightarrow \text{UO}_3 \cdot x\text{H}_2\text{O} \downarrow + \text{Mg}(\text{NO}_3)_2$	4
	$2\text{UO}_2(\text{NO}_3)_2 + 2 \text{NaOH} \rightarrow \text{Na}_2\text{U}_2\text{O}_7 + 4\text{NaNO}_3 + 3\text{H}_2\text{O}$	5

The primary analytical techniques employed in this chapter represent approaches that have not previously been systematically examined for utility in nuclear forensic applications. These techniques were investigated to evaluate their own utility, and develop a highly characterized set of exemplars using traditional accepted practices in order to form a solid foundation for subsequent application to novel methods. One novel method, NIR spectroscopy is examined in this chapter, and a second, morphology, is the entire focus of Chapter 5.

4.2 Methods

This study utilized a combination of laboratory synthesized materials serving as exemplars and samples of real-world origin. This unique, paired sample set provided enhanced confidence that observed signatures are robust and representative of

industrial factors not easily replicated in a pristine laboratory setting. For example, scaling effects on mixing and mass transport and nuances based on variations in flow sheet conditions may create differences in product characteristics.

4.2.1 Synthesis of uranium precipitates and oxide exemplars

A suite of uranium powder exemplars was synthesized using a variety of precipitants and temperature conditions, as well as some novel conversions from initial solid phases (Table 4-3). All precipitation reactions utilized laboratory stocks of uranyl nitrate hexahydrate. Precipitations were performed from 1.0 M uranyl nitrate stock solutions and generally 1.0 M reagents. The concentrations were chosen as generically representative for the reactions of interest rather than to mimic specific process conditions, as flow sheet concentrations vary in practice. As a result, this work inherently assumed that concentrations of uranyl and reagents did not result in primary effects—future efforts should confirm the validity of this assumption. Furthermore, the work was performed using nitrate species in the starting solutions. In practice, many uranium ore milling operations operate flow sheets based on the sulfate system. While it is unlikely that the anion plays a significant role in the signatures studied, future verification of this assumption would be prudent.

Reactions were generally carried out in disposable centrifuge tubes, utilizing manual mixing with the end-point monitored using pH paper. As an exception, the precipitation using ammonium carbonate was performed in a filtration funnel, as the product was previously reported to be readily filterable. Following precipitation, slurries were centrifuged, decanted, and rinsed with deionized water before final solid and

liquid separation by centrifugation. Precipitate cakes were air dried in an 85 °C oven overnight and confirmed to be at constant mass. Dried precipitates were then comminuted by hand with a mortar and pestle. These powders served as the base material for additional heat treatments, which were performed in a muffle furnace with the powder placed in acid cleaned quartz or alumina boats. Selected samples were reduced to the UO₂ phase in a tube furnace using a flowing atmosphere of 4 percent hydrogen in argon.

Table 4-3: Summary of conditions used to synthesize uranium oxide exemplars

Type	Agent	Preparation Conditions	Temps., °C
Aqueous precipitations	Ammonium hydroxide	1.0 M uranyl nitrate precipitated with 1.0 M ammonium hydroxide solution to a pH ~8	85, 150, 400 600, 750
	Ammonia gas	Gas bubbled into 0.5 M uranyl nitrate solution to a pH ~8	85
	Sodium hydroxide	1.0 M uranyl nitrate precipitated with 1.0 M sodium hydroxide solution to a pH ~8	85, 150, 400 600, 750
	Magnesia	1.0 M uranyl nitrate precipitated with 15 wt % magnesia slurry	85, 150, 400 600, 750
	Hydrogen peroxide	1.0 M uranyl nitrate precipitated with 30 % hydrogen peroxide solution	85, 150, 400 600, 750
	Ammonium carbonate	1.0 M uranyl nitrate precipitated with saturated ammonium carbonate to pH ~8	85, 150, 400 600, 750
	Solid processes	Direct metal oxidation	Uranium metal turnings directly oxidized in (1) air and (2) moist air
Oxidation of uranium hydride		Uranium metal turnings hydrided and then oxidized in flowing moist argon	400
Denitration		Ground uranyl nitrate oxidized in air	300, 600
Oxidation of tetrafluoride		Uranium tetrafluoride powder oxidized in moist, flowing air	400

For the solid processes, materials were treated as described in Table 4-3.

Generally, the starting compounds were ground by hand in mortar and pestle, transferred to an acid cleaned furnace boat, and then heated under the stated

conditions. Reactions involving flowing argon, hydrogen, or humidified atmospheres were performed in a quartz tube furnace. Uranium metal turnings were first rinsed in acetone and dilute nitric acid in order to remove mineral oil residue from storage and eliminate minor oxide layers.

4.2.2 Analytical Methods

Thermogravimetric analysis and differential scanning calorimetry were performed using a Netzsch Jupiter simultaneous thermal analysis instrument. Sample sizes were approximately 10 mg with a compressed air flow rate of 20 mL/min and heating rate of 20 °C/min for the range 25–750 °C. All precipitates were initially dried to constant mass at 85 °C.

Specific surface area measurements were performed using a Quantachrome Quadrasorb instrument along 20 point adsorption and desorption isotherms using nitrogen as the absorbate at liquid nitrogen temperature. Prior to analysis, samples were degassed at 50 °C under vacuum for at least 12 hours. Quality control was established with periodic measurements of Quantachrome's reference standards 2001 ($10.24 \pm 0.57 \text{ m}^2/\text{g}$) and 2007 ($2.85 \pm 0.20 \text{ m}^2/\text{g}$). Calculations of the specific surface area were performed using the instrument software based on Brauner, Emmett and Teller theory [55]. Isotherms were taken using krypton as the absorbate in an attempt to obtain porosity information; however, these were found to be unsuccessful due to a pore size range that was too large.

Powder XRD was performed using a Bruker-AXS D8 Advance powder diffractometer using a step size of 0.019 at a rate of 2 seconds per step. Prior to

analysis, samples were hand ground in a mortar and pestle and deposited using a dispersion in alcohol onto a low-background silicon wafer sample holder fitted with a dome for confinement of the dispersible radioactive material. Phase identification was performed using Bruker's DIFFRACplus EVA software package against the 2009 database issued by the International Centre for Diffraction Data.

NIR spectra were acquired using an Analytical Spectral Devices Inc. Labspec Pro spectrometer with three detectors spanning the spectral range from 350–1000, 1000–1800, and 1800–2500 nm. Fiber optic bundles transmitted light from a 20 W tungsten halogen source to and from the sample. Spectra were scanned in 1 nm steps with a spectral resolution of approximately 10 nm. The samples required no preparation and 10 spectra were acquired for each sample in about 1 second. Spectral processing was accomplished using The Unscrambler[®] software package, version 10.1 (CAMO Inc, Oslo Norway). Raw spectra were preprocessed and presented using the standard normal variate to minimize baseline shifts and multiplicative interferences of particle size as recommended by Barnes [87].

4.2.3 Real-world samples

Lawrence Livermore National Laboratory (LLNL) possesses a large collection of uranium ore concentrate samples obtained from various sources. The literature was comprehensively reviewed to identify applicable process information pertinent to these samples (Table 4-4). For purposes of this study, process parameters of interest included the precipitation reagent and the conditions of post-precipitation thermal treatments

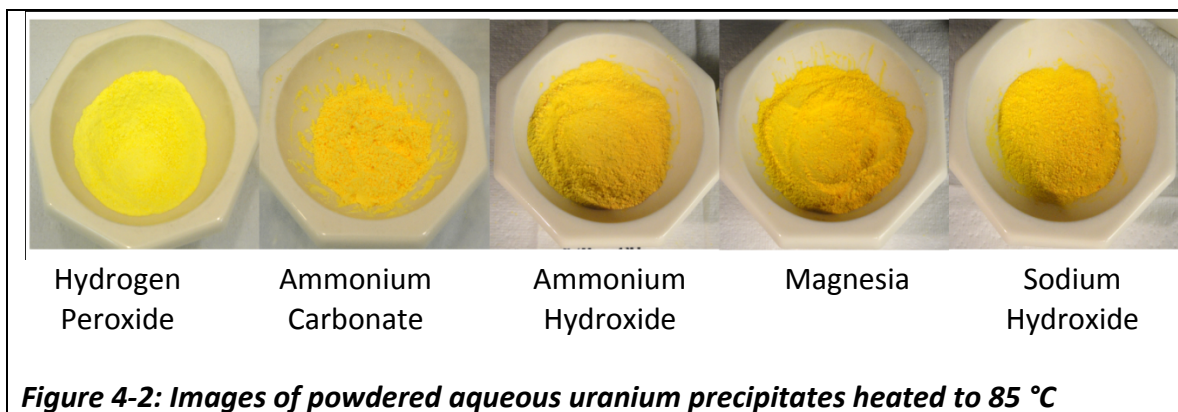
(i.e., drying or oxidation). The results of phase analysis performed using XRD are also provided in Table 4-4.

Table 4-4: Process history derived from the literature and phase analysis of several commercially produced uranium ore concentrates

Precipitant	Plant	Location	Temperature, °C	References	Major phases determined by XRD
Hydrogen peroxide	Crow Butte	Dawes County, Nebraska	Vacuum dryer	[88]	UO ₄ ·2H ₂ O, U ₃ O ₈
	Rabbit Lake	Saskatchewan, Canada	110	[89] [90][91]	UO ₄ ·2H ₂ O, UO ₃ ·0.8H ₂ O
	El Mesquite	Duval County, TX	177	[92]	UO ₄ ·2H ₂ O, UO ₄ ·4H ₂ O, UO ₃ ·2H ₂ O
	Irigaray	Johnson County, Wyoming	Not reported	[93]	UO ₄ ·2H ₂ O, UO ₄ ·4H ₂ O
	Uranium Resources Inc	Duval County, Texas	Vacuum dryer	[94]	UO ₄ ·2H ₂ O, 2UO ₃ ·NH ₃ ·3H ₂ O
	Mobil	Bruni, TX or Crownpoint, NM	Not reported	[95]	UO ₄ ·2H ₂ O
Ammonia	Ranger	Northern Territory, Australia	600–800	[96] [97]	UO ₃ and U ₃ O ₈
	Key Lake	Saskatchewan, Canada	750	[98] [99][100] [90]	U ₃ O ₈
	Federal American Partners	Gas Hills, WY	600	[101][24]	U ₃ O ₈
	Olympic Dam	South Australia	760	[91][90]	U ₃ O ₈
	Rössing	Swakopmund, Namibia	500	[102] [103][90]	UO ₃ and U ₃ O ₈
	NUFCOR	Westonaria, South Africa	500	[104]	UO ₃ and U ₃ O ₈
	Milliken Lake	Elliot Lake, Ontario, Canada	Not reported	[105] [22] [106]	2UO ₃ ·3NH ₃ ·3H ₂ O
Magnesia	South Alligator	N. Territory, Australia	84	[96]	No match
	Anaconda Bluewater Facility	Grants, New Mexico	90–120	[24]	No match
	Rum Jungle	N. Territory, Australia	320	[96]	No match
	COMUF	Mounana, Gabon	Not reported	[107]	No match
	Dyno	Bancroft, Ontario, Canada	Not reported	[108]	No match
	Gunnar	Lake Athabasca, Saskatchewan, Canada	Steam heated	[105]	No match
Sodium hydroxide	Ranstad	Sweden	Not Reported	[109] [110]	Na(UO ₂)O(OH)
	SOMAIR	Niamey, Niger	Not Reported	[111]	Na(UO ₂)O(OH) Na ₂ U ₂ O ₇
	Susquehanna-Western, Inc	Falls City, TX	Not Reported	[24]	No match
	El Dorado	Beaverlodge, Canada	Not reported	[91] [101][105] [22]	Na _{0.35} UO _{2.95} Na _{0.31} U ₃ O ₈ , U ₃ O ₈

4.3 Results and Discussion

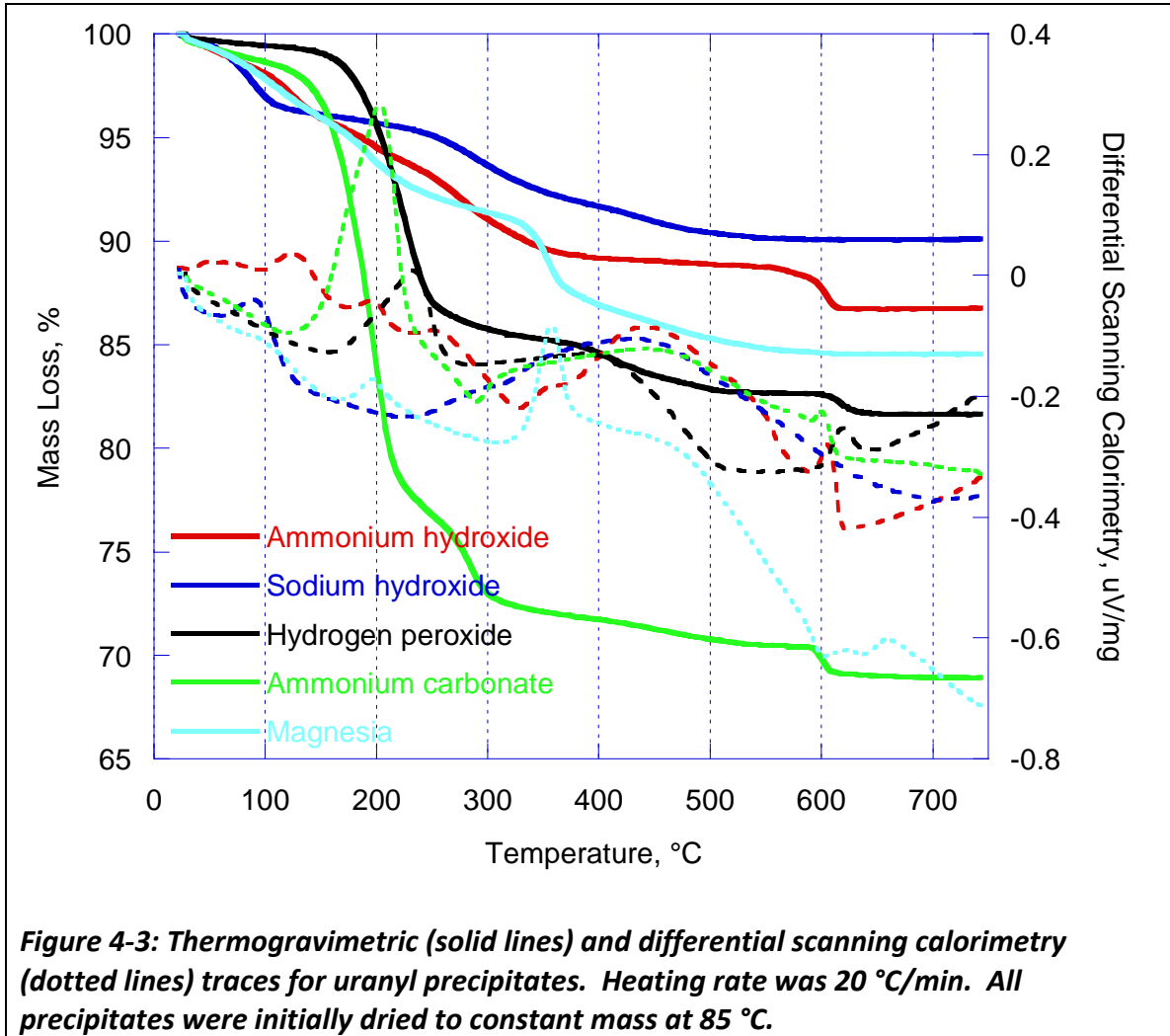
The laboratory-derived precipitates and resulting oxides formed the stereotypical yellow (Figure 4-2) and blackish-green powders commonly associated with these uranium compounds. While there are color differences detectable by eye, the objective of this study is to develop unbiased, quantifiable, and reliable techniques suitable for forensic applications.



4.3.1 Thermogravimetric methods can distinguish uranyl precipitates

Simultaneous thermogravimetric analysis and differential scanning calorimetry performed on each of the uranyl precipitate compounds revealed distinct curves for mass loss and reaction energetics (Figure 4-3). While this result is expected for different initial chemical compounds, thermogravimetric methods have not been explored for the purposes of nuclear forensics. This observation is surprising given that thermogravimetric methods are widely applied in conventional forensics, simple to perform, and are widely used to characterize unknown materials; for example, the differentiation of glove materials [112]. Other than the application by Hausen [113] for the general study of yellow cakes, the thermogravimetric behavior of uranyl compounds

has been limited to the study of individual compounds rather than comparative applications.



Characteristic temperatures and associated mass losses were obtained from the thermogravimetric behaviors (Figure 4-3) and compiled with corroborating literature for each precipitate (Table 4-5). The literature provides insights into the specific reaction mechanisms as a function of temperature. Overall, thermogravimetric analysis demonstrated the ability to distinguish uranium precipitates produced by different processes. As discussed below in Section 4.3.3, phase analysis of uranium precipitates

using powder XRD analysis often yields incomplete or amorphous results.

Thermogravimetric analysis is complementary technique, which utilizes only a small sample size and provides a relatively quick analysis. The addition of coupled off-gas analysis instrumentation (either infrared or mass spectroscopy) could further strengthen thermogravimetric analysis as a robust tool for the analytical characterization of a sample of interest to nuclear forensics.

Table 4-5: Thermogravimetric signatures for common uranyl precipitates

Precipitate	Characteristic Temperature, °C	Associated Mass Loss, %	Characteristic Energetic Events, °C	Corroborating References
Ammonium hydroxide	100–350	10	125, 195, 260	[114][115][116]
Ammonium carbonate	120–210	20	200, 600	[117][118][119]
Hydrogen peroxide	150–250	12	235	[120][121]
Sodium hydroxide	100–500	6	90	[122][123]
Magnesia	330–370	3	195, 360	none

4.3.2 Specific surface area is not indicative of process history

Specific surface areas were measured for the laboratory-derived exemplars and selected real-world powders (Tables 4-6 and 4-7). The measurements revealed a wide range of specific surface areas across the different precipitation chemistries. In general, a trend of decreasing surface area with increasing process temperature was observed for the laboratory-derived exemplars, with the exception of a minor increase in surface area noted for several of the 400 °C samples. This result is consistent with the observations of Woolfrey [124], who noted maximum specific surface areas associated with the thermal decomposition of ammonium uranates occurred in the range of 350–

450 °C. Woolfrey explained the increase in surface area as the likely result of the competition between the increased surface area associated with the decomposition of the initial precipitate and the decreased surface area associated with sintering of the resulting oxide phases. His theory appears reasonable.

While a comparison of the specific surfaces areas for the exemplars at 85 °C suggests the potential to discriminate based on precipitation process, these differences are minimized as process temperature is increased. Furthermore, examination of the real-world samples suggests that substantial overlap exists in the range of surface areas produced by a given precipitation process with most samples in the range of 1–20 m²/g. This wide range is likely the result of the accumulation of impacts from additional process parameters, such as mixing and mass transfer effects, liquid-solid separations, and solids handling.

Table 4-6: Measured specific surface area values for laboratory-derived exemplars, m²/g

Process	85 °C		150 °C		400 °C		600 °C		750 °C	
	Mean	Error	Mean	Error	Mean	Error	Mean	Error	Mean	Error
Ammonium hydroxide	13.54	0.07	13.11	0.15	15.18	0.09	7.83	0.36	1.82	0.12
Ammonia gas	32.98	0.14	--	--	--	--	--	--	--	--
Sodium hydroxide	20.55	0.42	13.66	0.20	13.08	0.05	11.20	0.20	2.83	--
Magnesia	37.54	0.13	26.51	0.90	44.37	0.27	16.64	0.17	7.23	0.06
Hydrogen peroxide	6.92	0.20	7.81	0.22	6.56	--	1.66	0.05	1.05	0.15
Ammonium carbonate	1.96	0.26	--	--	--	--	2.39	0.12	--	--

Note: Error expressed as the 95 % confidence level of 3 measurements

Table 4-7: Measured specific surface areas for selected real-world samples, m²/g

Precipitant	Sample	Mean	Error
Hydrogen peroxide	Crow Butte	6.44	0.08
	Rabbit Lake	5.26	0.21
	Mobil	8.67	0.41
Ammonia	Ranger	4.15	0.03
	Rössing	4.10	0.13
	NUFCOR	12.18	0.14
Magnesia	South Alligator	18.27	0.07
	Anaconda	21.13	0.11
	COMUF	9.35	0.06
Sodium hydroxide	Ranstad	1.76	0.07
	SOMAÄR	6.61	0.11
	El Dorado	20.82	0.08

Note: Error expressed as the 95 % confidence level of 3 measurements

Additional research on process dependent trends with specific surface area was performed using data obtained from the literature for samples of UO₂ (Table 4-8), which also permitted the examination of the gas phase process routes. The resulting data (Figure 4-4) reinforce the two general conclusions of this study: (1) specific surface areas do not appear to correlate with production method in a manner sufficient to discriminate process history and (2) specific surface areas tend to decrease with increasing process temperature.

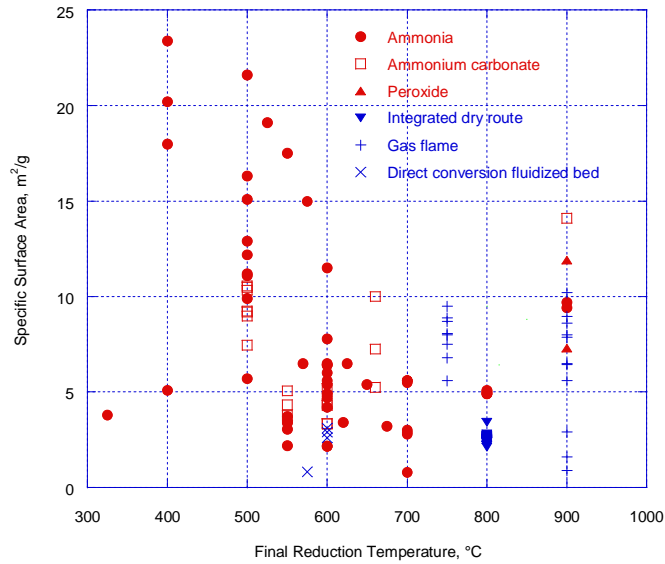


Figure 4-4: Literature values for the specific surface area of uranium dioxide as a function of temperature and production process. Aqueous and gas phase processes are noted in red and blue, respectively.

Table 4-8: Summary of literature sources used in Figure 4-4

Author	Process examined
Woolfrey [125]	Ammonia
Janov [26]	Ammonia
Balakrishna [126]	Ammonia
Ching-Tsven Huang [127]	Ammonia
Doi [128]	Ammonia
Kim [129]	Ammonium carbonate
Lee [130]	Ammonium carbonate
Pan [131]	Ammonium carbonate
Choi [132]	Ammonium carbonate
Marajofsky [133]	Ammonium carbonate
Lee and Yang [134]	Ammonium carbonate
Clayton [135]	Ammonia, ammonia carbonate, peroxide,
Hastings [18]	Peroxide
Ion [33]	Integrated dry route
Knudsen [136]	Direct conversion fluidized bed
Carter [137]	Integrate dry route
de Hollander [138]	Flame
Dada [36]	Flame

4.3.3 Phase analysis by powder XRD

Powder XRD was performed on each of the laboratory derived exemplars and real-world samples to determine chemical phase. Identified chemical phases as a function of precipitation process and thermal treatment are provided in Table 4-9 for the exemplars and in Table 4-4 for the real-world samples. In general, the identified phases correlate well between both sample sets when precipitant and temperature treatment are considered. Phase information as a function of temperature also agrees well with the previously discussed thermogravimetric methods in Section 4.3.1 and the associated literature. However, XRD analysis alone is insufficient to ascertain definitively the process history for many of the samples as indicated by the shaded regions in Table 4-9. Results are summarized below for each precipitant:

Hydrogen peroxide: At low temperatures (85 and 150 °C), the exemplars were determined to be uranyl peroxide hydrates, known as studite and metastudite ($\text{UO}_4 \cdot 2\text{H}_2\text{O}$ and $\text{UO}_4 \cdot 4\text{H}_2\text{O}$). These same phases were identified in the real-world samples with reported low process temperatures (Rabbit Lake and El Mesquite). Based on this information, a low process temperature can reasonably be inferred for the Crow Point, Irigaray, Uranium Resources Inc., and Mobil samples. At increased temperatures, the peroxide decomposes into UO_3 at 400 °C, which is in turn converted to U_3O_8 at 600 and 750 °C.

Ammonium hydroxide: At low temperatures (85 and 150 °C), precipitates with ammonia were found to form ammonia uranium oxide hydrates ($\text{UO}_3 \cdot z\text{NH}_3 \cdot x\text{H}_2\text{O}$).

These compounds represent a mixture of stoichiometries and are commonly referred to in industry as ammonium uranates or ammonium diuranate.

The Milliken Lake sample matches this phase, suggesting that it was dried at similar temperatures. At increased temperatures, the ammonium and water volatilize leaving UO_3 at 400 °C, which is in turn converted to U_3O_8 at 600 and 750 °C. The other six real-world samples display identical process history and resulting phases of U_3O_8 .

Ammonium carbonate: At 85 °C, the original ammonium uranyl carbonate precipitate is found. At increased temperatures, the precipitate is decomposed into UO_3 and U_3O_8 . The real-world samples available for this precipitant have very limited source information; however, XRD identified ammonium uranyl carbonate, suggesting a low temperature drying of an ammonium carbonate precipitate.

Magnesia: At low temperatures (85–400 °C), uranyl precipitated with magnesia results in an amorphous phase not readily identifiable through XRD pattern matching. This result is consistent with all of the real-world samples processed at low temperatures and which also resulted in amorphous XRD patterns. Crystallinity returns at 600 and 750 °C with the formation of magnesium uranium oxides of various stoichiometries. For further confirmation, several of the real-world samples were heated to 750 °C and the resulting powders were identified as magnesium uranium oxides of the same stoichiometries as the exemplars. The presence of a significant magnesium rich phase is a strong indicator that magnesia was used as a precipitant.

Table 4-9: Major phase composition of laboratory-derived exemplars by powder x-ray diffraction

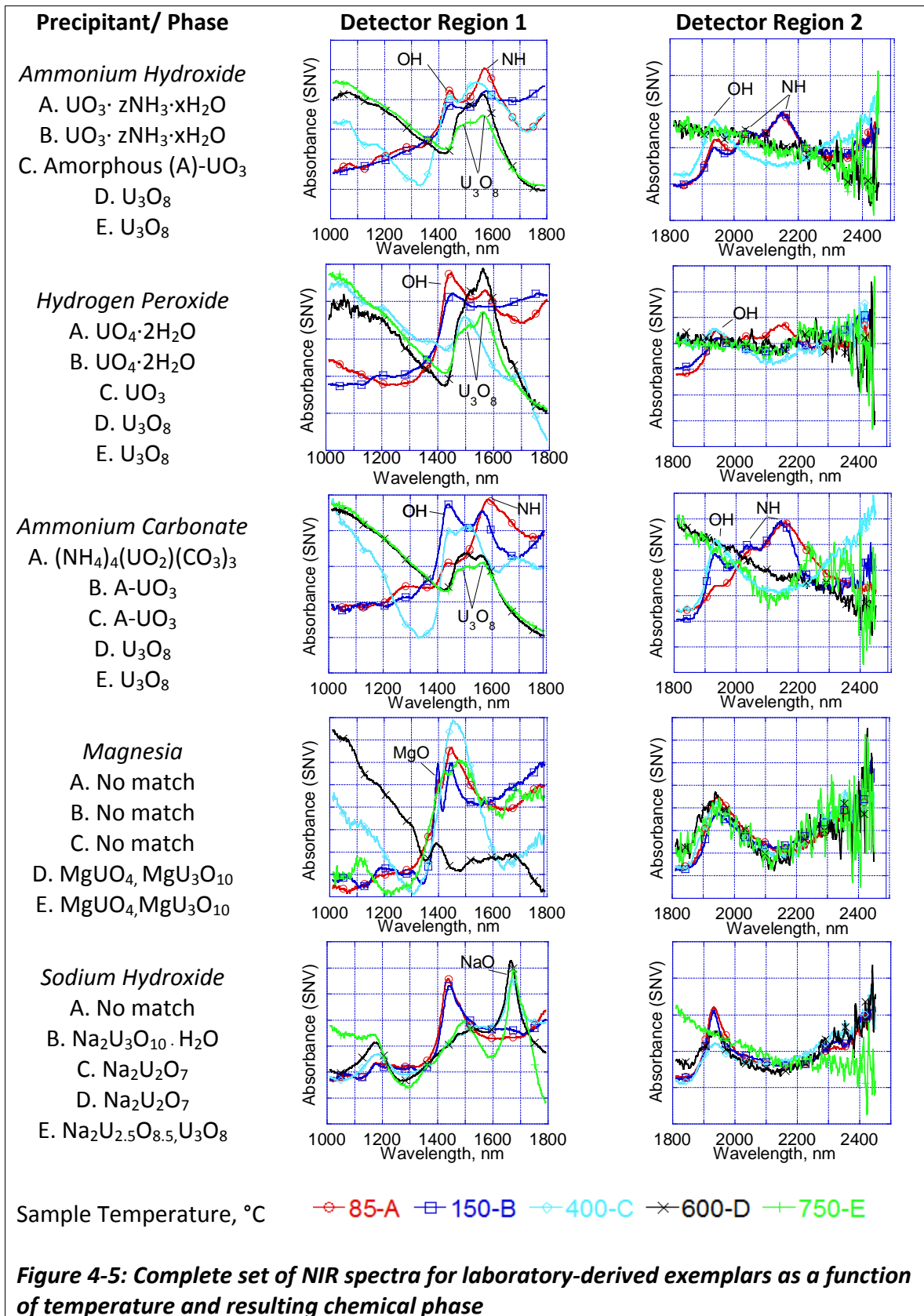
Precipitant	Processing temperature, °C				
	85	150	400	600	750
Ammonium hydroxide	Ammonia uranium oxide hydrate ($\text{UO}_3 \cdot z\text{NH}_3 \cdot x\text{H}_2\text{O}$)	$\text{UO}_3 \cdot z\text{NH}_3 \cdot x\text{H}_2\text{O}$	Amorphous uranium trioxide (A- UO_3)	Triuranium octoxide (U_3O_8)	U_3O_8
Hydrogen peroxide	Metastudite ($\text{UO}_4 \cdot 2\text{H}_2\text{O}$)	$\text{UO}_4 \cdot 2\text{H}_2\text{O}$	UO_3	U_3O_8	U_3O_8
Ammonium carbonate	Ammonium uranyl carbonate (NH_4) ₄ (UO_2)(CO_3) ₃	A- UO_3	A- UO_3	U_3O_8	U_3O_8
Sodium hydroxide	No match	Sodium uranium oxide hydrate ($\text{Na}_2\text{U}_3\text{O}_{10} \cdot \text{H}_2\text{O}$)	Clarkeite ($\text{Na}((\text{UO}_2)\text{O}(\text{OH})))$) Sodium uranium oxide ($\text{Na}_2\text{U}_2\text{O}_7$)	$\text{Na}_2\text{U}_2\text{O}_7$	Sodium uranium oxide ($\text{Na}_2\text{U}_{2.5}\text{O}_{8.5}$) U_3O_8
Magnesia	No match	No match	No match	Magnesium uranium oxides (MgUO_4) ($\text{MgU}_3\text{O}_{10}$)	MgUO_4 $\text{MgU}_3\text{O}_{10}$

Note: shaded areas represent regions where XRD analysis yields insufficient information to determine process origin.

Sodium hydroxide: At 85 °C, uranyl precipitated with sodium hydroxide results in an amorphous phase not readily identifiable through XRD pattern matching. Above this temperature, sodium uranium oxides of various compositions were identified. Similar compounds were identified in the real-world samples suggesting processing temperatures above 150 °C, although confirmatory information was not available in the literature. As with magnesium, the presence of significant sodium rich phase is a strong indicator that sodium hydroxide was used as a precipitant.

4.3.4 NIR can distinguish uranyl precipitates and identify oxides

With some additions and modifications, the work in this section has been reported in the literature [139]. NIR spectra were taken for all laboratory-derived exemplars and are presented with chemical phase information obtained through powder XRD pattern matching (Figure 4-5). The two NIR regions are presented separately since different detectors are used in each region. Peak assignments for O-H, N-H, and other groups are indicated in Figure 4-5 and are discussed later. Each uranium phase resulted in a unique spectrum, sufficient to distinguish the origin of a given sample by visual evaluation of the spectra. These differences are evident for each type of precipitate heated to 85 °C (top of Figure 4-6) in the first NIR detector region. Note that common absorption wavelengths were shared by several samples because of common functional groups (e.g, O-H).



As process temperatures increased, spectral changes occurred consistent with the change in chemical species. The NIR spectra were nearly identical for each of the U_3O_8 samples with dominant absorption features at 1505 and 1565 nm (bottom of Figure 4-6 bottom). This result suggests that NIR is insufficiently sensitive to morphological differences to distinguish reliably between chemically identical species derived through different routes, as discussed in Chapter 5.

The complexity of the NIR spectral region can make specific assignment of features difficult; however, absorption bands were assigned corresponding to the functional groups of the various uranium compounds using available information and simple experiments. The literature on NIR spectroscopy of uranium compounds is very limited with most of the published information authored by Frost and focused on the examination of mineral phases including, calcium uranyl phosphates (autunites) [140], uranyl arsenates [141], uranyl selenites (haynesite) [141], uranyl carbonates (rutherfordines) [142], uranyl selenites (haynesite) [143], and copper uranyl phosphates (torbernites and metatorbernites) [144].

No spectral similarities were observed between the laboratory-derived exemplars and these mineral phases, despite the analogous functionalities of the carbonate group (observed by Frost at 1650, 1700, and 1750 nm), and the uranyl group (observed by Frost at 1060 and 1144, nm). Hanchar [145] also assigned uranyl to a broad absorption at 714 nm, which was not observed in any of these minerals.

In general, NIR spectral features are primarily attributable to the overtone and combination bands of C-H, O-H, and N-H bonds [146]. In addition, there are some

absorption features that arise from crystal field effects and electronic transitions in the actinides [147]. In Figure 4-5 and Figure 4-6, many of the low temperature samples, particularly the 85° C set, exhibit characteristic absorption peaks for the water O-H bonds at 1450 and 1940 nm, which arise from the first overtone and combination of asymmetric stretching and bending, respectively.

Similarly, the overtone of the N-H stretch near 1480 nm and the stretch and bend combinations at 2050 and 2150 nm were observed in the ammonium hydroxide and ammonium carbonate derived precipitates. Other overtones for functional groups expected based on the species were not observed, including carbonate (2550 and 2350 nm) and peroxide (2060 nm for aqueous species). The absorption features near 1505 and 1565 nm observed in the U₃O₈ samples do not appear to be overtones as there are no corresponding absorptions in the higher wavelength region typically associated with combination bands, thus these absorptions are likely the result of crystal field effects or electronic transitions.

Analyses of pure solid reagents (magnesia and ammonium carbonate) were also performed for comparative peak assignments. For magnesia, the spectra demonstrate a unique absorption feature at 1395 nm, which was found to be present in all but the 750 °C synthetic sample. For ammonium carbonate, absorption features were observed at 1640, 1975, 2040, 2175nm—only the 2040 nm peak was found for the 85 °C ammonium uranyl carbonate synthetic samples.

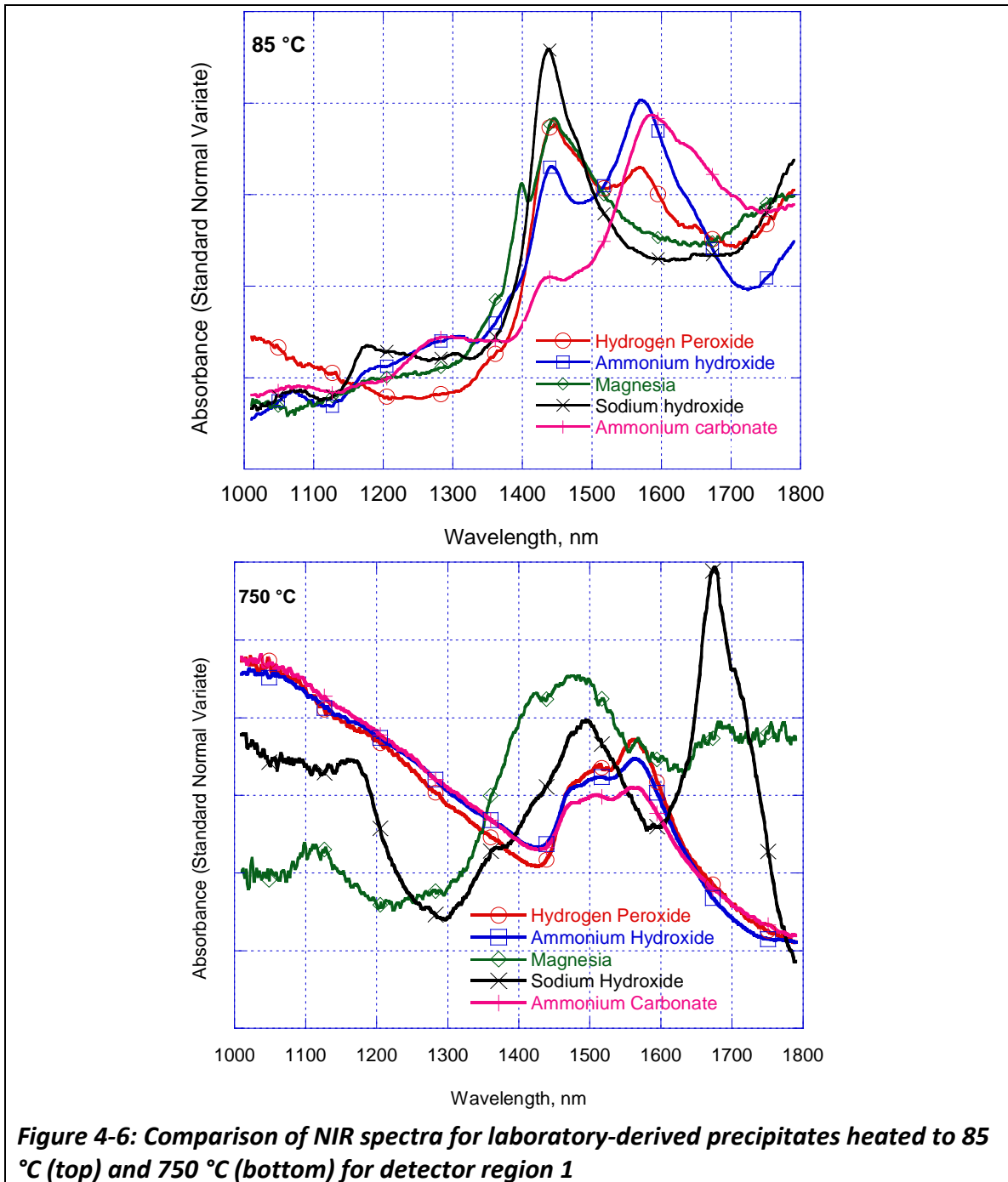
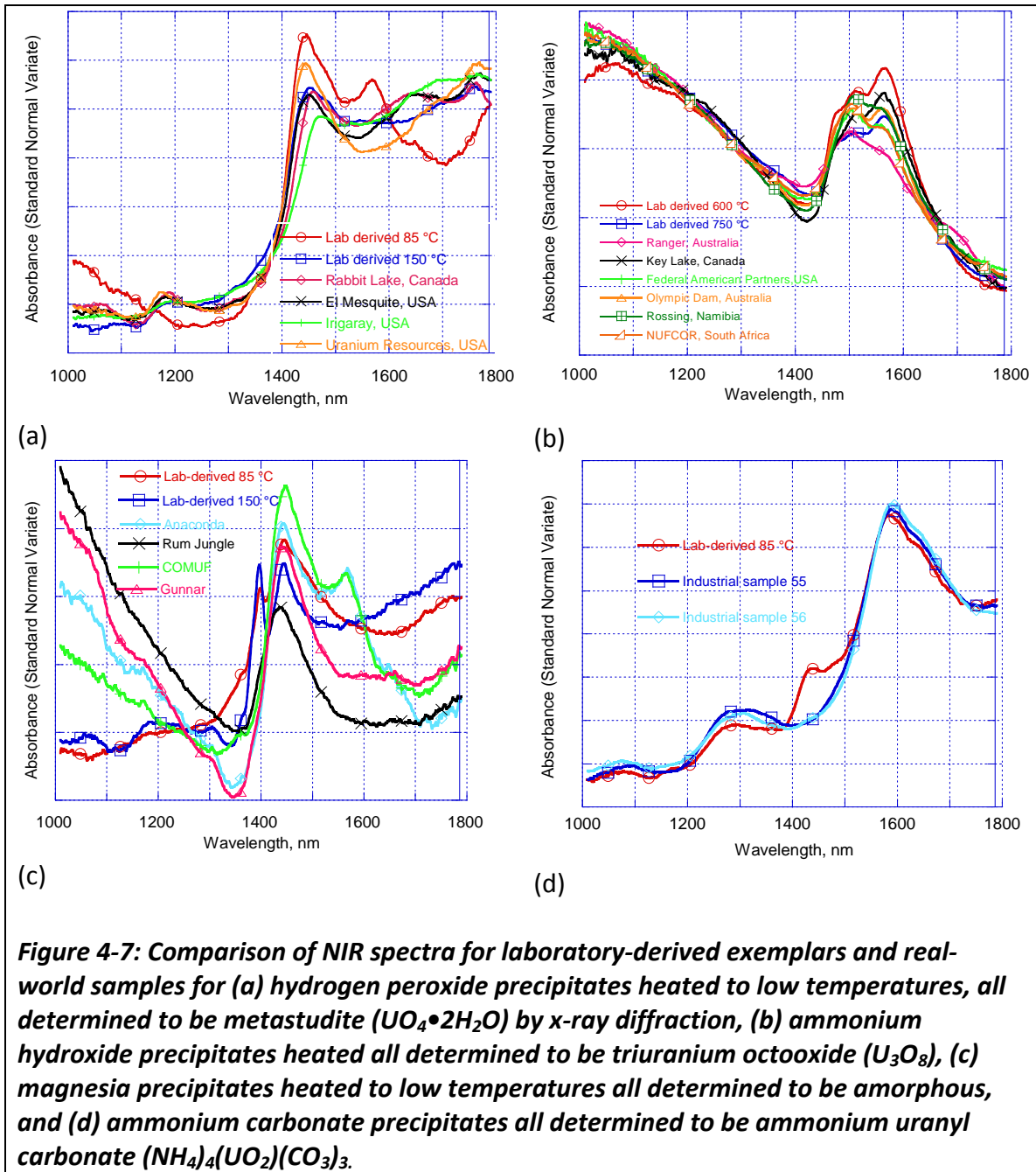


Figure 4-6: Comparison of NIR spectra for laboratory-derived precipitates heated to 85 °C (top) and 750 °C (bottom) for detector region 1

Edison [148] and Varga [19] provide infrared analysis of some relevant uranium ore concentrates where the O-H and N-H fundamentals located around 2900 and 3185 nm were identified, respectively. Corresponding first fundamental overtones would

appear around 1440 and 1580 nm, of which the 1440 nm absorption was observed for all samples and the 1580 nm absorption observed with the ammonium carbonate (1585 nm) and ammonium hydroxide samples (1570 nm). The other fundamental infrared spectrum features observed in these studies occur at wavelengths outside the NIR region.

Overall, comparisons of NIR spectra between the lab-derived exemplars and the real-world samples were favorable (Figure 4-7). This result suggests that the NIR spectra for the chemical phases produced for a given process and temperature are not significantly perturbed by real-world factors (e.g., minor constituents), thereby providing confidence that this technique offers a valid tool for nuclear forensic applications. In fact, the NIR technique was further advanced by Klunder [149] through the application of principal component analysis to the investigation of additional real-world samples and was able to demonstrate generally good segregation of chemical species.



4.4 Conclusions and suggested areas for further study

This study identified the uranium precipitates and oxides mostly likely to be encountered in a nuclear forensic application and developed a systematic set of well-characterized laboratory-derived exemplars and real-world samples for application of conventional and novel analytical forensics tools. This study reached the following conclusions and suggested areas for future study:

- Thermogravimetric methods can distinguish uranyl precipitants of different process origins. Further, differences in the rates of mass loss at elevated temperatures suggest that additional research is warranted to ascertain whether this tool is capable of distinguishing process origins for chemically similar oxide phases produced at elevated temperature.
- Despite common application in industry, specific surface area is not indicative of process history. This study identified significant overlap in surface areas for powders derived from different processes, particularly as process temperatures are increased. As a result, while a given process line may produce material of a characteristic specific surface area, the value may be insufficient to distinguish it from other processes.
- Characterization by powder XRD demonstrated good agreement in the identified chemical phases between the laboratory-derived exemplars and the real-world samples. XRD can reveal process history for powders of certain precipitant and temperature combinations; however, higher temperatures result in either

amorphous phases or identical chemical species that require additional techniques to discern the process history.

- NIR spectroscopy can distinguish uranyl precipitants and identify uranium oxides. NIR also demonstrated good spectral agreement between laboratory-derived exemplars and real-world samples. Consequently, NIR represents a promising new tool for nuclear forensic applications warranting additional study with diverse samples.

The sample set developed in this chapter was also utilized in Chapter 5. Suggested areas of research that are pertinent to both chapters are presented in Chapter 5.

Chapter 5 Morphology as a signature in uranium precipitates and oxides

This chapter continues the study of uranium precipitates and oxides for signatures indicative of chemical process history with an exclusive focus on morphology. The set of laboratory-derived exemplars and real-world samples developed and characterized in Chapter 4 was systematically studied for morphology using scanning electron microscopy (SEM). The results of this study indicate that each process results in a precipitate with a unique, characteristic morphology and that each precipitate subsequently decomposes to an oxide in a pseudomorphic manner. In other words, the morphology of the original precipitate is largely preserved in the resulting oxide. Consequently, morphology offers a distinctive forensic tool to help elucidate the process history of otherwise chemically identical uranium oxides. Consistency between laboratory-derived exemplars and real-world samples further underpins these results; however, the effects of sintering at elevated temperatures mask morphology and make differentiation difficult.

5.1 Literature suggests a link between process and morphology

A review of the literature provided indications suggestive of a link between chemical process history and morphology advantageous to nuclear forensics. In particular, several authors observed differences in the physical properties of uranium oxide powders as a function of production method. In the only published research with an explicit focus on forensics, Hastings [18] compared uranium oxides produced as a function of the firing temperature and noted differences in physical appearance,

density, and particle size distribution. These properties are often correlated with morphology.

Historically, researchers examined properties of uranium oxide powders to understand and optimize subsequent production of nuclear fuels. Their experiments focused largely on characteristics of the fuel, including the morphology of grains in the sintered pellets, as a function of the properties of the precursor oxide powder. The objective of Chapter 6 is to carefully examine this link between powder and resulting fuel pellet. However, since these researchers invariably provided some characterization and discussion of the processes used to produce the precursor powders, the literature is reviewed below for insights into forensic applications for both powders and pellets.

Andreev [150] investigated the macro- and micro-structure of uranium dioxides produce through precipitation with ammonia and the dry routes of gas flame and fluidized beds. The author found remarkably different morphologies based on SEM analysis. Similarly, Burk [151] found a distinction in the particle size distributions between uranium dioxide powders originating from the reduction of the precipitate with ammonia as compared to the reduction of uranium trioxide pretreated with ammonium nitrate.

Pajo [152] [153] found differences in the surface roughness of fuel pellets to be specific to the production plant and pellet type, but did not discuss the specific production processes. Lee and Yang [134] compared uranium dioxide derived from precipitation with ammonia and ammonium carbonate by mercury porosimetry and found differences in the pore size distribution between the powders. These differences

translated into variations in the pore structure and density of the final pellet. Cordfunke [154] noted differences in fuel pellets produced under identical conditions except for the precursor powders derived from ammonia and peroxide processes.

Assmann [155] also observed microstructure and surface differences between fuel derived from powders originating from precipitation with ammonia, ammonium carbonate, and each of the three dry production routes. In other work, Assmann [156] observed that precipitation conditions determined properties of the resulting ammonium carbonate precipitate, which transferred to the subsequent uranium dioxide powders and onto grains within the final sintered pellet.

Overall, the literature suggests that morphological process signatures do exist in uranium powders and fuel pellets. Researchers were primarily interested in producing high quality nuclear fuel, but their results provide confidence that the systematic examination intended by this study will establish morphology as a useful process signature.

5.2 Sample imaging and processing

The samples investigated in this chapter were those laboratory-derived exemplars and real-world samples produced and characterized in Chapter 4. Samples for SEM analysis were prepared by physical transfer from surfaces onto carbon adhesive stubs on aluminum pin mounts. For non-conductive matrices, a 5 nm iridium metal coating was applied to minimize charging effects on the sample. Imagery was obtained using a FEI Inspect F SEM instrument (Chapter 2). Secondary electron imaging generally utilized an accelerating voltage of 5 kV. Backscatter electron imaging generally utilized an

accelerating voltage of 15 kV. Working distances were typically 11.5 mm. Energy dispersive spectroscopy (EDS) was performed using an EDAX Apollo silicon drift detector with the associated Genesis software package.

In most cases, multiple images of each sample were obtained over a range of magnifications. This method resulted in the most accurate characterization of a given sample. For example, many of the powders exhibit variable morphologies that are often difficult to capture in a single frame. As a result, the reader is cautioned that the single instance images used for qualitative comparisons throughout this chapter may inherently contain bias. While a conscientious effort was made to select representative images, the reader is strongly encouraged to consult the additional images provided in the Appendix to allow for the broader perspective and individual interpretation.

Image analysis was accomplished using the Morphological Assessment of Materials for Attribution (MAMA) software under development by Los Alamos National Laboratory [67]. Image analysis was performed using algorithms for texture and most of the images are presented at a magnification of 50,000X based on the finding in Chapter 3.

5.3 Results and Discussion

5.3.1 SEM imagery reveals morphology characteristic to precipitation process

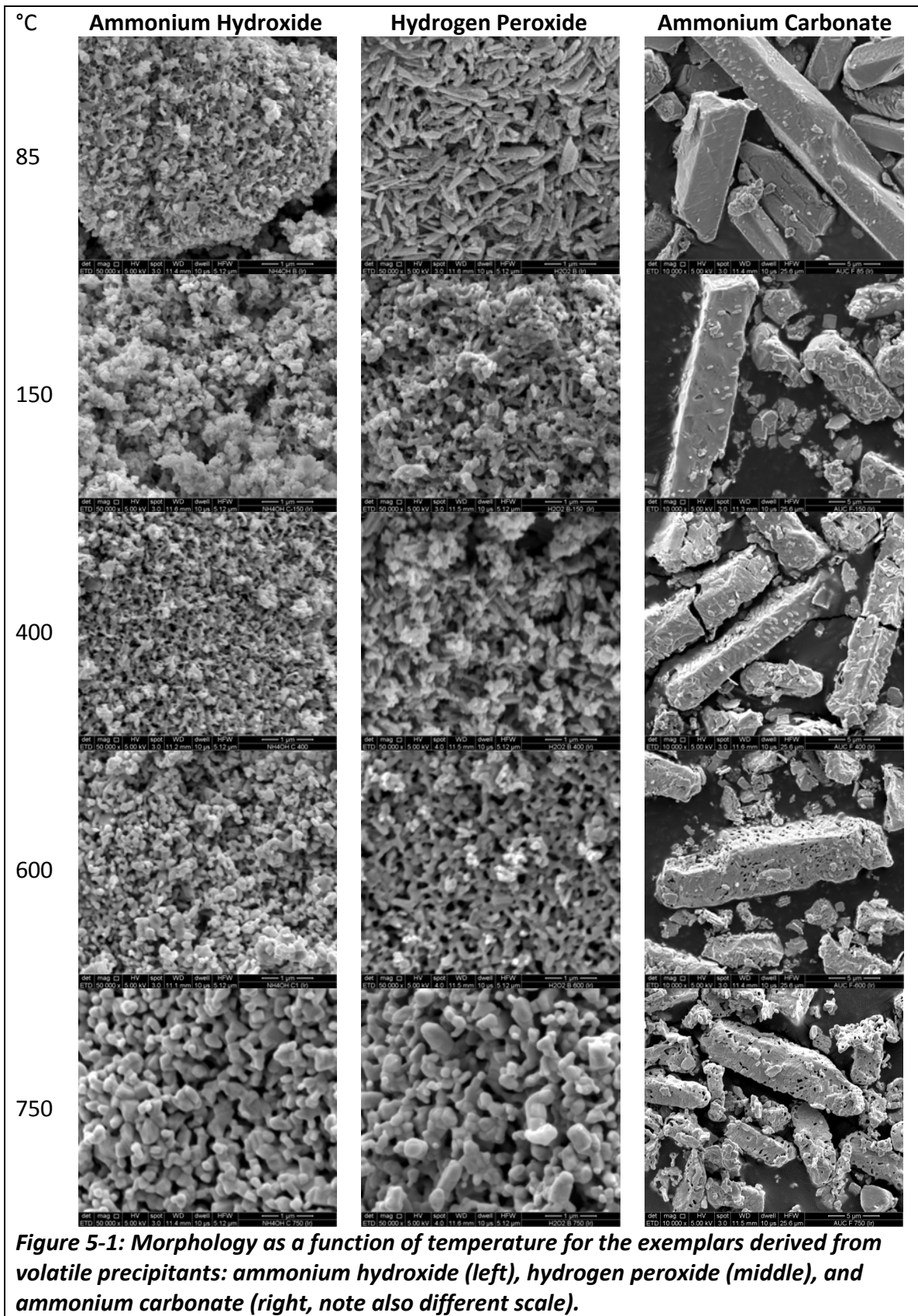
The morphology of uranyl precipitates and resulting oxide exemplars was examined as a function of process temperature (Figure 5-1 and Figure 5-2). Table 5-1 provides qualitative descriptions of the observed morphology using terminology

consistent with the Particle Morphology Glossary developed by the National Institute of Standards and Testing [157].

Table 5-1: Qualitative descriptions of the morphological signatures associated with uranium precipitates

Precipitant	Qualitative description of morphology
Ammonium hydroxide	Agglomerates of thin platelets that decompose into grapelike clusters and begin to sinter at 600 °C
Hydrogen peroxide	Thin shards that begin bridging at 400 °C and continue to sinter as temperatures are increased. The sintered material is similar in appearance to the clusters observed with ammonium hydroxide; however, slightly more directional order remains consistent with the original shards
Ammonia carbonate	Distinct euhedral rhomboids or broken rhomboids preserved as temperature increases, though the surfaces become porous
Magnesia	Clusters of needle-like formations that individually expand with increased temperature, but preserve their general arrangement
Sodium hydroxide	Agglomerates of thin platelets similar in appearance to ammonium hydroxide, though generally flatter or more spread at all temperatures

The key observations from these image sets include: (1) each precipitate generally displays a unique morphology and (2) substantial aspects of this unique morphology are maintained in most of the powders through temperatures up to 600 °C. The first observation is not particularly surprising—each precipitate represents a unique compound(s) with its own distinct crystal structure and associated morphology.



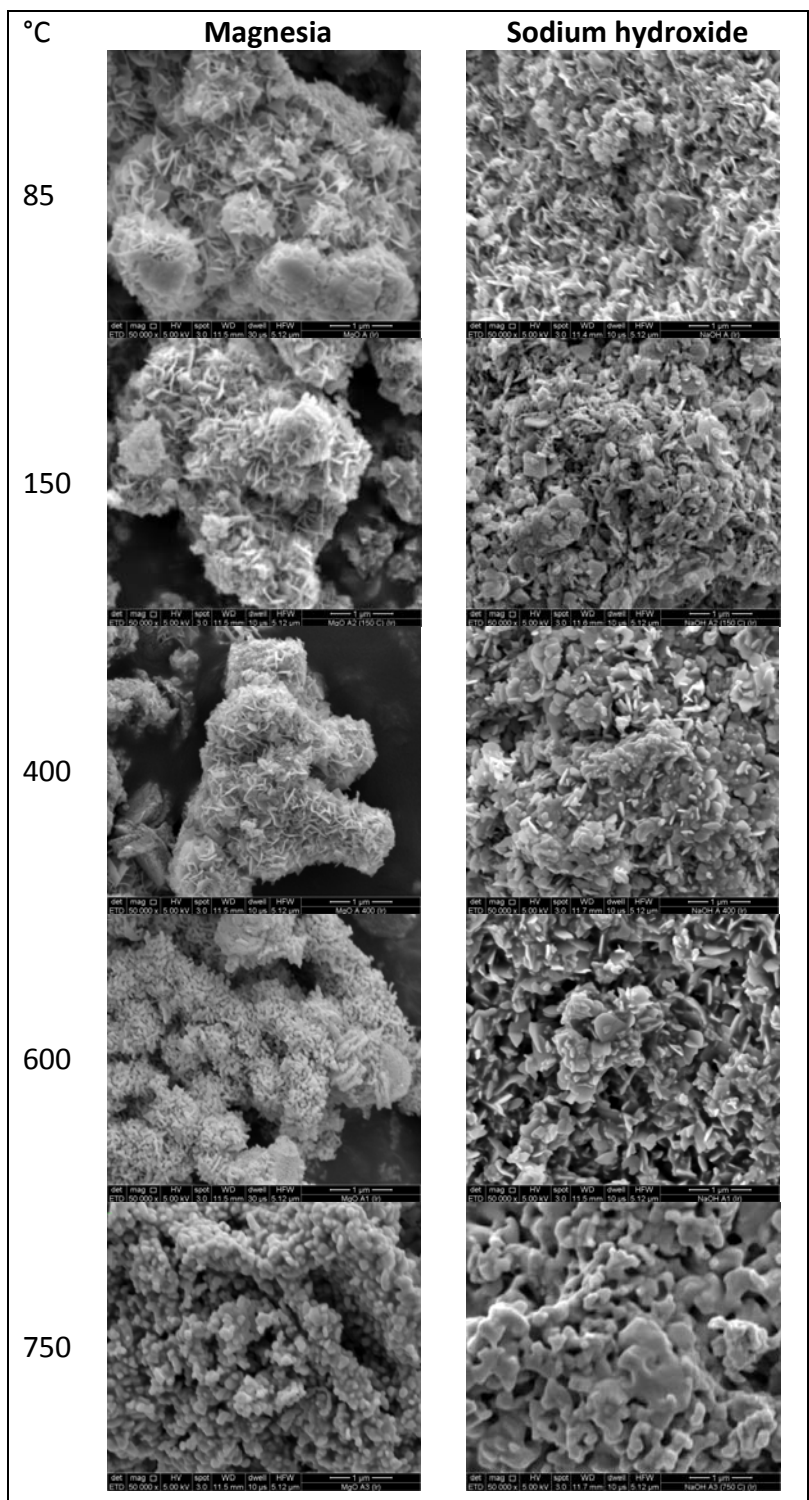


Figure 5-2: Morphology as a function of temperature for the exemplars derived from non-volatile precipitants: magnesia (left) and sodium hydroxide (right)

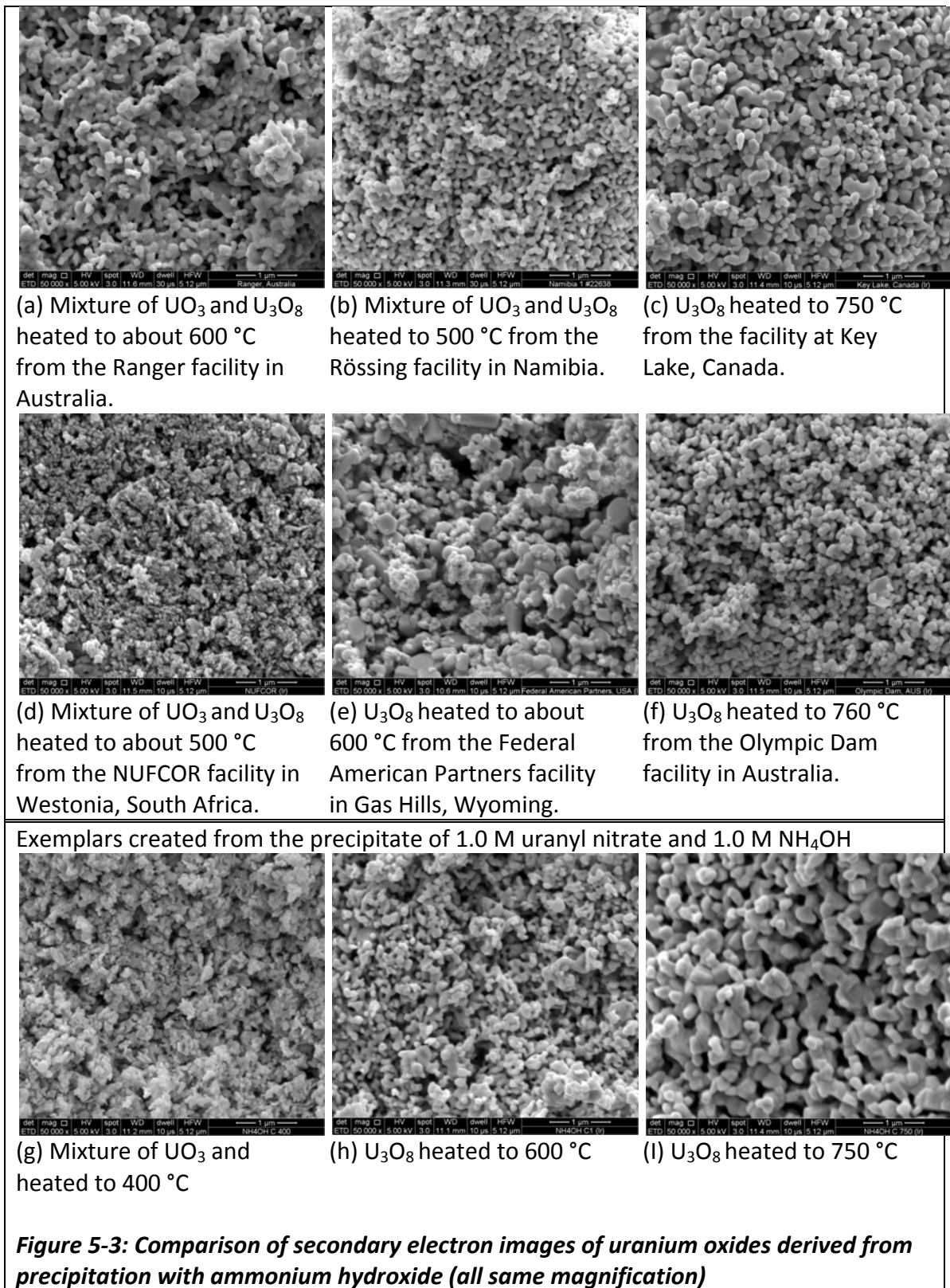
However, this result substantiates the value of morphology as a standalone technique for the determination of the process history.

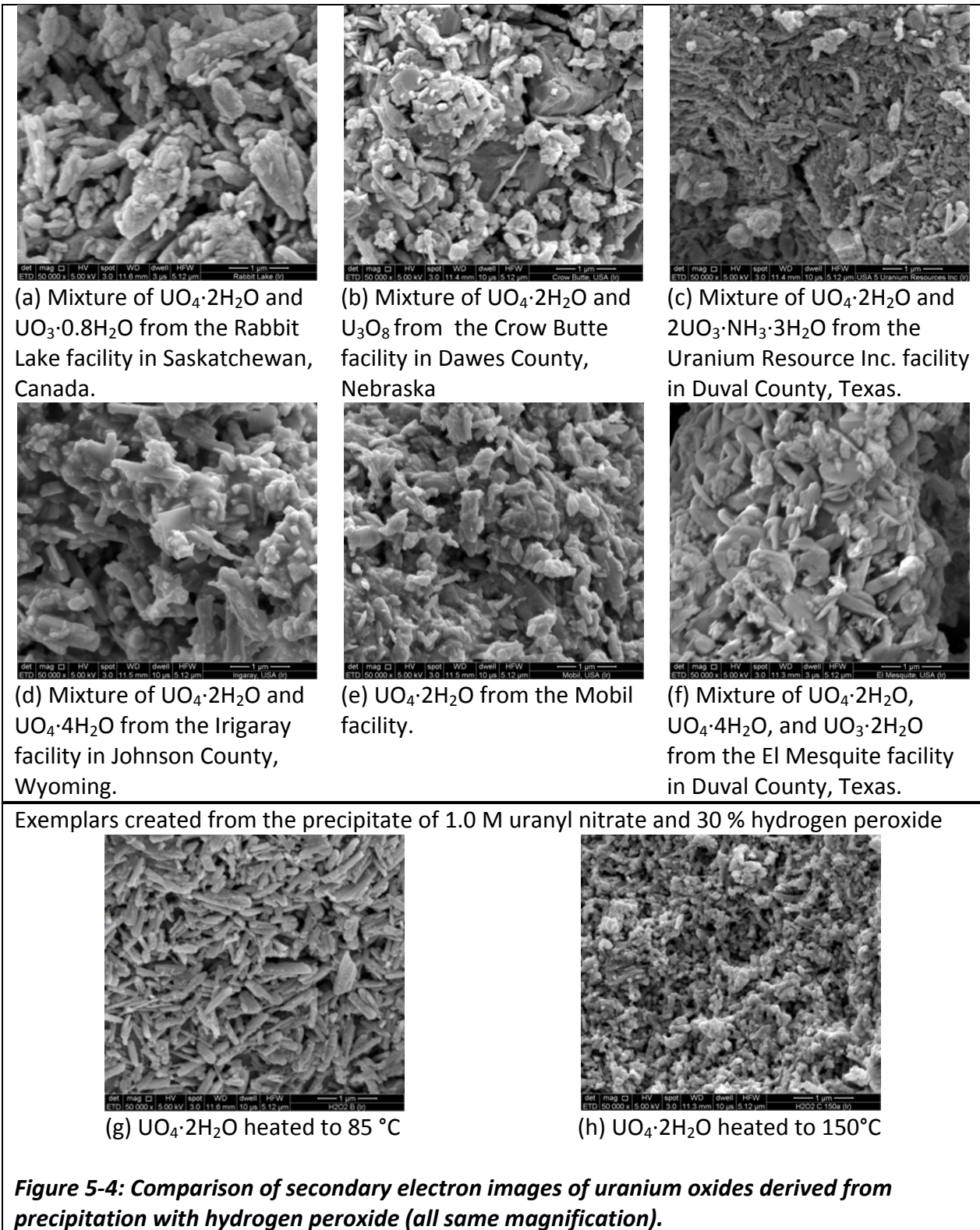
The second observation—morphology is generally maintained as precipitates are decomposed into various uranium oxides—is unexpected and may have important implications for forensics. In particular, the thermogravimetric and powder x-ray diffraction (XRD) results presented in Chapter 4 indicate that in all cases the volatile precipitating agents were decomposed at temperatures of 400 and 600 °C, resulting UO_3 and U_3O_8 species that provide no other indicator of process origin. The observation that morphological features are distinguishable for these samples provides a new tool to discern the history of otherwise chemically identical powders.

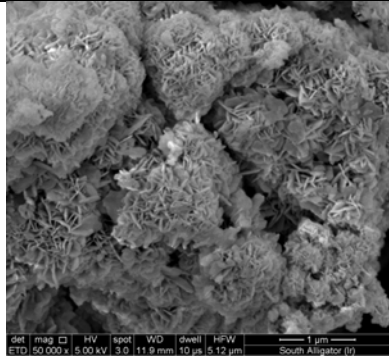
The utility of morphology is reinforced further by the examination of real-world samples representing each precipitation process (Figures 5-3 through 5-7). These images demonstrate favorable qualitative comparisons with the laboratory-derived exemplars for similar precipitation and thermal treatments. For example, the images of the real-world samples in Figure 5-4 all depict the shard-like morphology characteristic of precipitation with hydrogen peroxide, also displayed by the exemplars.

Unfortunately, the available set of real-world samples does not provide an opportunity to examine the comparative morphologies of uranium oxides produced with known different precipitation histories. In particular, a comparison of real-world U_3O_8 produced using the ammonia, hydrogen peroxide, and ammonium carbonate precipitation processes would be useful to determine if the distinct morphologies observed with the laboratory exemplars are preserved. These particular precipitation

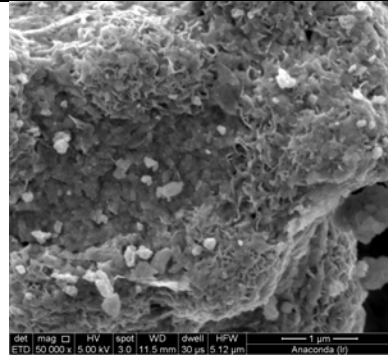
processes are real-world significant; however, the majority of the samples currently available at Lawrence Livermore National Laboratory are uranium ore concentrates and are, therefore, more likely to be precipitates dried at low temperatures rather than refined oxides or process intermediates.



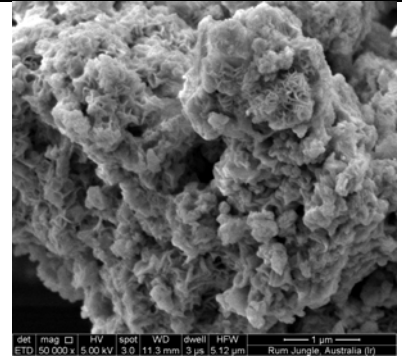




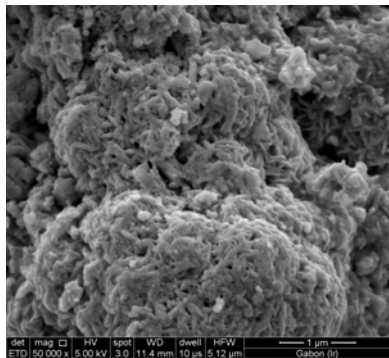
(a) Uranium ore concentrate from the South Alligator facility in N. Territory, Australia.



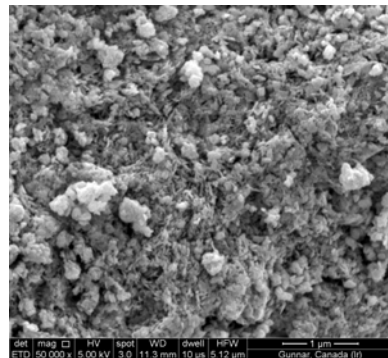
(b) Uranium ore concentrate from the Anaconda facility in Grants, New Mexico.



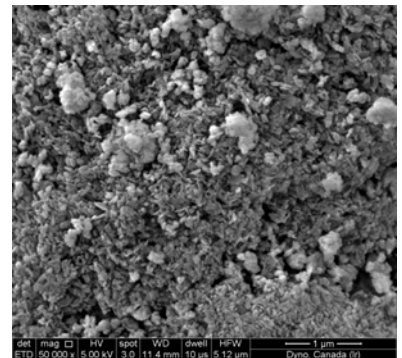
(c) Uranium ore concentrate from the Rum Jungle facility in N. Territory, Australia.



(d) Uranium ore concentrate from the Compagnie des Mines d'Uranium de Franceville in Mounan, Gabon.

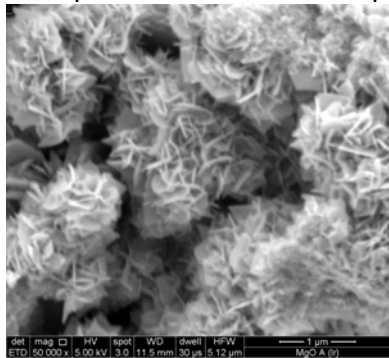


(e) Uranium ore concentrate from the Gunnar facility in Saskatchewan, Canada.

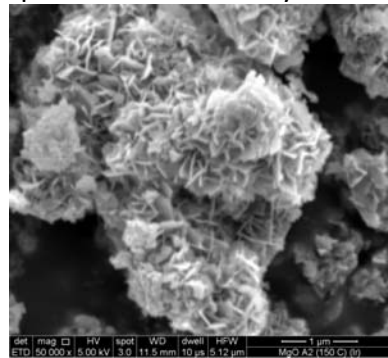


(f) Uranium ore concentrate from the Dyno facility in Bancroft, Canada

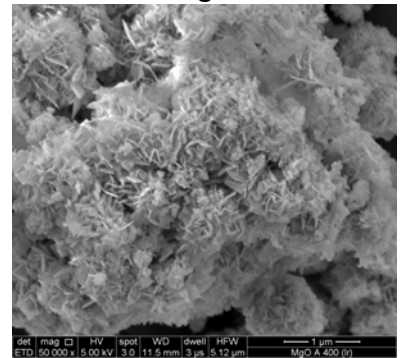
Exemplars created from the precipitate of 1.0 M uranyl nitrate and 15 wt % magnesia



(g) Precipitate dried at 85 °C

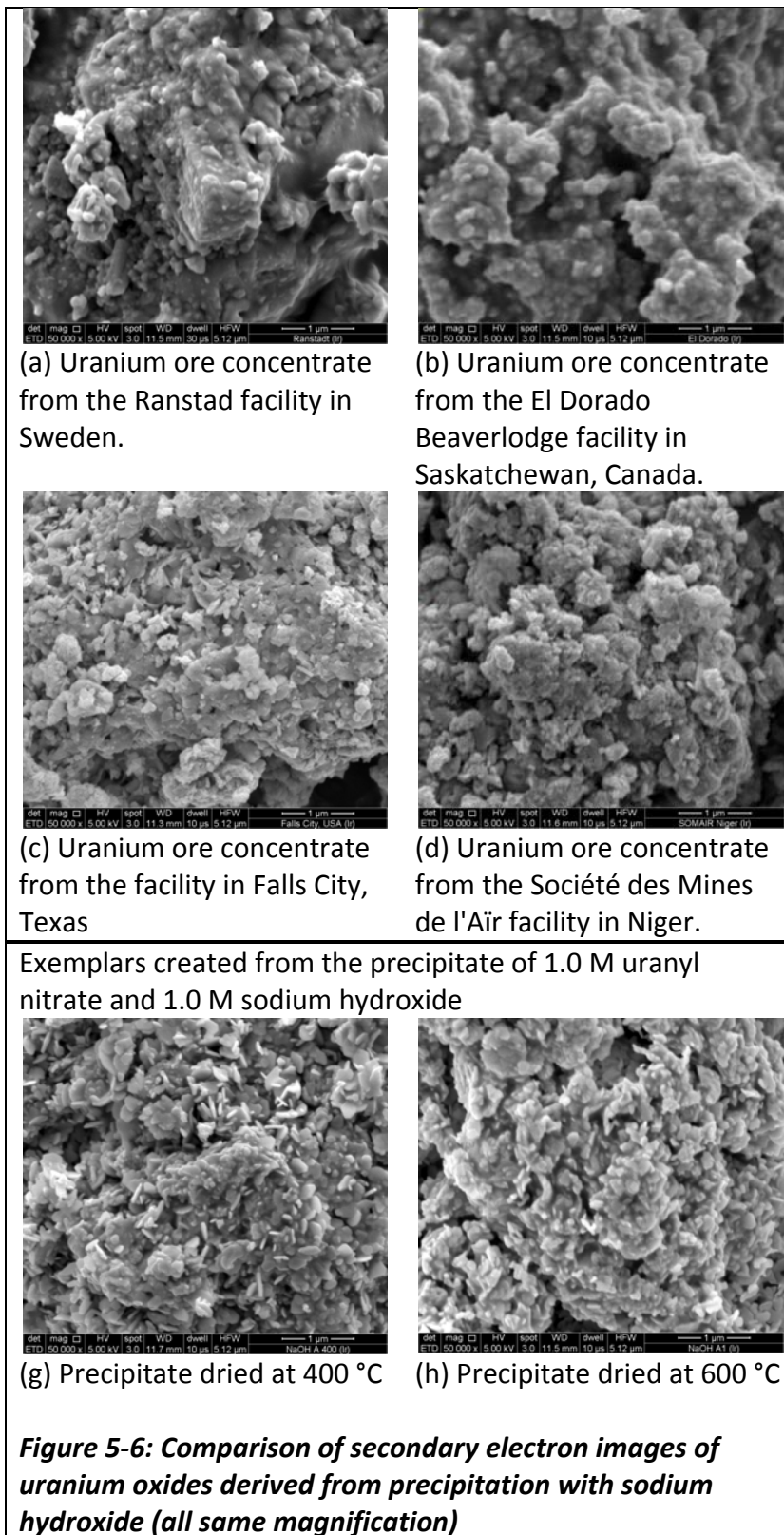


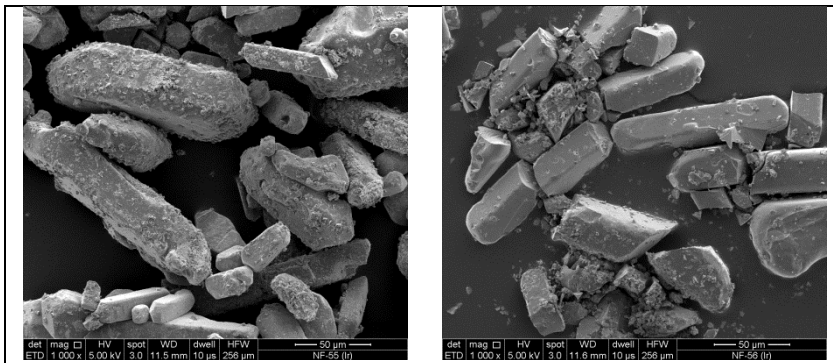
(h) Precipitate dried at 150 °C



(i) Precipitate dried at 400 °C

Figure 5-5: Comparison of secondary electron images of uranium oxides derived from precipitation with magnesia (all same magnification).

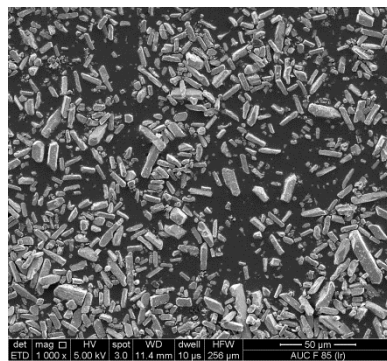




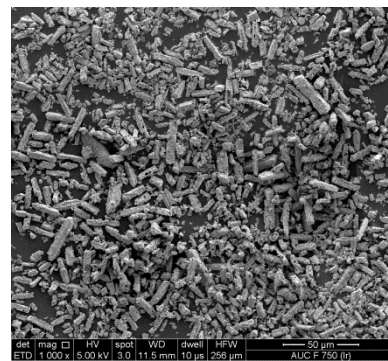
(a) Industrial sample LLNL-55

(b) Industrial sample LLNL-56

Exemplars created from the precipitate of 1.0 M uranyl nitrate and saturated ammonium carbonate



(f) Precipitate dried at 85 °C



(g) Precipitate dried at 750 °C

Figure 5-7: Comparison of secondary electron images of uranium oxides derived from precipitation with ammonium carbonate (all same magnification)

5.3.2 Quantitative image analysis using texture requires additional efforts

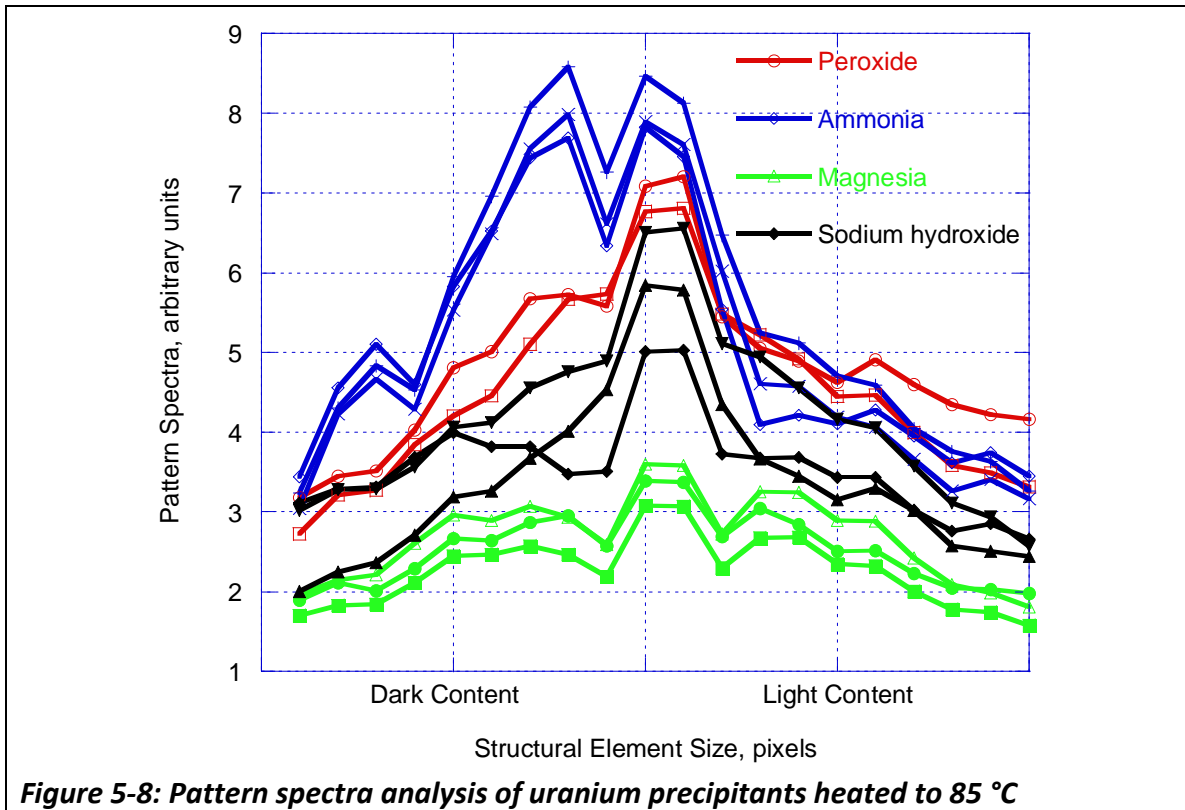
This section examines the application of quantitative image analysis techniques in an attempt to strengthen the utility of morphology as a forensics tool. Section 5.3.1 presented compelling qualitative evidence in the similarity of morphology for uranium oxides and precipitates with common process histories. Section 3.5 examined texture as a quantitative tool for image analysis and determined the optimum magnification, texture analysis parameters, and characterized the variation in texture observed within a given sample. These results were used to perform image analysis on the textures

displayed in the image sets previously presented. The objective of this study was to evaluate the application without further investigation or refinement of image analysis algorithms, which is beyond the scope of this radiochemistry dissertation. Note that the system associated with precipitation using ammonium carbonate was excluded from this study given the obvious morphology and lack of textural qualities displayed by these samples.

The application of texture analysis to three images of each of the precipitates (85 °C samples) revealed good distinction and separation (Figure 5-8). This texture analysis was performed using the pattern spectra function in MAMA with the default settings. The pattern spectra algorithm is conceptually similar to the granulometric curve presentation commonly used in geosciences—a mathematical sieve is applied to the light and dark image content, measuring what remains, changing the sieve size, and continuing onward. Section 3.5 examined the repeatability of pattern spectra for 10 samples of the same powder and observed a mean value of the spread of spectra across the full range of 0.4 with a variance of 0.05. Application of these values to Figure 5-8 indicates that adequate separation exists to distinguish quantitatively the powders using pattern spectra.

Encouraged by this observation, image analysis of textures was applied to the exemplars and real-world samples presented in Figures 5-3 to 5-7. The texture values for each of the images in these figures were determined using MAMA for pattern spectra, as well as the three other texture metrics judged most promising techniques based on sensitivity studies. These metrics include the features described by Connors

[78] for cluster prominence, inertia, and inverse difference based on an implementation of the gray-level co-occurrence matrix described by Haralick [77].



The spectra for each of these four texture metrics were determined and the results analyzed using principal components analysis. Principal component analysis is a multivariate technique commonly applied to data exploration and pattern recognition [158]. Principal components analysis transforms the multivariate data set of texture values into a derived coordinate system representing the directions of the first and second highest variance for the data—these are the first and second principal component. The scores plot resulting from the analysis in this study (Figure 5-9) indicates that the combination of these texture metrics resulted in poor clustering,

meaning that the differences in textures were insufficient to make quantitatively reliable determinations.

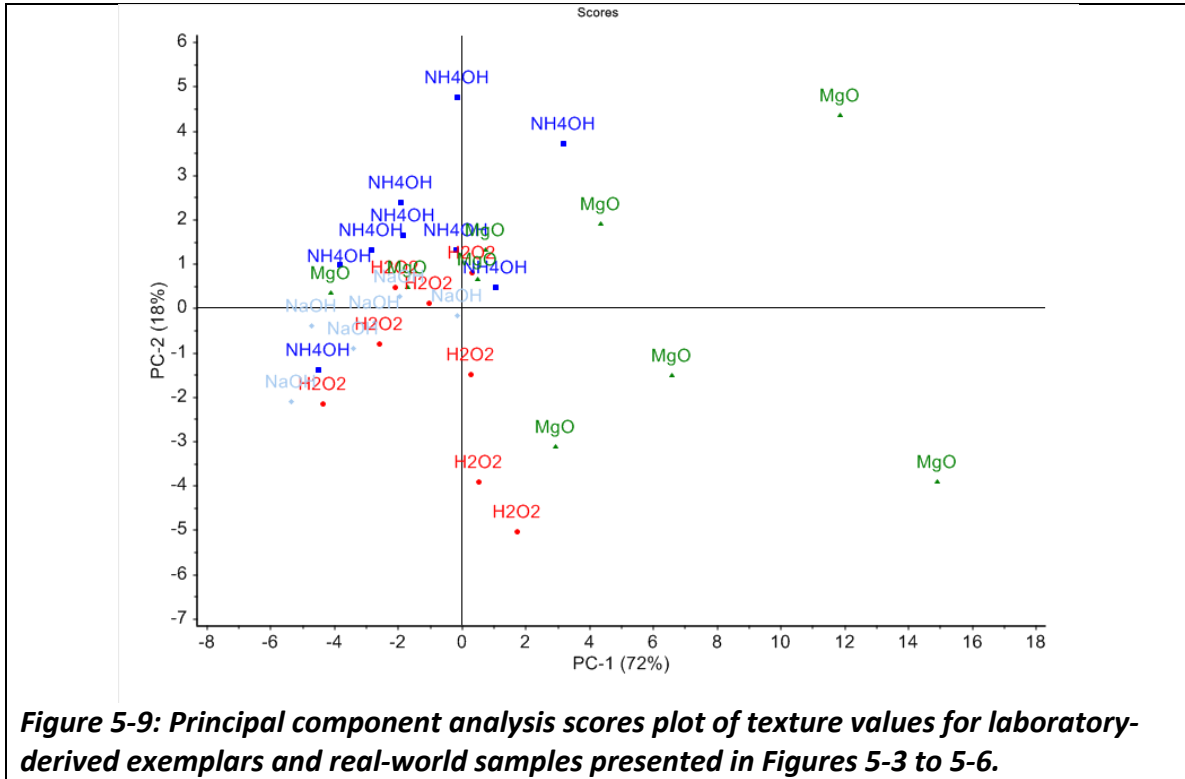


Figure 5-9: Principal component analysis scores plot of texture values for laboratory-derived exemplars and real-world samples presented in Figures 5-3 to 5-6.

Overall, these two studies indicate that image analysis using texture offers promise as a quantitative forensics tool. Specifically, textural analysis demonstrated distinct groupings for triplicate images of each exemplar. However, application of this method to a broader sample set was unsuccessful and indicates additional efforts are necessary for this technique to succeed. Fundamentally, if a qualitative visual comparison is successful as shown in this study, technological improvements should enable eventual quantitative comparisons.

5.3.3 Morphological signatures driven by a pseudomorphic behavior in uranium

A key observation from Section 5.3.1 was that morphological features are preserved when uranium precipitates are heated and transition to oxides. The

significance of this observation is that morphology can provide a forensics tool to elucidate the process history for otherwise chemically identical uranium oxides (Figure 5-10). Given the high potential utility of this tool, this section reviews the literature in order to establish a fundamental understanding of the phenomenon and characterize its reliability as a signature.

Cordfunke [159] first noted a phase transition that preserved morphology—termed pseudomorphism in the geosciences community [160]—in uranium. The pseudomorphic decomposition of uranyl peroxide to amorphous uranium trioxide preserving the needle-like morphology at temperatures up to 500 °C was observed. Similarly, Doi [128] found that the morphology of ammonia precipitates of uranyl nitrate persisted at temperatures below 600 °C and further noted that the morphology of subsequent uranium dioxide was highly driven by the initial precipitate, which in turn appeared to be a function of the concentration of uranium nitrate. This study reproduced the behaviors observed by both Cordfunke and Doi. Pseudomorphs have also been observed in uranium ores [161]. Reetz and Haase [162] generalized an observation of pseudomorphic decompositions in the preparation of oxide powders based on the morphology of the initial precipitate in thorium, yttrium, and beryllium oxide systems.

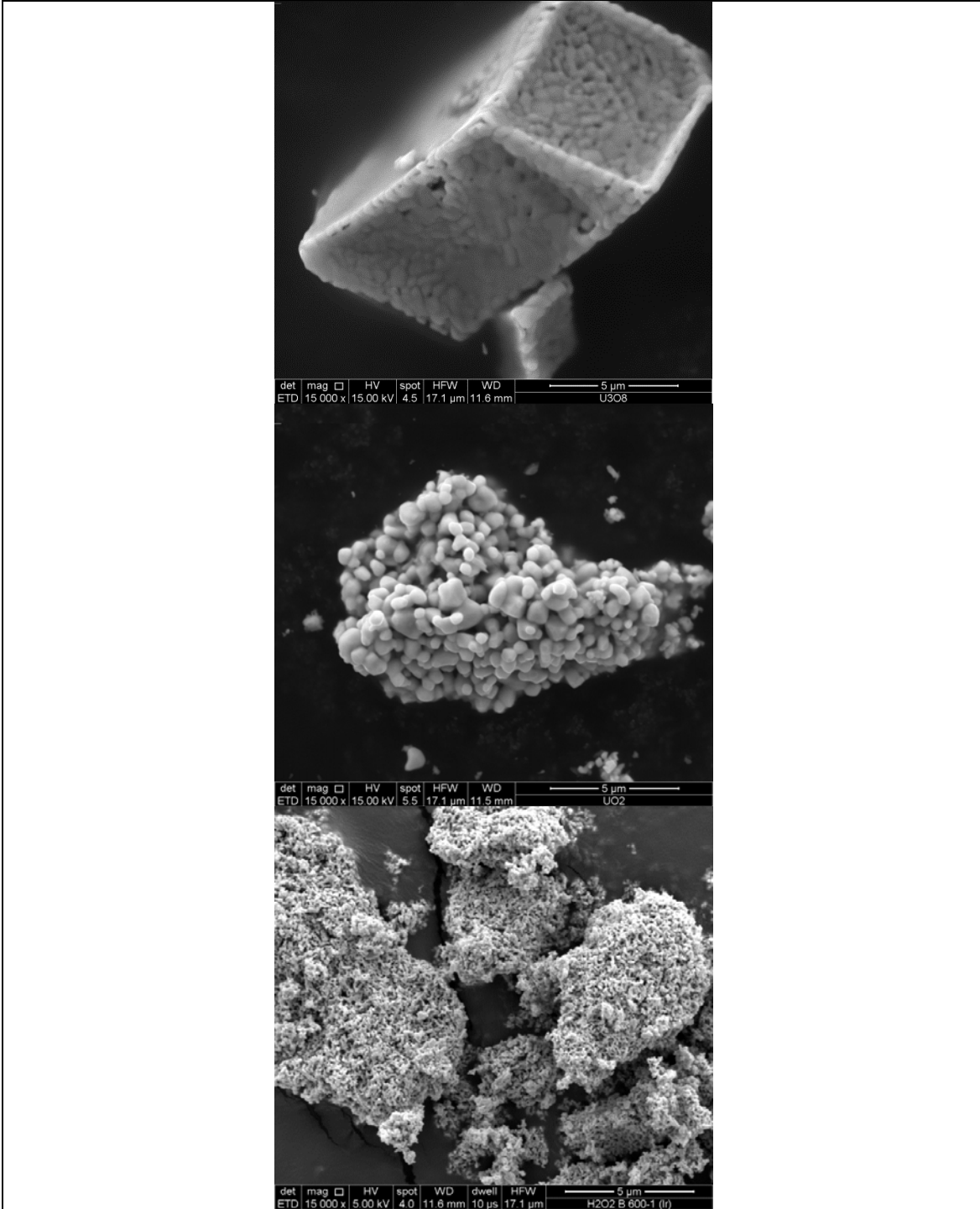


Figure 5-10: Demonstration of the utility of pseudomorphic transitions in the comparison of uranium oxides produced at 600 °C resulting from precipitation with ammonium carbonate (top), ammonia (middle), and hydrogen peroxide (bottom)

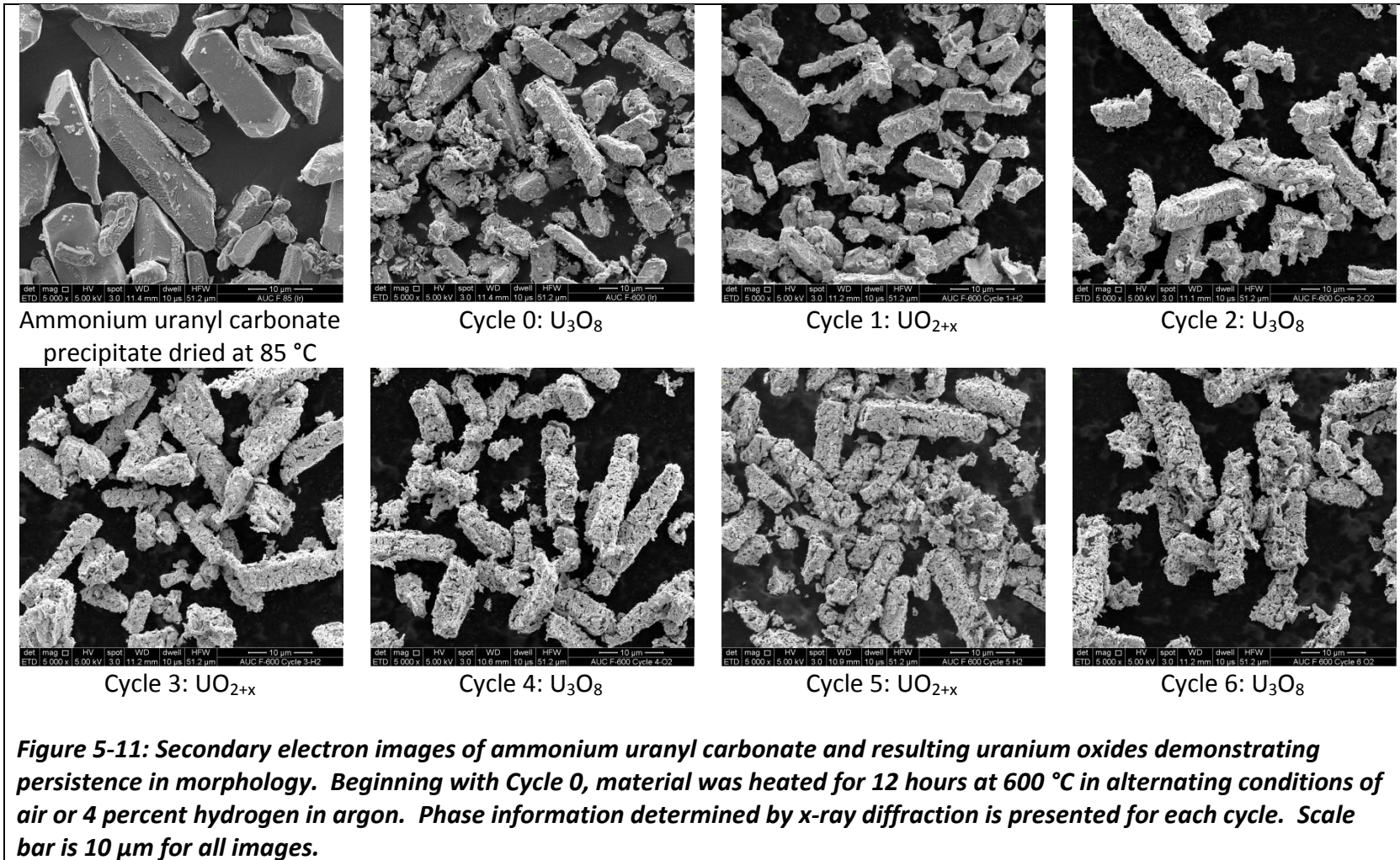
However, none of these authors proposed a mechanism for the observed pseudomorphic transitions. In geochemistry, pseudomorphism is frequently explained by substitution processes or simultaneous dissolution and precipitation reactions [163][164][165]. Neither of these mechanisms provides satisfactory explanations for the solid-gas environments associated with these thermal oxidation transitions.

To explore pseudomorphic behavior in uranium oxide powder systems, this study examined the persistence of the rhombohedral grain morphology of ammonium uranyl carbonate (AUC) exposed to repeated cycles under oxidizing and reducing atmospheres. The distinctive nature of the AUC grains makes it an excellent choice to probe this phenomenon. AUC also represents a specific compound and associated crystal structure, as compared to some of the mixed species produced through the other precipitation processes (e.g., ammonium uranates).

AUC powder was placed in a furnace boat and exposed to either room air or 4 % hydrogen in argon for 12 hour cycles at 600 °C in a tube furnace. An aliquot of the powder was removed and analyzed after each cycle. SEM analysis indicated that the rhombohedral morphology generally persisted through all 6 cycles (Figure 5-11) with two exceptions. First, the crystal sizes appeared to shrink from the precipitate to the first U_3O_8 phase (Cycle 0). Second, porosity and fragility (e.g., crystals that appear fractured or broken) increased with each cycle. Note that the experiment terminated at Cycle 6 due to insufficient remaining material rather than loss of original morphology. Powder XRD analysis (Figure 5-12) revealed a consistent return to the U_3O_8 structure upon oxidizing cycles and formation of the hyperstoichiometric UO_{2+x} structure upon

reducing cycles. Values of x ranged from 0.12 to 0.33 (U_3O_7) and increased with each cycle.

The persistence of the rhombohedral morphology through these cycles is quite remarkable and difficult to rationalize given the crystal properties of the associated phases (Table 5-2). The transition from AUC to U_3O_8 represents a threefold increase in density, a change in symmetry, and associated changes in lattice parameters. The shrinkage in crystal size accounts for the density differences, but it is unclear how the changes to the symmetry and lattice parameters were accommodated.



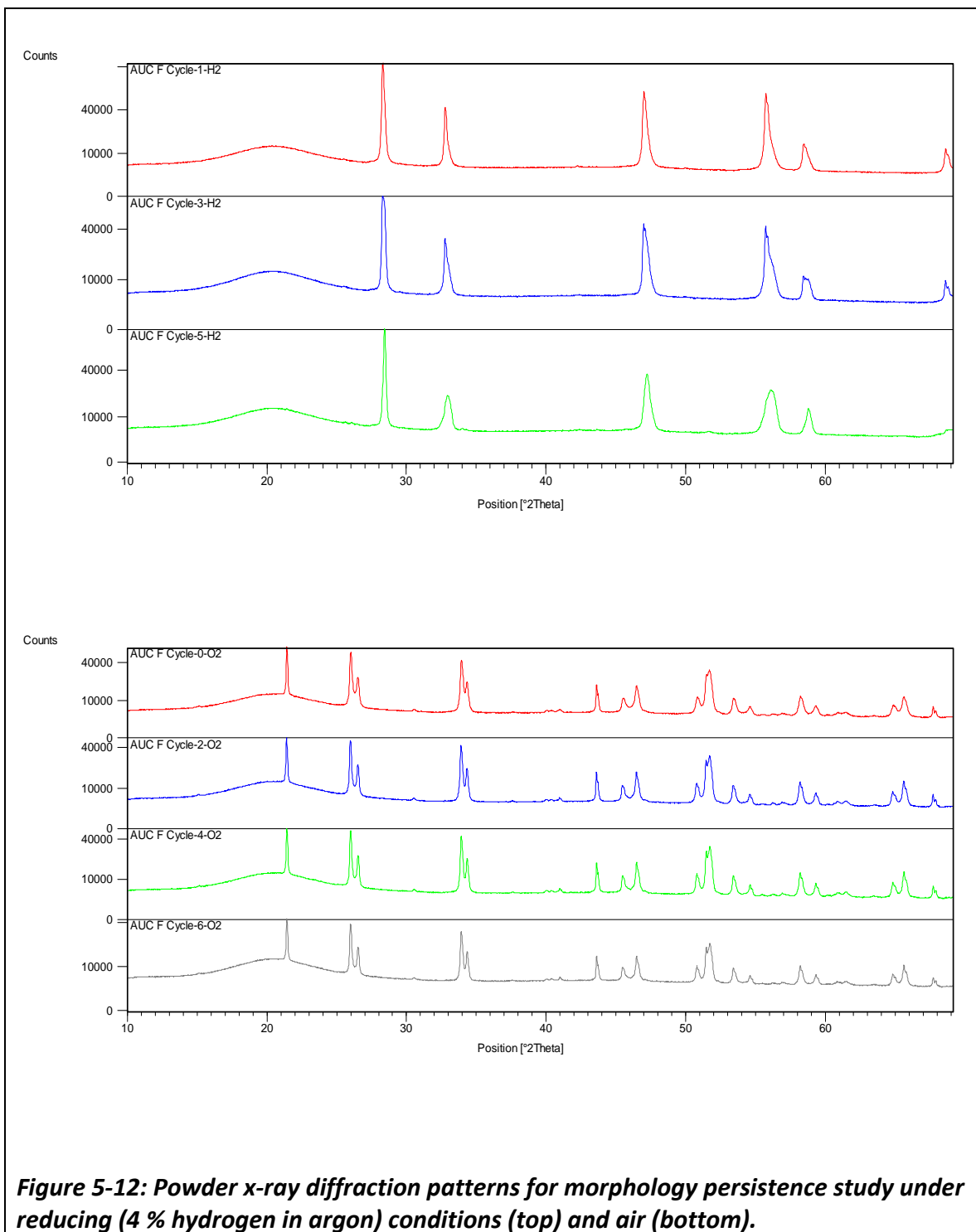


Figure 5-12: Powder x-ray diffraction patterns for morphology persistence study under reducing (4 % hydrogen in argon) conditions (top) and air (bottom).

Likewise, the transition from U_3O_8 to UO_{2+x} represents a 23 % change in density, a change in symmetry, and associated changes in lattice parameters.

Table 5-2: Crystal properties for species relevant to persistence study

Phase	Space Group	Symmetry	Lattice Parameters, Å	Density, g/cm ³	Ref.
AUC (NH ₄) ₄ (UO ₂)(CO ₃) ₃	C2/c	Monoclinic	a = 10.68 b = 9.38 c = 12.85	2.7	[166]
UO ₂	Fm3m	fcc	a = 5.47	10.95	[21]
U ₄ O ₉	I43d	bcc	a = 5.411	10.299	[21]
B-U ₃ O ₇		tetragonal	a = 5.383 c = 5.497	10.60	[21]
α-U ₃ O ₈	C2mm	orthorhombic	a = 6.716 b = 11.960 c = 4.147	8.395	[21]

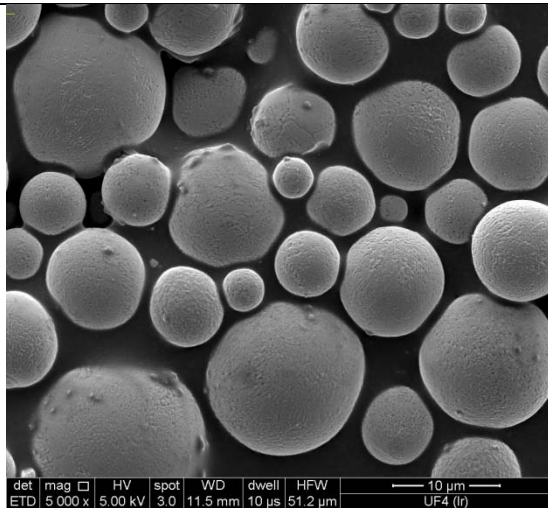
The study of the transition mechanisms between species in the uranium-oxygen system is an area of active debate and several authors have recently published investigations putting forth theories on the topic. Garrido [167] examined the oxidation of UO₂ to U₃O₇ using neutron diffraction and found that all of the uranium atoms and 70 % of the oxygen atoms were unaffected by the phase change. Garrido concluded that oxygen clusters transfer within a postulated cuboctahedral arrangement.

More recently Desgranges [168][169][170] performed research, including similar neutron scattering experiments on the *in situ* oxidation of UO₂ to U₃O₈, and concluded that the transition occurs in three stages: (1) formation of oxygen cuboctahedra, (2) development of a gradient and rearrangement of the cuboctahedra, and (3) yield of the “topological frustration” imposed by the cuboctahedra permitting the ordered stacking in U₃O₈. One could postulate the reversibility of these stages and conclude that slight

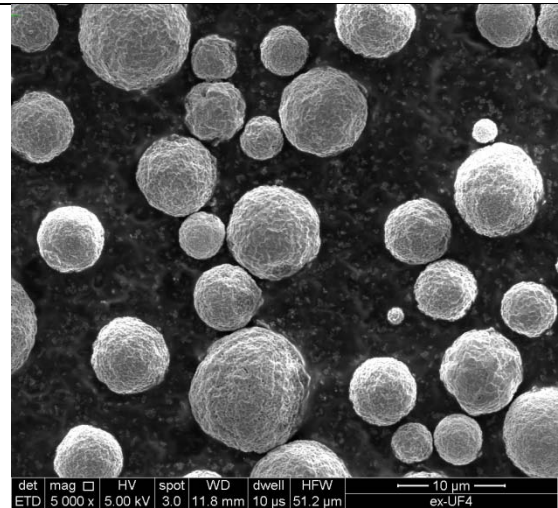
shifts of the oxygen cuboctahedra result in insignificant outward distortion of the overall crystal responsible for the pseudomorphic transition.

These findings offer a potential explanation for the pseudomorphic behavior observed during the oxide cycling of the persistence study; however, an explanation is also needed for phase transitions from non-oxide species, such as the precipitates examined in the balance of this chapter. Furthermore, this study also observed similar pseudomorphic behavior during the thermal oxidation of uranium tetrafluoride and uranium hydride solids (Figure 5-13). At this point, the best available explanation is that during oxidation reactions of non-oxide uranium compound, oxygen diffuses into the crystal structure displacing non-uranium atoms forming a sea of clusters that generally permits the retention of the outward structure. Clearly, additional study is needed to validate this explanation.

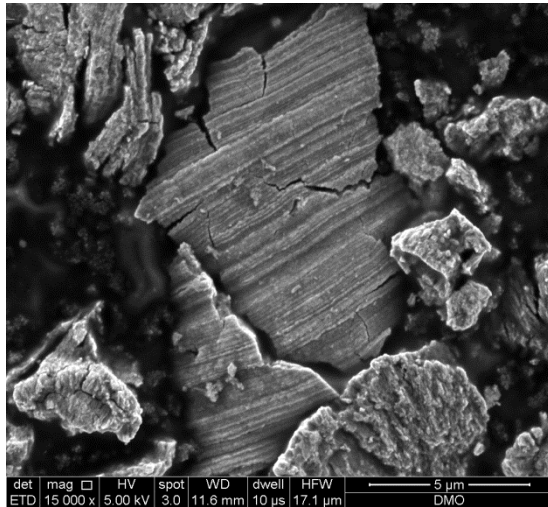
Overall, the persistence of the rhombohedral morphology in the AUC cycling study indicates that pseudomorphic transitions are a robust phenomenon suitably reliable for forensic applications. However, the mechanisms responsible for pseudomorphic phase transitions are poorly understood and represent a topic of intrigue for solid-state chemists requiring further detailed study beyond the scope of this dissertation.



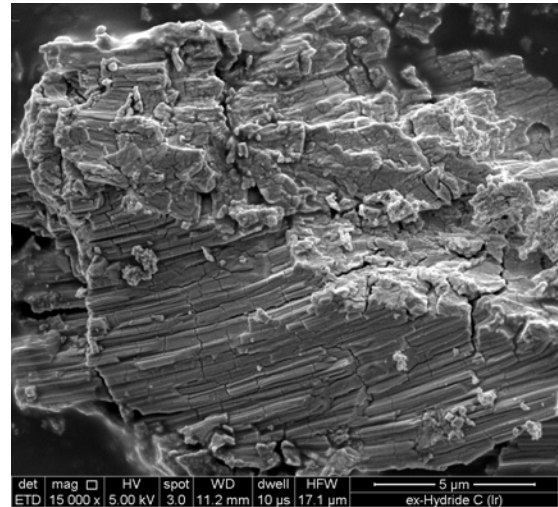
(a) Uranium tetrafluoride



(b) Uranium oxide produced from the oxidation of uranium tetrafluoride



(c) Uranium oxide produced from the direct oxidation of uranium metal



(d) Uranium oxide produced from the oxidation of uranium hydride

Figure 5-13: Examples of pseudomorphic transitions in other uranium bearing compounds

5.4 Conclusions and suggested areas for further study

Overall, this chapter demonstrated that morphology represents a useful signature to distinguish the process history in uranium precipitates and resulting oxides. Key supporting conclusions and suggested areas for future study include the following:

- Each of the commonly encountered precipitation processes for the uranyl ion displayed a unique morphology in the laboratory-derived exemplars. Furthermore, real-world samples produced using similar process chemistry displayed morphologies resulting in good qualitative visual comparisons with exemplars of comparable process history. Additional research is warranted to prepare and compare exemplars utilizing variations in flow sheet parameters and chemistry (e.g, sulfate instead of nitrate).
- Uranium precipitates decompose and transition to oxides in a pseudomorphic manner. This property represents an important development in nuclear forensics that enables the determination of process history for samples of otherwise chemically identical uranium oxides. Confirmation of this phenomenon in real-world samples is necessary. Subsequently, industrial samples of uranium oxides derived using the ammonia, hydrogen peroxide, and ammonium carbonate processes should be obtained and analyzed to validate that the pseudomorphic transitions observed in the laboratory are reproducible in industry.
- Image analysis using algorithms for texture shows promise as a tool to quantitatively distinguish and classify the process origin of uranium precipitates and oxides;

however, additional research and refinement of texture algorithms is required to mature this technique to a level suitable for forensics.

- The pseudomorphic phase transition phenomena observed in uranium species is robust and can be relied upon for forensics applications. Further probing of the chemical mechanism(s) that facilitate these transitions is warranted. Furthermore, the effects of milling and other physical insults encountered in industrial product conveyance should be examined.

Chapter 6 Process signatures in uranium oxide nuclear fuels

This chapter examines uranium oxide nuclear fuel pellets for signatures indicative of chemical processing history. Examination of a series of fuel pellets synthesized in the laboratory and pellets obtained from commercial nuclear manufacturers for physical and chemical signatures using secondary electron microscopy (SEM) revealed qualitative visual differences in the grain structures. However, measurement of simple morphological descriptors using image analysis methods failed to identify sufficient quantitative differences to elucidate effects of the type of precursor oxide or binder type. Additional investigation of the commercial fuel pellets revealed several features indicative of their known process flowsheets, as well as several currently unexplained features that require additional efforts to evaluate their forensic value. Overall, the study identified a few signatures in fuel pellets and several potential signatures that require investigation with the aid of additional process specific information.

6.1 Identification of potential signature generating aspects of fuel manufacturing

Historically, uranium dioxide has been the prevalent fuel for nuclear reactors worldwide. Consequently, there is considerable information in the literature, including textbooks, regarding the commonly utilized fuel manufacturing processes [23] [171]. An understanding of the various manufacturing processes is necessary to identify sources of potential manufacturing signatures. This section provides a summary of the manufacturing process and identifies process steps that may create forensic signatures.

The fuel manufacturing process begins with the arrival of uranium feedstock at the manufacturing facility as either: (1) a cylinder of uranium hexafluoride from an

enrichment facility, (2) uranyl nitrate solution resulting from the nitric acid dissolution of either scrap uranium oxides or nuclear fuel as part of a reprocessing operation, or (3) prepared uranium dioxide (UO_2) from another facility. For convenience, it is common to segregate the uranium conversion step into dry processes and wet processes (Chapter 2). In a dry process, uranium hexafluoride is sublimed to a gas, heated, and reacted in an atmosphere containing water vapor and hydrogen gas. The dry process results in the direct production of ceramic grade UO_2 . In a wet process, uranium is precipitated from an aqueous solution, rinsed, thermally decomposed, and then reduced in a hydrogen atmosphere to form UO_2 .

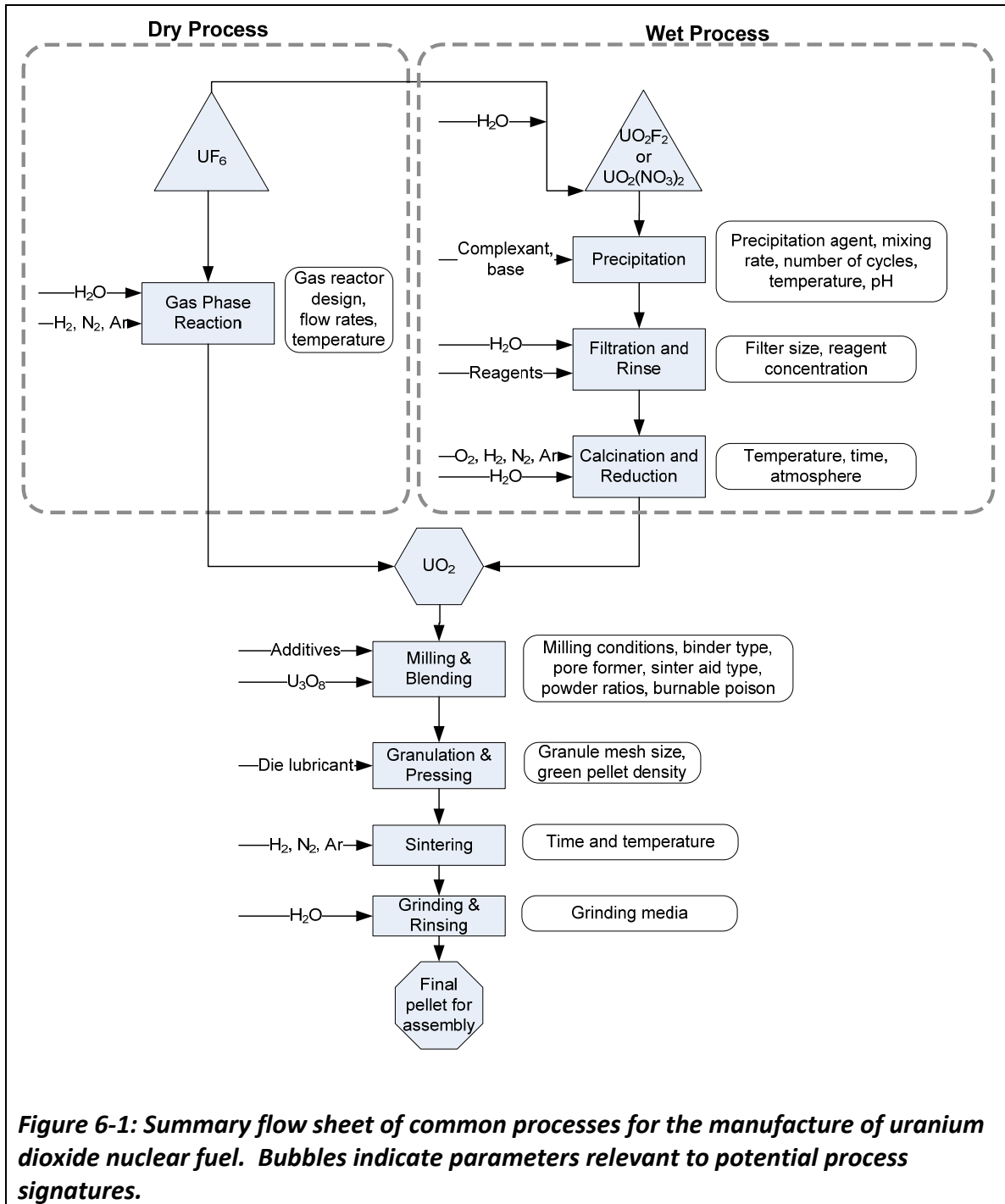
Once UO_2 is produced, powders are blended to achieve the desired isotopic enrichment and prepared to attain the density of the final pellet including the following possible steps:

- Milling
- Pre-compaction and granulation to improve the flow and packing properties of the powder
- Mixing with additives (e.g., sintering aids, binders, and burnable poisons), and blending with other UO_2 powders or recovered triuranium octoxide (U_3O_8)

The blended powder is then compacted—forming what is commonly referred to as a green pellet—and sintered in a reducing atmosphere at temperatures in the range of 1600–1800 °C. Sintered pellets are typically ground to precise dimensions, rinsed, and dried prior to assembly into a fuel rod, which will represent the end point of this

study. Pajo [172] and Kristo [173] previously demonstrated that basic geometric measurements and macroscopic features can be indicative of the manufacturer. This study will expand beyond these signatures to examine morphology and microscopic features.

In addition to the processing method used to generate UO_2 , there are several other steps in the fuel manufacturing process that warrant study for potential signatures (Figure 6-1). In particular, pellet characteristics are typically improved using additives, which can be grouped into three categories: (1) inorganic sinter aids, (2) organic binders, pore formers and lubricants, and (3) burnable lanthanide poisons. The type of additive and its impact on the resulting pellet properties warrants study. The type of binders and pore formers may have different decomposition behaviors resulting in different pores with different geometric characteristics. Similarly, other powder preparation techniques such as milling and granulation may result in signatures in the final sintered pellet.



6.2 Evidence of morphological signatures in the literature

As introduced in Chapter 5, several researchers identified links between the final sintered fuel pellet and the properties of the precursor oxide powder. Additional

literature supports this link and suggests the potential value of morphological signatures in fuel pellets. For example, Chorokov [153] found differences in the surface roughness of fuel pellets to be specific to the production plant and pellet type. Lee and Yang [134] compared uranium dioxide derived from ammonia and ammonium carbonate by mercury porosimetry and found differences in the pore size distribution between the powders, which translated into differences in the pore structure and density of the final pellet. Similarly, Choi [132] examined the influence of conditions used to derive UO_2 using the ammonium carbonate precipitation process and observed differences in the open pore volumes of the sintered pellets. Glodeanu [174] reached similar conclusions on the need for stringent powder characteristics to ensure appropriate quality for pellet microstructure.

In general, the above authors obtained measurements on the pellets that should directly correlate with the morphology of UO_2 grains. For example, open pore volume and grain size directly contribute to morphology of the pellet grain structure. Published research utilizing direct measurements of grain morphology in sintered uranium bodies is limited. Gündüz [175] studied the microstructure of uranium–gadolinium oxide fuels using the measurement of fractal dimensions to characterize the effects on pellet grain structure. Arnould [65] applied image analysis to study the densification of cerium oxide compacts, which is commonly utilized as a surrogate for the actinides.

6.3 Methods

6.3.1 Process analysis of commercially produced fuel pellets

Larwence Livermore National Laboratory (LLNL) previously obtained samples of nuclear fuel pellets from three commerical manufacturers for nuclear forensics research. The pellets were accompanied with limited information related to their manufacturing process (e.g., specifications, analytical data, etc) and were examined for foresenic signatures in a preliminary study [173]. Manufacturing process information from each of the vendors was compiled using the strategy outlined in Figure 6-1 as a guide (Table 6-1). The names of the vendors are protected in support of an agreement to access their proprietary information and the process conditions are condensed to reflect an overall summary of the various pellet designs offered by each vendor.

Table 6-1: Comparison by manufacturer of selected process parameters for commercial nuclear fuel pellets

Process Parameter	Manufacturer		
	A	B	C
<i>UO₂ Production Method</i>	Wet conversion using ammonium hydroxide	Direct Conversion Fluidized Bed	Integrated dry process
<i>Blend Additives</i>	Ethylene stearamide (binder)	Ethylene stearamide (binder) Ammonium oxalate (pore former) Azodicarboamide (pore former)	Silicon dioxide (sintering aid) Aluminum stearate (binder) Azobisformamide (pore former)
<i>Limits on recycled U₃O₈ add-back, wt %</i>	≤ 8	Not specified	≤ 30
<i>Powder Physical Preparation</i>	Unspecified	Pre-pressed to unspecified pressure and granulated to 12 mesh	Hammer milled, roll compacted, and granulated to unspecified conditions
<i>Green density, g/cm³</i>	6.45	~6	5.7–6.6
<i>Sintering Conditions</i>	4 hours at 1735 °C 7.3 hours total	2.3 hours at 1750 °C 8 hours total time	4 hours at 1800 °C 21 hours total time

6.3.2 Synthesis of miniaturized fuel pellets in the laboratory

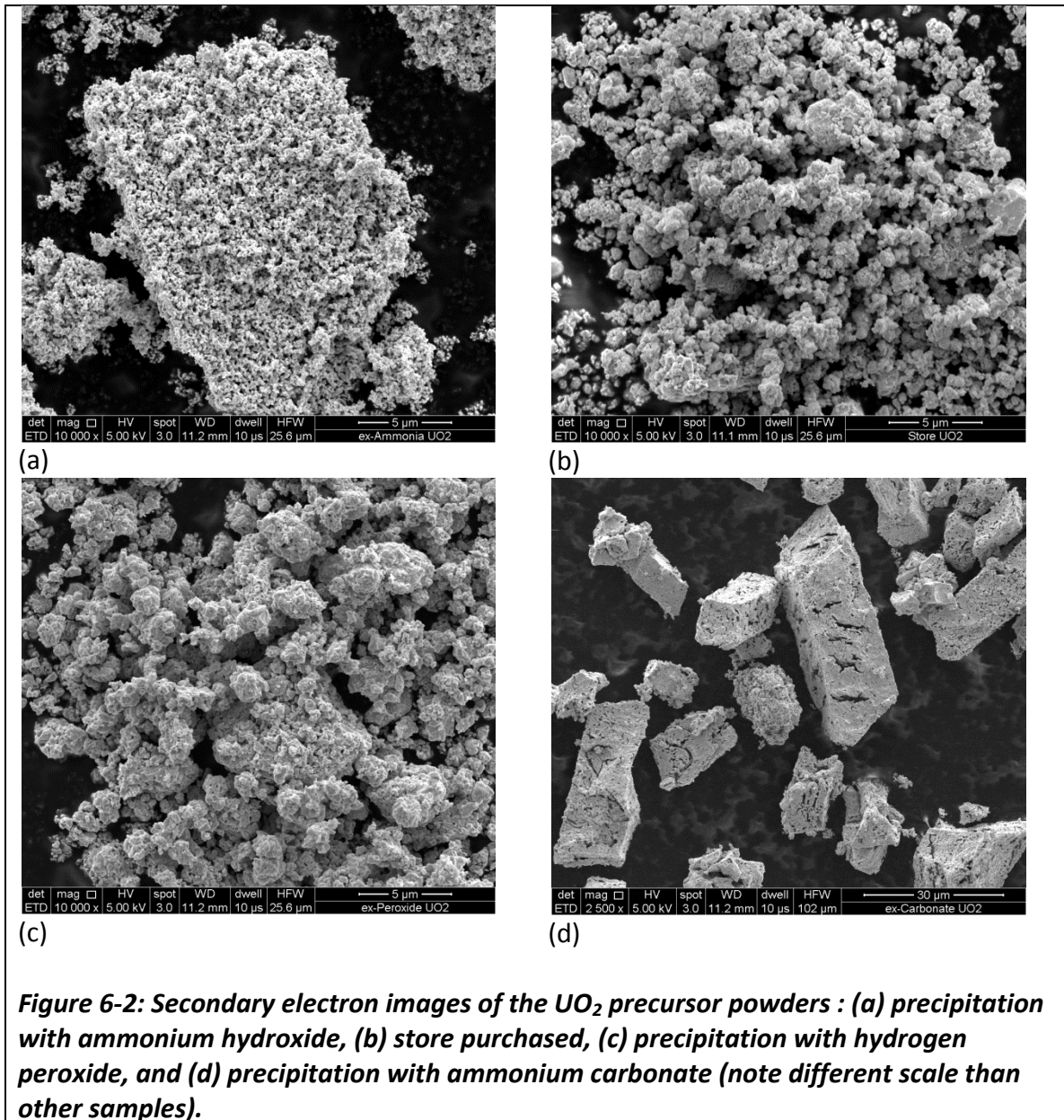
This study synthesized miniature uranium oxide fuel pellets in the laboratory to examine the effects of the precursor oxide production route and binder type on grain morphology. Pellets were produced using precursor UO_2 powders derived through precipitations from 1.0 M uranyl nitrate stock solutions using the following:

- 1.0 M ammonium hydroxide to pH 8–9
- 30 % hydrogen peroxide
- Saturated ammonium carbonate to pH 8–9

The ammonium carbonate and hydrogen peroxide precipitations were conducted in centrifuge cones, washed with equal volumes of deionized water, centrifuged, and decanted. The ammonium carbonate precipitation was conducted in a filtered funnel and similarly washed. All precipitates were air dried overnight in an oven at 85 °C, hand ground with mortar and pestle, and oxidized overnight to U_3O_8 in a box furnace at 750 °C. Each sample of U_3O_8 was ground again in mortar and pestle before reducing in batches for 6–12 hours in a tube furnace at 600 °C with an atmosphere of 5 % percent hydrogen in argon. All of the batches for a given precipitate were blended and the phase of the resulting mixture confirmed using powder x-ray diffraction. In addition, experiments utilized a fourth precursor UO_2 powder based on a commercially produced material by Alfa Aesar (#12108, Lot K22M14O), henceforth referred to as the “store” powder.

Previous investigations on the morphology of these precursor powders (Chapter 5) suggested that each type of UO_2 powder would result in unique morphology.

Scanning electron microscopy confirmed that each of these precursor powders exhibited a unique morphology (Figure 6-2). Based on experience gained in Chapter 5, the store powder exhibited morphology consistent with uranium oxides produce by the thermal denitration of uranyl nitrate.



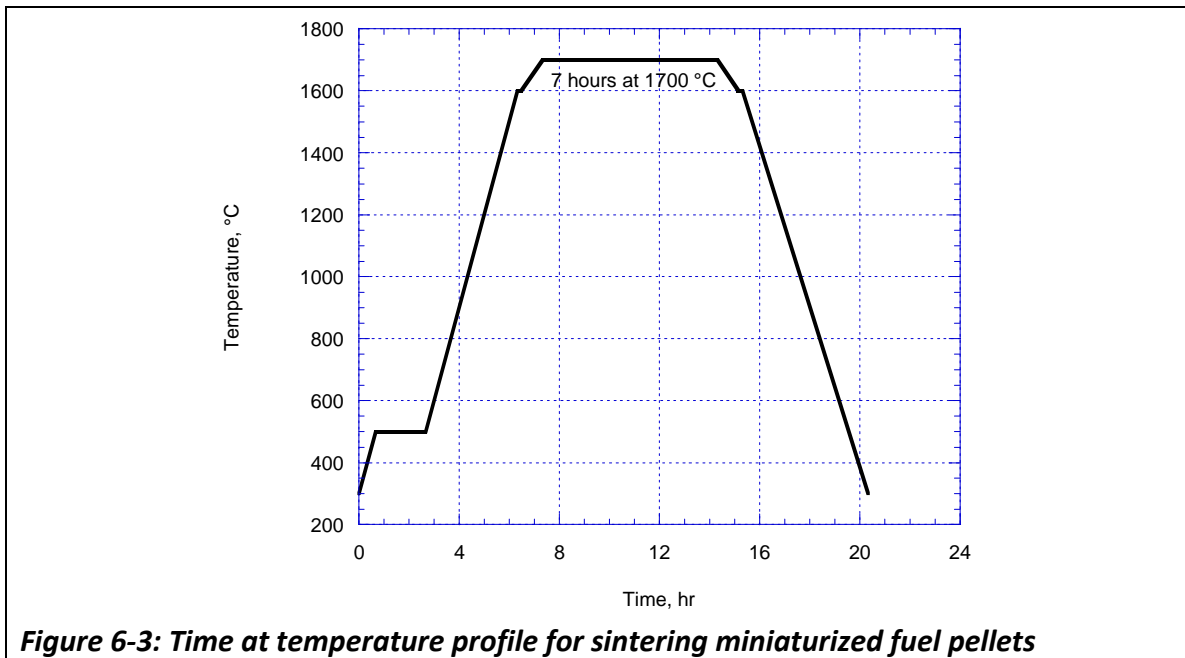
As discussed in Section 6.2, the literature suggested that differences in morphology would manifest as density changes in the resulting sintered pellet. Commercial nuclear fuel manufacturers typically produce pellets with a final sintered density of better than 90 % of the theoretical density and in many cases 95-97 % of theoretical, depending on the reactor customer. The theoretical density of UO_2 is 10.96 g/cm^3 [23][21]. Scoping experiments determined the conditions necessary to produce pellets with consistent, high densities for each binder and the four types of precursor powder. The binders investigated were ethylene stearamide, aluminum stearate, and zinc stearate.

Allen and McConnell [176] performed these scoping studies as part of the Radiochemistry Fuel Cycle Summer School. They examined the use of 0.25–1.25 weight percent ethylene stearamide and aluminum stearate with store and ammonium carbonate-derived UO_2 . They identified optimal binder contents in the range of 0.3–0.8 weight percent for each combination of binder and powder. This binder content resulted in pellets with peak densities greater than 90 % of theoretical. Subsequently, all pellets used a nominal binder content of about 0.5 weight %.

The synthesis of the miniaturized fuel pellets used the following procedure. The desired additives and UO_2 powder were mixed in a vortex mixer for approximately 30 seconds. About 0.5 g of the homogenized powder mixture was weighed, poured into a 6.35 mm (1/4 inch) die, and pressed to 500 MPa with the pressure held approximately constant for 1 minute. These unsintered pellets, otherwise known as “green pellets”, were extracted from the die set, weighed, height measured, and placed in a high

temperature alumina furnace boat lined with molybdenum metal plate to prevent interaction with the boat. The use of molybdenum boats is also a common industry practice.

The pellets were sintered in a flowing mixture of 5 % hydrogen in argon using a controlled atmosphere tube furnace manufactured by MTI Corporation in Richmond, California. All pellets were sintered for 7 hours at 1700° C according to a prescribed time at temperature profile (Figure 6-3). The profile included 90 minutes at 500 °C for binder decomposition. The heating rates used in the profile were dictated by limitations on the furnace components. The consistency of sintering conditions between furnace runs was monitored using TempTabs (www.temptab.com), which are ceramic materials engineered to contract at consistent rates when exposed to elevated temperature. Sintering conditions, as indicated by TempTab size, varied less than 1 percent.



6.3.3 SEM imaging and image analysis

Commercial pellets and pellets synthesized in the laboratory were analyzed using an FEI Inspect F SEM instrument. A spring-loaded, top-justified sample mount using tantalum washers as spacers was used to hold the uncoated and unpolished pellets for imaging. Backscatter electron imaging provided the best contrast for grain boundary analysis and was performed with an accelerating voltage of 15 kV and a working distance of 11.5 mm. In select cases, energy dispersive x-ray spectroscopy was performed using an EDAX Apollo silicon drift detector with the associated Genesis software package.

Image analysis was performed on the SEM imagery of pellet grain structures consistent with the development discussed in Chapter 3. Images of commercial pellets were manually segmented and the morphological descriptors measured using the ImageJ software [66]. Images of laboratory-derived pellets were fully processed using the MAMA software [67]. Most of the pellets were imaged at a magnification of 2500 X with 5–10 images obtained from spatially diverse locations on the pellet surface. Qualitative scoping studies did not indicate any systematic spatial variations. The number of images obtained and analyzed was driven by the need to obtain total counts of about 500 or more grains.

6.4 Results and discussion

Commercially produced and laboratory-derived nuclear fuel pellets (Figure 6-4) were examined for signatures of interest to nuclear forensics. The grain morphology was evaluated in both sets of pellets to identify possible trends with process. The

commercial pellets were also broadly examined for other microscopic features that might be indicative of the process history or environment.

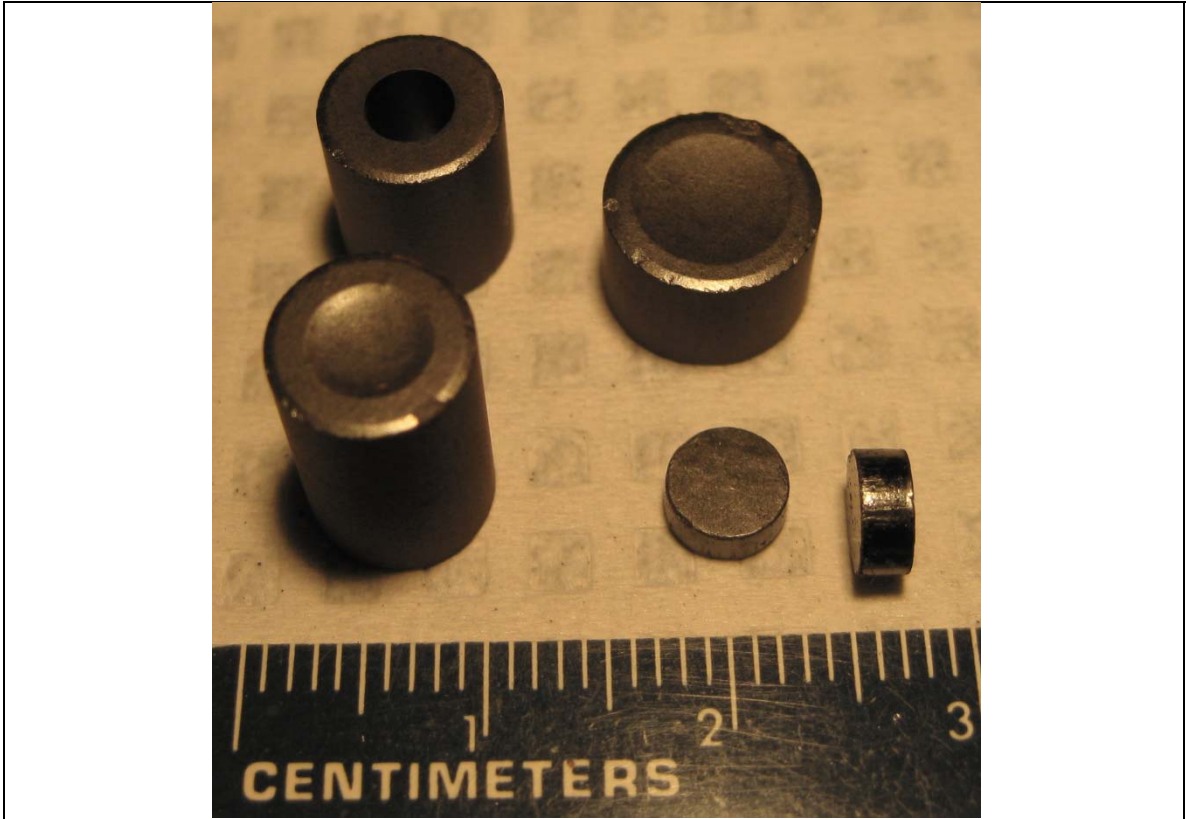


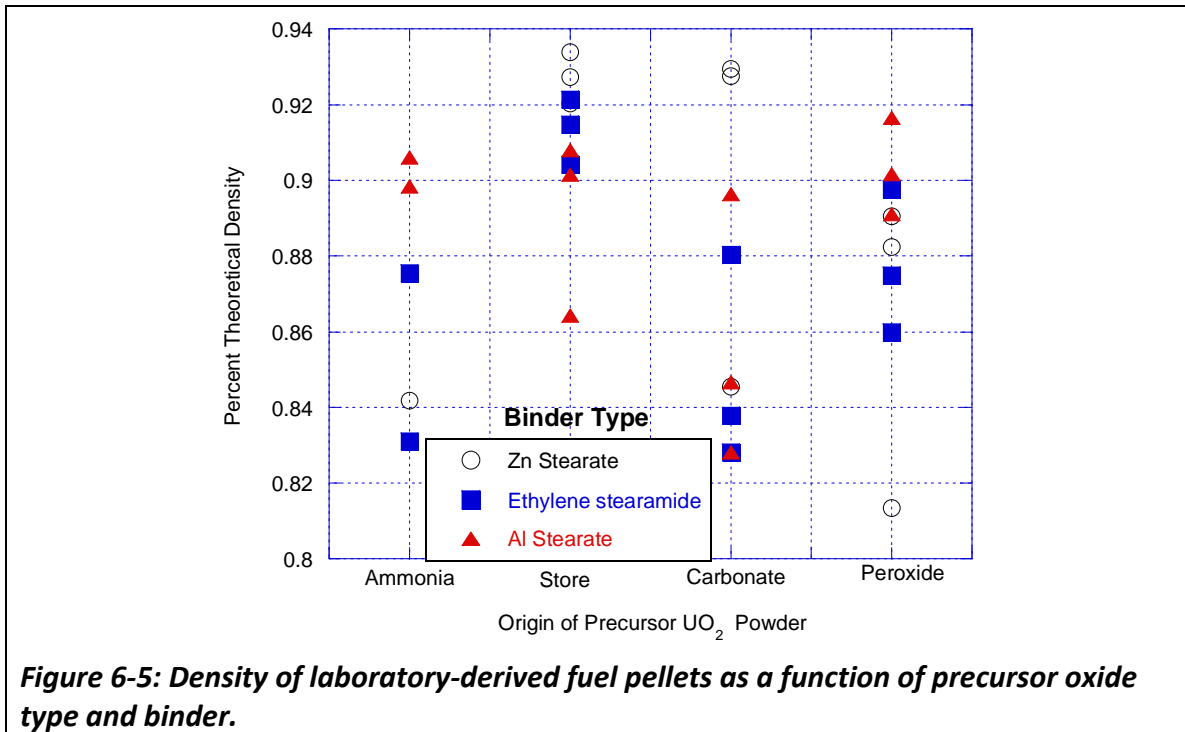
Figure 6-4: Examples of three commercial nuclear fuel pellets (top left) and two miniature pellets synthesized in the laboratory (bottom right).

6.4.1 Grain morphology is visually distinct, but quantitatively non-specific

This study produced a set of 36 laboratory-derived miniature nuclear fuel pellets to examine the effects of the binder type and the chemical production method used for precursor UO_2 powder on sintered grain morphology. The pellet set included 4 precursor oxide types and 3 binders (Section 6.3.2). Triplicate pellets were produced from a common powder blend representing each combination of oxide and binder; however, each of the triplicate pellets was sintered separately. The blends of powder

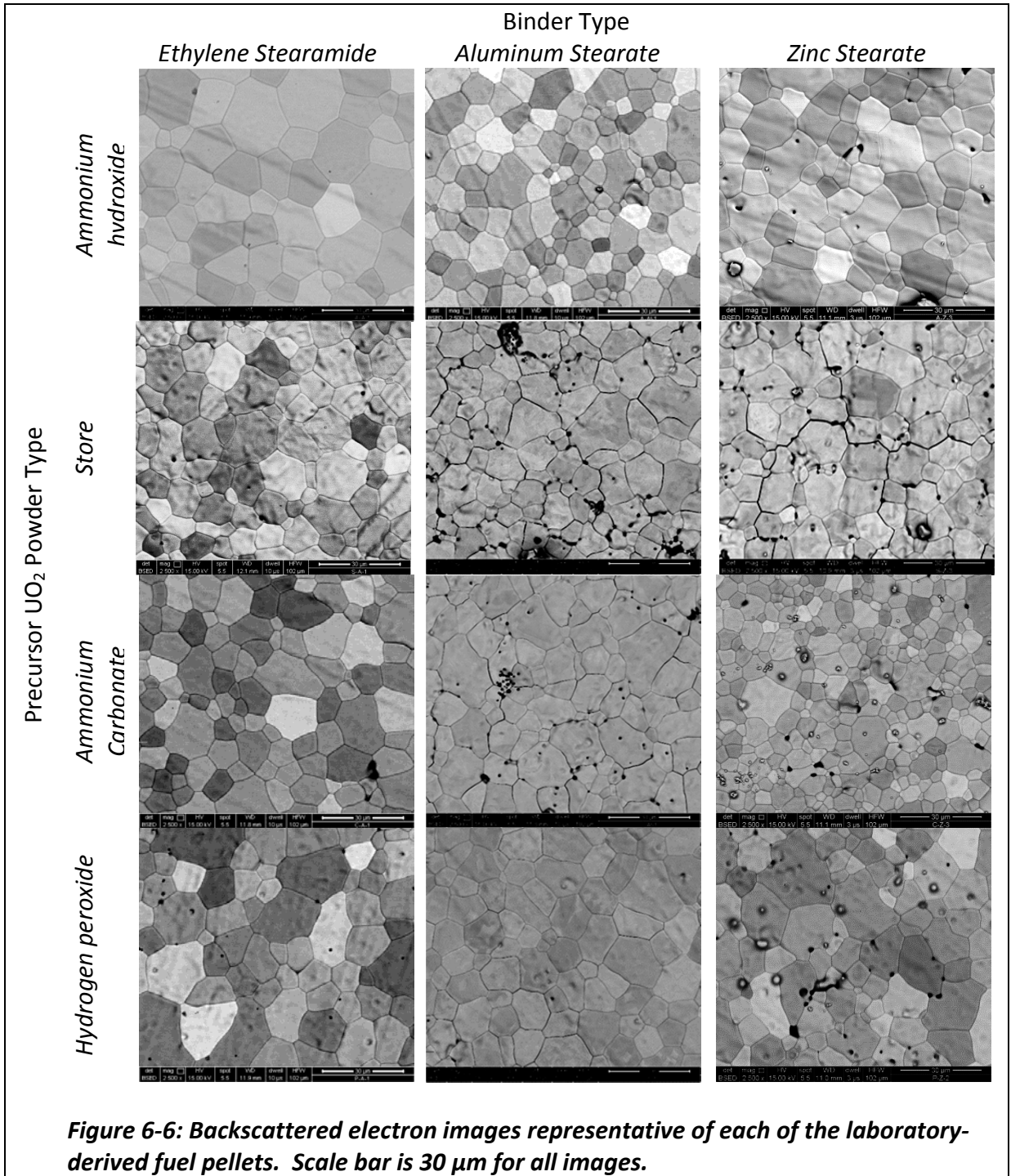
and binder were selected to produce pellets of similar densities and quality comparable to industry (greater than 90 % of theoretical density).

The observed final pellet densities were more diverse and lower than desired (Figure 6-5). A definitive explanation for these results is not readily apparent, though likely causes include insufficient sintering or lack of homogeneity in the powder blends prior to pressing. Note that several of the sintered pellets split, particularly those created using zinc stearate as a binder, rendering precise density measurements difficult using manual measurements. Despite some pellets with densities approximately 6 % lower than desired, the overall quality and porosity of pellet surfaces remained sufficient to support examination of the grain morphology.



Overall, the laboratory-derived pellets exhibited some visually evident differences in porosity and grain size as a function of their process origin (Figure 6-6).

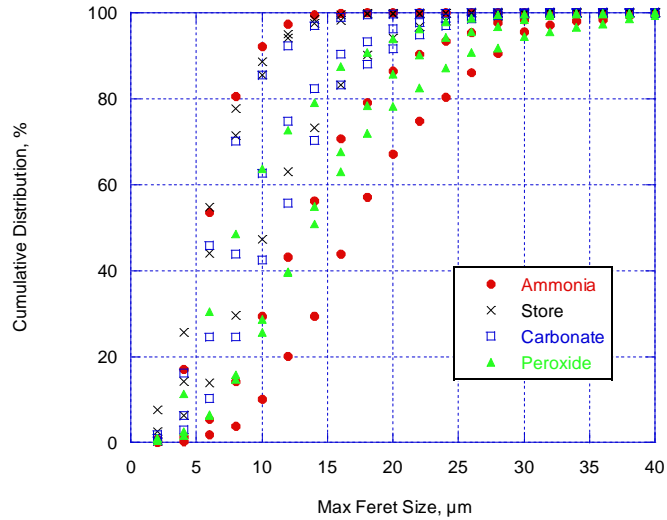
An obvious feature of interest is the vivid variation in shading among grains on several of the pellets (e.g., ammonium carbonate with ethylene stearamide). Such variation in signal is unexpected for a backscattered electron image of a homogenous material.



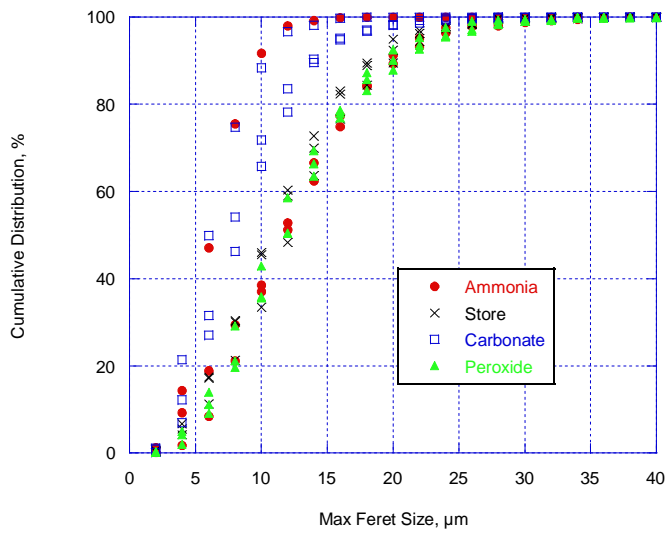
Energy-dispersive x-ray spectrometry of contrasting grains confirmed no detectable difference in composition. Several pellets were then polished to investigate the potential for differences in grain heights to contribute to the phenomenon. The polishing significantly reduced the phenomenon, suggesting that it may have originated from conductivity variations in each grain. The phenomenon was also observed with some of the commercial pellets. As discussed in Section 6.4.2, this phenomenon may also be an artifact of minor variations in grain oxygen to uranium ratios resulting in subtle conductivity differences.

Quantitative measurements of morphological descriptors for grains were taken to support an objective comparison between pellets. Further, reliable qualitative comparison is also difficult when using the single images displayed in Figure 6-6. Consistent with the outcomes from Chapter 3, measurements and associated descriptive statistics were taken for grain area, maximum Feret diameter, and aspect ratio (Table 6-2 to Table 6-4).

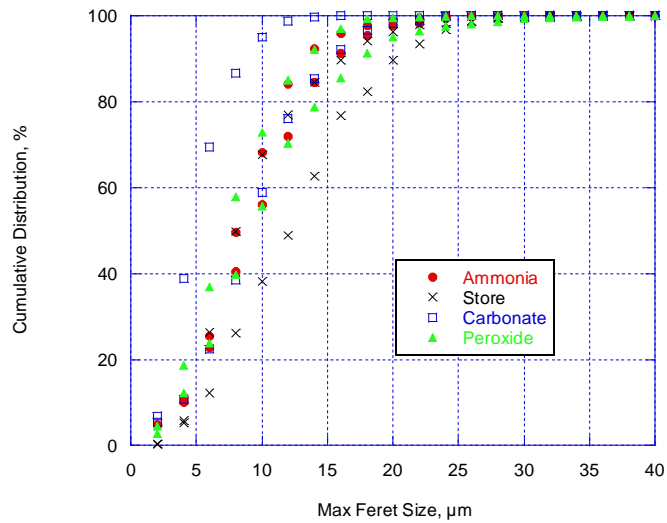
The data for maximum Feret diameter (Figure 6-7) fail to indicate trends useful for grain morphology as a signature. In particular, the distributions are similar in shape and little consistency is exhibited between triplicate pellets. Similarly, the data for mean grain area and aspect ratio (Figure 6-8) fail to reveal obvious trends with respect to either precursor powder type or binder. These results are unexpected for a number of reasons. First, while qualitative, the grain structures displayed in Figure 6-6 demonstrate some obvious variations. Appropriate quantitative methods should be able to observe this variation. Second, addition of aluminum stearate as binder is



Ethylene Stearamide



Aluminum Stearate



Zinc Stearate

Figure 6-7: Cumulative distribution curves for maximum Feret size as a function of precursor UO_2 and binder.

commonly thought to result in increased grain sizes, which was not observed in this study.

Overall, the measurement of simple morphological descriptors performed on the grain structures was insufficient to differentiate reliably between the type of precursor UO_2 powder and binder of laboratory-derived fuel pellets. Given the slight qualitative visual differences, it is possible that application of more sophisticated morphological descriptors (e.g., fractal analysis) or techniques not yet developed will prove better at distinguishing the pellets. It is also possible that grain morphology is not as sensitive to precursor material and binder type as indicated in the literature for pore geometries, densities, and other pellet properties.

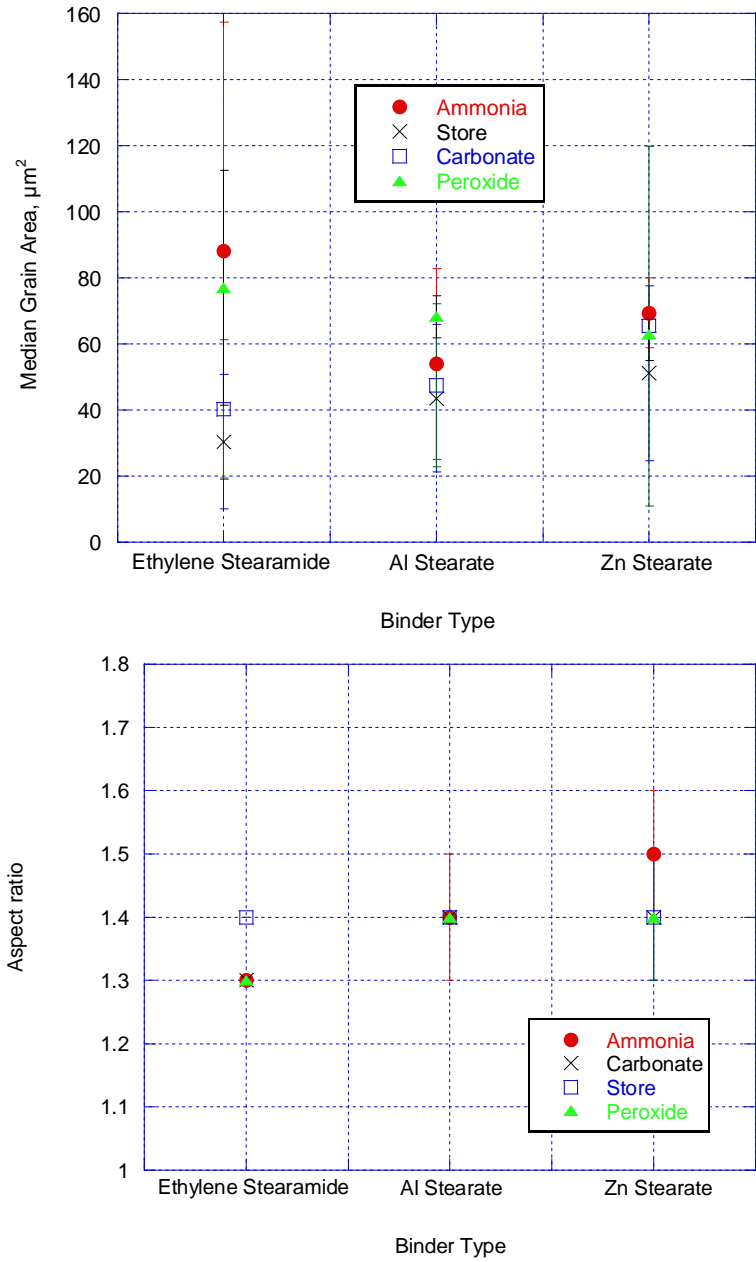


Figure 6-8: Variation of median grain area (top) and aspect ratio (bottom) as a function of binder and precursor UO_2 powder. Error bars represent the standard deviation ($n=3$).

Table 6-2: Measurements of morphological descriptors in pellets using ethylene stearate as a binder

		Ammonia			Store			Ammonium Carbonate			Hydrogen Peroxide		
	Count	317	965	743	558	706	915	648	632	679	530	525	600
Area, μm^2	D10	50.8	6.0	26.4	12.1	6.6	2.7	10.8	17.4	6.0	26.1	23.9	7.2
	D50	156.2	17.8	90.6	53.8	21.0	16.4	38.6	62.0	20.2	93.8	101.0	36.1
	D90	415.4	46.7	256.8	165.4	61.0	54.5	135.6	185.6	65.7	268.5	344.0	151.3
	Span	2.3	2.3	2.5	2.8	2.6	3.2	3.2	2.7	3.0	2.6	3.2	4.0
	Mean	202.8	22.9	120.2	77.4	30.4	24.1	61.1	86.3	29.1	123.9	155.6	64.0
	Variance	25591.0	366.3	11402.5	5535.4	1591.4	648.6	4384.4	6356.7	807.3	12061.2	28819.5	5813.7
	Kurtosis	4.2	5.6	5.8	6.9	141.3	20.6	8.7	5.7	18.1	6.4	6.9	9.4
	Skewness	1.8	2.1	2.1	2.2	9.2	3.1	2.5	2.1	3.1	2.1	2.4	2.6
Max Feret, μm	D10	10.0	3.6	7.1	5.3	3.6	3.6	4.5	5.9	3.6	7.1	6.9	3.8
	D50	17.4	5.9	13.0	10.3	6.3	6.3	8.5	11.3	6.3	13.2	13.8	8.3
	D90	27.6	9.7	21.7	17.8	10.9	10.9	15.8	18.9	11.4	21.9	25.1	17.3
	Span	1.0	1.0	1.1	1.2	1.2	1.2	1.3	1.2	1.3	1.1	1.3	1.6
	Mean	18.0	6.2	13.8	11.1	7.0	7.0	9.6	11.8	6.9	14.0	15.2	9.6
	Variance	46.5	5.8	35.9	26.9	10.4	10.4	23.0	28.6	9.7	36.9	62.4	31.2
	Kurtosis	0.2	1.2	1.6	0.9	15.4	15.4	1.5	2.5	2.5	1.1	1.3	1.6
	Skewness	0.6	0.9	1.0	0.8	2.4	2.4	1.2	1.1	1.2	0.8	1.1	1.2
Aspect Ratio	D10	1.1	1.1	1.1	1.1	1.1	1.1	1.1	1.1	1.1	1.1	1.1	1.1
	D50	1.3	1.3	1.3	1.3	1.3	1.3	1.3	1.3	1.3	1.3	1.3	1.3
	D90	1.6	1.6	1.6	1.7	1.6	1.7	1.6	1.6	1.6	1.6	1.6	1.6
	Span	0.4	0.4	0.4	0.5	0.4	0.4	0.4	0.4	0.4	0.4	0.4	0.4
	Mean	1.3	1.3	1.3	1.4	1.3	1.4	1.3	1.4	1.3	1.3	1.3	1.3
	Variance	0.1	0.1	0.1	0.2	0.1	0.1	0.1	0.1	0.1	0.0	0.1	0.1
	Kurtosis	9.2	8.8	42.5	72.3	4.4	11.0	17.5	5.8	4.2	6.6	8.0	7.6
	Skewness	2.3	2.2	4.4	6.4	1.6	2.5	2.9	2.0	1.6	1.9	2.1	2.0

Table 6-3: Measurements of morphological descriptors in pellets using aluminum stearate as a binder

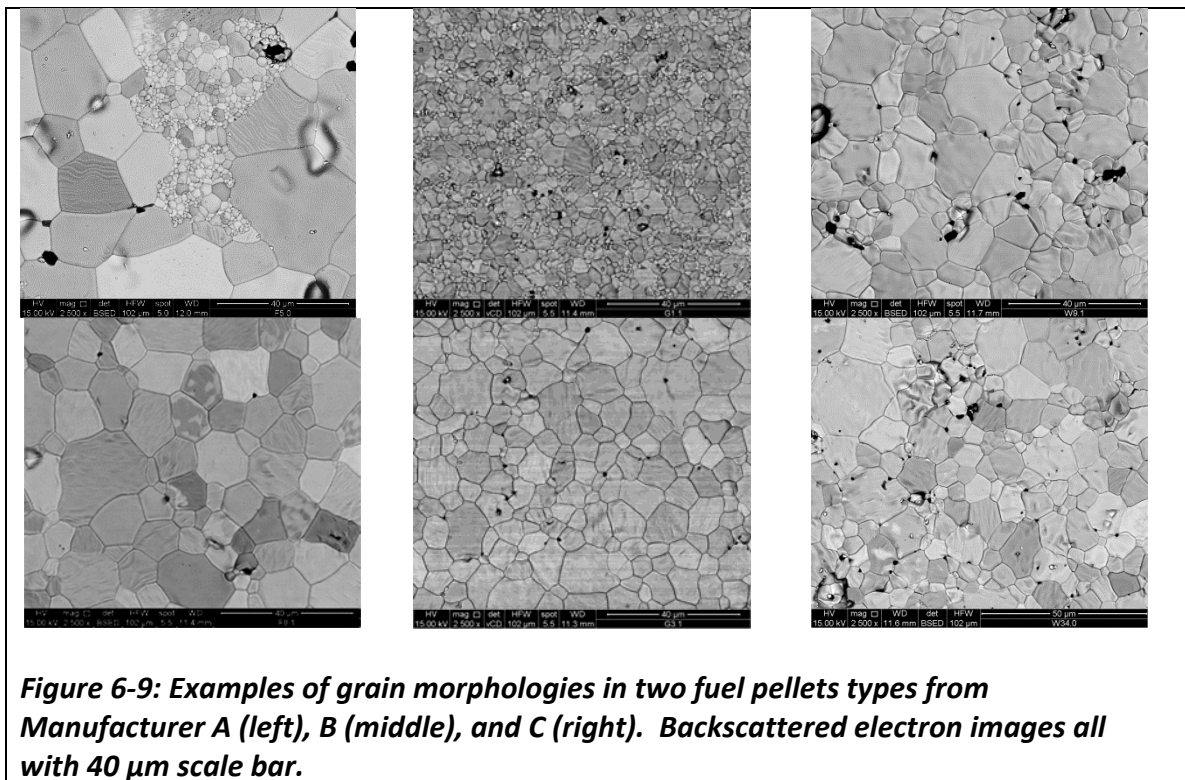
		Ammonia			Store			Ammonium Carbonate			Hydrogen Peroxide		
	Count	574	845	640	585	548	557	654	571	518	580	539	522
Area, μm^2	D10	22.0	6.8	6.2	10.7	10.3	5.1	16.7	6.4	8.7	20.2	14.6	15.5
	D50	72.5	20.6	68.7	56.2	56.6	17.7	76.0	31.2	35.4	72.5	71.3	61.0
	D90	213.4	51.1	209.0	164.9	182.7	54.1	220.4	100.1	109.6	190.1	218.3	203.4
	Span	2.6	2.1	3.0	2.7	3.0	2.8	2.7	3.0	2.8	2.3	2.9	3.1
	Mean	98.5	25.6	97.0	77.6	81.6	25.3	97.5	45.6	50.4	95.0	99.6	91.5
	Variance	7927.2	386.5	9819.0	6278.1	6786.5	539.0	6779.7	2484.7	2398.9	7166.8	8085.7	9689.8
	Kurtosis	6.2	4.7	5.6	10.4	7.2	5.3	3.6	12.3	10.0	11.5	3.8	8.9
	Skewness	2.1	1.8	2.0	2.6	2.3	2.0	1.6	2.9	2.5	2.5	1.8	2.6
Max Feret, μm	D10	6.3	3.6	4.1	4.8	4.6	3.2	5.9	3.8	4.2	6.5	5.5	5.4
	D50	11.6	6.1	11.7	10.5	10.6	6.0	12.1	7.7	8.4	11.9	11.9	11.0
	D90	19.9	9.7	20.0	18.4	18.5	10.3	20.1	13.8	14.0	19.1	20.6	19.9
	Span	1.2	1.0	1.4	1.3	1.3	1.2	1.2	1.3	1.2	1.1	1.3	1.3
	Mean	12.4	6.5	12.2	11.2	11.3	6.4	12.5	8.4	9.0	12.3	12.7	11.9
	Variance	28.5	6.0	39.4	29.9	30.4	8.1	28.8	18.2	16.7	26.6	33.5	36.1
	Kurtosis	1.1	0.8	0.6	1.8	0.9	0.8	0.0	3.4	1.6	2.0	0.6	1.5
	Skewness	0.9	0.7	0.7	1.0	0.8	0.9	0.5	1.4	1.0	0.9	0.7	1.1
Aspect Ratio	D10	1.1	1.1	1.1	1.1	1.1	1.1	1.1	1.1	1.1	1.1	1.1	1.1
	D50	1.3	1.3	1.3	1.3	1.3	1.3	1.3	1.3	1.3	1.3	1.3	1.3
	D90	1.6	1.6	1.7	1.7	1.7	1.7	1.7	1.6	1.8	1.7	1.7	1.7
	Span	0.4	0.4	0.5	0.4	0.4	0.4	0.5	0.4	0.5	0.4	0.4	0.4
	Mean	1.3	1.3	1.6	1.4	1.4	1.4	1.4	1.3	1.4	1.3	1.4	1.4
	Variance	0.1	0.0	1.4	0.1	0.1	0.1	0.1	0.1	0.1	0.1	0.2	0.1
	Kurtosis	28.0	6.6	33.7	39.3	8.5	4.7	4.2	4.8	3.7	4.6	217.1	8.5
	Skewness	3.5	1.9	5.6	4.7	2.2	1.6	1.7	1.7	1.6	1.8	12.1	1.9

Table 6-4: Measurements of morphological descriptors in pellets using zinc stearate as a binder

		Ammonia		Store		Ammonium Carbonate		Hydrogen Peroxide	
	Count	552	409	583	374	501	525	573	525
Area	D10	10.7	21.6	9.9	10.9	19.9	6.9	13.0	12.5
	D50	61.9	76.9	32.4	69.9	104.0	26.9	68.4	57.3
	D90	152.4	204.8	131.3	211.7	276.9	94.0	204.5	195.4
	Span	2.3	2.4	3.7	2.9	2.5	3.2	2.8	3.2
	Mean	76.5	103.0	55.3	93.9	128.1	38.5	93.7	87.1
	Variance	4311.8	8673.9	4577.3	7727.9	12276.5	1364.4	8845.4	8219.3
	Kurtosis	8.4	19.1	22.5	7.1	5.9	5.0	13.0	10.1
	Skewness	2.1	3.1	3.7	2.0	2.0	2.0	2.7	2.6
Max Feret	D10	3.8	4.0	4.5	5.2	3.8	2.3	3.1	3.6
	D50	9.2	8.1	8.1	12.0	9.2	4.7	7.2	9.2
	D90	15.7	13.2	16.2	20.2	15.5	8.7	12.9	17.6
	Span	1.3	1.1	1.4	1.2	1.3	1.4	1.4	1.5
	Mean	9.5	8.1	9.3	12.4	9.4	5.1	7.6	10.1
	Variance	22.9	54.8	24.4	33.5	19.8	6.4	26.9	32.7
	Kurtosis	0.9	136.9	4.2	0.2	0.3	0.8	90.7	2.3
	Skewness	0.6	-9.5	1.6	0.5	0.4	0.9	-5.8	1.2
Aspect Ratio	D10	1.1	1.1	1.1	1.1	1.1	1.1	1.1	1.1
	D50	1.3	1.3	1.3	1.3	1.3	1.3	1.3	1.3
	D90	1.8	1.7	1.7	1.8	1.8	1.6	1.7	1.8
	Span	0.5	0.5	0.4	0.5	0.5	0.4	0.4	0.5
	Mean	1.5	1.4	1.4	1.5	1.4	1.3	1.4	1.4
	Variance	0.9	0.2	0.1	0.5	0.3	0.0	0.1	0.1
	Kurtosis	36.2	63.4	34.7	83.6	82.7	3.4	21.0	16.3
	Skewness	5.6	6.5	4.0	7.8	7.7	1.5	3.4	3.0

Examination of 24 commercially produced fuel pellets indicated obvious qualitative differences (Figure 6-9). However, manufacturers typically produce multiple types of pellets using different specifications, resulting in comparisons that may be inappropriate to generalize. The qualitative visual differences for two pellet types from each manufacturer displayed in Figure 6-9 demonstrate this issue.

This study examined 7, 5, and 8 different pellet types from Manufacturers A, B, and C, respectively. Recognizing the complexity introduced from multiple pellet types, the approach for assessing the quantitative morphological measurements considered all pellet types and then examined process information to develop signatures based on a link with a particular aspect of the process, rather than by manufacturer.



The grain area and aspect ratio was measured for all pellets (Figure 6-10). The data on grain area indicate some groupings by manufacturer, though Manufacturers B and C appear to produce pellet types with two distinct grain size distributions. A limited study of two pellets from a given batch from each of these manufacturers indicates that there is some variation of grain area within a given batch, but the magnitude of this variation is insufficient to explain the wider differences observed. The most likely source of this variation is the use of different precursor powders or blends of powders. Unfortunately, insufficient information on the powder blends used in each pellet batch is available to ascertain the validity of this premise.

The morphological measurements also indicate that a very narrow range of aspect ratios is present in the grains of commercial pellets (Figure 6-10 bottom). The typical median value observed for the commercial pellets was similar to the laboratory-derived pellets, suggesting that this morphological descriptor is inherent to UO_2 grains and insensitive to differences associated with processing. As a result, aspect ratio does not appear to be a candidate process signature.

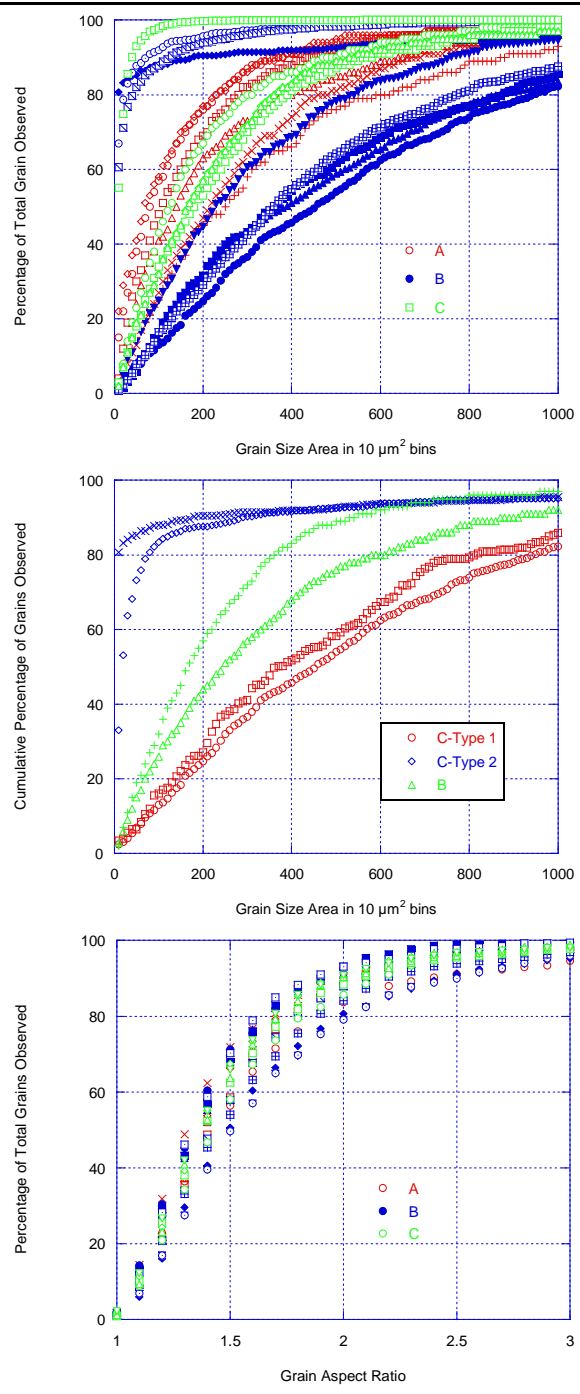


Figure 6-10: Morphological descriptor measurements for commercial pellets from three manufacturers: distribution of grain area (top), sample of variation in grain area within a pellet type (middle), and aspect ratio (bottom)

6.4.2 Other pellet features of forensic interest

Systematic examination of the commercial fuel pellets identified several types of features that may be indicative of process history (Table 6-5). These features stem from more traditional forensic origins, yet may be indicative of aspects of the processing history for the fuel pellets. In some cases, examination of common flow sheets (Figure 6-1) explained the features. These features were reproduced with synthetic pellets to confirm the suspected source of the signature. In other cases, additional research is required to ascertain a source and assess the forensic value. The remainder of this section presents the features and discusses their possible origin.

Table 6-5: Potential features of forensic interest observed on commercial fuel pellets

<i>Feature</i>	<i>Likely source</i>
Alumina particles present on the pellet surface	Aluminum stearate binder
Grain surface textures	Stoichiometric variation between grains
Molybdenum particles	Furnace boat material
<i>Unexplained features of potential value</i>	
Aluminum enriched grain eruptions	
Ring pores	
Micrograin areas	
Sand-like surface debris	
Dimples and bumps	

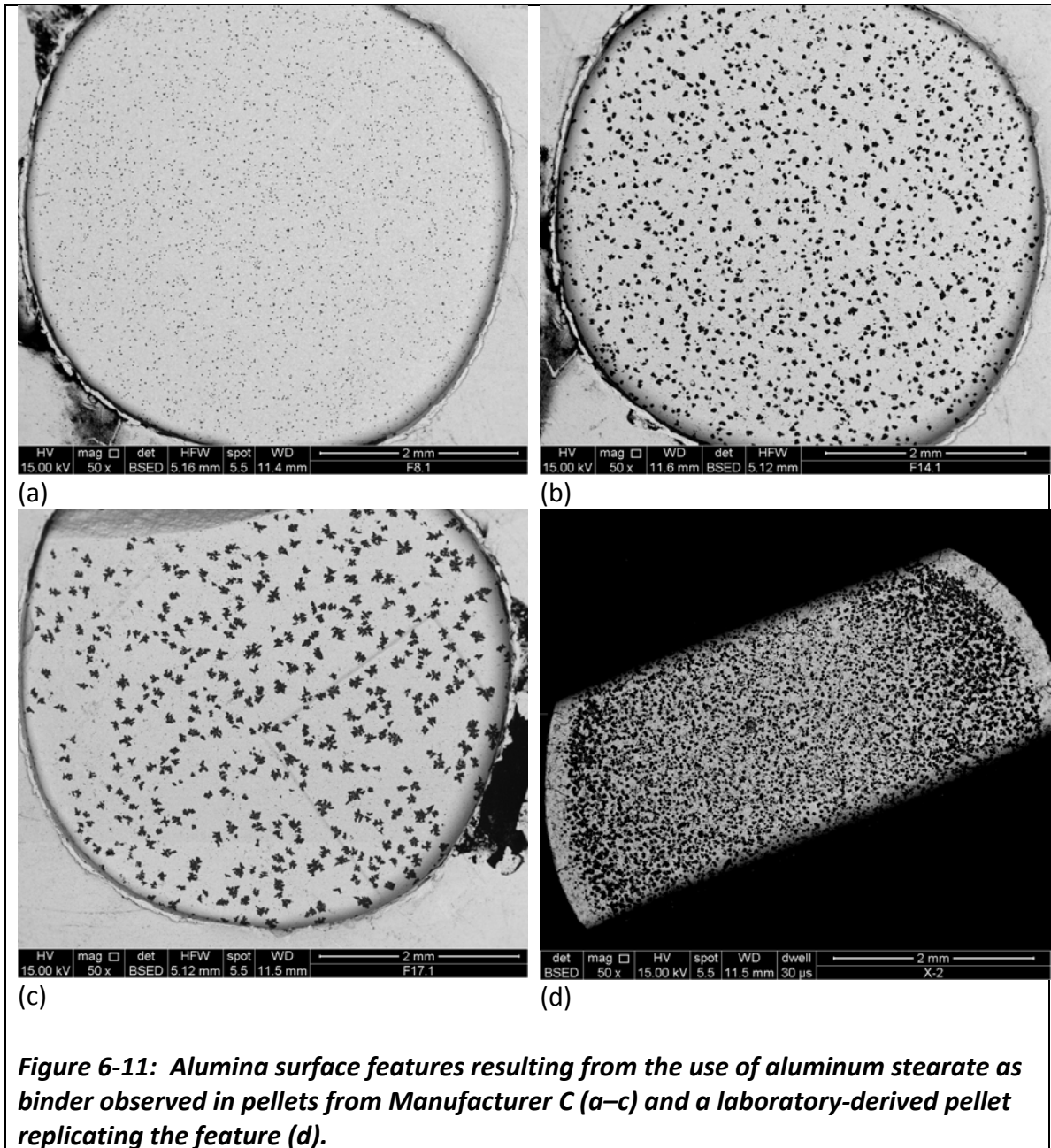
This study observed the prevalence of features containing aluminum in fuel pellets produced by each of the three commercial manufacturers. Potential sources of aluminum in a fuel pellet include the following:

- Binder or sintering aid, likely as aluminum stearate
- Die lubricant, likely as aluminum stearate dissolved in solvent

- Residual from separation processes, either as part of the matrix (used fuel) or as a process additive (salting agent)
- Grinding compound
- Refractory materials used in furnace

Most of the pellets from Manufacturer C exhibited aluminum features on the pellet surface varying in size from about 5–50 μm (Figure 6-11 a-c). These features tend to emerge at the triple points and grain boundaries. Compositional analysis using EDS indicated stoichiometries consistent with alumina (Al_2O_3). Review of the flow sheet information indicated that Manufacturer C uses aluminum stearate as binder, but also utilized this compound as die lubricant. The presence of alumina on the inside of a surface pore and an internal void exposed from pellet sectioning (Figure 6-12) suggests an origin inherent to the matrix, consistent with binder, rather than contamination from the processing environment resulting from a die lubricant.

A pellet was synthesized in the laboratory with aluminum stearate binder to test this theory. The resulting pellet, created using an exaggerated quantity of aluminum stearate binder (1.0 weight percent), produced similar alumina features, confirming the theory (Figure 6-11 d). The increased quantity of alumina features in the laboratory-derived pellet suggested that a possible explanation for the variation in the quantity and size of these features was the variation in the amount of aluminum stearate required for each specification. However, review of the specifications and batch blend information for the three pellet types identified that similar binder contented was used (about 0.2 weight %).



Differences were also observed in the morphology of the alumina features (Figure 6-12). Some features were highly structured and crystalline, while others were amorphous and diffuse. A satisfying explanation is not apparent and requires additional specific processing details (e.g., precise time at temperature curves) for the

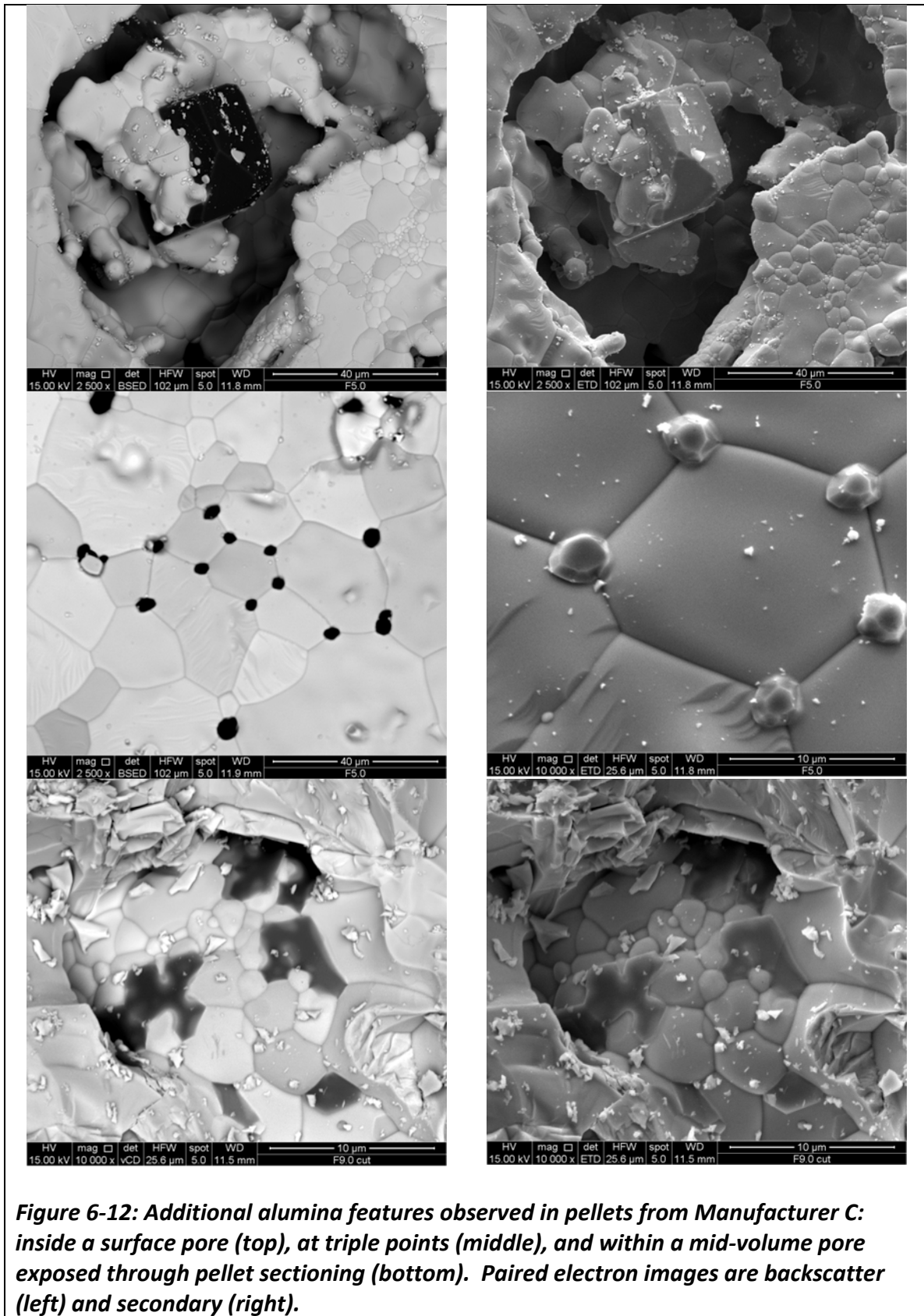


Figure 6-12: Additional alumina features observed in pellets from Manufacturer C: inside a surface pore (top), at triple points (middle), and within a mid-volume pore exposed through pellet sectioning (bottom). Paired electron images are backscatter (left) and secondary (right).

given pellet, as well as additional measurements on the features. However, these differences may be a source of further information indicative of the process environment and warrant additional study. For example, Wriedt [177] reports at least five polymorphs of Al_2O_3 and eight other potential stoichiometries for aluminum oxide compounds.

Pellets from Manufacturer A also displayed some unique features (Figure 6-13 top). Specifically, most of these pellets displayed what appeared to be large collections of micrometer to nanometer sized surface debris. EDS indicated that the composition of this material was consistent with the UO_2 of the bulk pellet. The obvious explanation is that this debris originates from final grinding steps used for finishing. However, all of the manufacturers grind their pellets using wet centerless grinding operations and similar features were not observed on pellets produced by the other Manufacturers or with the laboratory-derived pellets. A further explanation may reside in differences associated with the subsequent rinsing process. As a result, there is insufficient detail to provide a more conclusive explanation of the occurrence of this feature with Manufacturer A.

Several pellets from Manufacturer A displayed irregular grain surface eruptions enriched in aluminum (Figure 6-13 bottom). The process information received from Manufacturer A indicates that no aluminum containing additives or environmental lubricants were used in the production process. Further, all uranium is initially derived from a uranium hexafluoride source—aluminum fluoride is not volatile—eliminating the potential for carry-over of either dissolved aluminum (e.g., from aluminum cladding) or

aluminum salting agent. As a result, the origin of this feature is unclear, but warrants additional research given its prevalence and uniqueness to this manufacturer.

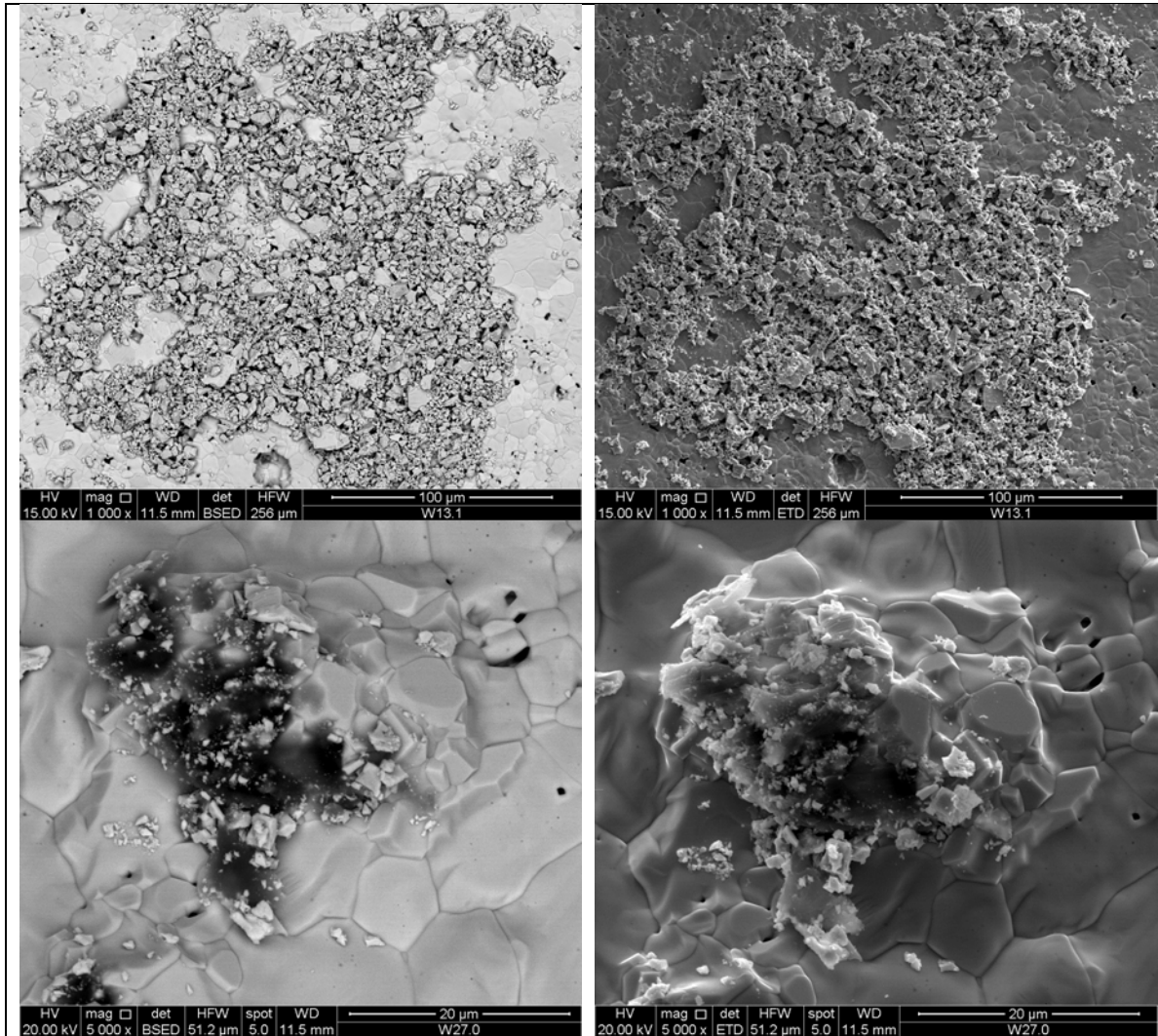


Figure 6-13: Unique features observed on pellets from Manufacturer A: sand-like surface debris (top) and aluminum-rich grain eruptions (bottom). Paired secondary (left) and backscattered electron images at same scale.

Unique grain surface textures represent another class of features observed on the commercial pellets. The pellets exhibited grain surfaces that were smooth, rippled, or stepped (Figure 6-14). He [178] and O'Neil [179] observed similar textures and used EDS, micro-Raman, and current sensing atomic force microscopy techniques to identify

the cause as subtle grain specific variation in the U/O ratio. From a nuclear forensics standpoint, these surface texture features may provide insights into techniques used to control stoichiometry during the sintering processing. Unfortunately, details are not available on this aspect of the process for the manufacturers.

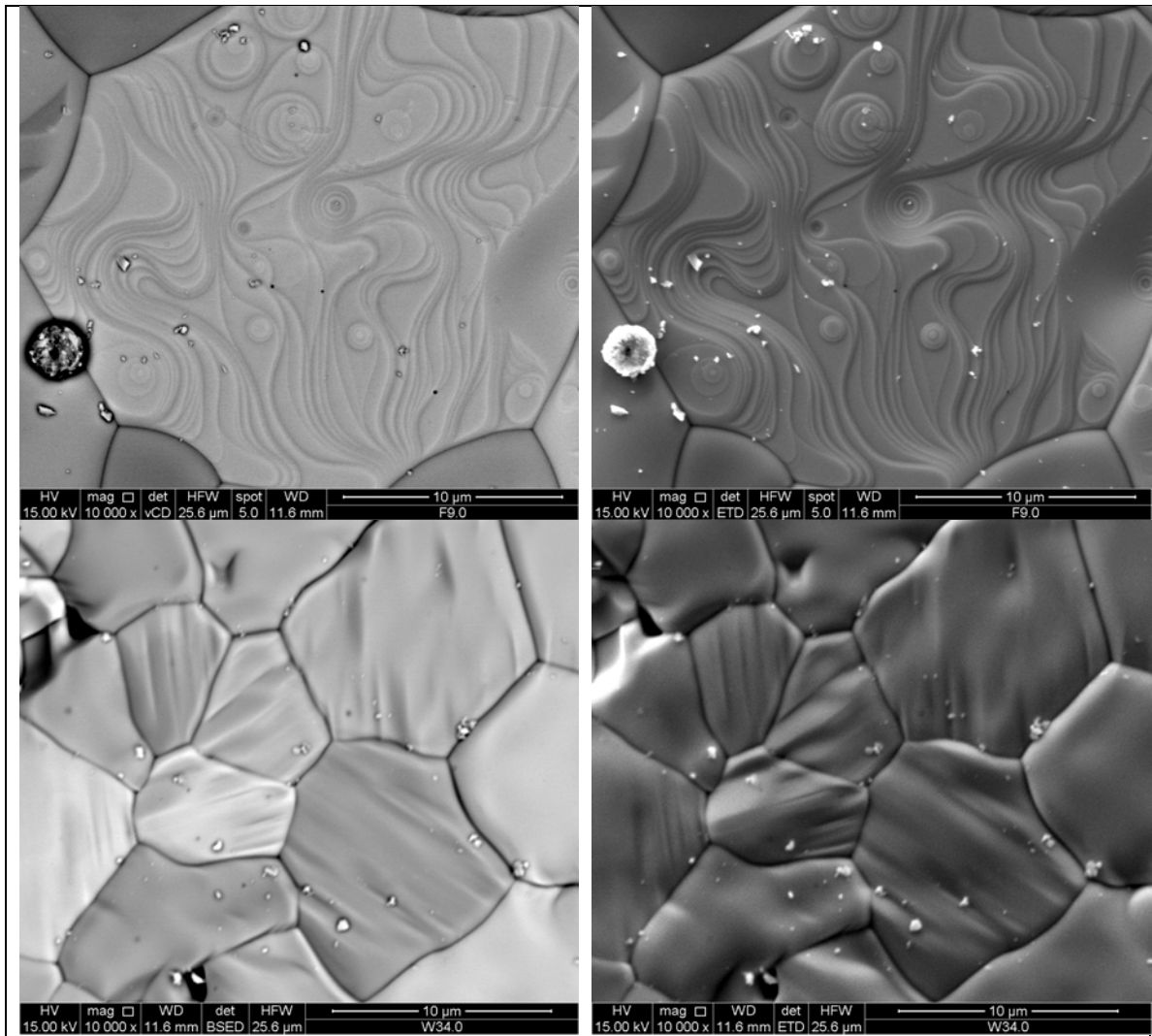


Figure 6-14: Grain surface textures found on commercial pellets: stepped (top) and ripples (bottom). Paired backscattered (left) and secondary electron (right) images.

Several pellets from Manufacturers C and An exhibited bumps and dimples, respectively (Figure 6-16). These features are specific to an individual manufacturer and their origin is currently unexplained. EDS indicated no significant compositional differences between the feature and other nearby grains and a review of flowsheet information provided no obvious link to the feature. The features are reported to facilitate further research should a need develop and are listed in Table 6-5.

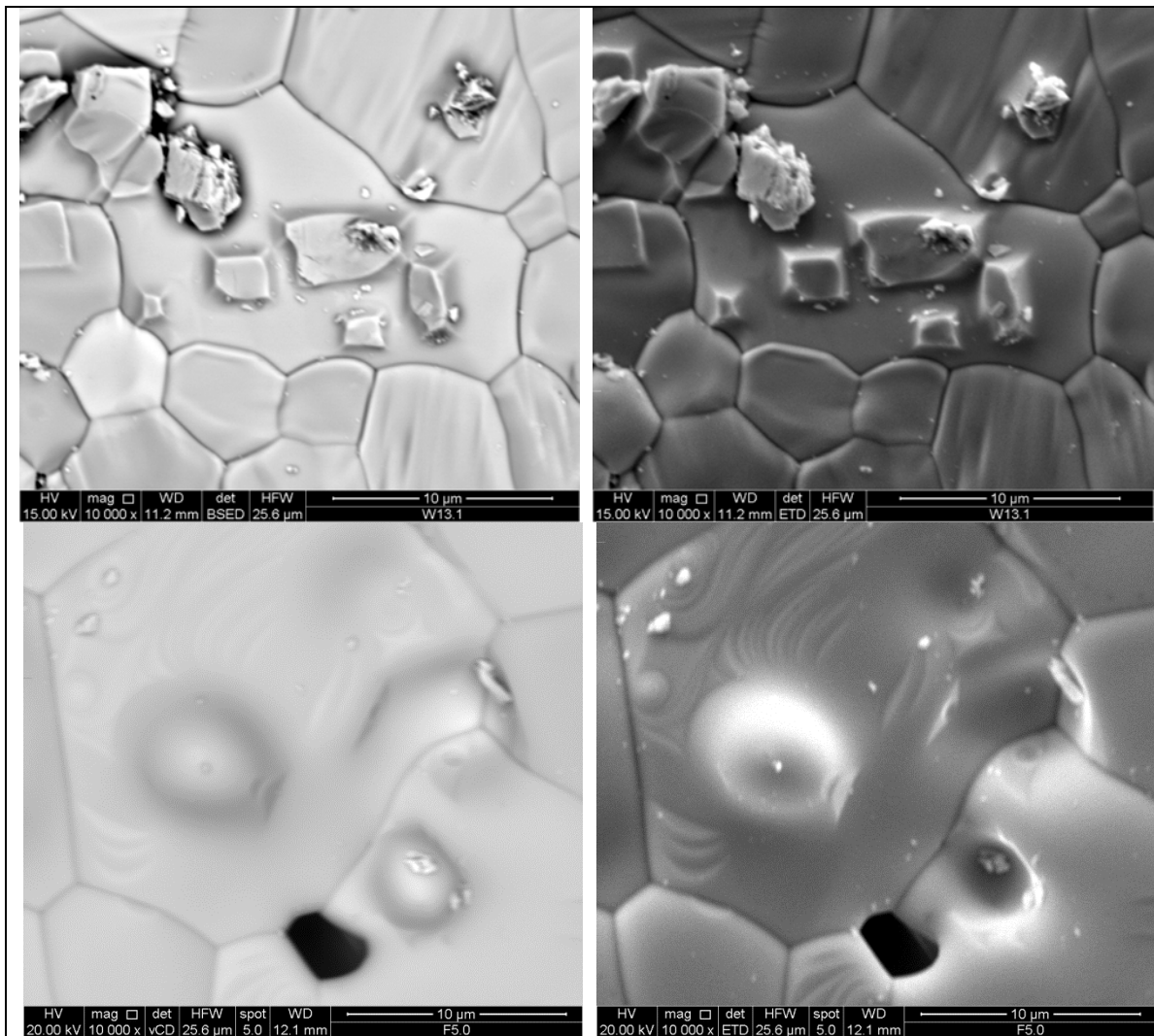


Figure 6-15: Unexplained surface features found on commercial pellets: bumps (top) and dimples (bottom). Paired backscattered (left) and secondary electron (right) images.

Pellets from Manufacturers C and A also exhibited unique micrograin areas and ring pores, respectively (Figure 6-16). An apparent explanation for the micrograins could be the addition of U_3O_8 add-back into the powder blend; however, pellet batch information indicated that several pellet types did not present the feature and contained equivalent or greater amounts of add-back.

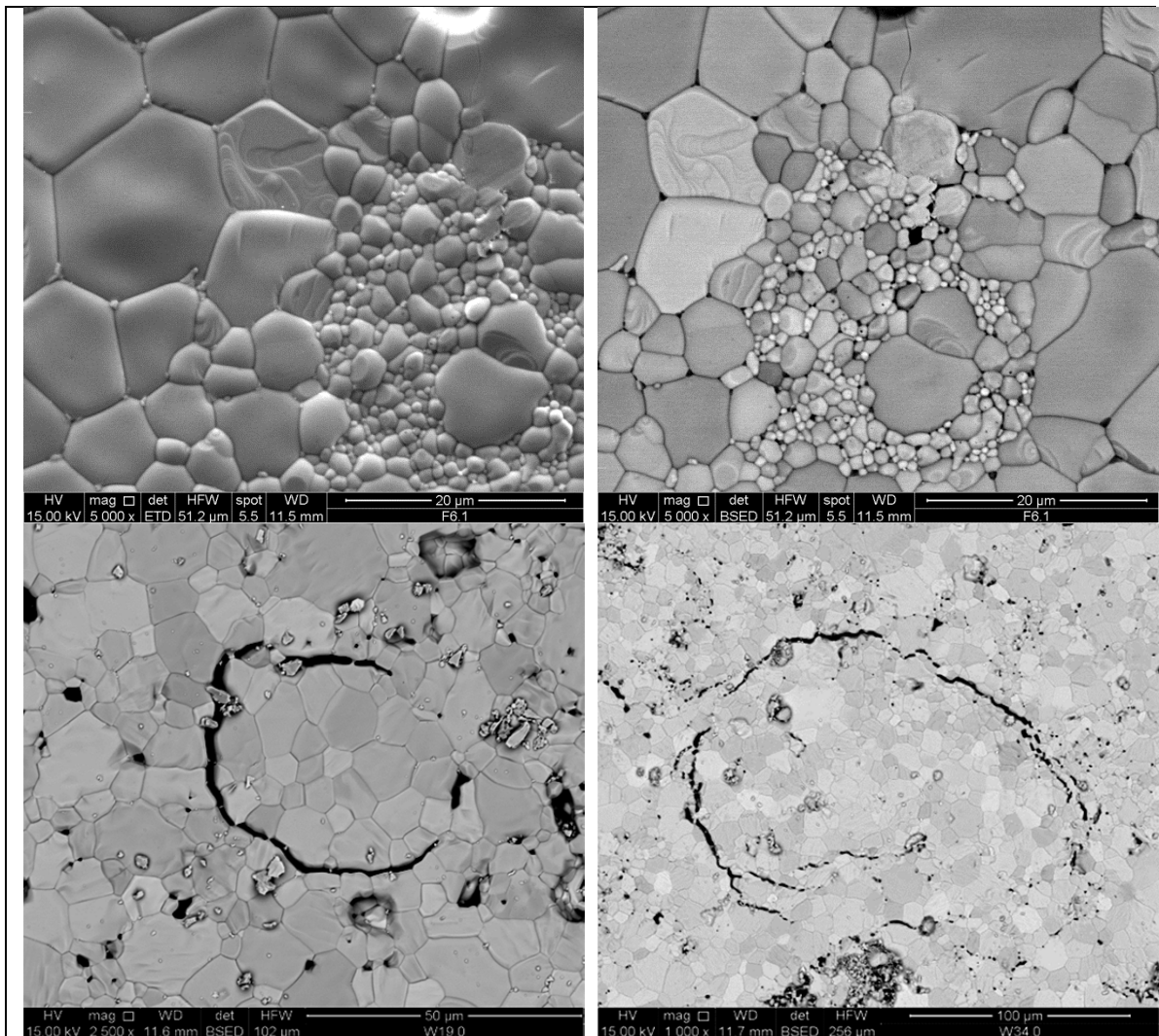


Figure 6-16: Other unexplained features found on commercial pellets: micrograin areas (top) and ring pores (bottom). Paired backscattered (left) and secondary electron (right) images for the micrograin area and separate backscattered electron images for the ring pores.

Further, pellets synthesized in the laboratory to test this hypothesis failed to reproduce the phenomenon. Similarly, an obvious explanation for the presence of ring pores could be the use of pore former; however, Manufacturer A did not indicate the use of pore formers. In addition, ring pores were not observed in pellets from Manufacturer C, which is known to utilize pore former. The origin of these features remains unexplained.

The remaining observed features are indicative of the processing environment. Numerous pellets from Manufacturer A exhibited surface particles containing molybdenum (Figure 6-17). EDS indicated that the molybdenum particles were an oxide form; however, the relative ratios were inconsistent with MoO_3 suggesting that the particles were likely partially oxidized metal. Each of the manufacturers utilizes molybdenum metal furnace boats, which is the most likely source of the particles. It is unclear why only Manufacturer A's pellets contained the molybdenum particles. Other observed features included surface deposits consisting of carbon compounds and various metals, such as stainless steel. Traditional forensic analysis of these materials may reveal useful information, but is beyond the scope of this study.

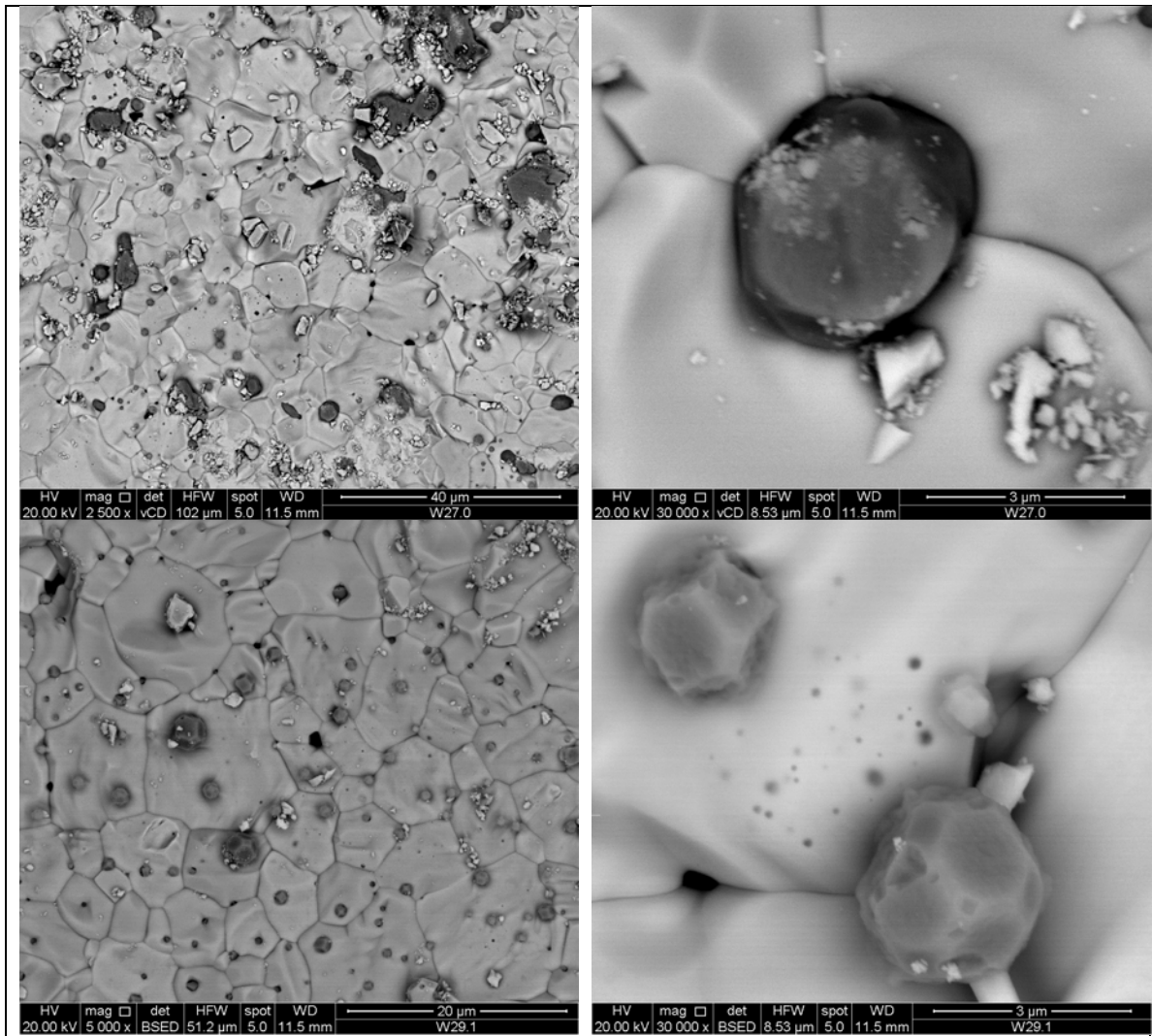


Figure 6-17: Molybdenum features observed on commercial fuel pellets. All images backscatter electron

6.5 Conclusions and suggested areas for further study

This study examined uranium oxide nuclear fuel pellets synthesized in the laboratory and obtained from commercial manufacturers to ascertain whether grain morphology served as signature indicative of production processes. This study also

compared features observed on the commercial pellets with flowsheet information to assess other possible process signatures. Results include the following:

- Measurement of simple morphological descriptors (i.e., Feret diameter, aspect ratio, and area) failed to provide a reliable signature to distinguish between precursor oxide or binder type for the laboratory-derived and commercial pellets. Of these descriptors, grain area shows the most potential for future research. As a result, this study recommends similar experiments with improved control and quantitative characterization of the particle sizes in powder blends for comparison with the sintered pellet.
- Qualitative visual differences in the grain structures of the pellets suggest that application of more advanced morphological descriptors may identify features that correlate with process parameters. In any case, reference samples are needed to confirm the validity of the method.
- This study observed a number of interesting features on the commercial pellets that may eventually prove to be useful forensic signatures; however, additional process detail and further measurements are necessary to validate these signatures. For example, process information failed to explain areas of micrograins, circle pores, and surface bumps. These potential signatures are likely the result of very specific characteristics of the process and their applicability to guide broader research on process signatures is likely limited. As a result, other researchers should consider revised priority on continued research in this area.

Chapter 7 Insights into oxygen isotope ratios as a process signature

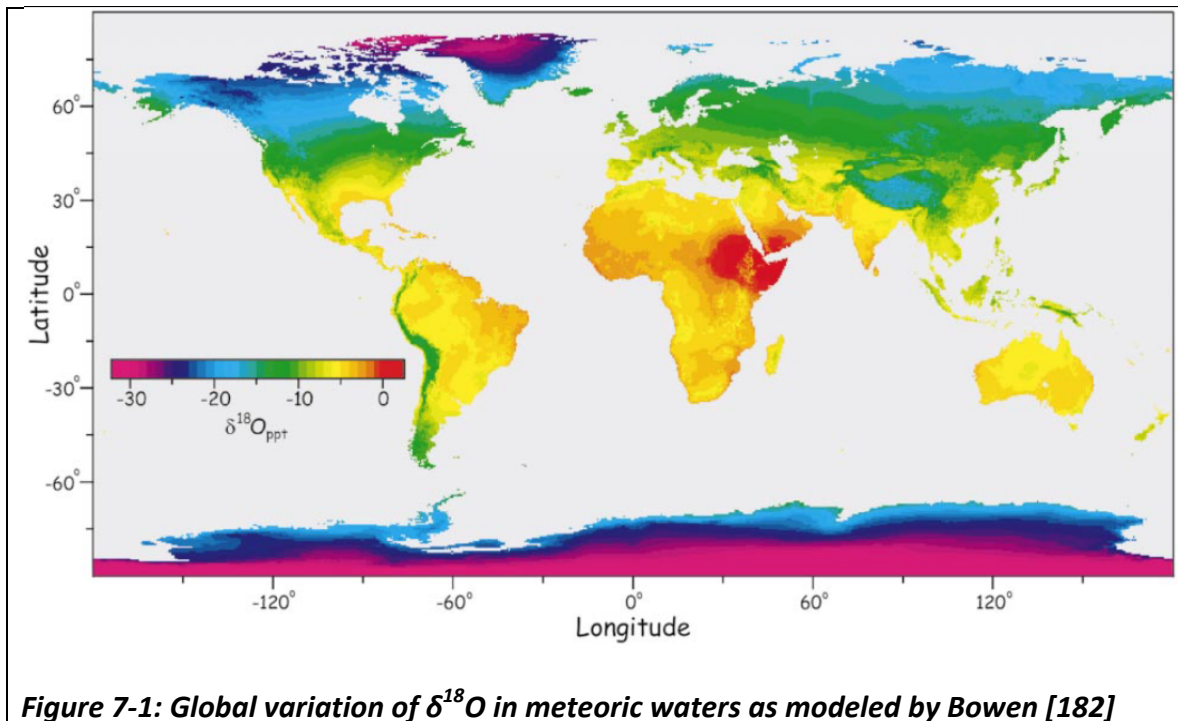
This chapter examines the potential for stable oxygen isotope ratios in triuranium octoxide (U_3O_8) to provide a signature indicative of the geographic location of origin or chemical process. The chemical processes that could create such a signature are examined and experiments performed to investigate oxygen isotope ratios in real-world samples of known origin. The performed experiments also provided fundamental information on the previously unknown equilibrium oxygen isotope fractionation in the U_3O_8 –air system. The equilibrium fractionation data aids in the interpretation of the real-world sample measurements and facilitates assessment of the overall viability of using oxygen isotope ratios in U_3O_8 as a signature in nuclear forensics.

Overall, this study suggests that the ability to use oxygen isotope ratios as a geolocation signature is unfounded for samples of U_3O_8 . The oxygen isotope ratios measured in 15 real-world samples neither correlated with the $^{18}O/^{16}O$ ratio of local meteoric waters nor consistently supported an alternative fractionation value. Further comparison with the air equilibrium value appropriate for the process temperature also failed to explain the oxygen isotope ratios observed in the real-world samples. Limited analysis of oxygen self-diffusion rates in this system highlighted the sensitivity to the particle size and morphology of the U_3O_8 and time at temperature profiles for the process. Consequently, diffusion processes during the thermal treatment of the real-world oxides likely constrained oxygen exchange such that the final value failed to reflect the conditions of either the origin or the process.

7.1 The premise of oxygen isotope fractionation as a geolocation signature

The premise that the oxygen isotope ratio in uranium oxides might serve as a geolocation signature is based on the fact that oxygen atoms in uranium oxides exchange with oxygen atoms in water from their local environment. These oxygen exchange processes occur both in nature, as well as in aqueous nuclear chemical processing environments. As described in Chapter 2, the oxygen isotopes in water molecules fractionate in the natural environment based on conditions that vary systematically around the world. These conditions are nearly constant in time and well monitored. For example, the International Atomic Energy Agency monitors the oxygen isotope ratio in meteoric waters through their Global Network on Isotopes in Precipitation [180]. Data for oxygen isotope ratios are commonly presented relative to Standard Mean Ocean Water (SMOW) [48] and noted as $\delta^{18}\text{O}$ (see Chapter 2 for terminology). The ratio data from geographic monitoring can be applied to models accounting for spatial, elevation, and temperature differences, such as Bowen [181][182] used to create maps of $\delta^{18}\text{O}$ in meteoric water as a function of geography (Figure 7-1).

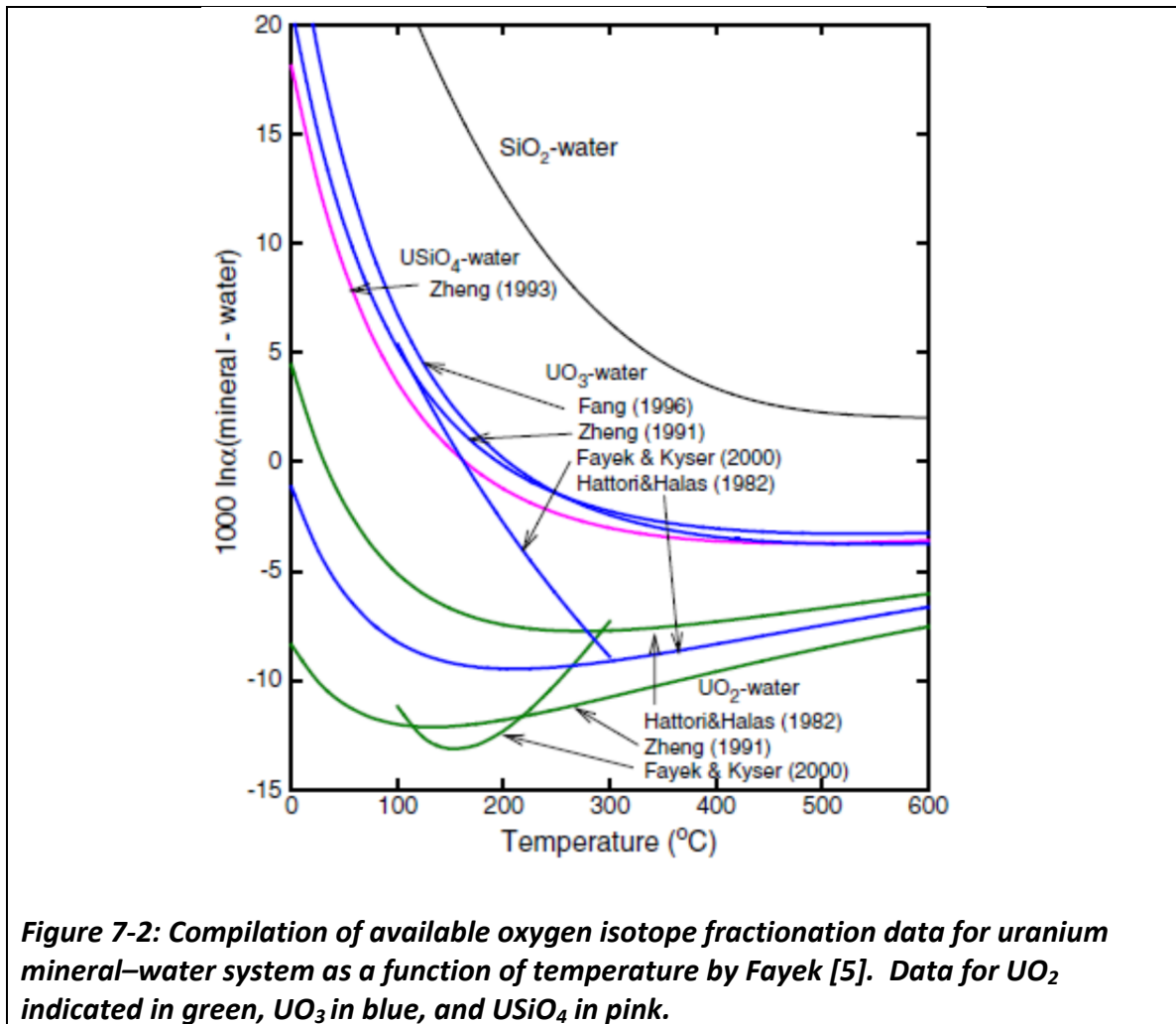
The wide geographic variation of $\delta^{18}\text{O}$ in meteoric waters depicted in Figure 7-1 clearly indicates that a capability to trace nuclear material based on this variation represents an alluring forensic technique. The development of such a technique necessitates an understanding of the exchange and fractionation processes between oxygen atoms in meteoric water and materials of interest to nuclear forensics. Unfortunately, the literature contains sparse data illuminating these processes.



Pajo [183] studied five samples of U_3O_8 and six uranium dioxide (UO_2) fuel pellets and found that the oxygen isotope ratios of the materials varied with their geographic origin and also correlated with the respective oxygen isotope ratio of the local precipitation. Recently, Fayek [184] comprehensively reviewed data on the oxygen isotope composition of more than 250 samples of uranium ore. The author observed significant geographic variation in oxygen isotope ratios and concluded that it may provide a useful forensic indicator, particularly if combined with other indicators such as lanthanide ratios. However, Fayek did not attempt to correlate observed oxygen isotope ratios with meteoric waters.

Data applicable to the fundamental fractionation reactions are also incomplete, inconsistent, and founded on mostly modeling results with limited experimental data.

Fayek's [184] review of uranium ores also summarized the sources of fractionation data for uranium mineral–water systems and developed a figure for comparison (Figure 7-2). As an example of the inconsistency, there are discrepancies in the fractionation factors—noted as $1000 \ln \alpha$ (mineral–water)—for UO_2 of about 100 percent at 100°C and about 25 percent above 500°C . Similar inconsistencies exist for the uranium trioxide (UO_3) system.



Fayek and Kayser [185] performed the only experimental measurements with data represented in Figure 7-2. They measured the oxygen fractionation between carbon

dioxide and samples of natural uraninite and synthetic UO_3 to calculate indirectly the fractionation between these compounds and water at temperatures of 0–300 °C. While not included in the figure, Johnston [186] measured the oxygen exchange between water and UO_3 , UO_2 , and U_3O_8 . However, Johnston's data focused on exchange rates rather than equilibrium values.

The remaining curves in Figure 7-2 originate from the results of modeling. Hattori and Halas [187] utilized crystal field models to calculate theoretical fractionation factors between water and UO_2 and UO_3 at temperatures in the range of 0–1000 °C. Zheng [188] [189] utilized the modified increment method to calculate the fractionation factor for a number of metal oxides, including uranium dioxide, over the temperature range of 0–1200 °C. Fang [190] used spectroscopic data to calculate fractionation factors between water and UO_3 .

7.2 Approach to study the fate of oxygen from meteoric water in the fuel cycle

This section analyzes the chemistry governing the fate of oxygen isotope ratios originating from meteoric water in the nuclear fuel cycle and develops an approach for targeted experiments to assess the viability of these ratios as a geolocation signature. Table 7-1 presents the key reactions governing the balance of oxygen isotope ratios in the nuclear fuel cycle grouped into reactions that imprint or perturb this ratio. The potential to imprint meteoric oxygen isotope ratios on product uranium oxide can occur during any of three types of exchange reactions: (1) oxides with locally derived water, (2) pyrohydrolysis reactions involving uranium hexafluoride and local process water, and (3) uranyl oxygen atoms with local process water used during aqueous processing. The

oxygen isotope fractionation expected for each of these reactions is poorly constrained (Section 7.1) and involves a complex fractionation process controlled by equilibrium, kinetics, and mass transfer. Aqueous reactions, in particular, involve additional potential sources of oxygen from other species in the system (e.g., reagents). Research on the pyrohydrolysis reactions may prove fruitful given the initial results of Pajo [183], but is beyond the scope of this study.

Table 7-1: Key chemical reactions governing the fate of oxygen isotope ratios from meteoric water in the nuclear fuel cycle

	Simplified example reactions	Fuel cycle applications
Equilibrium exchange reactions with the potential to imprint an oxygen isotope ratio	$U^{18}O_x + H_2^{16}O \leftrightarrow U^{16}O_x + H_2^{18}O$	Ore body with ground water or corrosion in the environment
	$U^{18}O_2F_2 + H_2^{16}O \leftrightarrow U^{16}O_2F_2 + H_2^{18}O$	Fuel manufacturing or environmental releases during enrichment
	$U^{18}O_2(NO_3)_6 + H_2^{16}O \leftrightarrow U^{18}O_2(NO_3)_6 + H_2^{18}O$	Solution exchange with the uranyl ion during chemical separations for ore concentration, purification, or recycling
Atmospheric oxygen perturbs imprinted ratio	$U^{18}O_x + {}^{16}O_2 \leftrightarrow U^{16}O_x + {}^{18}O_2$	Thermal oxidation of precipitates, scrap recycle

Alternatively, any potential oxygen isotope ratio imprinted in uranium oxide is likely to be perturbed during its lifetime through exchange with atmospheric oxygen, particularly during treatments at elevated temperatures such as a calcination process.

Dole [191] determined the worldwide fractionation of oxygen isotopes in the

atmosphere is nearly constant and 23.5 ‰ higher than that of average seawater (see Chapter 2 for terminology). As a result, an understanding of the equilibrium fractionation between uranium oxides and air would be useful in the interpretation of fractionation results on real world oxides. The literature does not currently contain these data.

7.3 Methods

Guided by the analysis in Section 7.2, this study focused on two experimental approaches: (1) analysis of the oxygen isotope fractionation in real-world samples of oxides with a comparison against local meteoric water and (2) determination of the equilibrium fractionation between air and uranium oxide. For both approaches, U_3O_8 was chosen as the best candidate for investigation given its ubiquity in the nuclear fuel cycle (Chapter 4) and its thermodynamic stability for reactions between uranium and air.

7.3.1 Analysis of real-world samples

Oxygen isotope ratios were measured on real-world samples of U_3O_8 possessed by Lawrence Livermore National Laboratory (LLNL). The oxygen isotope ratios for these samples were then compared to the nearest monitored meteoric water source, as reported by the International Atomic Energy Agency's Global Network on Isotopes in Precipitation [180]. Information for these samples related to processing, particularly the temperature for thermal oxidation, was compiled from the literature. For several of the samples, the oxygen isotope ratios and accompanying information on the origin of the samples were obtained from LLNL's Uranium Sourcing Database [192][193].

The information available on the origin of a particular sample warrants caution, as chain of custody procedures were not applied for the samples and there are a number of potential scenarios that could result in inaccurate information. For example, facilities may handle uranium ores, ore concentrates, and other process intermediates imported from other geographic areas. Similarly, facilities may have multiple process lines that could produce U_3O_8 under different conditions. Nonetheless, this approach is the best available outside of a concerted effort to collect samples under stringently monitored conditions.

7.3.2 Equilibrium oxygen isotope fractionation measurements

This study applied the partial exchange technique of Northrop and Clayton [194] to experimentally determine the equilibrium oxygen isotope fractionation in the U_3O_8 – dry air system. Briefly summarized following the explanation by O’Neil [195], the partial exchange technique utilizes a set of companion reactions with reactants similar in all aspects except for their initial isotopic composition. These reactants endure the same experimental conditions, particularly the time at temperature profile. The following general equation describes the technique:

$$\ln \alpha_{\text{initial}} = \ln K + B (\ln \alpha_{\text{initial}} - \ln \alpha_{\text{final}})$$

Where

α is the oxygen isotopic fractionation of the reactants (U_3O_8 and dry air)

K is the equilibrium fractionation for the system

Therefore, a plot of $\ln \alpha_{\text{initial}}$ against $(\ln \alpha_{\text{initial}} - \ln \alpha_{\text{final}})$ for a companion set of three or more samples provides the final fractionation factor, $\ln \alpha_{\text{final}} = \ln K$, as the y-intercept and the percent of exchange $(-100/B)$ as a function of the slope.

The companion experiments utilized four samples of U_3O_8 with varying initial oxygen isotope ratios. Two samples were produced by direct oxidation in air at 400 and 800 °C for 12 hours of uranium metal turnings cleaned with nitric acid. The third sample was produced through the air oxidation of isotopically altered UO_2 previously synthesized using the hydrothermal reaction of uranium metal turnings and ^{18}O enriched water (Cambridge Isotope Laboratories) at 200 °C in an argon purged Parr pressure vessel. The fourth sample was a commercially produced uranium ore concentrate of a previously measured oxygen isotope composition that complemented the range of initial fractionations. X-ray fluorescence measurements revealed no impurities above detection limits (generally 50–200 ppm) for all of the samples. The resulting sample set provided a diverse spread of $\delta^{18}\text{O}$ from -2.6 to 19.6 ‰.

Companion exchange experiments were conducted in a controlled atmosphere tube furnace with approximately 100 mg of each sample placed in gold foil thimbles collected in an alumina furnace boat (Figure 7-3). Prior to each use, the gold thimbles were cleaned in 2 percent nitric acid. Dry air for the experimental atmosphere was obtained by drawing normal room air through a Drierite gas purifying column and into the furnace tube using the house vacuum system. Dry air was utilized in order to eliminate potential fluctuations in $\delta^{18}\text{O}$ from variations in atmospheric water.

Partial exchange experiments examined the temperature range of 500–800 °C, which represented the temperatures most likely to be encountered for thermal oxidation of uranium precipitates [21]. Independent thermocouple measurements verified that isothermal conditions within ± 0.1 °C existed for the entire length of the furnace boat. At the end of each experimental run, the furnace clamshell was opened to facilitate rapid cooling of the sample, which typically cooled to less than 50 °C in 45 minutes.

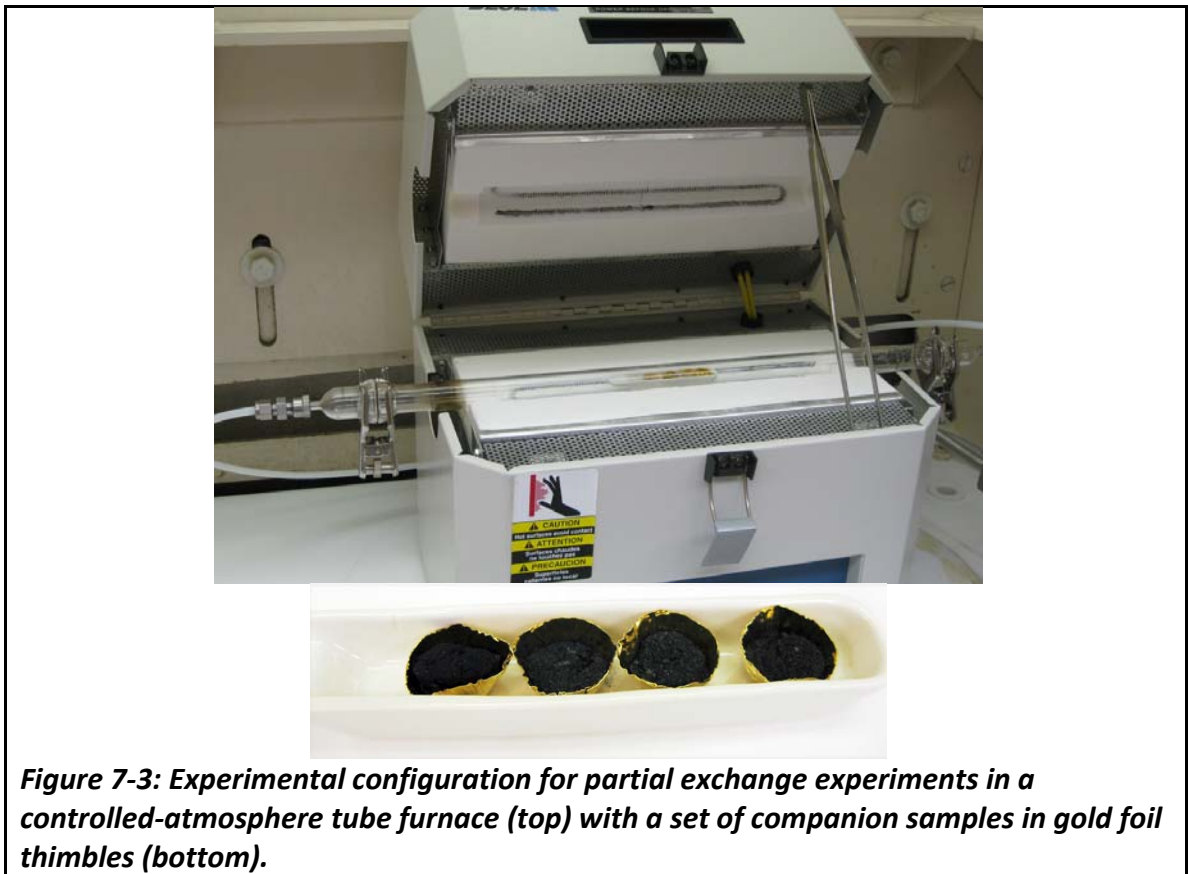
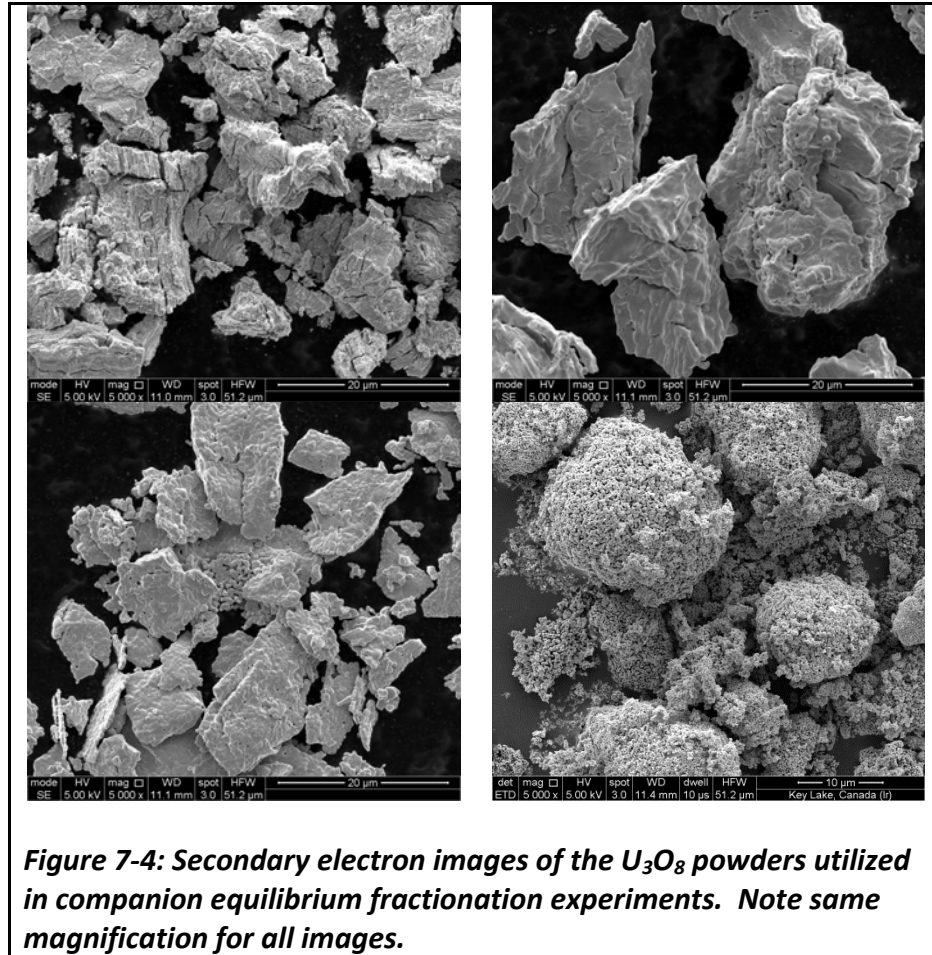


Figure 7-3: Experimental configuration for partial exchange experiments in a controlled-atmosphere tube furnace (top) with a set of companion samples in gold foil thimbles (bottom).

The prerequisites for valid application of the partial exchange technique were verified as follows. Powder XRD confirmed that the initial and final chemical phase for each sample was α -U₃O₈. Scanning electron microscopy of each sample indicated

similar grain sizes for each powder with typical grains and agglomerates in the size range of 5 to 50 μm for each sample (Figure 7-4).



7.3.3 Synthesis approach to equilibrium

Two additional types of experiments helped to identify the equilibrium oxygen isotope fractionation between U_3O_8 and dry air. These experiments utilized an approach where the initial reactants are compounds other than U_3O_8 . While these do not represent true exchange reactions, the chemistries involve simple oxygen addition,

which should minimize the common concerns with using the synthesis route to measure isotope equilibrium [195].

In one experiment, a set of synthesized UO_2 samples with variable initial oxygen isotope ratios underwent a companion type partial exchange experiment, as described in Section 7.3.2. The isotopically altered UO_2 samples were prepared through the hydrothermal reaction between uranium metal and a stoichiometric excess of waters with variable ^{18}O enrichments. The reactions were conducted in 23 mL Parr vessels purged with argon gas prior to closure. After 3 hours at 200 °C, the vessels were opened, headspace purged with additional argon, and an additional charge of water added to minimize the potential formation of uranium hydride. The vessels were then held at 200 °C overnight. This method was successful in producing UO_2 powders with an initial $\delta^{18}\text{O}$ of between -39.7 and 144.4 ‰.

In the second experiment, uranium metal foils were directly oxidized in air at temperatures between 400 and 900 °C. With this approach U_3O_8 was directly formed through the reaction of air with uranium metal—an oxygen-free matrix. The metal foils were rinsed with nitric acid and acetone prior to placement in a gold foil thimble to ensure removal of initial surface oxide (Figure 7-5).

7.3.4 Measurement of oxygen isotopic ratios

Samples of uranium oxides were analyzed for oxygen isotope ratios utilizing the High Vacuum Fluorination System (HVFS) at LLNL. Chapter 2 provides details on the principles of operation and design of the HVFS. For measurements in this study, 20–25 mg of sample was weighed into an acetone cleaned nickel sample holder. Each holder

was placed into a reaction vessel on the HVFS, the system pumped to vacuum, and the samples degassed for about 2 hours at 150 °C while under vacuum. After cooling, an excess of chlorine trifluoride reagent was cryogenically frozen into each reaction vessel, the vessel valve sealed, and the oxygen liberating reaction allowed to progress at 450 °C for at least 12 hours.

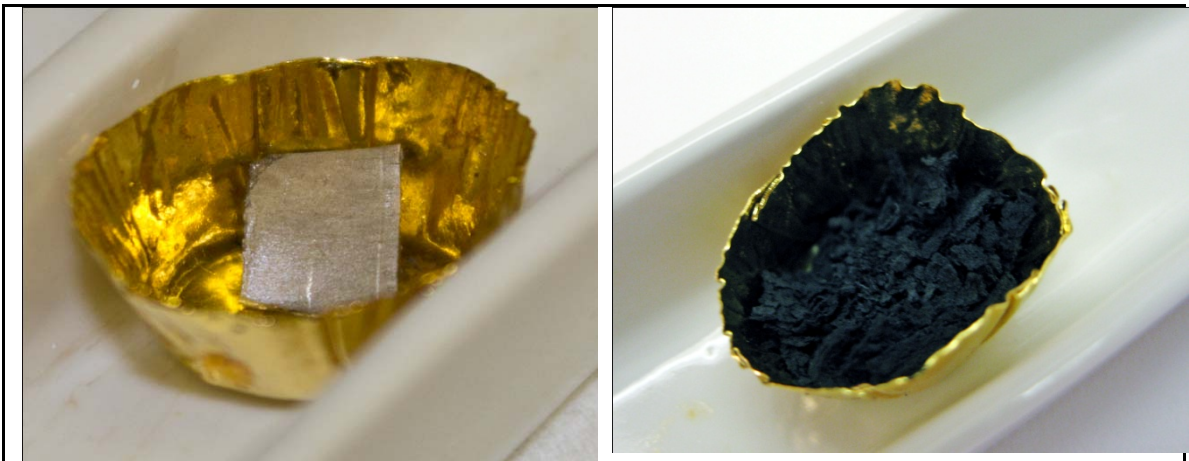


Figure 7-5: Experimental configuration for direct metal oxidation oxygen isotope fractionation experiments; furnace boat with gold foil thimble containing initial acid cleaned uranium metal (left) and resulting U_3O_8 sample after exposure to air at elevated temperature (right).

The liberated oxygen then reacted with an electrically heated carbon rod and was converted into carbon dioxide. The total volume of carbon dioxide generated was measured using a calibrated manometer and the gas sample frozen into a glass tube, which was flame sealed and removed from the line. The oxygen isotope ratios of the carbon dioxide samples were measured using a dual-inlet isotope ratio Prism 3 VG gas mass spectrometer.

Each run of the HVFS utilized two standards to account for potential fractionation during the analysis: (1) National Bureau of Standards material NBS-28, a

silicon dioxide material with a certified oxygen isotope ratio of $\delta^{18}\text{O} = 9.57 \text{ ‰}$ and (2) New Brunswick Laboratories Certified Reference Material 125a, a fuel pellet standard for uranium assay benchmarked at LLNL with an oxygen isotope ratio of $\delta^{18}\text{O} = -11.4 \text{ ‰}$. The typical analytical uncertainty for these measurements is about 0.1 ‰. All oxygen isotope fractionations are reported against the Standard Mean Ocean Water (SMOW) convention with an $^{18}\text{O}/^{16}\text{O}$ ratio of $(2005.20 \pm 0.43) \times 10^{-6}$ [48].

7.4 Results and discussion

7.4.1 Oxygen isotope ratios of real-world samples poorly correlate with local waters

Oxygen isotope ratios were measured for 15 real-world samples of U_3O_8 with information available on their probable geographic origin (Table 7-2). The samples were all obtained from ore milling facilities, increasing the likelihood that they originated from nearby deposits and used local meteoric water for processing. In contrast, uranium conversion facilities are likely to have received uranium materials from many different geographic origins. Powder x-ray diffraction (XRD) indicated that all samples were $\alpha\text{-U}_3\text{O}_8$. Likely temperatures used for thermal oxidation were obtained from the literature and are reported in Table 7-2.

The Ranger, Olympic Dam, and Key Lake facilities each had three samples measured (Table 7-2). For all three facilities, two of the three samples were consistent; however, the value of the third sample point was significantly beyond of the range of reproducibility commonly observed with standards. This result suggests that considerable variability may exist in the oxygen isotope ratios of material produced at the sample facility.

Table 7-2: Oxygen isotope ratios of real-world uranium oxides and nearby meteoric waters

Facility	Location	Possible process temperature, °C	References	Phase by XRD	$\delta^{18}\text{O}$ Sample, ‰ *	$\delta^{18}\text{O}$ Meteoric Water, ‰ *	Meteoric Water Location
Key Lake	Saskatchewan, Canada	750	[98][99] [100][90]	U ₃ O ₈	-2.6	-15.52	Wynyard, Canada
				U ₃ O ₈	-2.6		
				U ₃ O ₈	-4.7		
Olympic Dam	South Australia	750	[91][90]	U ₃ O ₈	1.4	-4.60	Adelaide, Australia
				U ₃ O ₈	1.4		
				U ₃ O ₈	0.2		
Ranger	Northern Territory, Australia	600	[96][97]	U ₃ O ₈	5.7	-5.32	Darwin, Australia
				U ₃ O ₈	5.7		
				U ₃ O ₈	2.6		
Federal American Partners	Gas Hills, Wyoming	600	[101][24]	U ₃ O ₈	5.4	-18.43**	Eastern Powder River Basin, WY
Karatou	Karatou, Kazakhstan	Unknown	----	U ₃ O ₈	-6.2	-6.59 [†]	Bishkek, Kyrgyzstan
Mary Kathleen	Queensland, Australia	700	[96]	U ₃ O ₈	3.0	-6.65	Alice Springs, Australia
NUFCOR	Westonaria, South Africa	500	[104]	U ₃ O ₈	12.4	-3.81	Pretoria, South Africa
Queensland	Jabiru, Australia	500	[96]	U ₃ O ₈	10.5	-3.75	Darwin, Australia
Palabora	Phalaborwa, South Africa	700	[196][197]	U ₃ O ₈	2.5	-2.76	Pretoria, South Africa

*Analytical uncertainty is about 0.1 ‰

**Result represents the mean of ground water data provided by the United States Geological Survey [198]

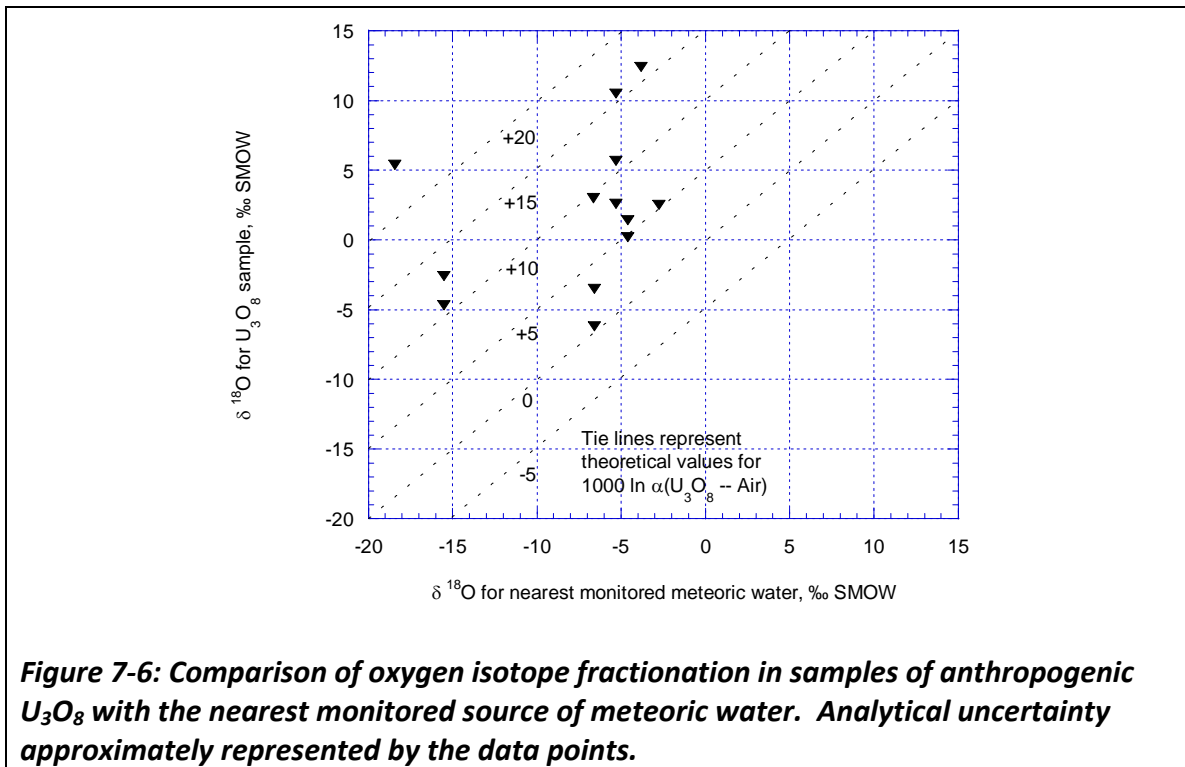
[†] Long-term weighted mean not provided by GNIP; value instead reflects simple mean of precipitation events

However, there are several caveats to consider associated with the samples. For example, the samples had incomplete collection date information and the date of collection has an uncertain nexus with the date of production. A future effort would be useful to obtain multiple samples under well-defined and monitored conditions.

The measured oxygen isotope ratios for the U_3O_8 samples were plotted against the ratios for the nearest source of monitored meteoric water mostly using the long-term weighted mean station data provided by the International Atomic Energy Agency's Global Network on Isotopes in Precipitation [180] (Figure 7-6). The oxide ratios correlate poorly with the water ratios even after accounting for the potential range of fractionation factors reported in the literature for UO_3 and UO_2 with water (Figure 7-2). Considering these equilibrium fractionations are with liquid phase water, they likely would have occurred at temperatures of less than 100 °C during either groundwater interaction with ore deposits or aqueous phase chemical separations. At these temperatures, the reported and modeled fractionations are bounded by about +15 ‰ for UO_3 at 25 °C to about -12‰ for UO_2 at 100 °C. For additional perspective, Zheng [189] calculated a fractionation between water and pitchblend, modeled by the author as $UO_2 \cdot 2UO_3$, of about -2 ‰ at 100 °C.

No equilibrium fractionation data have been reported for the aqueous uranyl system. However, Gordon and Taube [199] studied the kinetics of oxygen exchange between water and the uranyl ion in a perchloric acid system under various conditions and reported half lives for the exchange reaction ranging from 145 days to 4 years. In other work, these same authors [200] note that the presence of pentavalent uranium

ions, which is unlikely under most conditions, catalyzes the exchange between uranyl and water, but found it difficult to quantify this effect. More recent work by Mashirov [201] also found negligible exchange rates between uranyl oxygen atoms and water for acid concentrations above 0.2 M. At these rates the ability of aqueous phase processing to perturb previously imprinted oxygen isotopes appears quite limited.



If isotope exchange with oxygen in uranyl ions represents an implausible route to imprinting the oxygen isotope ratios of local waters, the other likely route would be oxidation during dissolution of uranium ore, in which uranium atoms are typically in the tetravalent state, such as in uraninite [21]. Gordon and Taube [202] studied oxygen transfer during the oxidation of aqueous tetravalent uranium ions and found that oxygen atoms are preferentially transferred from the oxidizing agent rather than the

aqueous solvent, suggesting that this process is unlikely to represent a signature imprinting step.

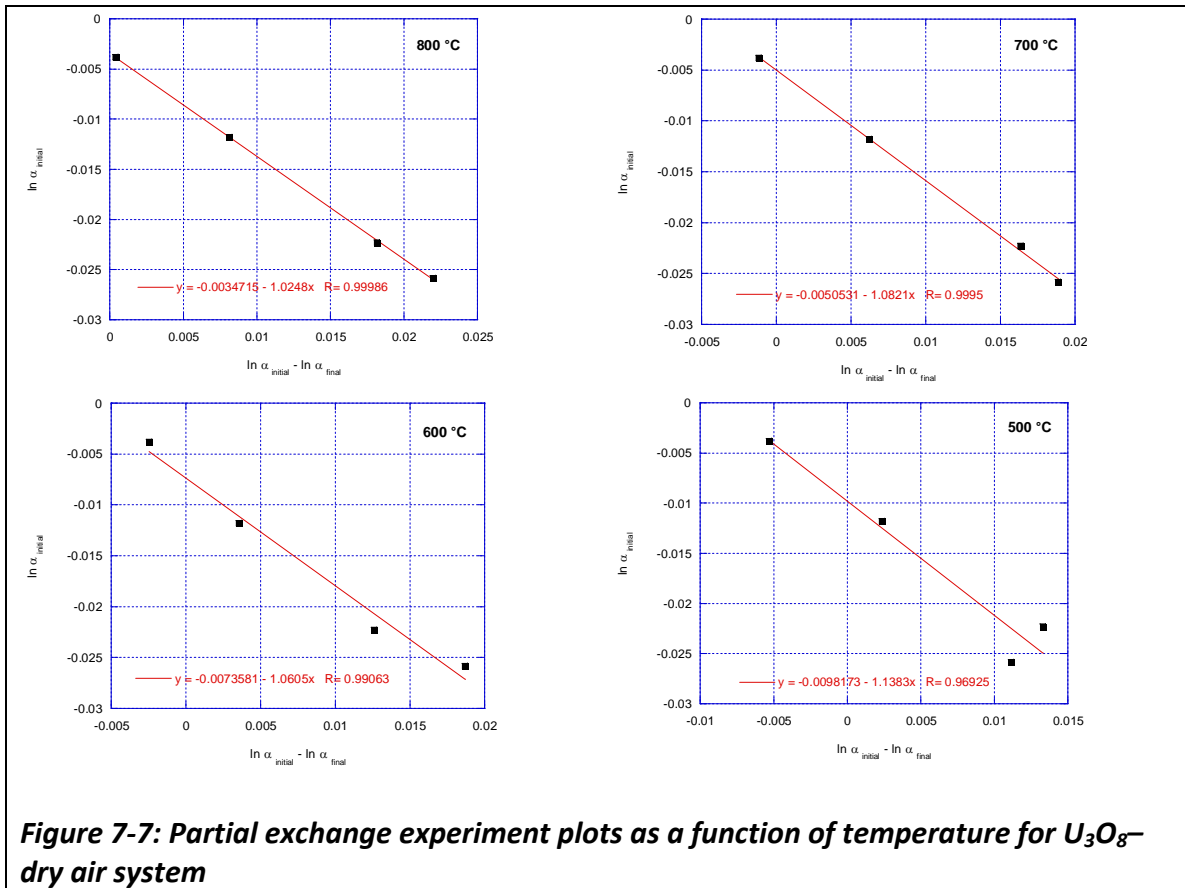
Overall, the data show a broad range in observed $^{18}\text{O}/^{16}\text{O}$ ratios that fail to correlate with any particular value. The literature indicates that oxygen exchange during aqueous processing is complicated by several factors and is unlikely to result in significant development of oxygen isotope ratio signatures.

7.4.2 Experiments yield first equilibrium oxygen isotope fractionation data for U_3O_8 -air system

The equilibrium oxygen isotope fractionation between U_3O_8 and air was measured using the partial exchange technique and two types of synthesis reactions utilizing uranium metal and UO_2 as initial reactants. The reaction between U_3O_8 and air represents the last step for most common processes involving the thermal treatment of many uranium compounds. The literature currently does not contain any experimental or modeling data for oxygen isotope fractionation in this system.

The partial exchange measurements were conducted at temperatures between 500 and 800 °C, corresponding to the temperatures expected for the formation of U_3O_8 in industrial applications [21]. The companion experiments demonstrated generally good linearity, indicating the validity of the experimental system (Figure 7-7). As discussed in Section 7.3.2, the slope and intercepts of these lines determine the percent of oxygen exchange and the equilibrium fractionation, noted as $\delta^{18}\text{O}$ Equilibrium in the tables.

The full results of the companion exchange experiments (Table 7-3) demonstrate the technique was valid. With the exception of the 800 °C experiment, the equilibrium values approached from both directions—the initial ratios in the reactants were both above and below the determined equilibrium value. For the 800 °C experiment, the initial powder with a $\delta^{18}\text{O}$ of 19.6 ‰ was just below the error range on the equilibrium value. The fractionation factors, noted as $1000 \ln \alpha_{\text{U}_3\text{O}_8\text{-air}}$, are all of reasonable magnitude and sign when gauged against the published fractionation factors for other uranium oxides and water (Figure 7-2).



The results of the synthesis companion reaction using UO_2 validated the equilibrium fractionation results (Table 7-4). Powder XRD indicated that the initial UO_2

samples all converted to U_3O_8 , as expected. At 800 °C, the value for $1000 \ln \alpha_{U_3O_8-air}$ using the synthesis approach with was -3.7 ± 0.1 , compared to -3.5 ± 0.2 for the exchange experiment using U_3O_8 . Based on this agreement, the need for additional data at other temperature points was dismissed.

Table 7-3: Oxygen isotope fractionation from U_3O_8 – dry air partial exchange experiments

<i>Temperature, °C</i>	500	600	700	800
<i>Time, hr</i>	120	140	96	90
<i>$\delta^{18}O$ U_3O_8 Samples, ‰</i>				
<i>Initial</i>			<i>Final</i>	
-2.6	8.6	16.2	16.4	19.6
0.9	14.3	13.6	17.4	19.3
11.5	13.9	15.1	17.8	19.8
19.6	14.2	17.1	18.4	20.0
% Exchanged	87.9	94.3	92.4	97.6
$1000 \ln \alpha_{U_3O_8-air}$	-9.8	-7.4	-5.1	-3.5
$\delta^{18}O$ Equilibrium	13.7	16.1	18.4	20.0
Standard Error	1.9	1.2	0.3	0.2

Table 7-4: Oxygen isotope fractionation resulting from the companion oxidation of UO_2 samples heated in dry air for 20 hours at 800 °C

<i>$\delta^{18}O$, ‰</i>	
<i>Initial UO_2</i>	<i>Final U_3O_8</i>
-39.7	19.5
-5.5	19.9
12.3	19.7
144.4	19.6
% Exchanged	100
$1000 \ln \alpha_{U_3O_8-air}$	-3.7
$\delta^{18}O$ Equilibrium	19.8
Standard Error	0.1

The results of the approach utilizing the direct-metal oxidation experiments were far less informative (Table 7-5). Two independent experiments lasting about 20 hours

each were performed at each temperature point ranging from 400–900 °C, except at 800 °C, which had an additional experiment held for 60 hours. The temperature range was broadened for these experiments due to the relative ease of conducting this style of reaction. The XRD results indicated that all samples phases were in the expected chemical form—U₃O₈, except for the 400 °C sample, which included some UO₃.

The observed fractionation values were highly inconsistent within any given temperature point and demonstrated no trend across the full range of temperatures. These results reinforce O’Neil’s [195] sage words, “Synthesis is not the fruitful line of approach that it would appear to be...” Possible explanations for these results include inconsistencies with either the reaction temperature or variation in the oxygen isotope ratio of the air, due to the presence of moisture, used in the reaction.

Table 7-5: Oxygen isotope fractionation for direct-metal oxidation experiments

Temp, °C	Time, hr	Product Phase	$\delta^{18}\text{O}$, ‰
400	20	U ₃ O ₈ , UO ₃	0.92
400	22	U ₃ O ₈ , UO ₃	-21.04
500	23	U ₃ O ₈	-21.17
500	19.5	U ₃ O ₈	-18.78
600	23	U ₃ O ₈	-6.85
600	22	U ₃ O ₈	2.42
700	22	U ₃ O ₈	-5.71
700	22	U ₃ O ₈	-2.68
800	21	U ₃ O ₈	11.50
800	22	U ₃ O ₈	2.22
800	60	U ₃ O ₈	15.75
900	20	U ₃ O ₈	3.89
900	19.5	U ₃ O ₈	1.40

Baker [203] identified that the auto-ignition point of uranium metal was in the range of 500–600 °C depending on metallurgical preparation. As a result, localized hotspots or elevated temperatures associated with a flame may have significantly perturbed fractionations in an inconsistent manner. However, a lack of melted gold, disturbed powder, or automatic furnace shutoff due to high temperature suggests that pyrophoric events did not occur.

Another possible explanation for the inconsistent results involves the role of variations in the oxygen isotope ratio of the air used for these reactions. Since the oxygen isotope ratio of atmospheric molecular oxygen is well known and nearly constant [191], any variation would likely have resulted from atmospheric water content in the untreated room air used for the experiments. These experiments were performed at LLNL during the months of August and September 2012. According to meteorological instrumentation at LLNL [204], the daily average absolute humidity varied from 5.5 to 11.0 g/m³ (i.e., peak relative humidity was 50 %) during this time period. These values reflect relatively dry air and generally insignificant daily variation. As a result, it is difficult to assign this as the primary contributor to the observed inconsistent data. Nonetheless, additional experiments utilizing dried air would eliminate this as a potential and should be considered for future research. Conversely, experiments using a controlled and significantly perturbed source of humidity could illuminate this issue. For purposes of this study, the companion exchange experiments and confirming UO₂ synthesis experiment yielded sufficient data.

Generally, the data in Table 7-5 yield an important insight on the utility of oxygen isotope fractionations as a forensic signature. These experiments were extremely straightforward with little obvious cause for experimental variation, yet the results are highly inconsistent, suggesting that there are significant key parameters that remain unidentified. Since the oxidation of metal to oxide for scrap recovery is a common route for the production of U_3O_8 , the results of these experiments suggest the need for skepticism in attempting to interpret oxygen isotope ratios for nuclear forensic applications.

7.4.3 Equilibrium oxygen isotope fractionation for U_3O_8 –air fails to explain ratios in real-world samples

The application of the results in Table 7-3 to explain the oxygen isotope fractionation observed for real-world samples as a function of processing temperature is summarized in Figure 7-1Figure 7-8. Note that this figure contains data for 27 other real-world U_3O_8 samples with uncertain geographic origin in addition to the samples listed in Table 7-2. Since the origin of these additional samples is unknown, literature indications of the process temperature were unavailable. However, the assumption that these samples were processed in the range of 500–800 °C is valid since powder XRD results confirmed the chemical phase of these samples as U_3O_8 .

The data in Figure 7-8 indicates that the real-world samples have not reached equilibrium with oxygen in the ambient air. One likely explanation is insufficient time at temperature to support complete diffusion of oxygen into the uranium particles during thermal oxidation of the precipitant. The key parameters for this process are the time

spent at elevated temperature and the rate of diffusion for oxygen within U_3O_8 and the various precursor precipitates.

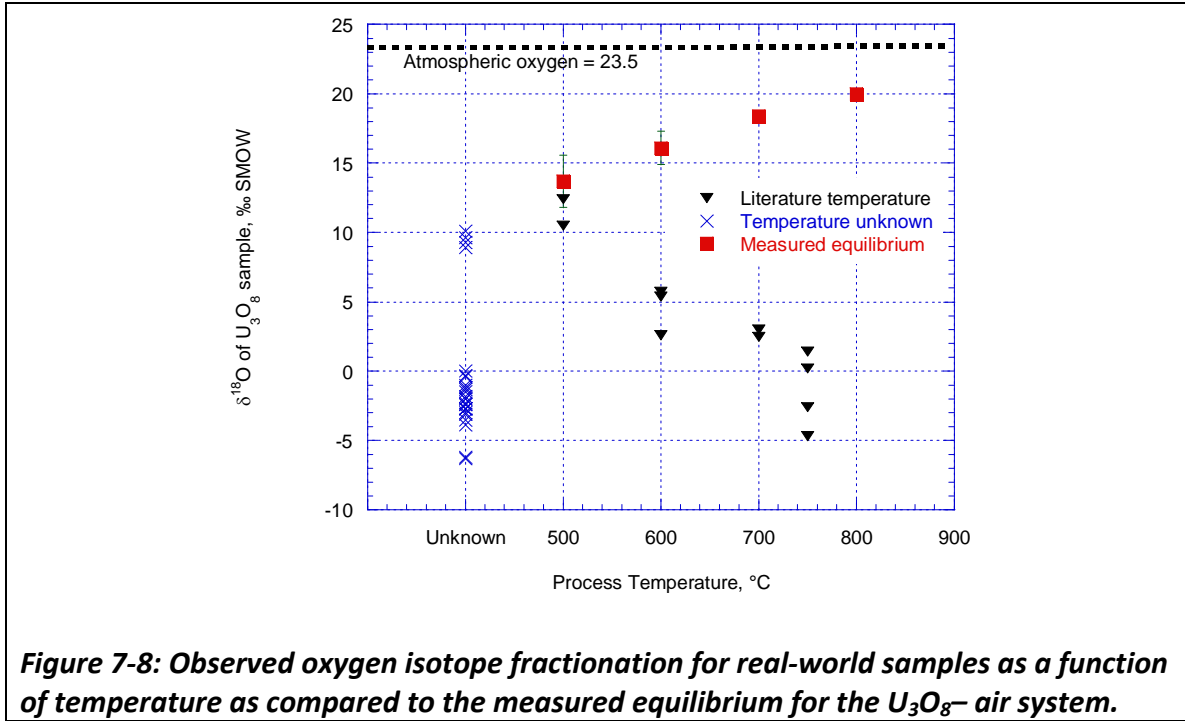


Figure 7-8: Observed oxygen isotope fractionation for real-world samples as a function of temperature as compared to the measured equilibrium for the U_3O_8 -air system.

The literature providing chemical process information for the real-world samples referenced in this chapter, as well as in Chapters 2 and 4, was reviewed to obtain information on the duration of thermal treatments. While temperatures were often available, little information was available on duration. Since these oxides are produced by commercial entities, it is reasonable to assume that efforts have been applied to minimize the duration of this energy intensive and, therefore, costly processing step. As a result, it is likely that the time spent at peak temperature was approximately a few hours and unlikely to exceed 10 hours.

Diffusion rates for oxygen in U_3O_8 are not currently available in the literature; however, there is significant literature available on UO_2 given its common application as a nuclear fuel. Fayek [205] recently reviewed the literature and measured oxygen diffusion rates in natural UO_2 . He observed different behaviors for the temperature regimes of 50–400 °C and 450–700 °C. At the elevated range of interest to this study, he reported the self-diffusion coefficient as $1.90e^{-5} \exp(-123,382 \text{ J/RT}) \text{ cm}^2/\text{s}$ with an activation energy of 123.4 kJ/mol. At these rates, diffusion processes could be expected to require equilibration times on the order of hours to hundreds of days, depending on particle size and the time-temperature profile.

A limited kinetic study for the U_3O_8 –air system using the companion partial exchange methodology provided a rough estimate of diffusion times and a comparison point to assess the applicability of the literature diffusion data for UO_2 . The experiment examined three durations at 800 °C and was not intended or designed to obtain a precise diffusion rate. Precise determination of diffusion rates would necessitate improved control of oxygen potential, impurities, and crystal properties (e.g., polycrystalline particle size and morphology or use of single crystals)[206].

The results of this limited kinetic study (Table 7-6) suggest that oxygen isotope equilibrium occurred rapidly—an exchange of approximately 95% was achieved in 6 hours—for these particular polycrystalline samples of U_3O_8 at 800 °C. Quantitative information on particle size and morphology, specifically the dimension that limits the diffusion rate for the morphology in these samples, is necessary to facilitate comparison with the literature. For example, particle sizes with a diffusion limiting dimension of 1

μm or less would be necessary for the oxygen diffusion rate in U_3O_8 to be similar to UO_2 , as measured by Fayek [205].

Table 7-6: Limited kinetic study of oxygen isotope exchange in U_3O_8 at 800°C

<i>Time, hr</i>	6	22.5	90
	$\delta^{18}\text{O}, \text{‰}$		
<i>Initial</i>		<i>Final</i>	
-2.6	18.9	19.0	19.6
0.9	16.7	17.7	19.3
11.5	18.9	18.4	19.8
19.6	19.3	19.0	20.0
% Exchanged	94.9	98.5	97.6
Error	7.8	4.2	1.2

Unfortunately, only qualitative scanning electron microscopy images were obtained for the powders (Figure 7-4). The combination of the thin, platelet-type morphology and the porosity of the powders used in this experiment (Figure 7-4) could plausibly be interpreted to result in a diffusion-limiting dimension of a similar magnitude. As a result, it is reasonable to conclude that the diffusion rates for both types of oxide are similar.

While additional study of the diffusion rates and particle sizes could refine these results, the critical outcome from this study is that the real-world samples, including those likely treated at 750°C , failed to achieve equilibrium with air. This strongly suggests that, irrespective of the oxygen diffusion rate in U_3O_8 and its precursor compounds, the actual particle sizes and time at temperature profiles used in commercial facilities result in partial equilibrium during thermal treatment. Consequently, oxygen isotope ratios in U_3O_8 are unlikely to provide a signature of interest to nuclear forensics. However, sensitivity analyses utilizing better information

on diffusion rates and real-world particle size information should be performed to confirm this conclusion.

The results of this study contradict the findings of Pajo [183], who observed a strong correlation between the oxygen isotope ratio of five samples of U_3O_8 and that of the associated meteoric water. An obvious explanation for this difference is not apparent. This study examined two of the samples measured by Pajo (Ranger and Olympic Dam) and found inconsistent oxygen isotope ratios (Section 7.4.1) for three samples from each facility. As previously discussed, a dedicated effort to obtain samples under controlled conditions for a period is necessary to resolve this question.

Another explanation could be the sample size associated with the Thermal Ionization Mass Spectrometry (TIMS) method that Pajo utilized for the determination of the oxygen isotope ratios. TIMS utilizes approximately a hundred nanograms versus the 20–25 milligrams used in this study for with the HVFS methodology. This smaller mass would be more sensitive to any potential oxide impurities. However, Pajo took care to compare their technique with more standardized methods of Secondary Ion Mass Spectrometry and Glow Discharge Mass Spectrometry [207]. A cross-institution exchange of samples would facilitate a better understanding of the discrepancy.

7.5 Conclusions and suggested areas for further study

This study examined the utility of using the oxygen isotope ratio in samples of U_3O_8 to serve as a forensic signature indicative of geographic origin. Oxygen isotope ratios were measured on 15 real-world samples with known geographic origin and process conditions obtained from the literatures. The first data on the oxygen isotope

equilibrium between U_3O_8 and air was also collected to help interpret the oxygen ratios observed in the real-world samples, including 27 additional real-world samples of unknown geographic origin. Overall, these experiments informed the following conclusions and suggested areas of further study:

- Oxygen isotope ratios in the real-world samples neither directly correlate with the oxygen isotope ratios of local meteoric water nor support a consistent alternative fractionation. Acquisition of additional samples, including multiple samples over time from the same facility, using established, uniform protocols and monitored conditions would fortify this result.
- Oxygen isotope ratios in real-world samples of U_3O_8 do not agree with the values for the U_3O_8 –air equilibrium fractionation experimentally determined in this study. Examination of oxygen self-diffusion coefficients in the literature and limited experimental results conducted in this study indicate that the real-world variability in particle sizes and time at temperature profiles is sufficient to complicate interpretation oxygen isotope ratios in U_3O_8 samples as a reliable geolocation signature.
- Given the negative results of this study and the multiple hours necessary to analyze oxygen isotope ratios in a single sample of uranium oxide, additional research should prioritize the conduct of sensitivity studies on the impacts of diffusion. These studies should be informed by acquisition of additional information on limiting diffusion lengths in common uranium particle morphologies and typical time at temperature profiles used in industrial

applications. Alternatively, the study of signatures resulting from reaction with uranium hexfluoride may represent a better application of resources.

Chapter 8 Summary of contributions

This chapter summarizes the primary contributions resulting from this dissertation. The preceding chapters each contained detailed conclusions, associated discussions, and suggested areas for further study. This chapter aggregates the primary conclusions and provides perspectives on the state and direction of research needed to mature process signatures. The primary contributions from this dissertation are listed below based on the author's assessment of significance:

1. Identified that uranium precipitates decompose and transition to oxides in a pseudomorphic manner. This property enables the determination of process history for samples of otherwise chemically identical uranium oxides—a capability that no other technique has demonstrated. [Chapter 5]
2. Reported the first equilibrium oxygen isotope fractionation measurements between dry atmospheric air and U_3O_8 . This result supported the conclusion that oxygen isotope ratios in U_3O_8 are not readily linked to meteoric waters, contrary to the literature. [Chapter 7]
3. Performed the first measurements using near-infrared reflectance (NIR) spectroscopy on a number of uranium precipitates and oxides, identified insights into their spectral features, and demonstrated the potential to distinguish and identify these phases. [Chapter 4]

4. Demonstrated the efficacy of thermogravimetric methods as a signature, eliminated specific surface area as a signature, and highlighted process conditions where powder x-ray diffraction may be insufficient to determine process history. [Chapter 4]
5. Excluded simple grain morphological descriptors as signatures of precursor oxide production route or binder type in nuclear fuel pellets, as well as observed a number of features that may provide potential signatures. [Chapter 6]
6. Identified areas where additional research is required to mature the use of quantitative morphology through image analysis as a forensic technique. [Chapter 3]
7. Developed and characterized an extensive set of exemplars and real-world powder and pellet samples for future studies. [Chapter 4]

Overall, the process signatures identified in this dissertation should be strengthened through additional validation using independent personnel, equipment, and blind samples. The nature of process signatures is that the resulting information is likely to be one element of a broad picture providing all discernable information regarding a given sample. The results of this study indicate the potential types of process information that may be identified using these techniques. This study also informs future analysts with the requirements on the samples sizes and sequencing requirements for consideration in their approach. In general, all of the promising techniques utilized in this study require small sample masses ranging from 10 mg for

thermogravimetric analysis to sub-microgram amounts for scanning electron microscopy.

A number of additional studies are suggested throughout this dissertation. Priority should be given to refining the utility of the morphological signatures resulting from pseudomorphic decomposition reactions, given this unique capability to distinguish the history between otherwise chemically identical samples. Refinement may be accomplished by systematically broadening the chemical conditions used for precipitations and monitoring the resulting changes in final oxide morphology. The novel nature of these pseudomorphic reactions also demands priority to probe the fundamental chemistry associated with these transitions.

Next, given the findings in this study and the enormous potential value of developing a geolocation signature, efforts should shift from examining oxides to investigating fractionation during the pyrohydrolysis reaction of uranium hexafluoride. While the application of this reaction is limited, pyrohydrolysis is naturally focused on processing of enriched uranium, an activity of high interest to nuclear forensics. Similarly, the promising results associated with NIR and the robust simplicity of the associated equipment, suggests the need to mature this tool and associated signatures.

Continued work on quantitative morphology is also warranted, but should first focus on the development of improved algorithms, calibration methods for the software-imaging hardware interface, sample preparation, and standards. These steps can be accomplished entirely without using radioactive materials, but should be performed in consultation with researchers who are knowledgeable on the techniques

and requirements for working with radioactive materials. The value of continued research on fuel pellets is questionable. This study suggests that very specific process information will be necessary to derive broader signatures on grain morphology and the other identified surface features of potential forensic value. In reality, fuel pellets of any element pose relatively low risk and efforts would likely be better spent on refining techniques for powders or metals, such as morphology and thermogravimetric analysis.

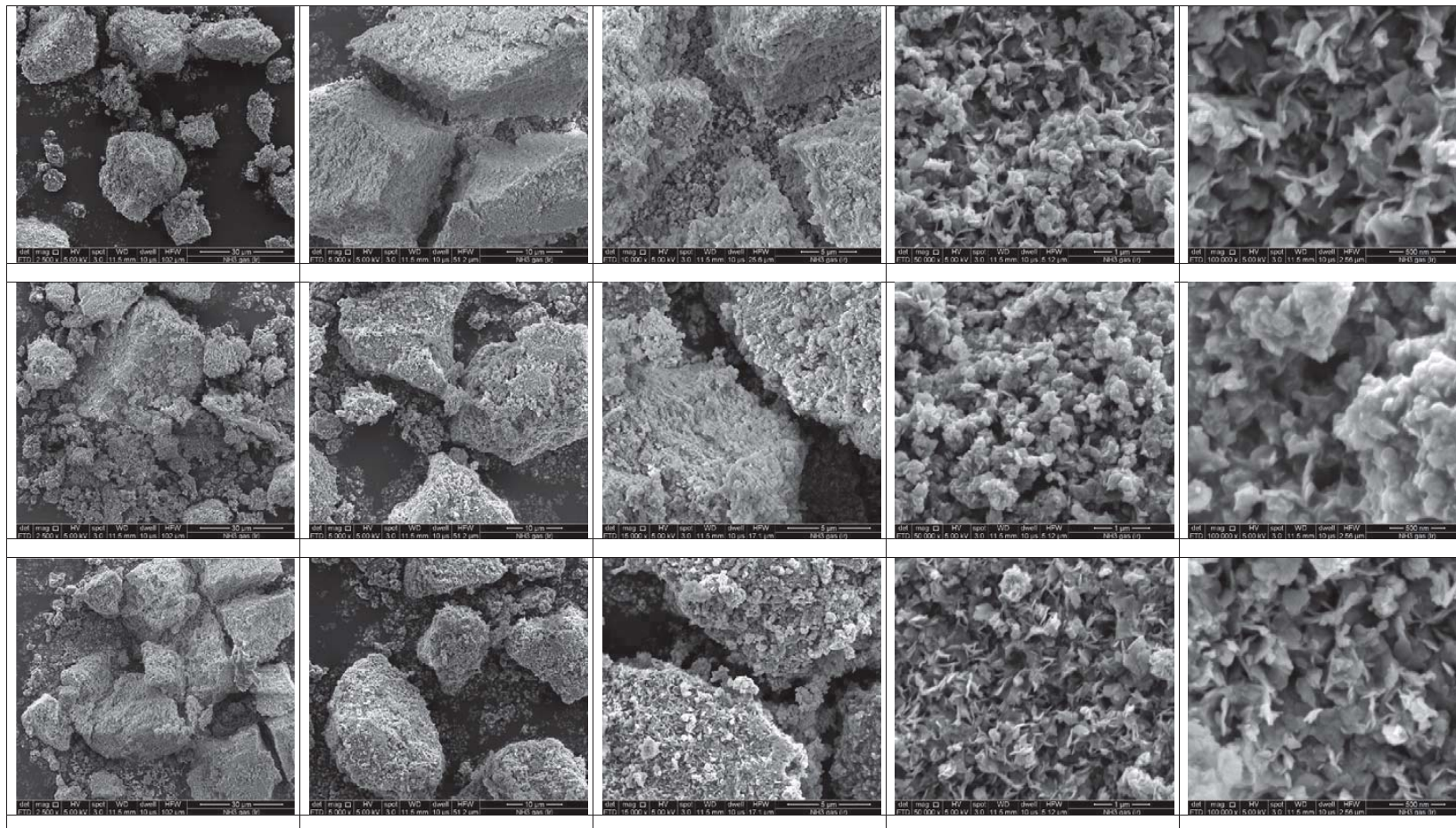
In conclusion, this dissertation explored and expanded process signatures available to the nuclear forensics community. Some of the examined areas warrant additional efforts and many other areas likely remain available for assessment. The importance of this field requires continued investment in training, equipment, and acquisition of suitable samples to advance techniques and fully validate preliminary signatures.

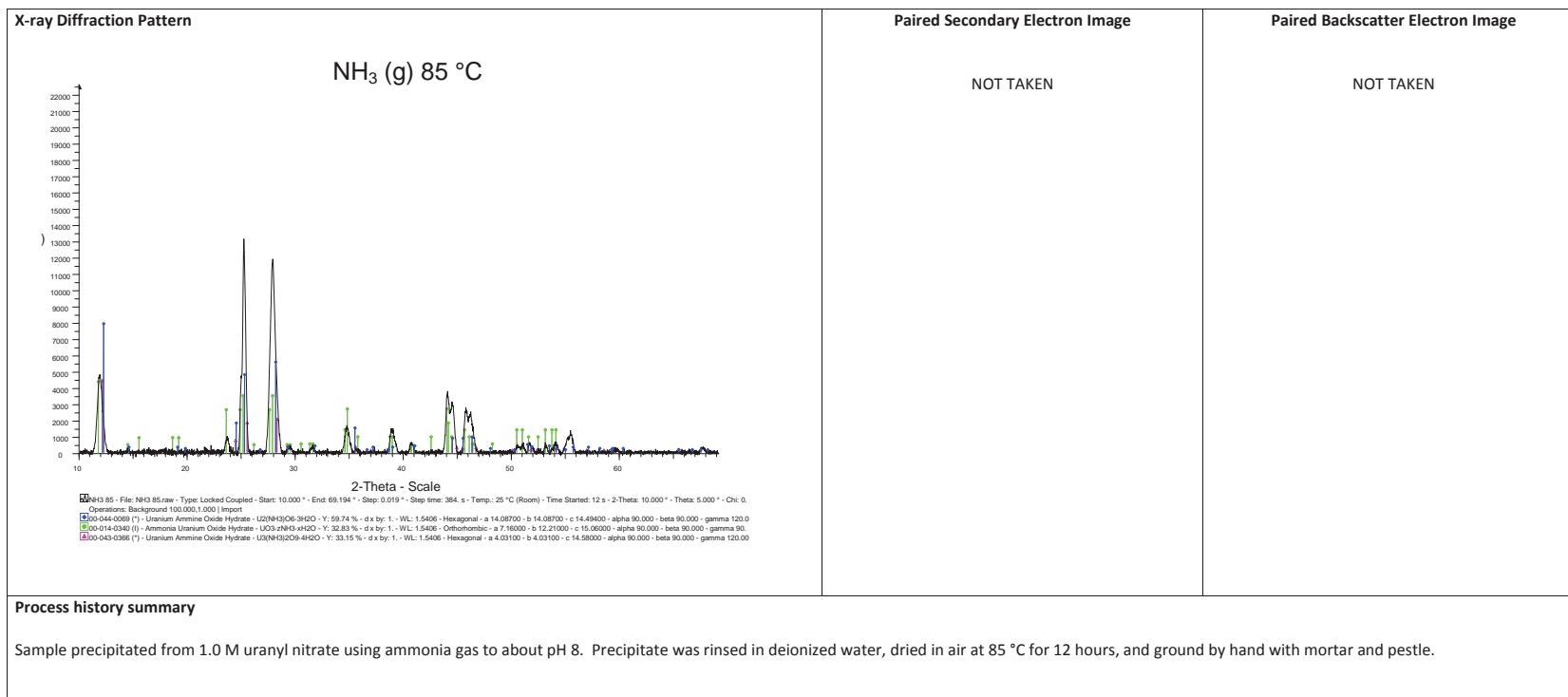
APPENDIX: Scanning electron image sets and x-ray diffraction patterns

	<i>Page</i>
Ammonia	
Precipitate uranyl nitrate and ammonia gas heated to 85 °C	183
Precipitate of uranyl nitrate and ammonium hydroxide heated to 85 °C	185
Precipitate of uranyl nitrate and ammonium hydroxide heated to 150 °C	187
Precipitate of uranyl nitrate and ammonium hydroxide heated to 400 °C	189
Precipitate of uranyl nitrate and ammonium hydroxide heated to 600 °C	191
Precipitate of uranyl nitrate and ammonium hydroxide heated to 750 °C	193
Uranium ore concentrate from the Federal American Partners facility in Gas Hills, Wyoming, USA	195
Uranium ore concentrate from the Key Lake facility in Saskatchewan, Canada	197
Uranium ore concentrate from the Milliken Lake facility in Canada	199
Uranium ore concentrate from the Rössing facility in Namibia	201
Uranium ore concentrate from the NUFCOR facility Westonaria, South Africa	203
Uranium ore concentrate from the Olympic Dam facility in Western Australia	205
Uranium ore concentrate produced at the Ranger facility in the Northwest Territory, Australia	207
Hydrogen Peroxide	
Precipitate of uranyl nitrate and hydrogen peroxide heated to 85 °C	
Precipitate of uranyl nitrate and hydrogen peroxide heated to 150 °C	209
Precipitate of uranyl nitrate and hydrogen peroxide heated to 400 °C	211
Precipitate of uranyl nitrate and hydrogen peroxide heated to 600 °C	213
Precipitate of uranyl nitrate and hydrogen peroxide heated to 750 °C	215
Uranium ore concentrate from Crowe Butte, USA	217
Uranium ore concentrate from the El Mesquite facility in Duval County, Texas, USA	219
Uranium ore concentrate from the Irigaray facility in Johnson County, Wyoming, USA	221
Uranium ore concentrate from Mobil, USA	223
Uranium ore concentrate from the Rabbit Lake facility in Saskatchewan, Canada	225
Uranium ore concentrate from the Uranium Resources Inc. facility in Duval County Texas, USA	227
Ammonium Carbonate	
Precipitate of uranyl nitrate and ammonium carbonate heated to 85 °C	231
Precipitate of uranyl nitrate and ammonium carbonate heated to 85 °C	233
Precipitate of uranyl nitrate and ammonium carbonate heated to 400 °C	235
Precipitate of uranyl nitrate and ammonium carbonate heated to 600 °C	237
Precipitate of uranyl nitrate and ammonium carbonate heated to 750 °C	239
Industrial Sample NF-55	241
Industrial Sample NF-56	243

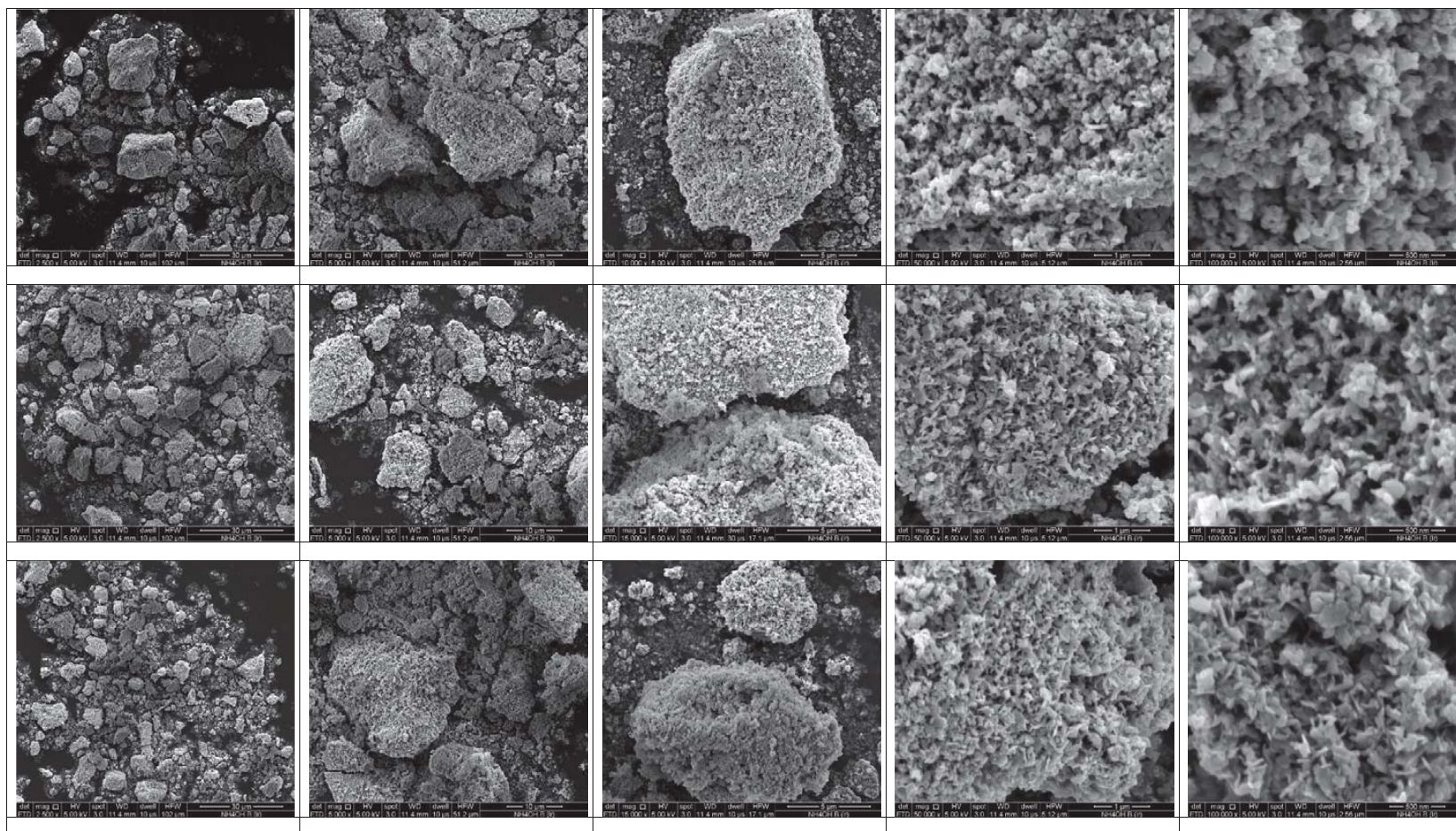
	<i>Page</i>
Magnesia	
Precipitate of uranyl nitrate and magnesia heated to 85 °C	245
Precipitate of uranyl nitrate and magnesia heated to 150 °C	247
Precipitate of uranyl nitrate and magnesia heated to 400 °C	249
Precipitate of uranyl nitrate and magnesia heated to 600 °C	251
Precipitate of uranyl nitrate and magnesia heated to 750 °C	253
Uranium ore concentrate from the Anaconda Company Bluewater Plant in Grants, New Mexico	255
Uranium ore concentrate from the COMUF facility Mounana, Gabon	257
Uranium ore concentrate from the Dyno facility in Bancroft, Ontario, Canada	259
Uranium ore concentrate from the Gunnar facility in Lake Athabasca, Saskatchewan, Canada	261
Uranium ore concentrate from the Rum Jungle facility in Australia	263
Uranium ore concentrate from South Alligator, Australia	265
Sodium Hydroxide	
Precipitate of uranyl nitrate and sodium hydroxide heated to 85 °C	267
Precipitate of uranyl nitrate and sodium hydroxide heated to 150 °C	269
Precipitate of uranyl nitrate and sodium hydroxide heated to 400 °C	271
Precipitate of uranyl nitrate and sodium hydroxide heated to 600 °C	273
Precipitate of uranyl nitrate and sodium hydroxide heated to 750 °C	275
Uranium ore concentrate from the El Dorado facility in Northwest Territories, Canada	277
Uranium ore concentrate from the Sequehanna Western Facility in Falls City, Texas, USA	279
Uranium ore concentrate from the Ranstad facility in Sweden	281
Uranium ore concentrate from the SOMAIR facility in Niger	283
Other Processes	
Uranyl hexanitrate heated to 600 °C	285
Uranium metal turnings directly heated to 400 °C	287
Uranium hydride heated to 400 °C	289
Uranium tetrafluoride, purchased	291
Uranium tetrafluoride heated in moist air to 400 °C	293
Commercially produced uranium dioxide powder blend	295

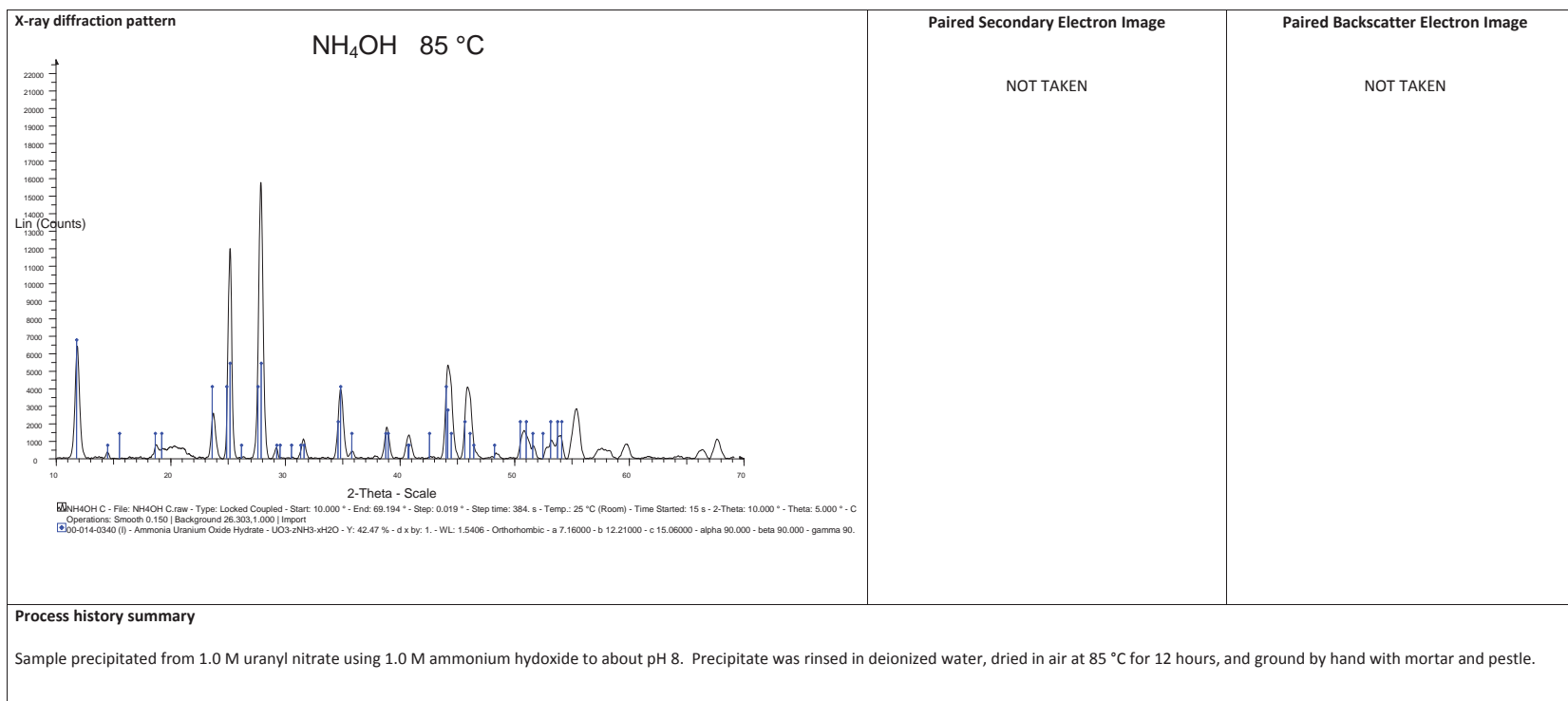
Morphology of the precipitate of uranyl nitrate and ammonia gas heated to 85 °C



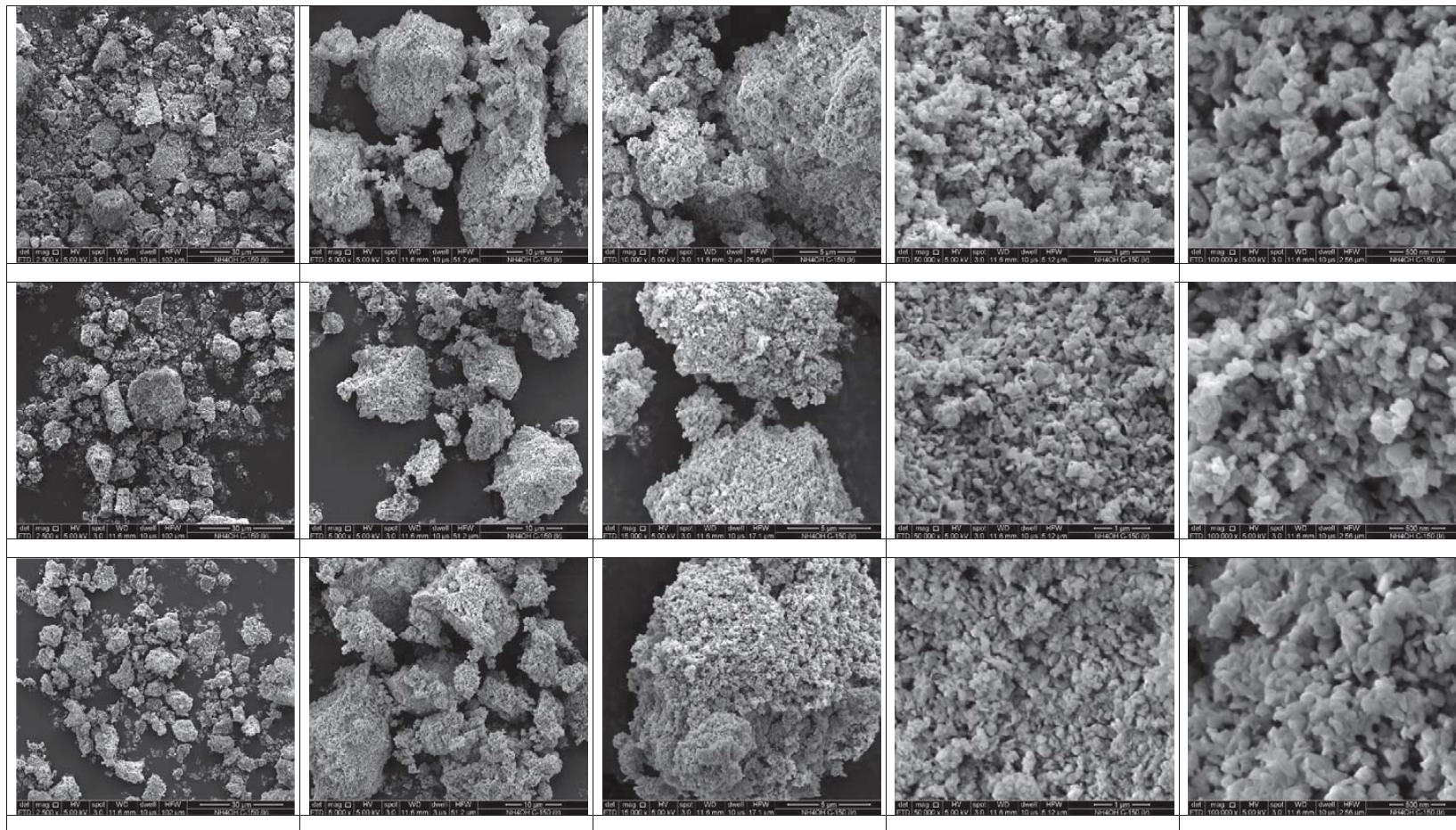


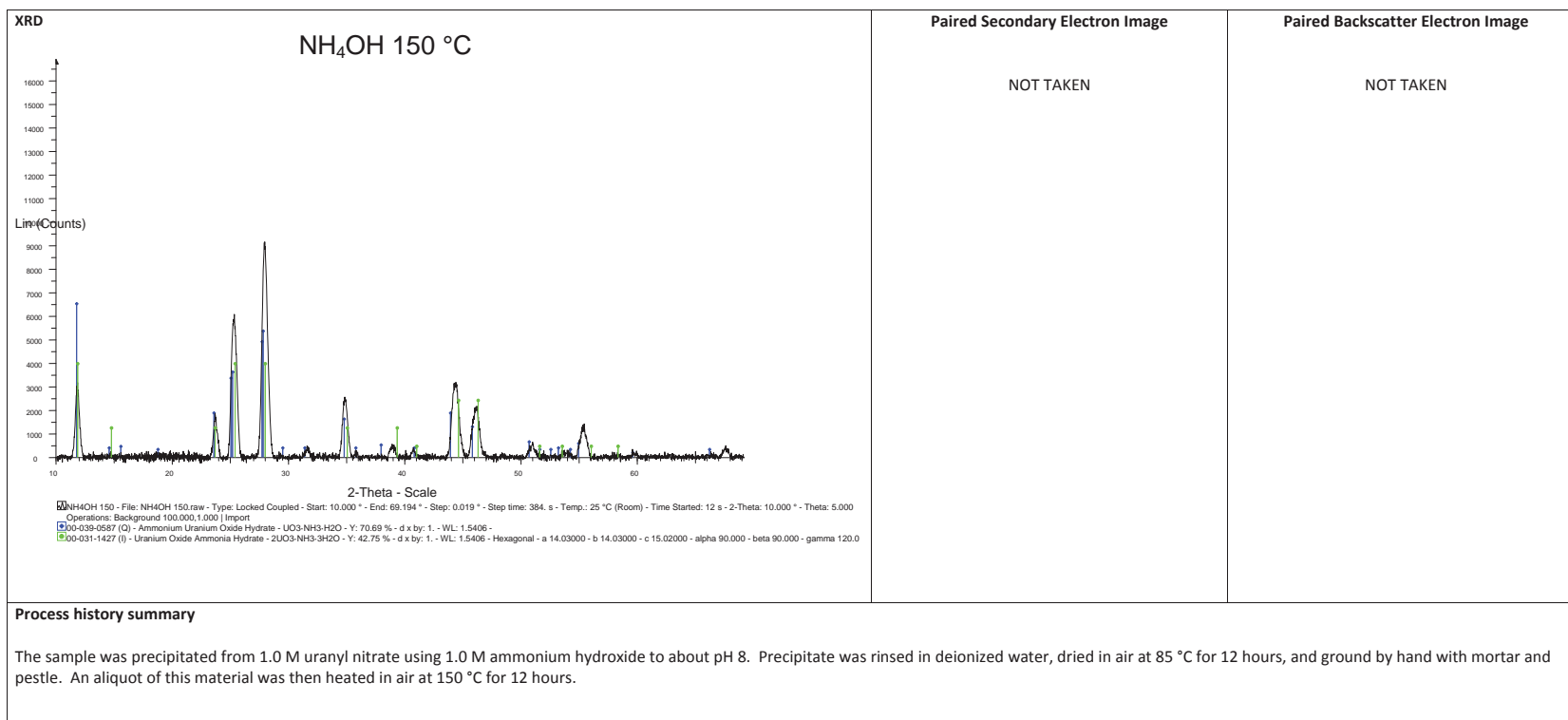
Morphology of precipitate of uranyl nitrate and ammonium hydroxide heated to 85 °C



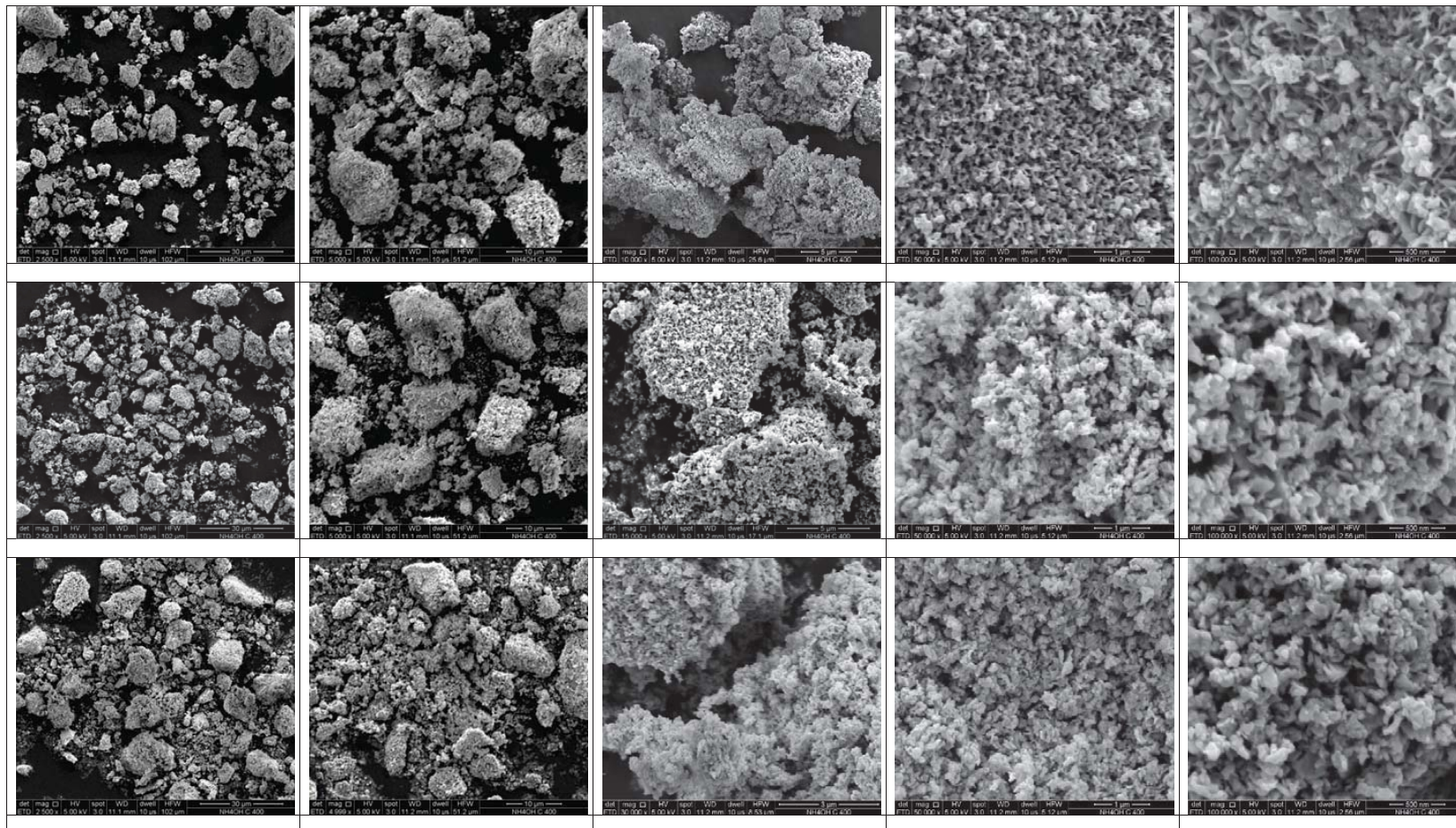


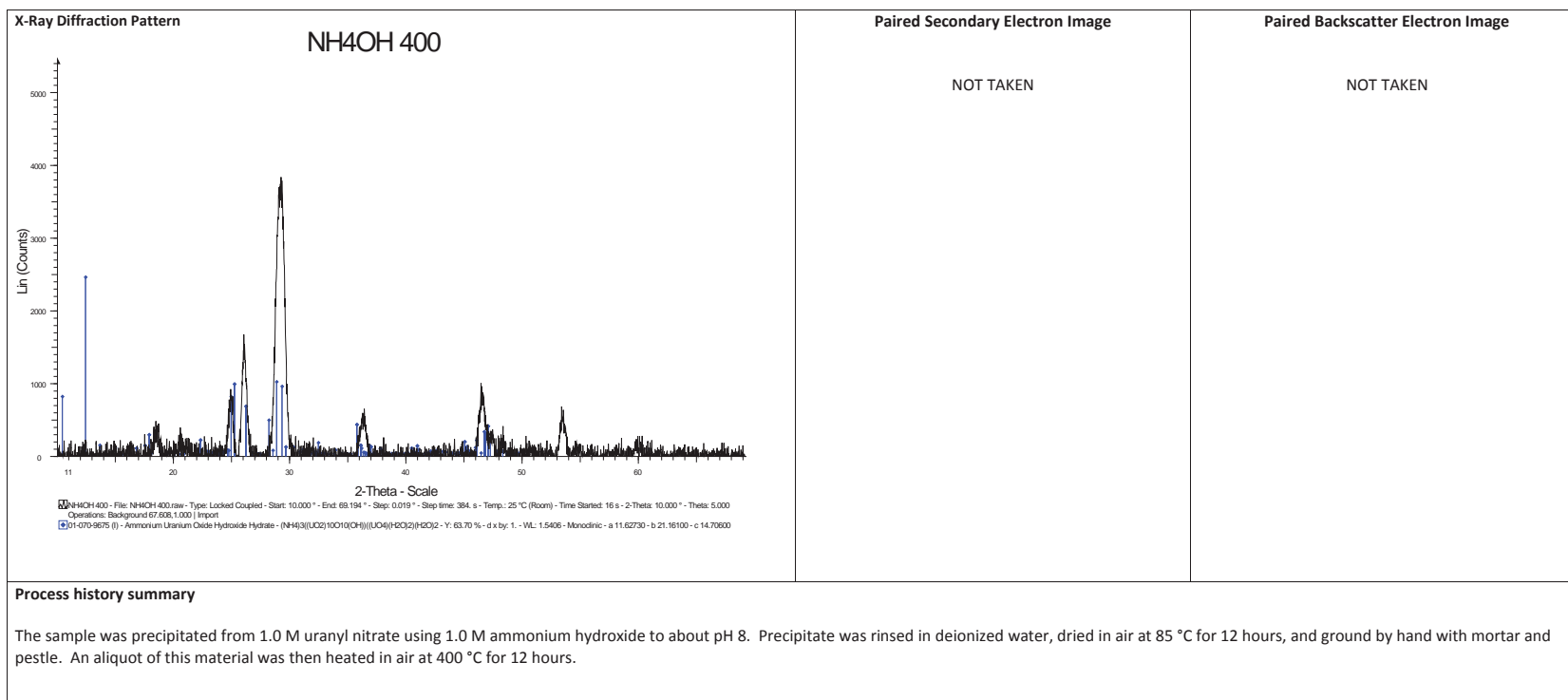
Morphology of the precipitate of uranyl nitrate and ammonium hydroxide heated to 150 °C



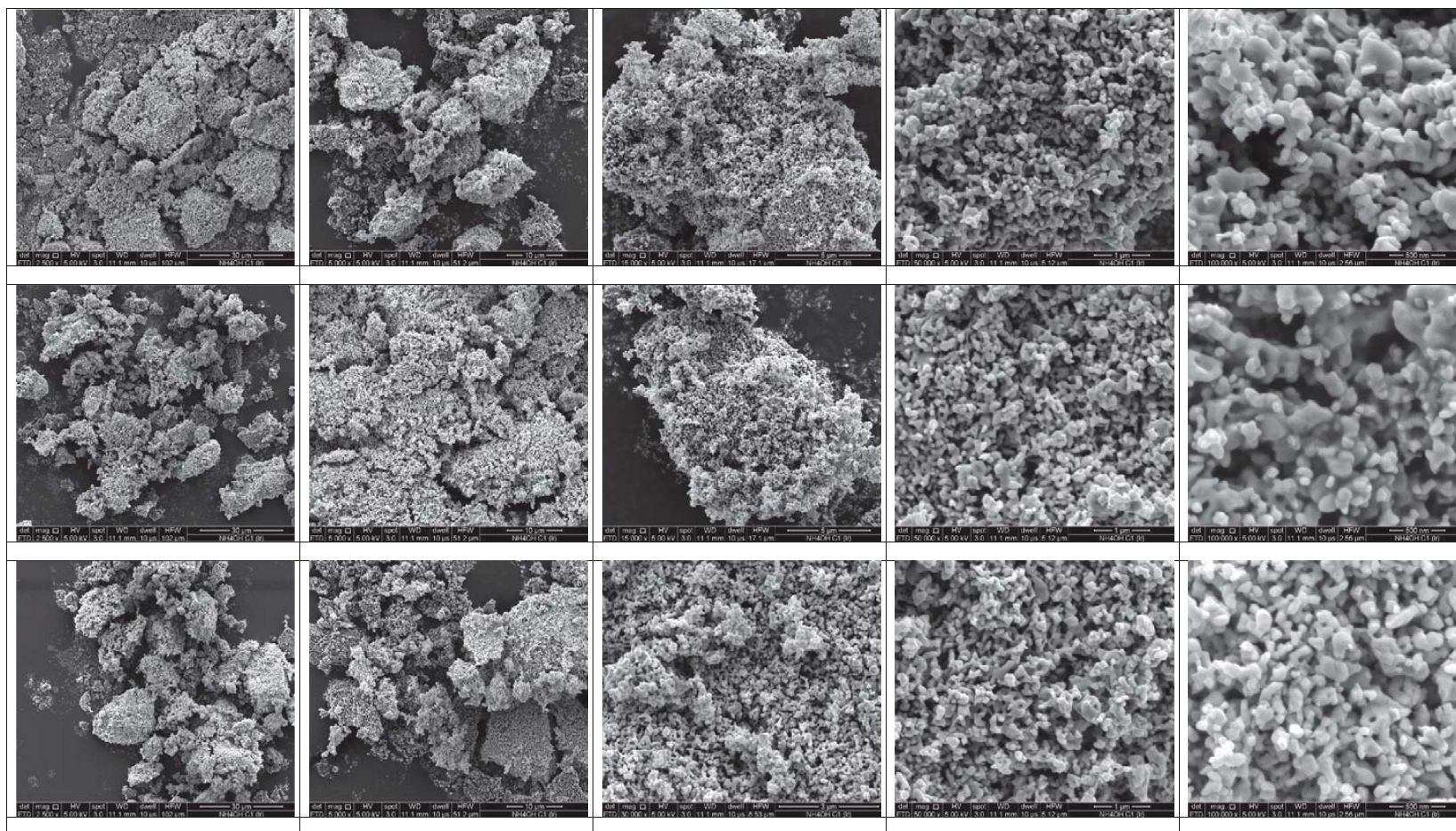


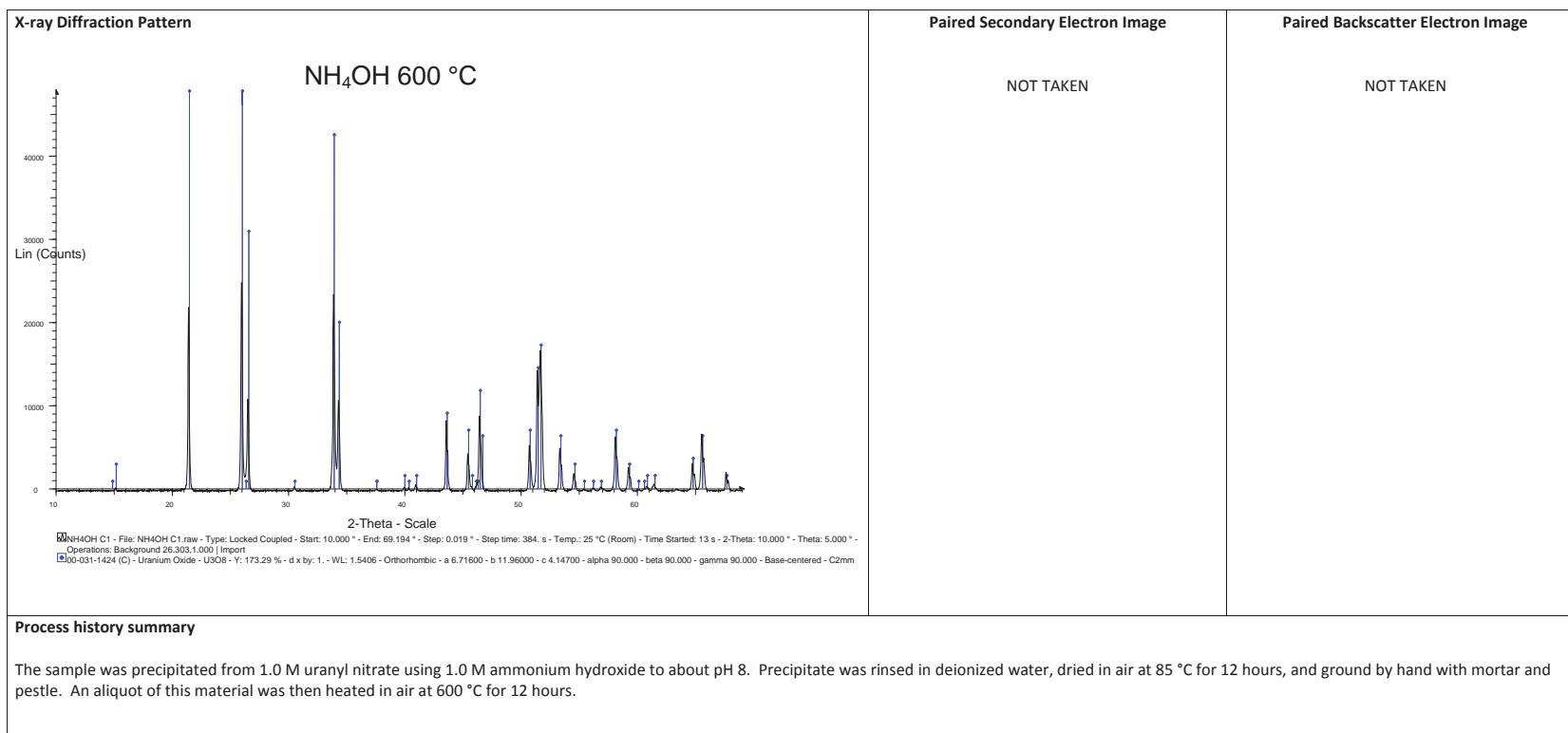
Morphology of the precipitate of uranyl nitrate and ammonium hydroxide heated to 400 °C



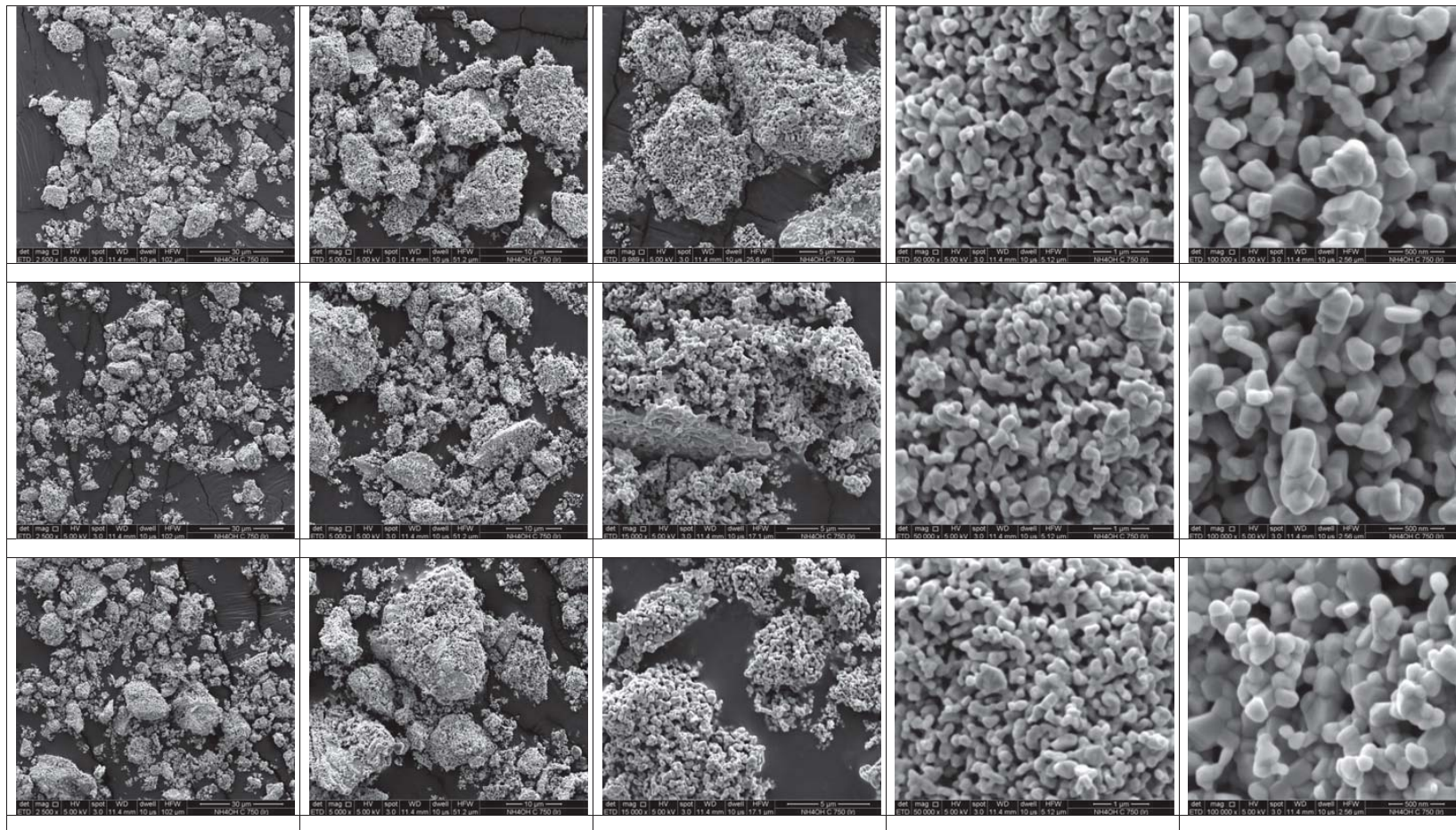


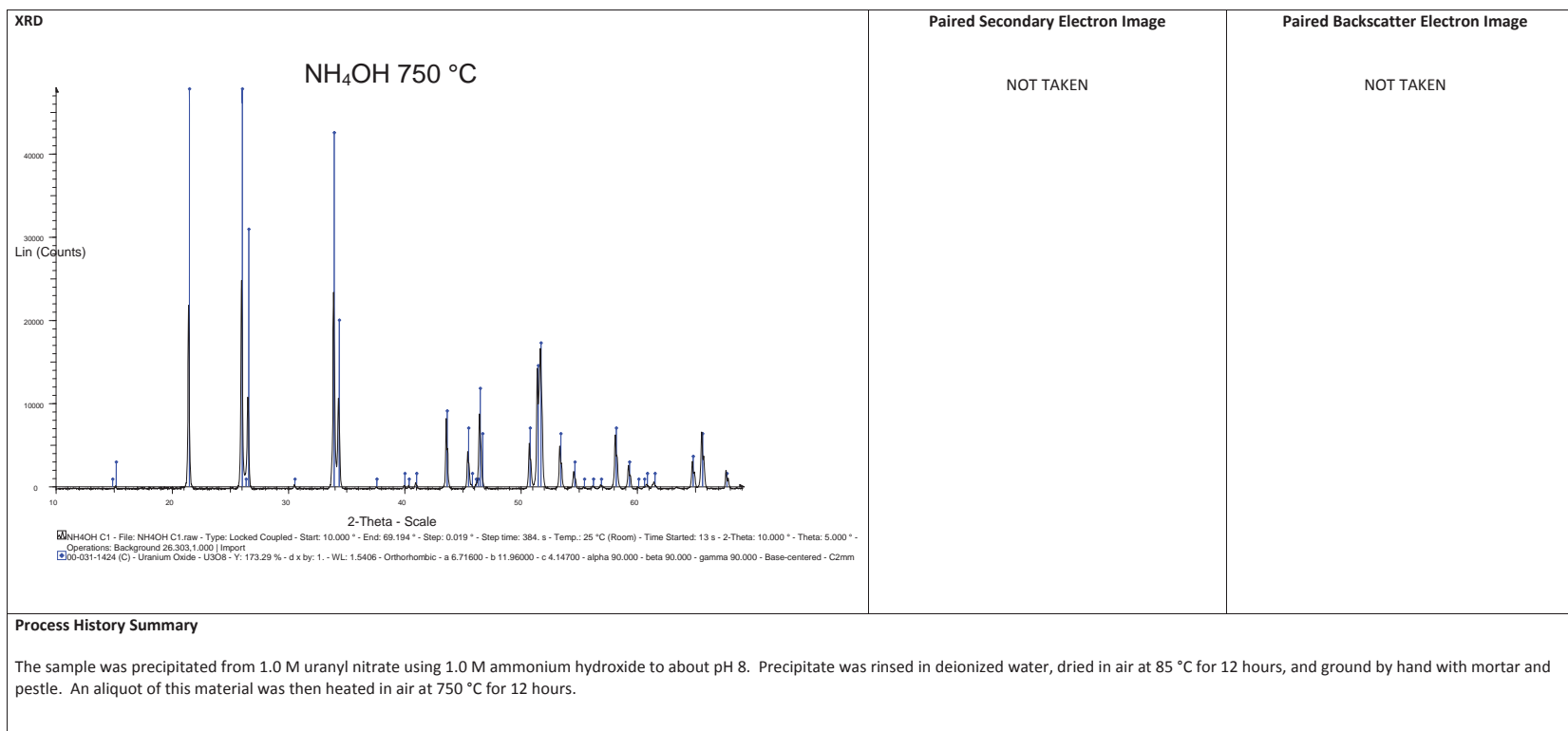
Morphology of the precipitate of uranyl nitrate and ammonium hydroxide heated to 600 °C



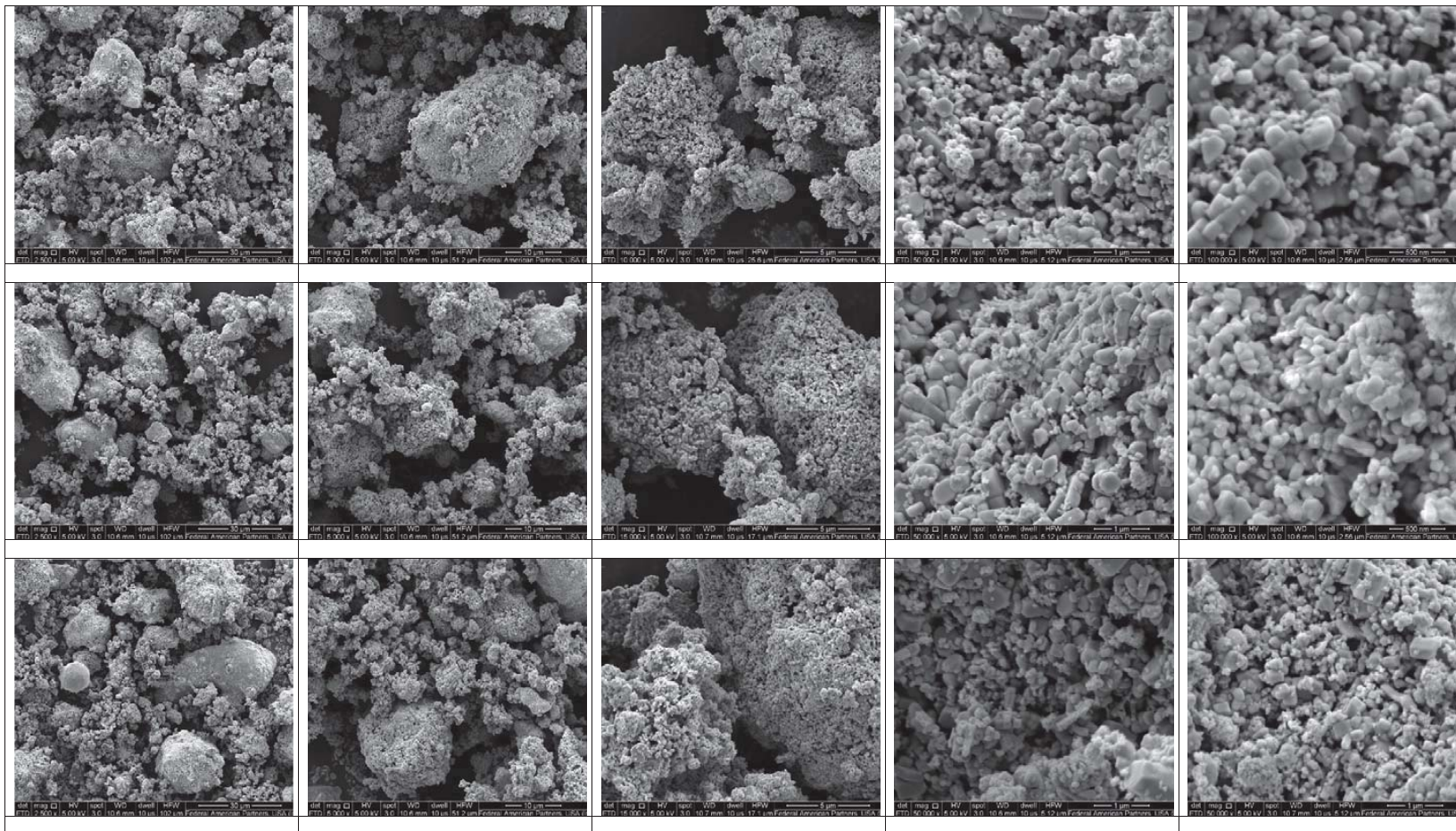


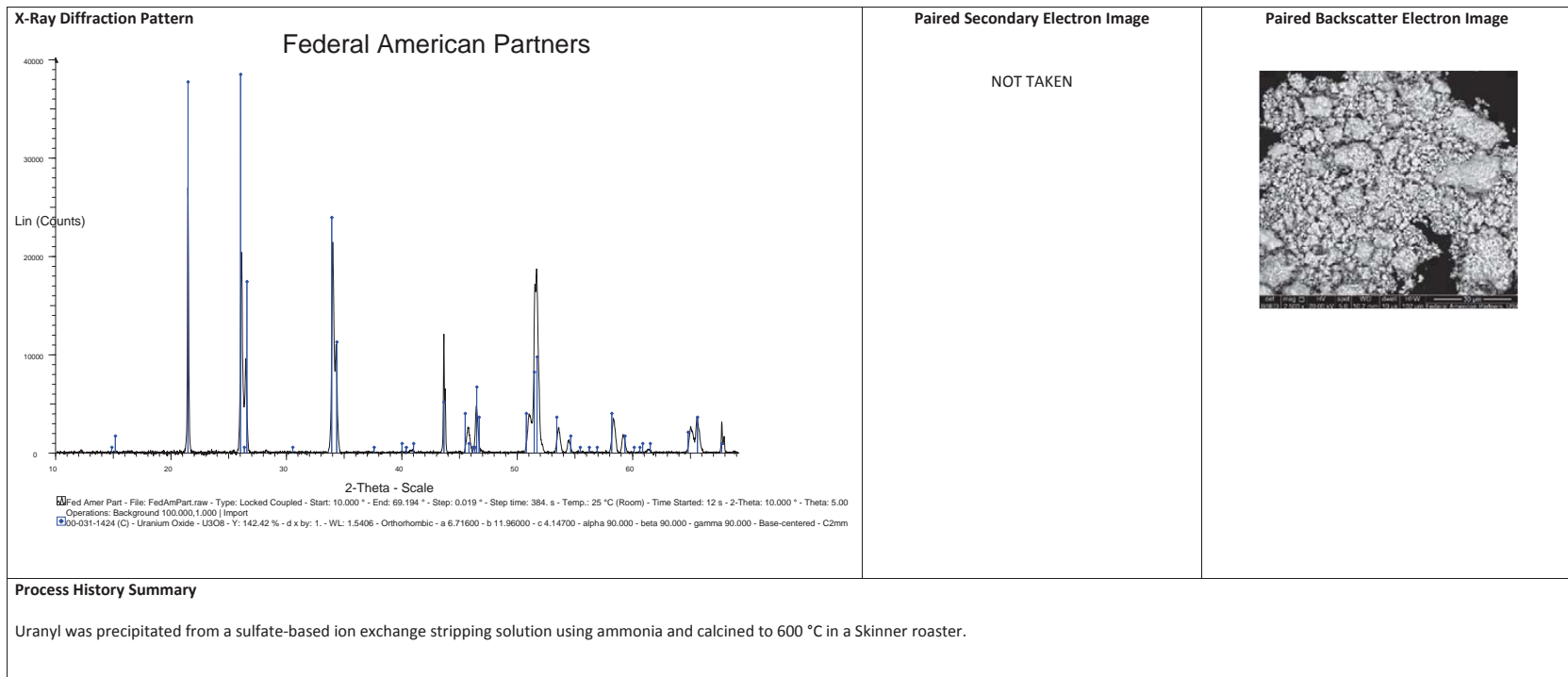
Morphology of the precipitate of uranyl nitrate and ammonium hydroxide heated to 750 °C



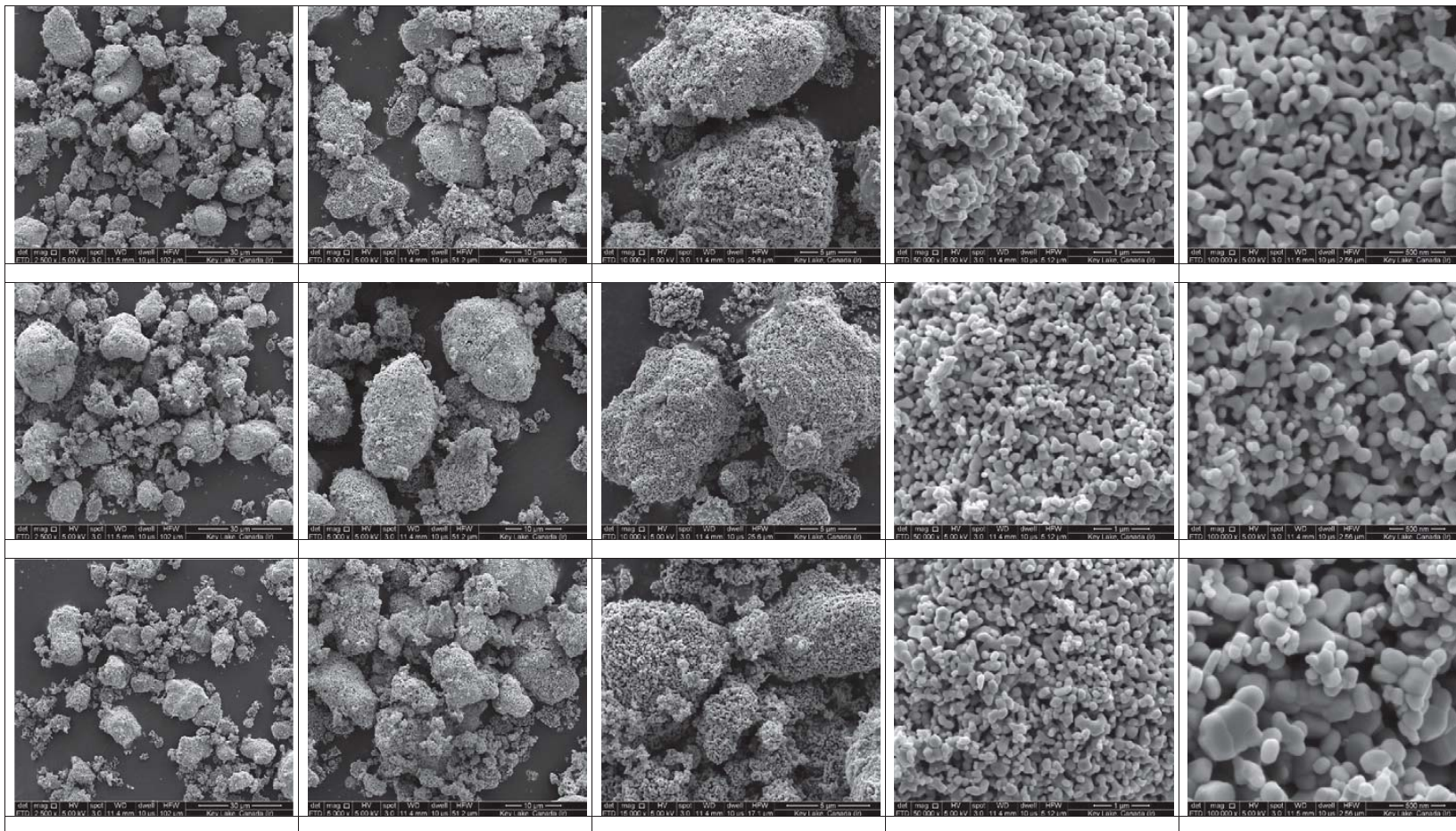


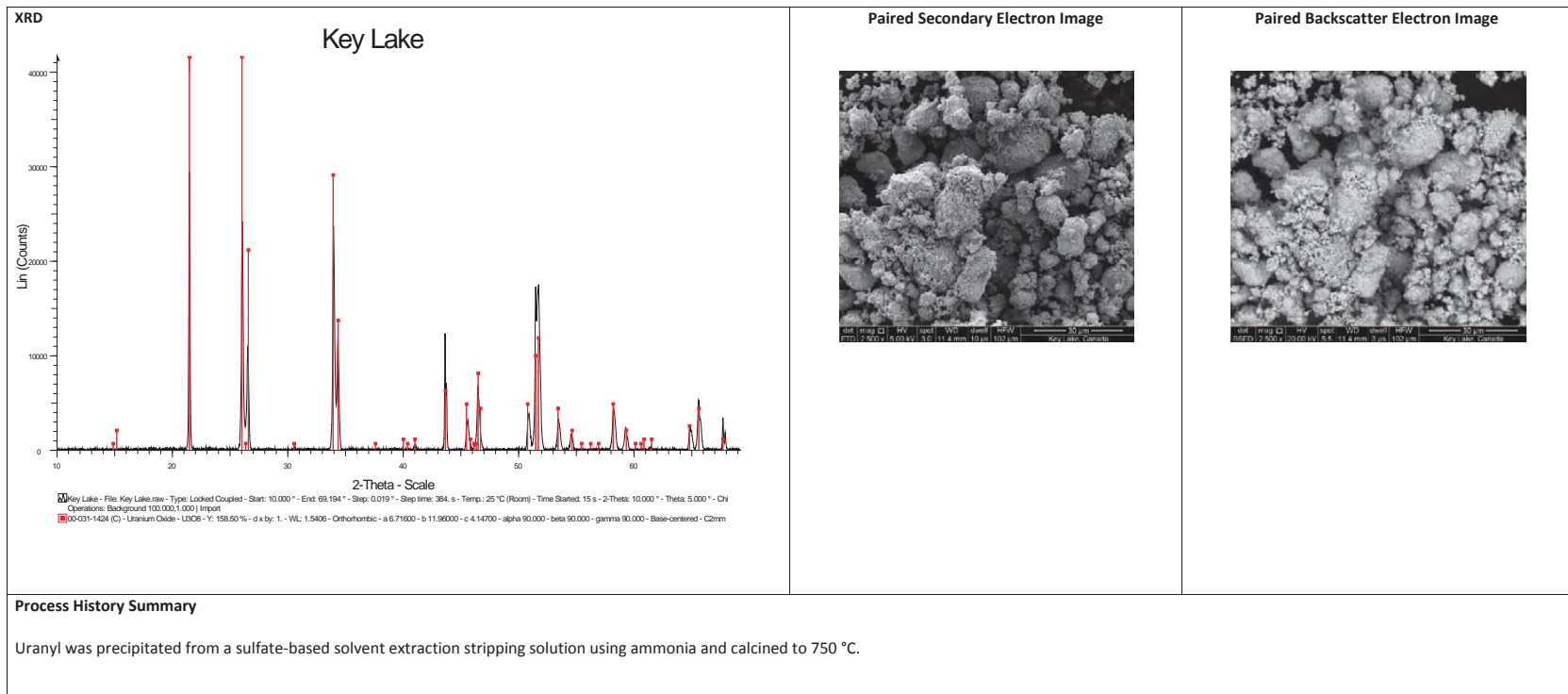
Morphology of uranium ore concentrate from the Federal American Partners facility in Gas Hills, Wyoming, USA



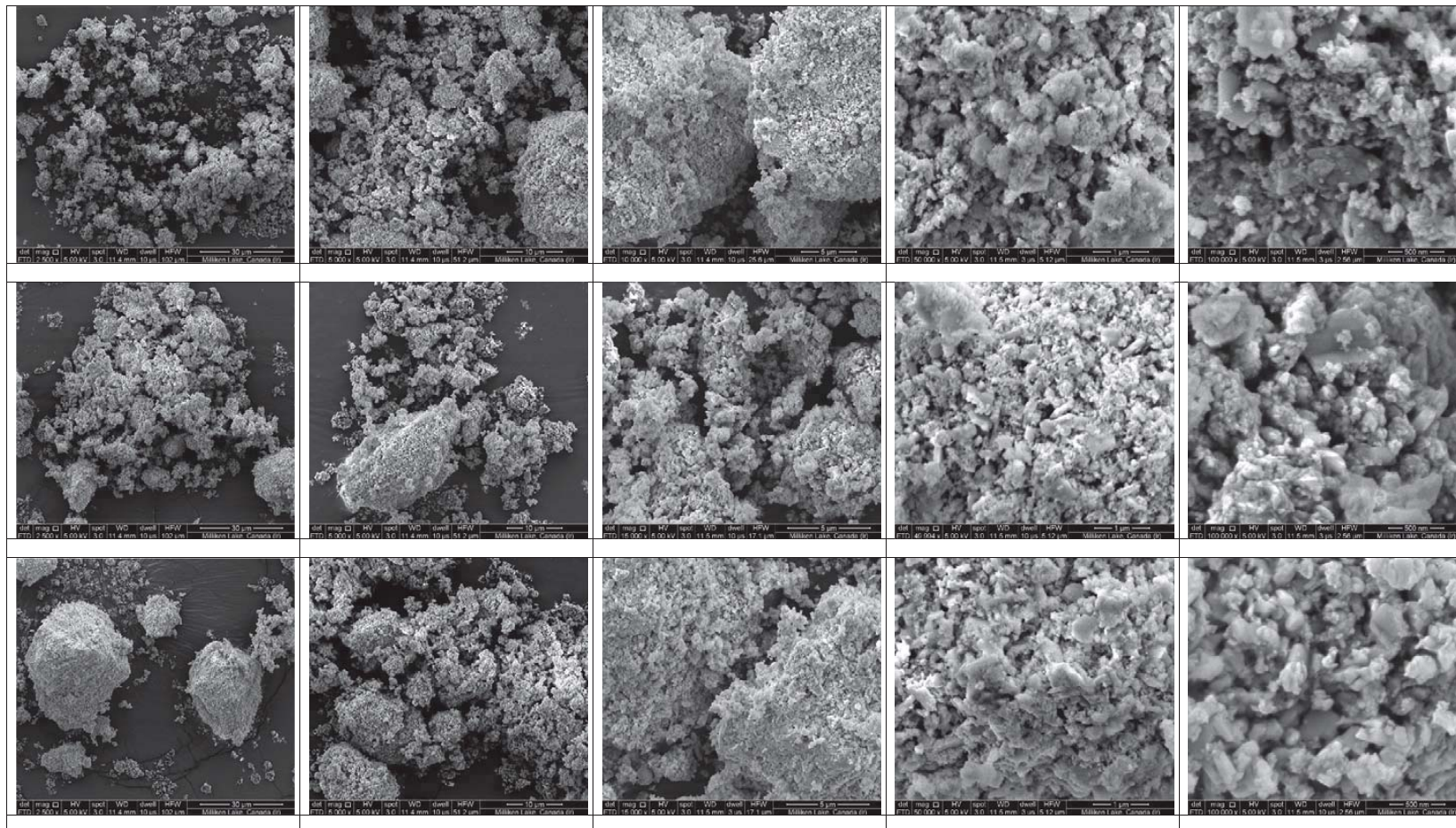


Morphology of uranium ore concentrate from the Key Lake facility in Saskatchewan, Canada

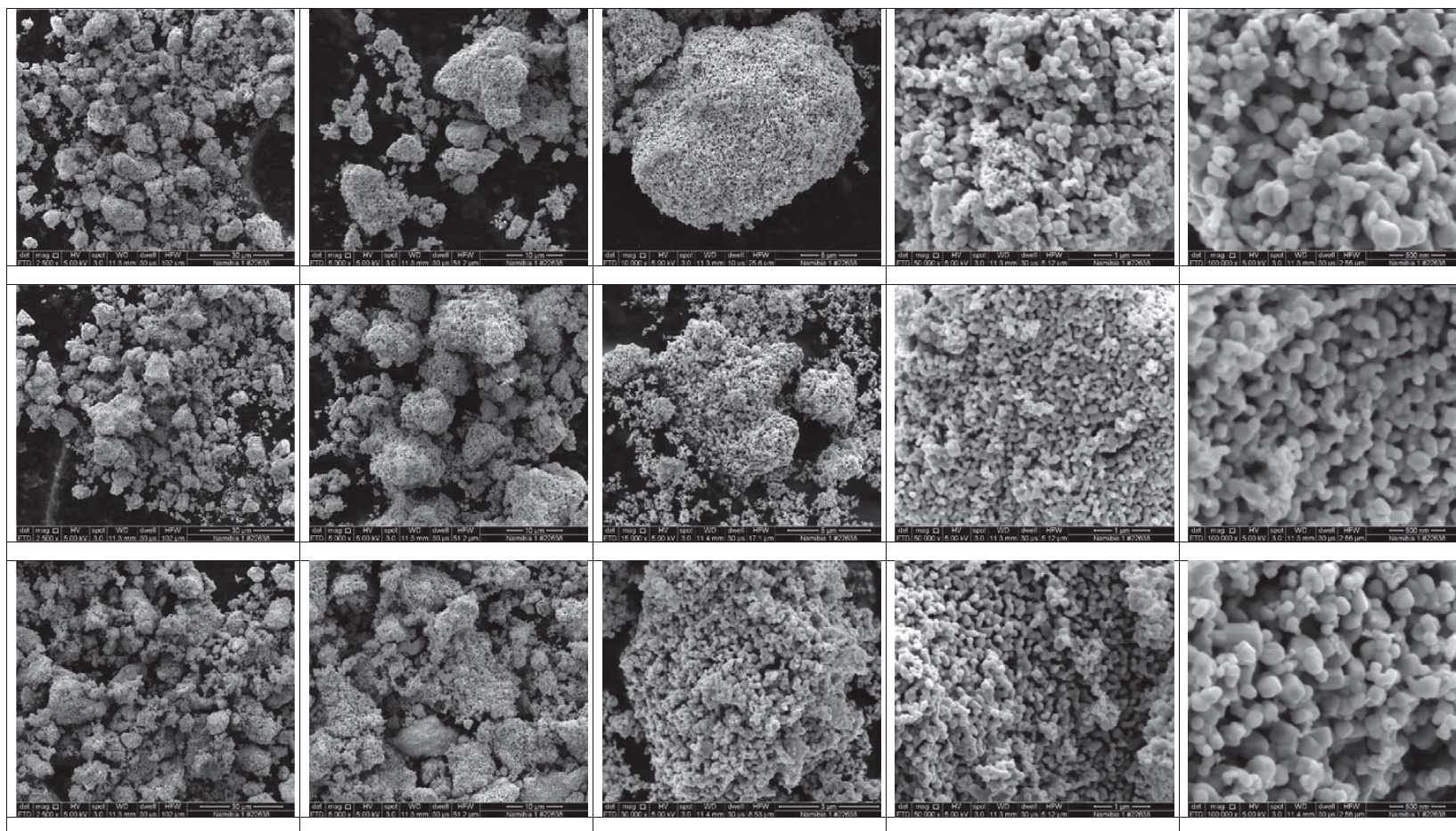


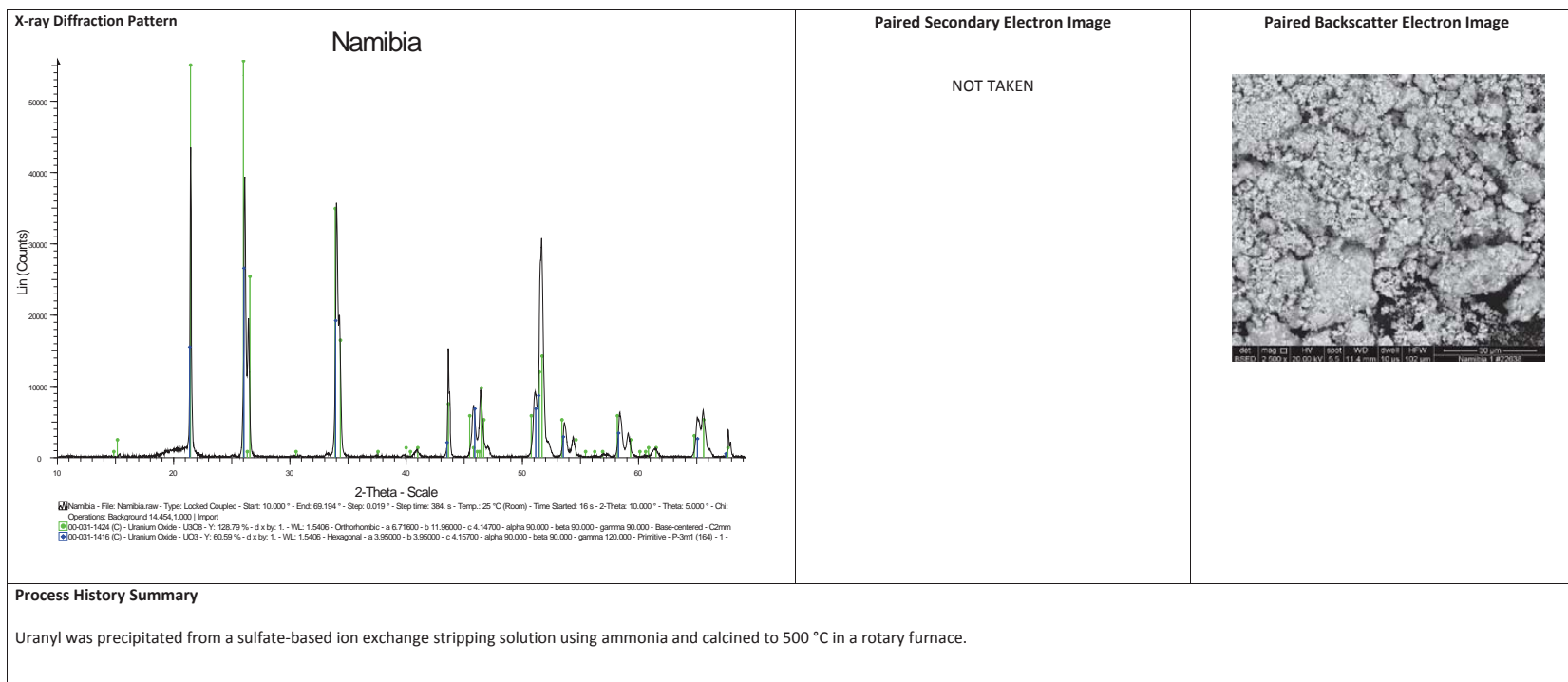


Morphology of uranium ore concentrate from the Milliken Lake facility in Canada

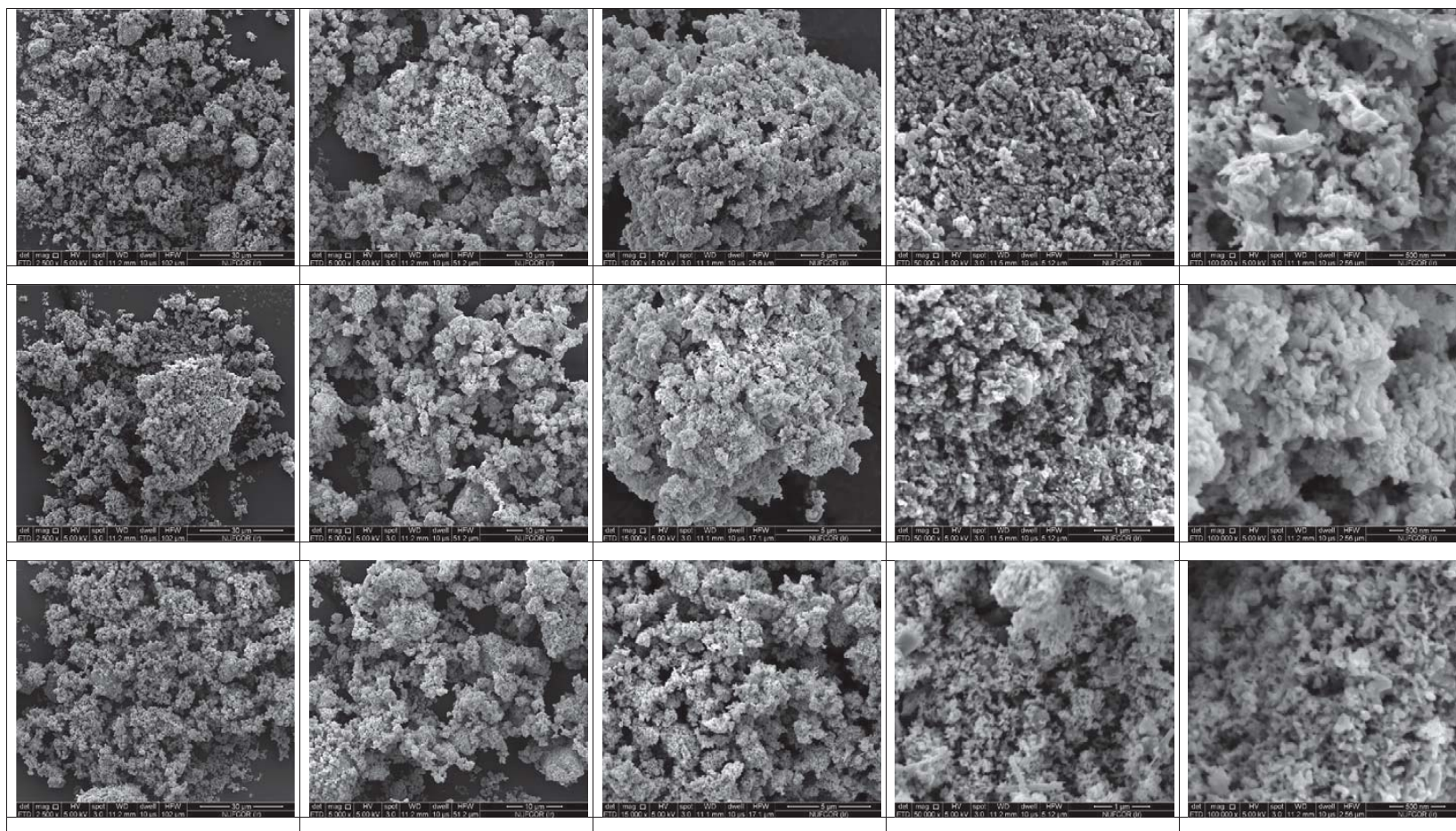


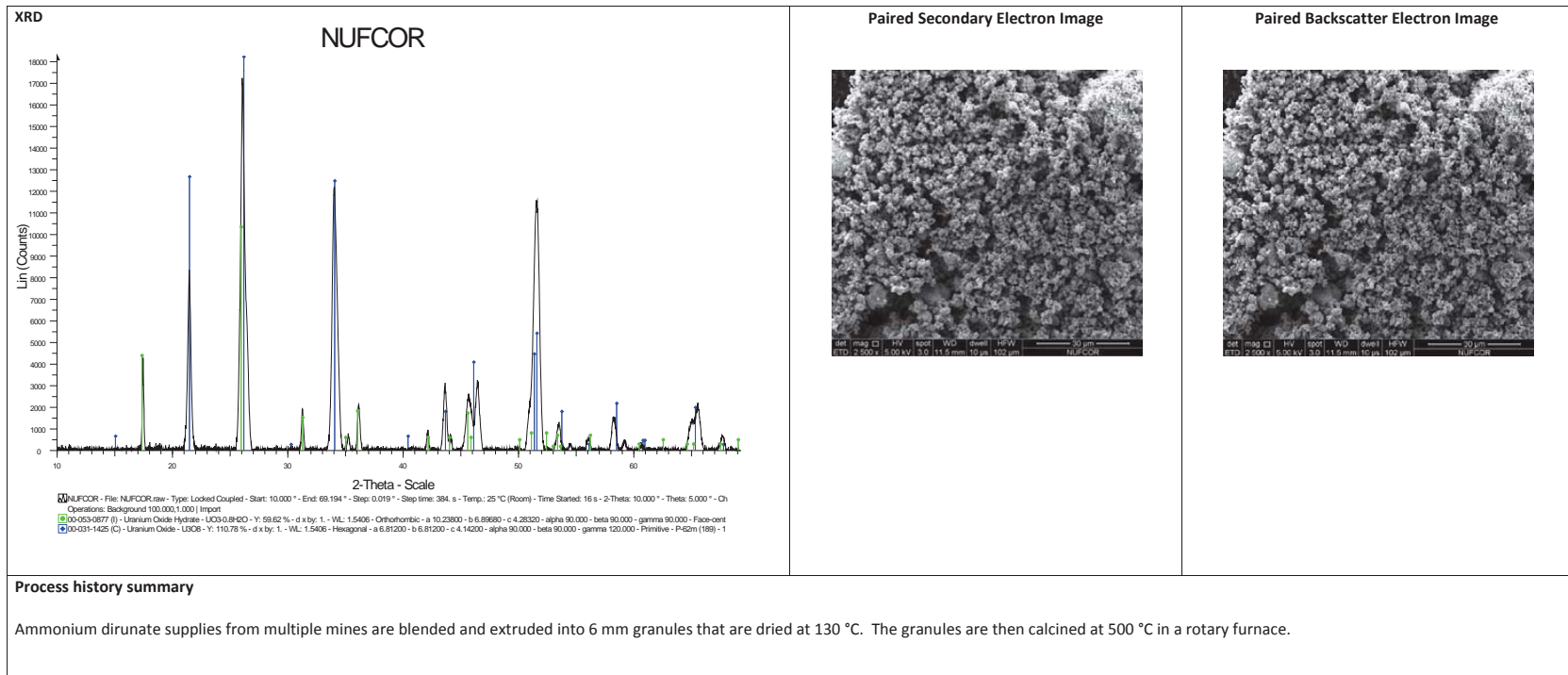
Morphology of uranium ore concentrate from the Rössing facility in Namibia



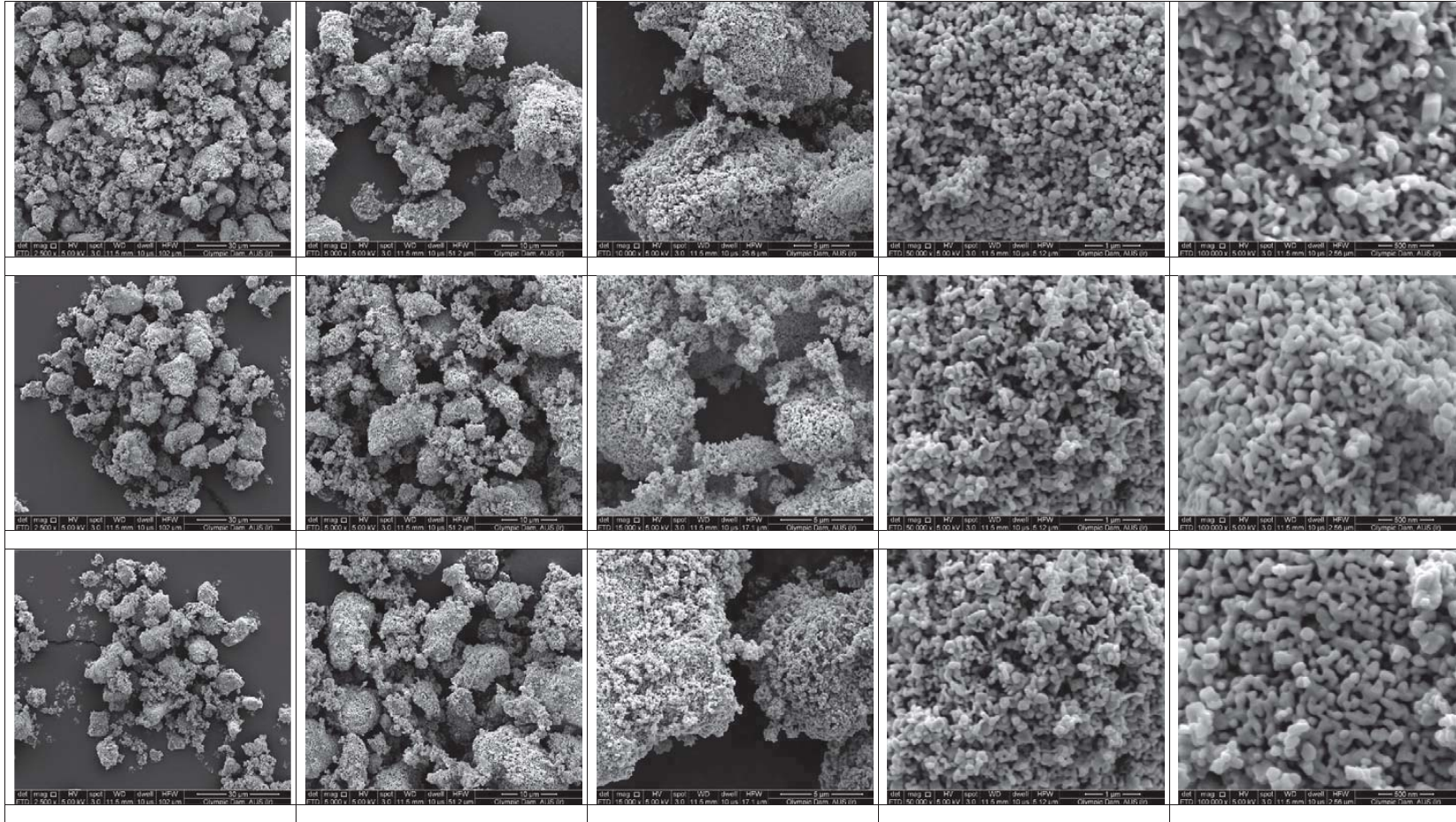


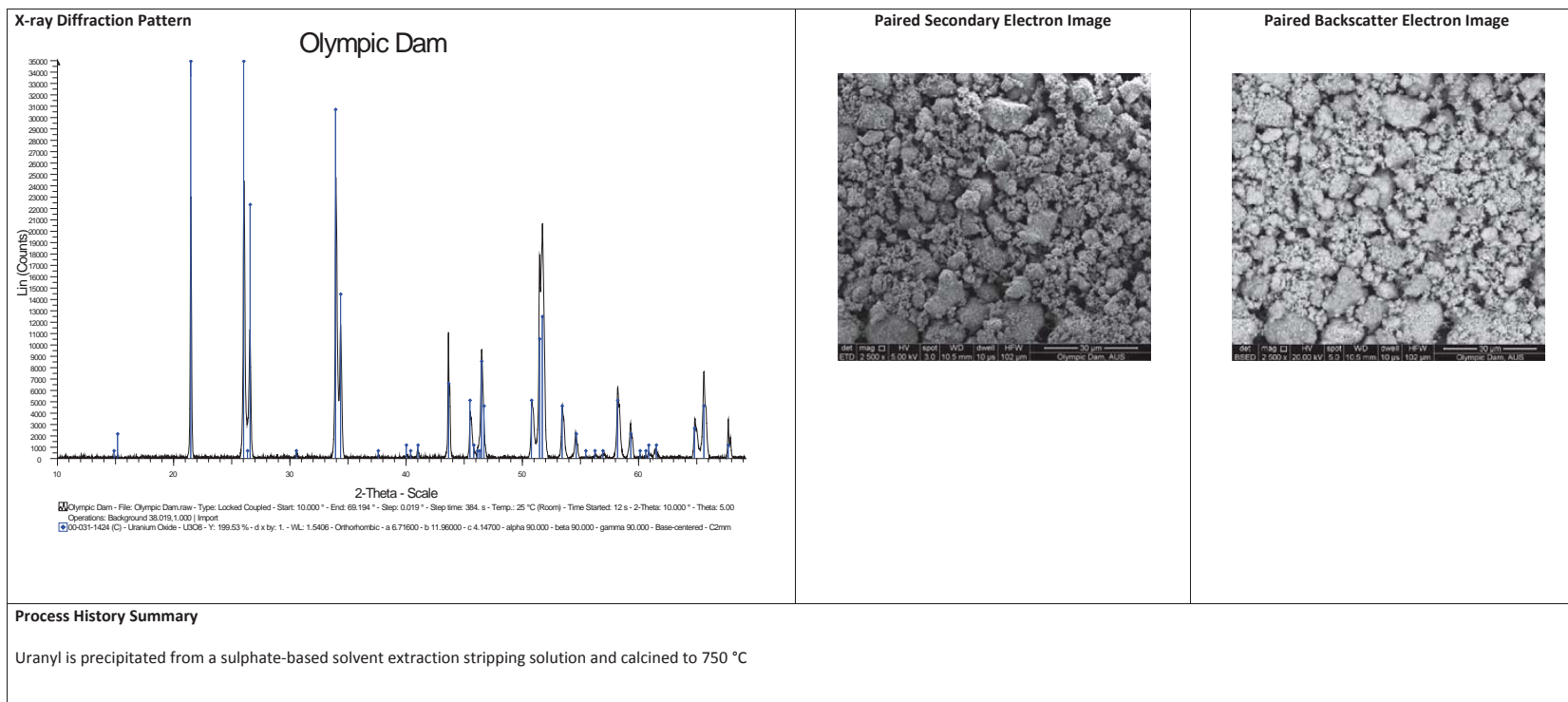
Morphology of uranium ore concentrate from the NUFCOR facility Westonaria, South Africa



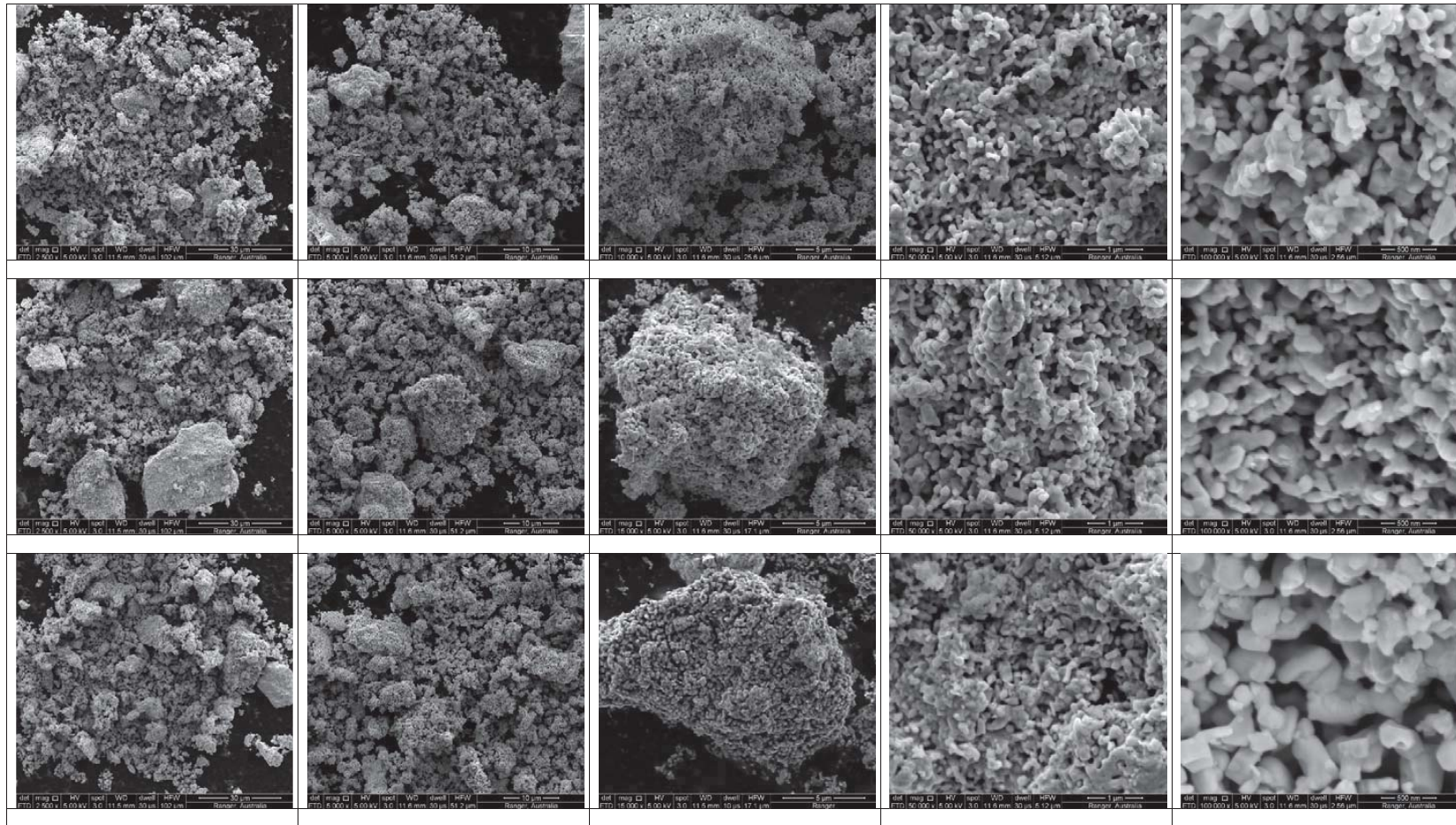


Morphology of uranium ore concentrate from the Olympic Dam facility in Western Australia

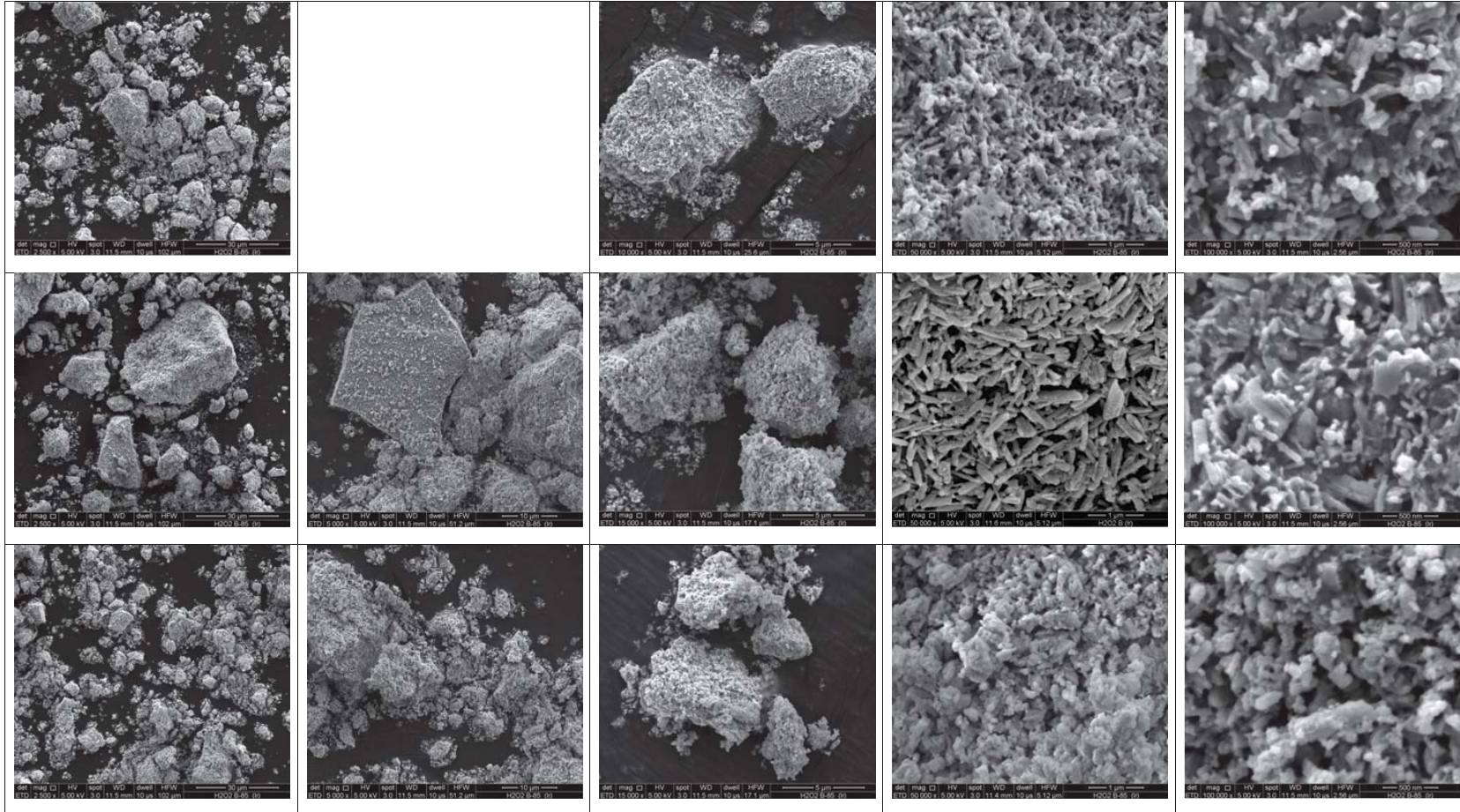


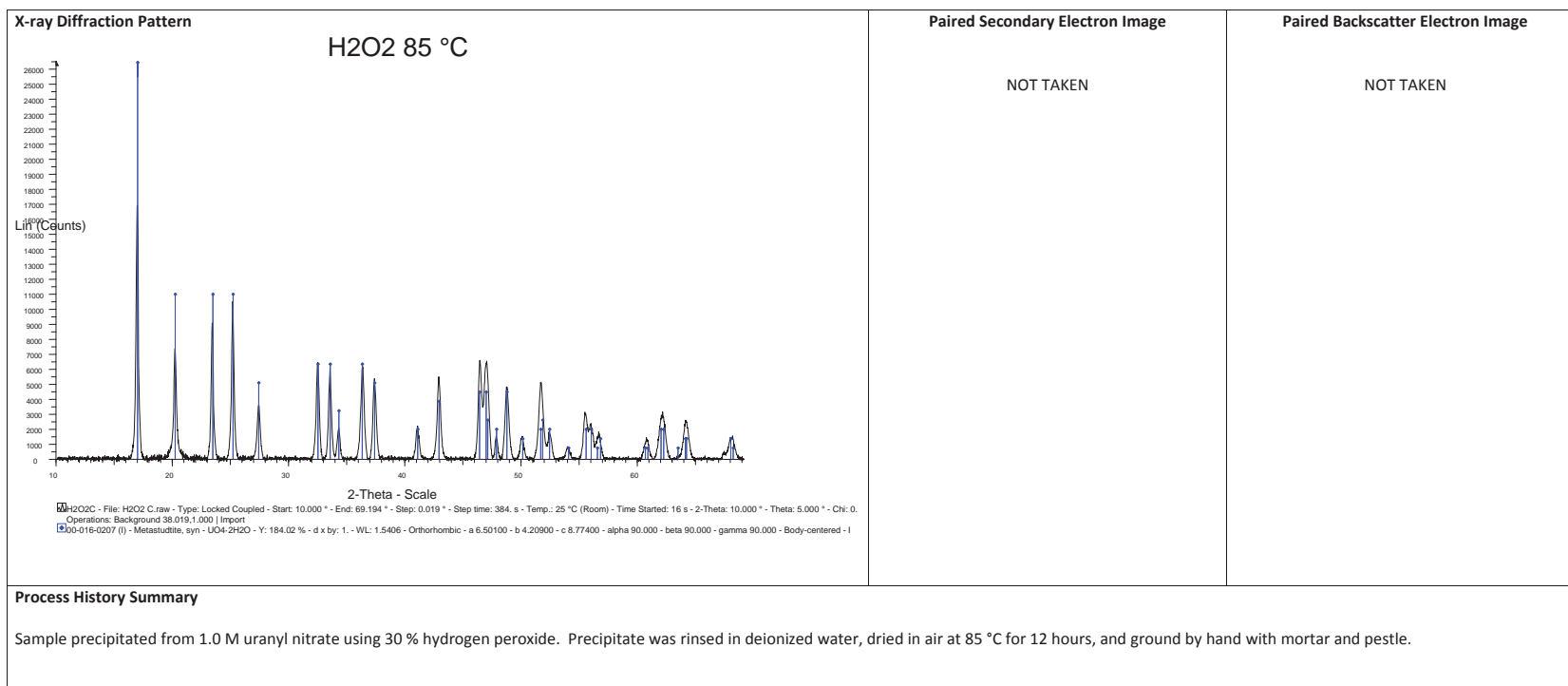


Morphology of uranium ore concentrate from the Ranger facility in the Northwest Territory, Australia

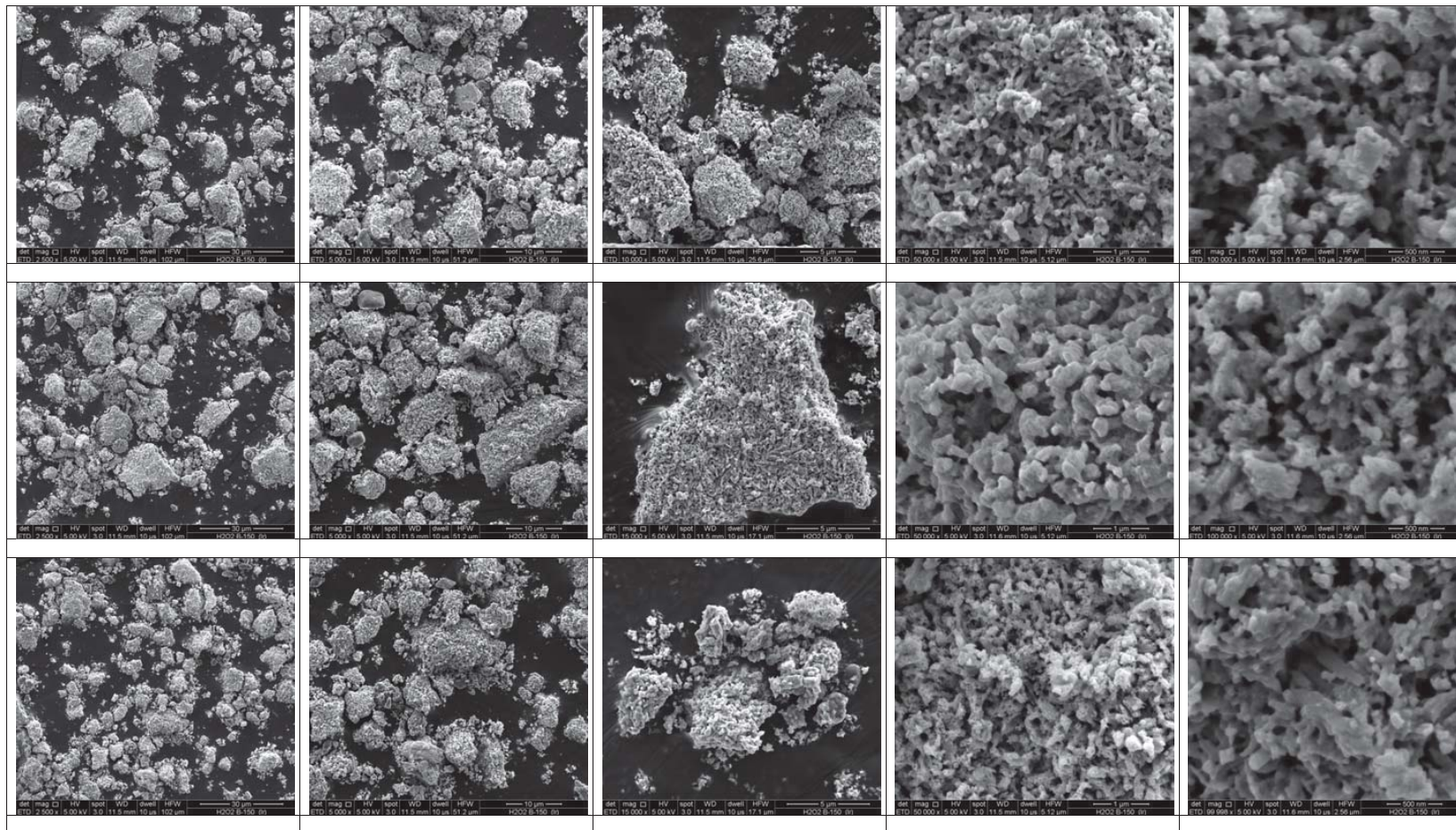


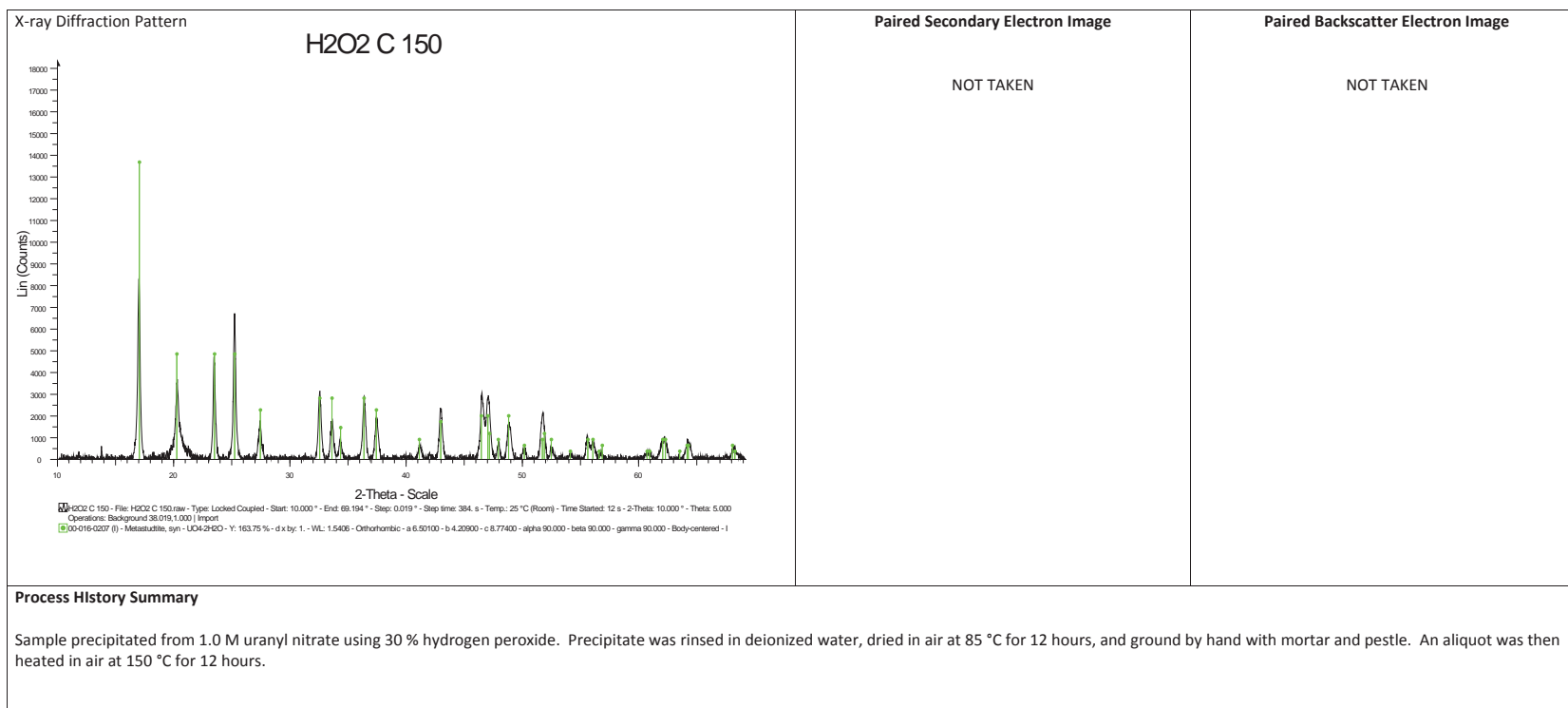
Morphology of the precipitate of uranyl nitrate and hydrogen peroxide heated to 85 °C



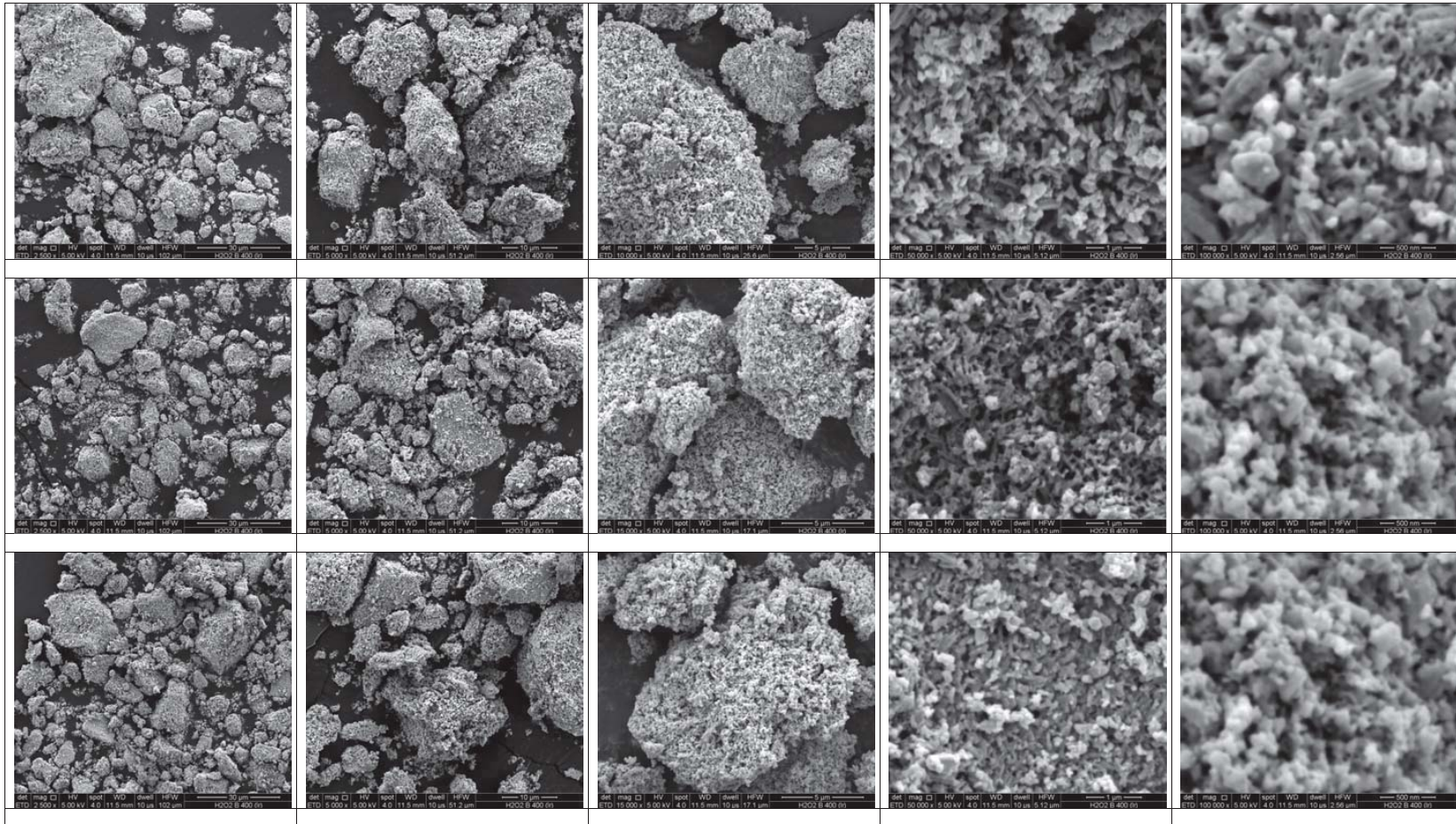


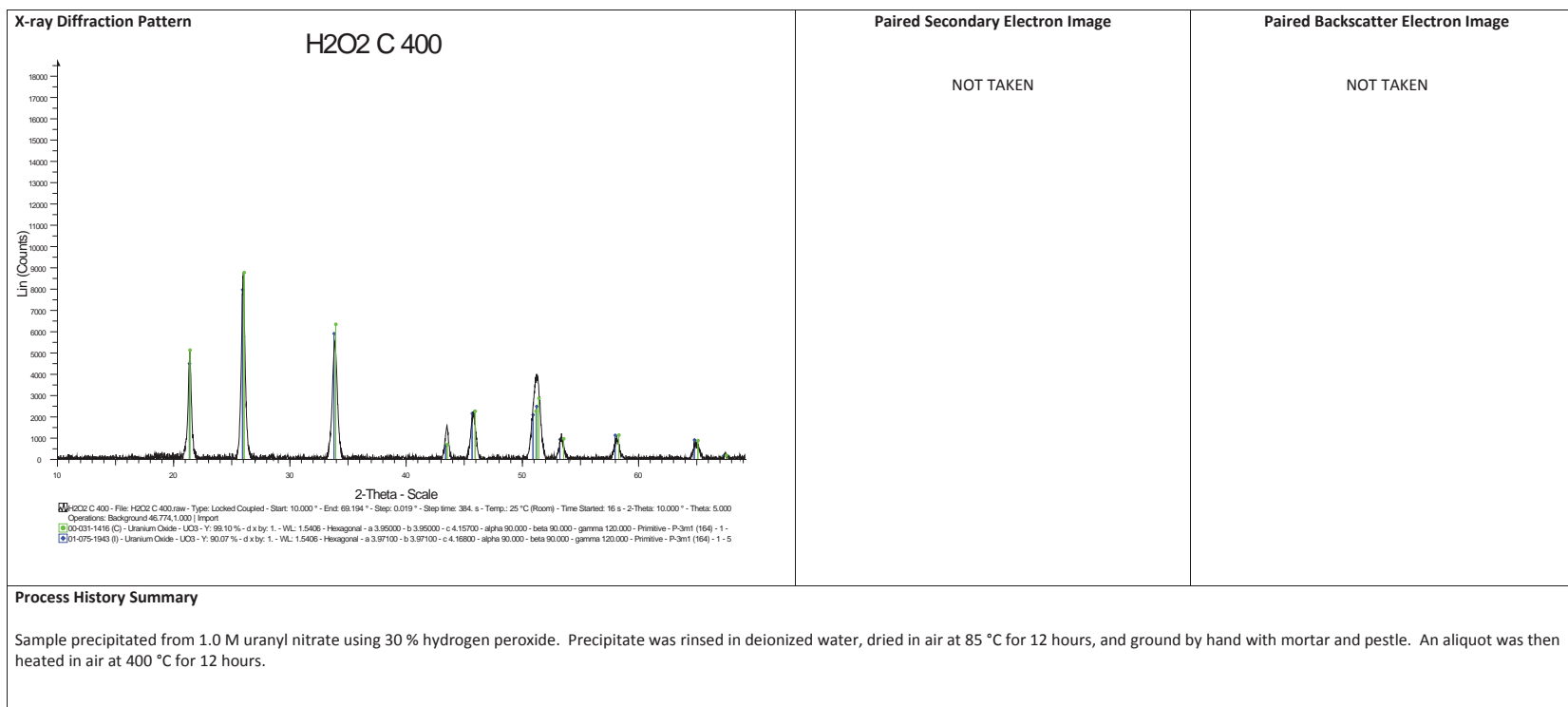
Morphology of the precipitate of uranyl nitrate and hydrogen peroxide heated to 150 °C



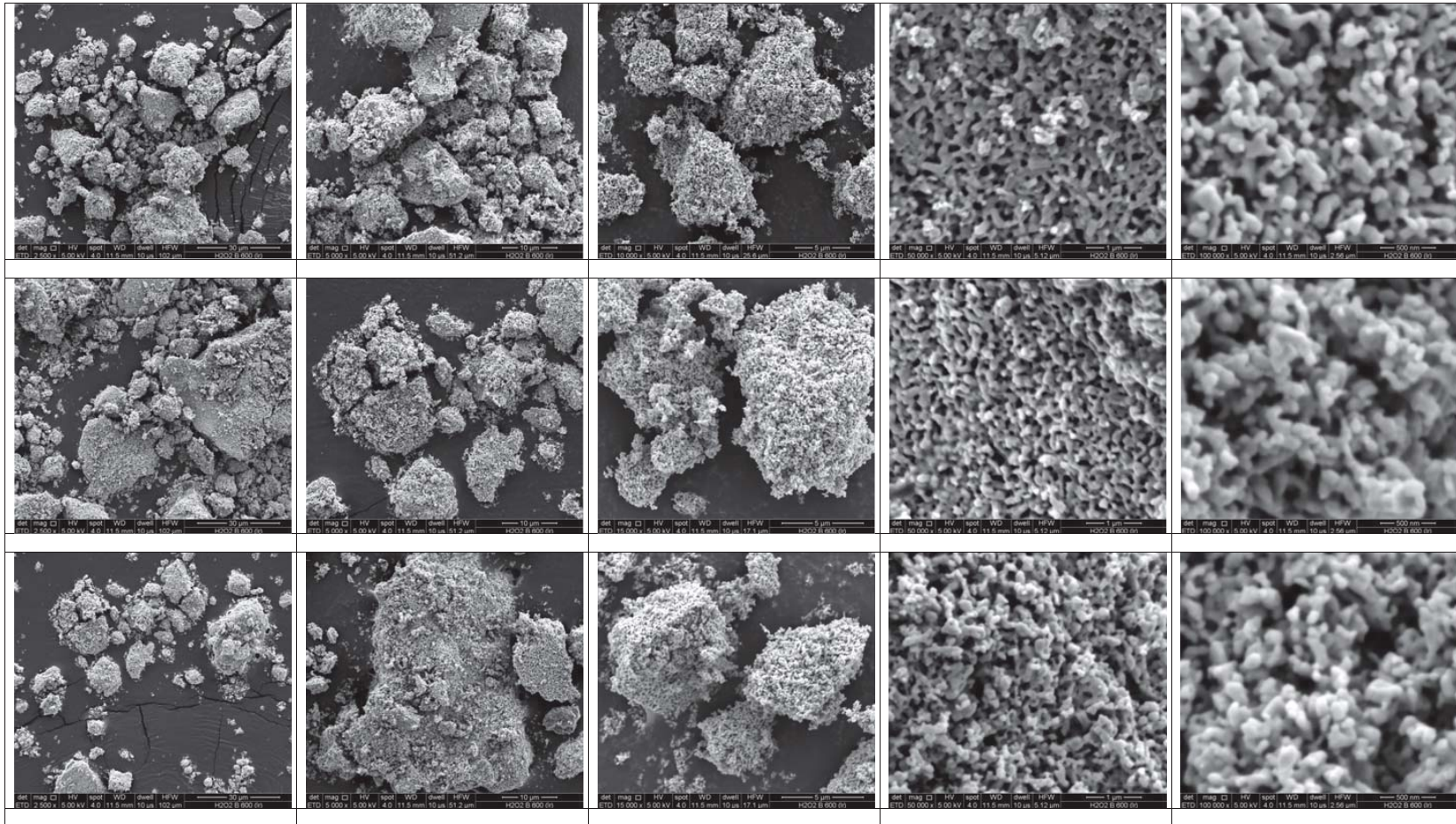


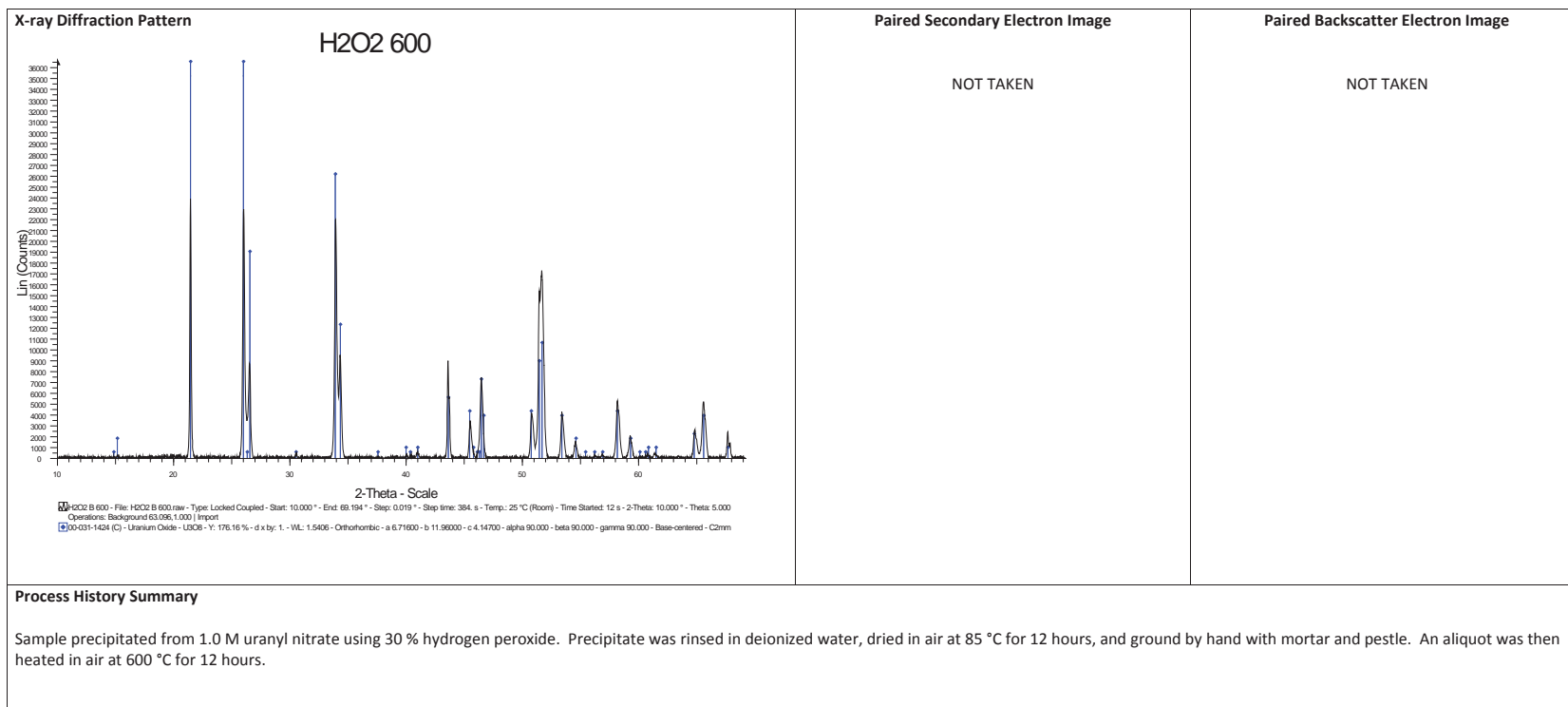
Morphology of the precipitate of uranyl nitrate and hydrogen peroxide heated to 400 °C



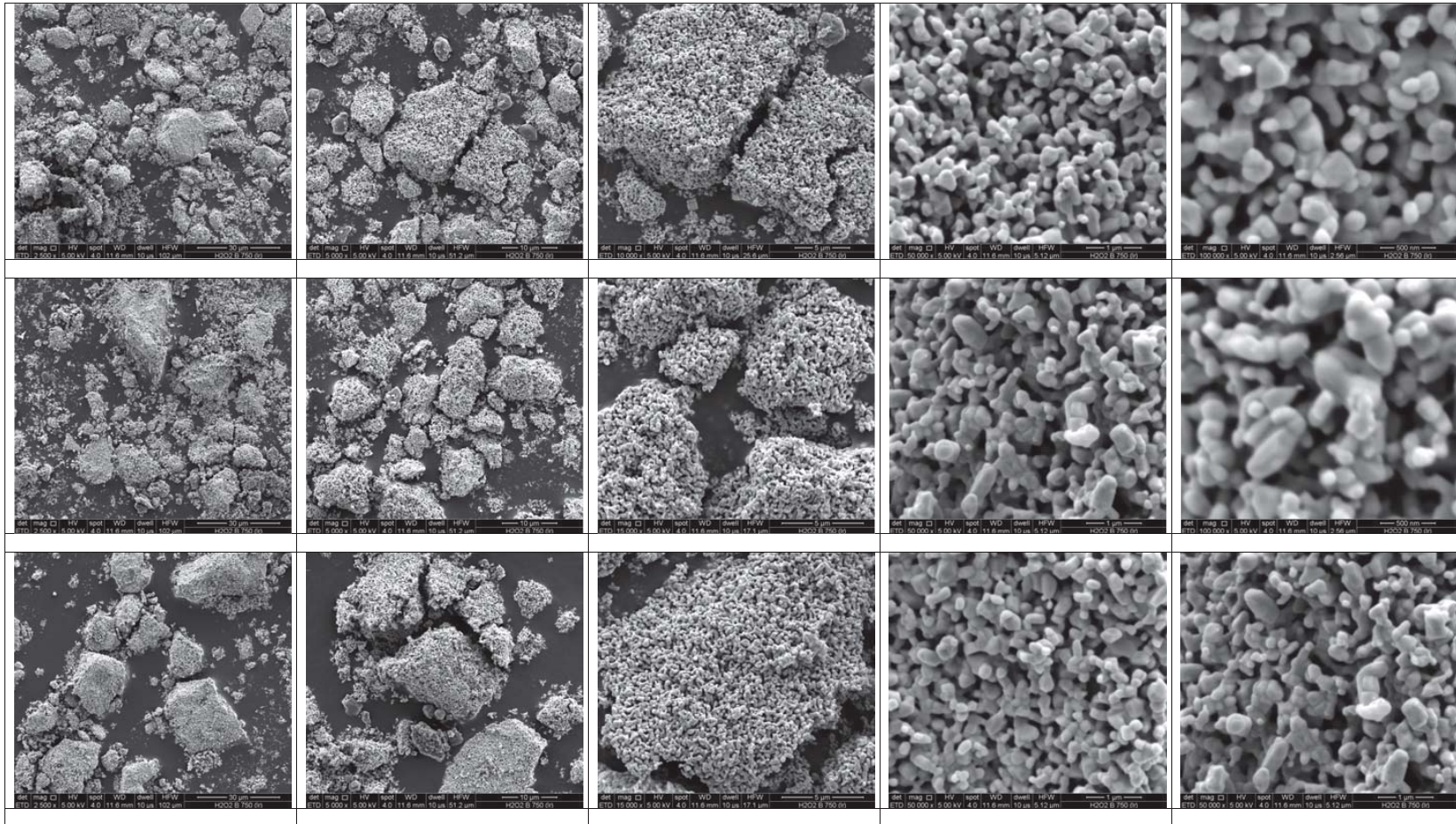


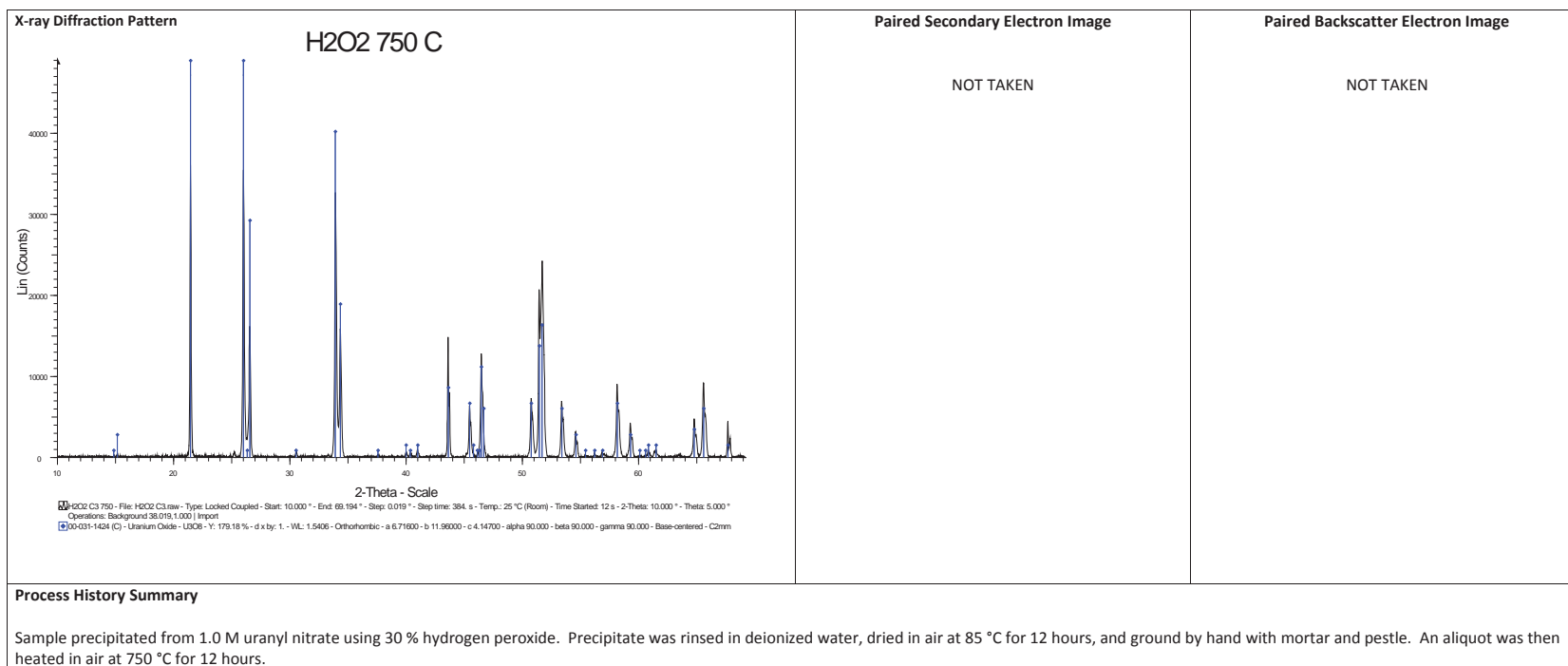
Morphology of the precipitate of uranyl nitrate and hydrogen peroxide heated to 600 °C



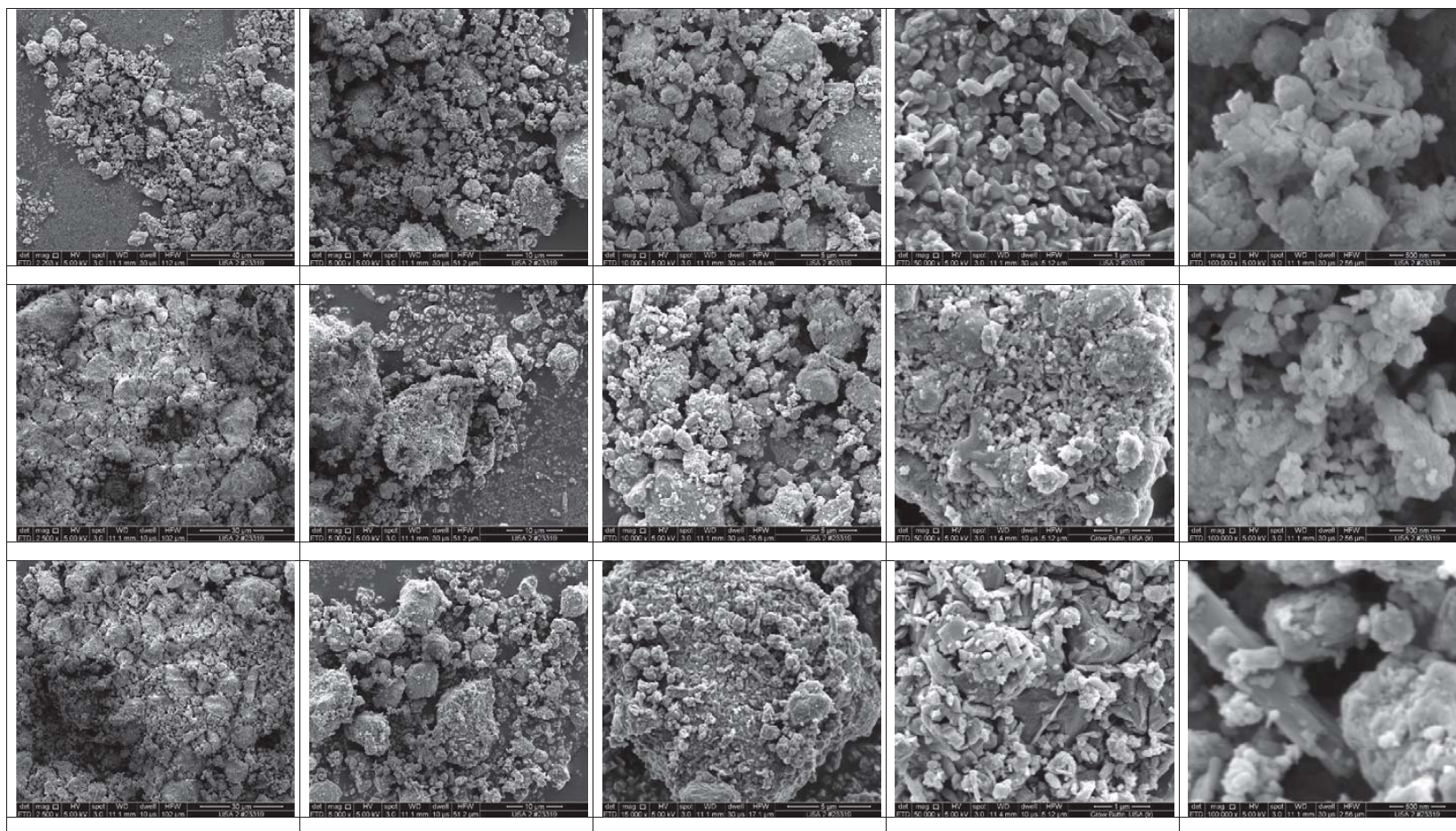


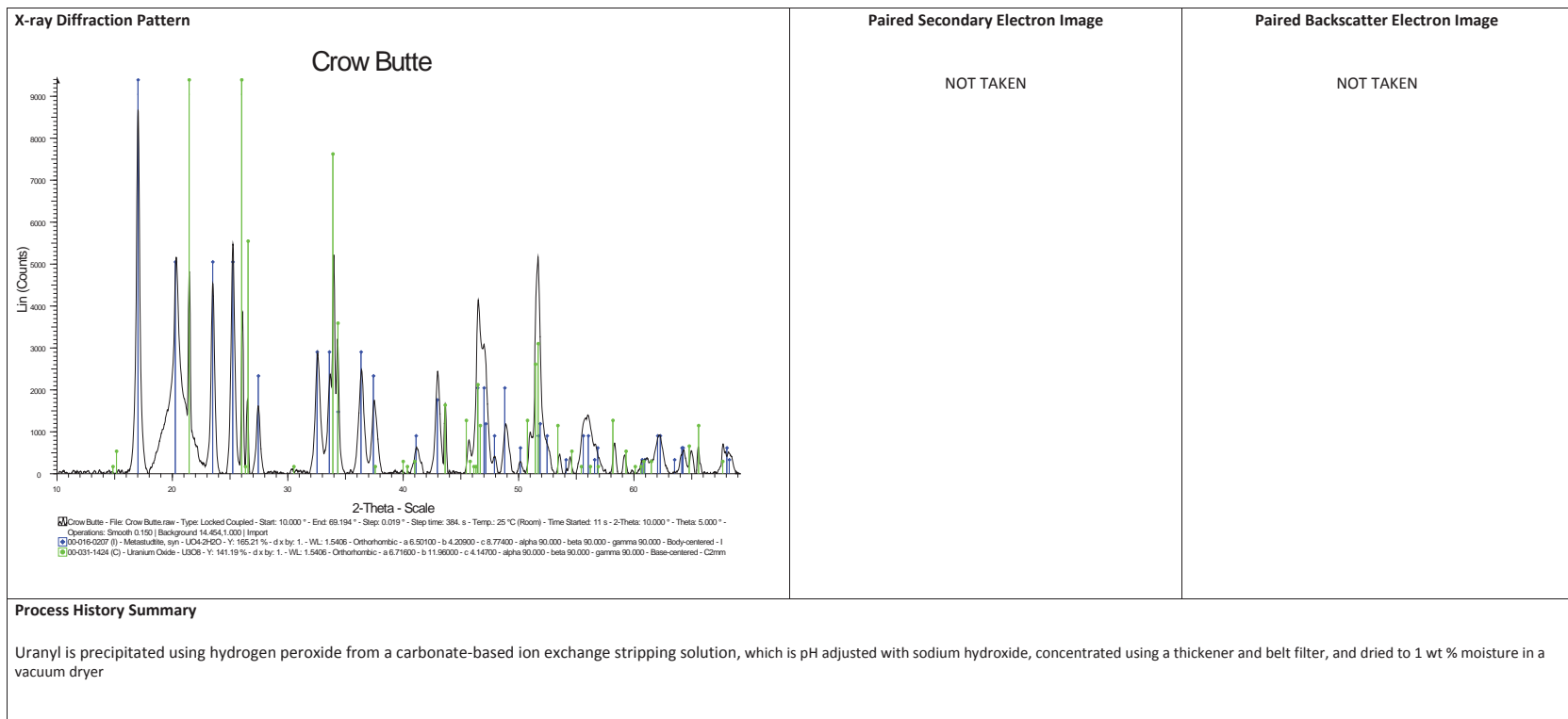
Morphology of the precipitate of uranyl nitrate and hydrogen peroxide heated to 750 °C



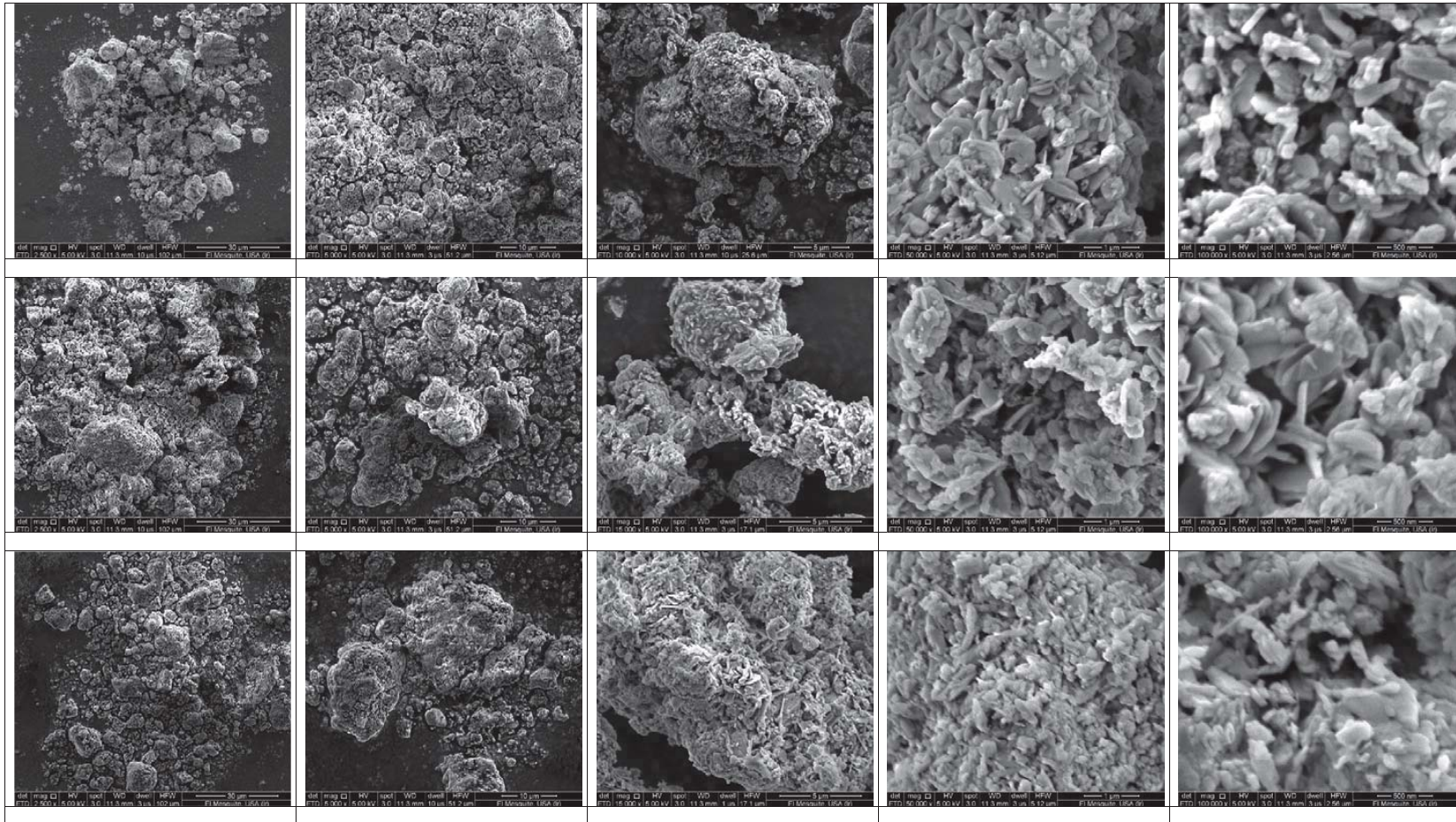


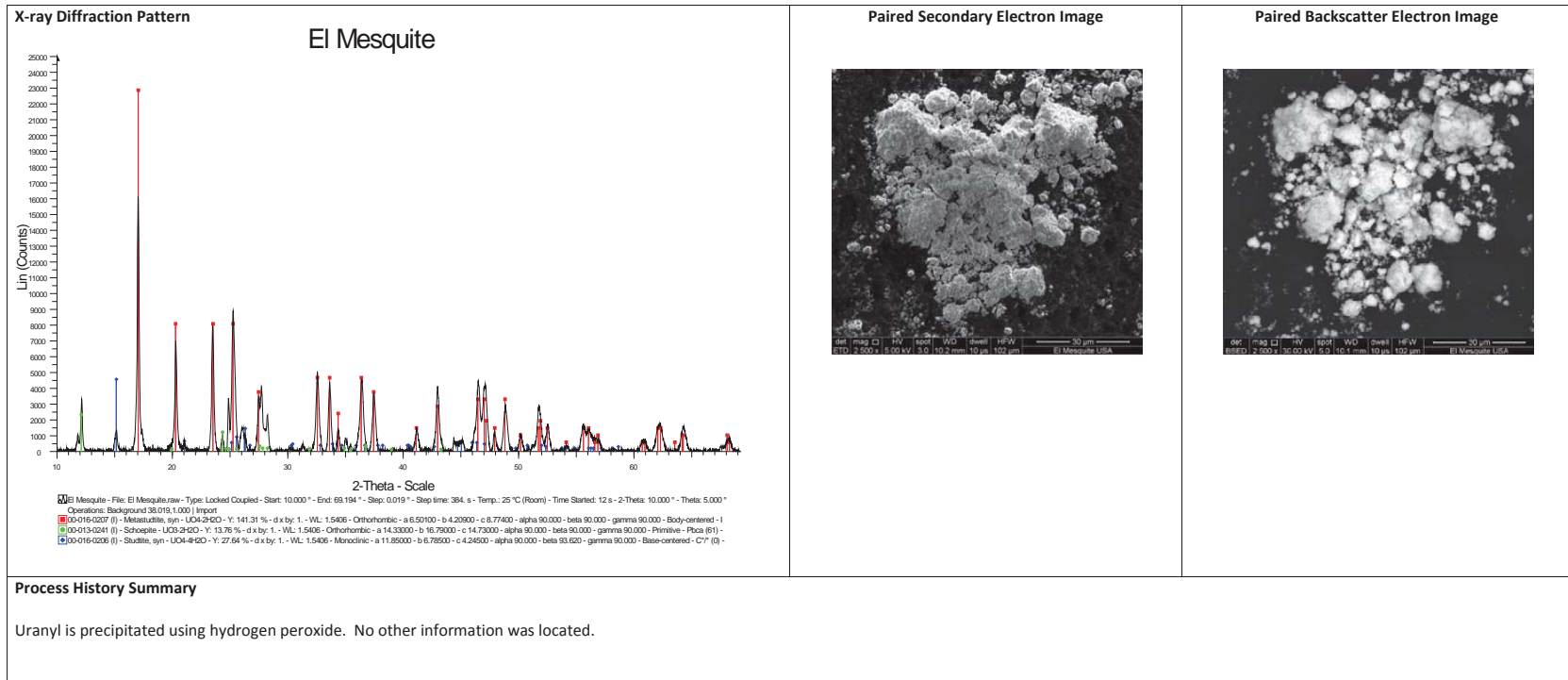
Morphology of uranium ore concentrate from Crowe Butte, USA



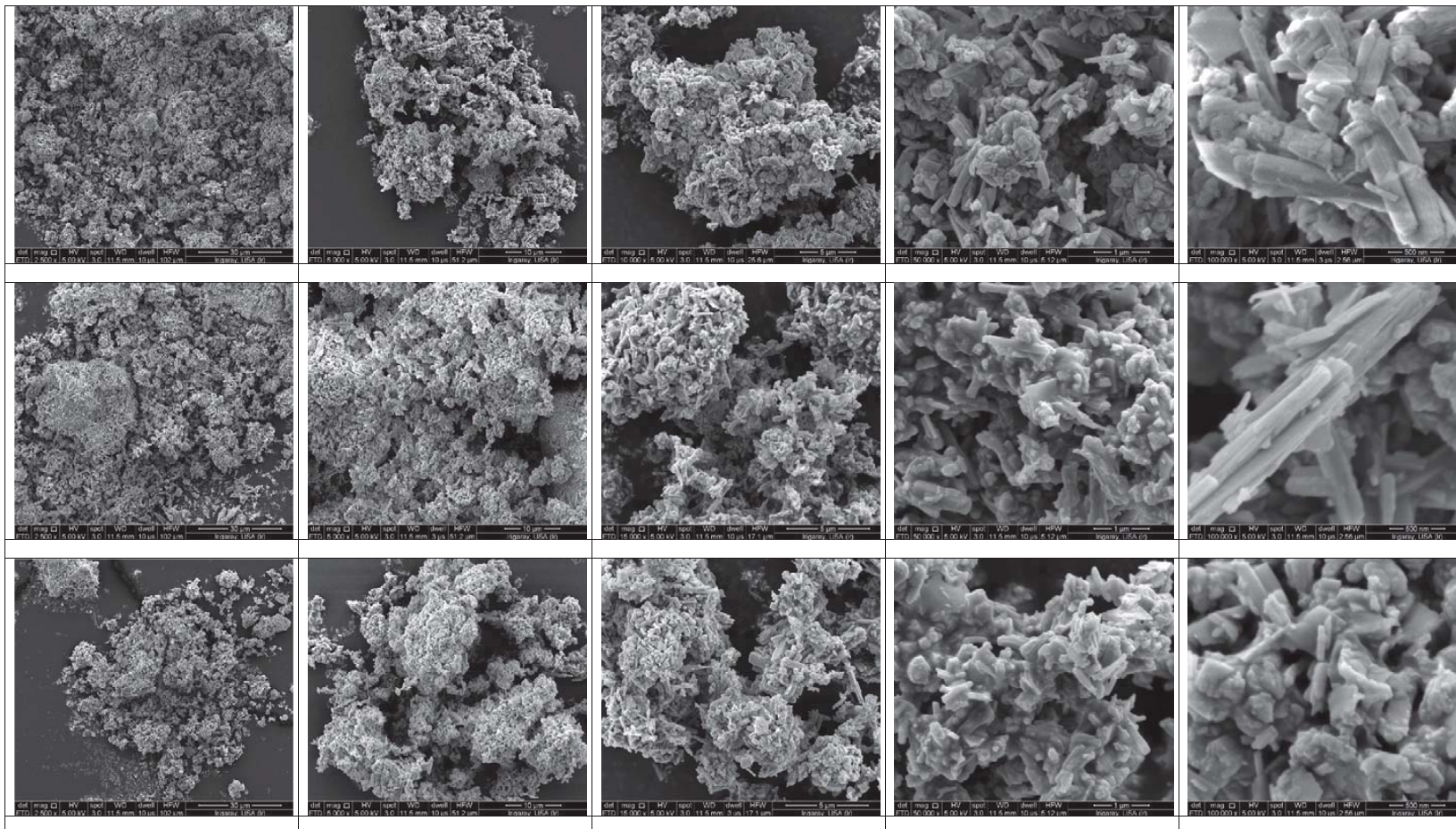


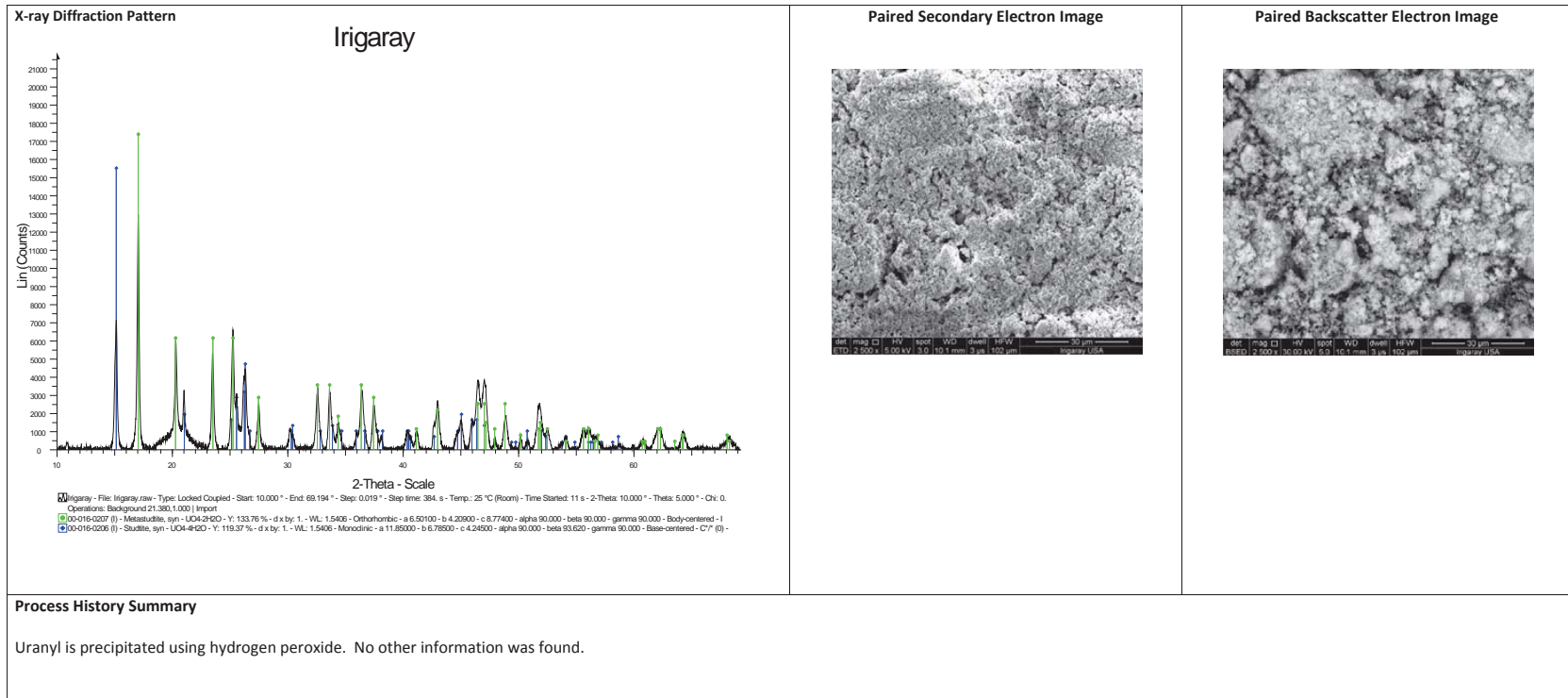
Morphology of uranium ore concentrate from the El Mesquite facility in Duval County, Texas, USA



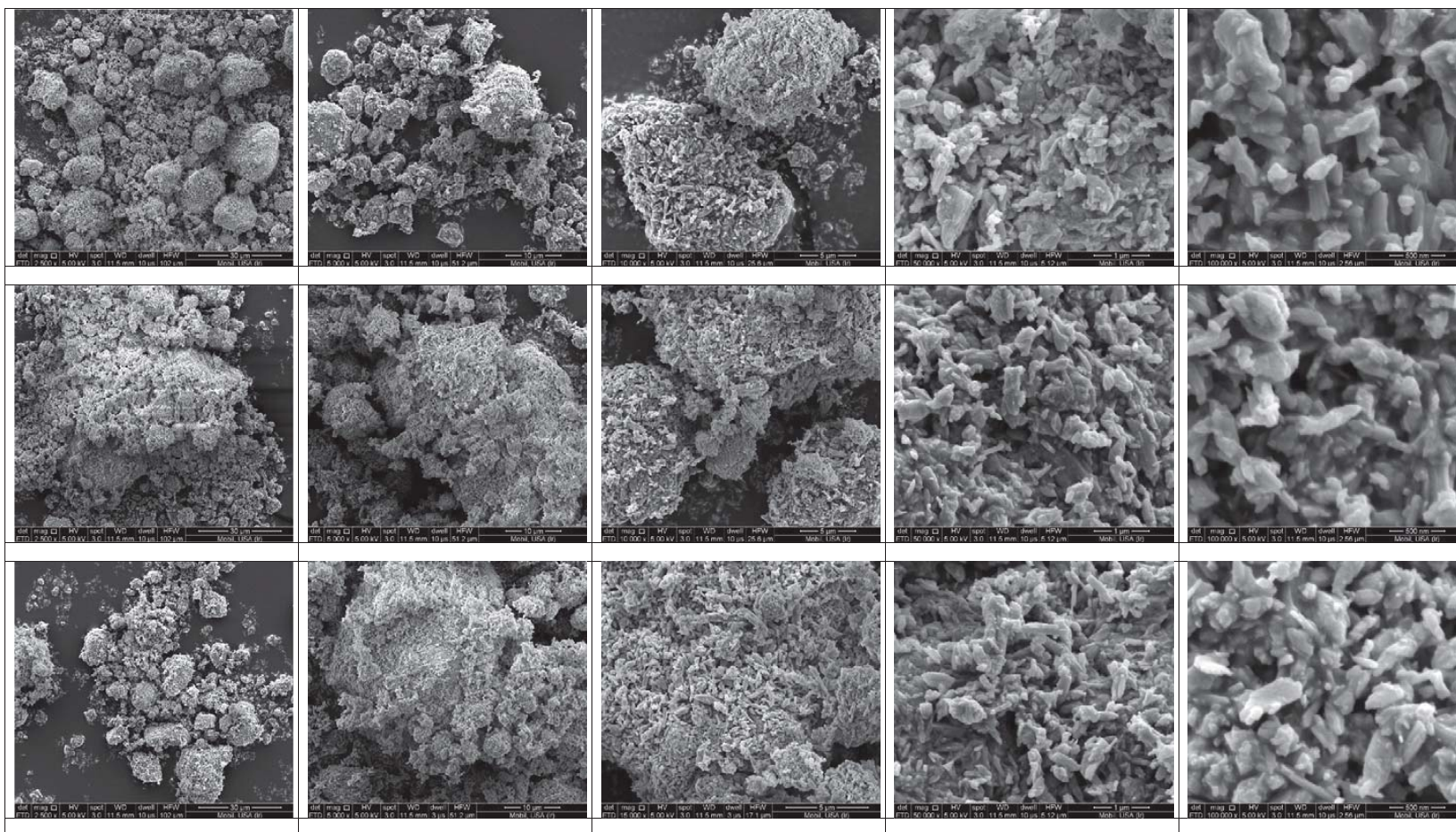


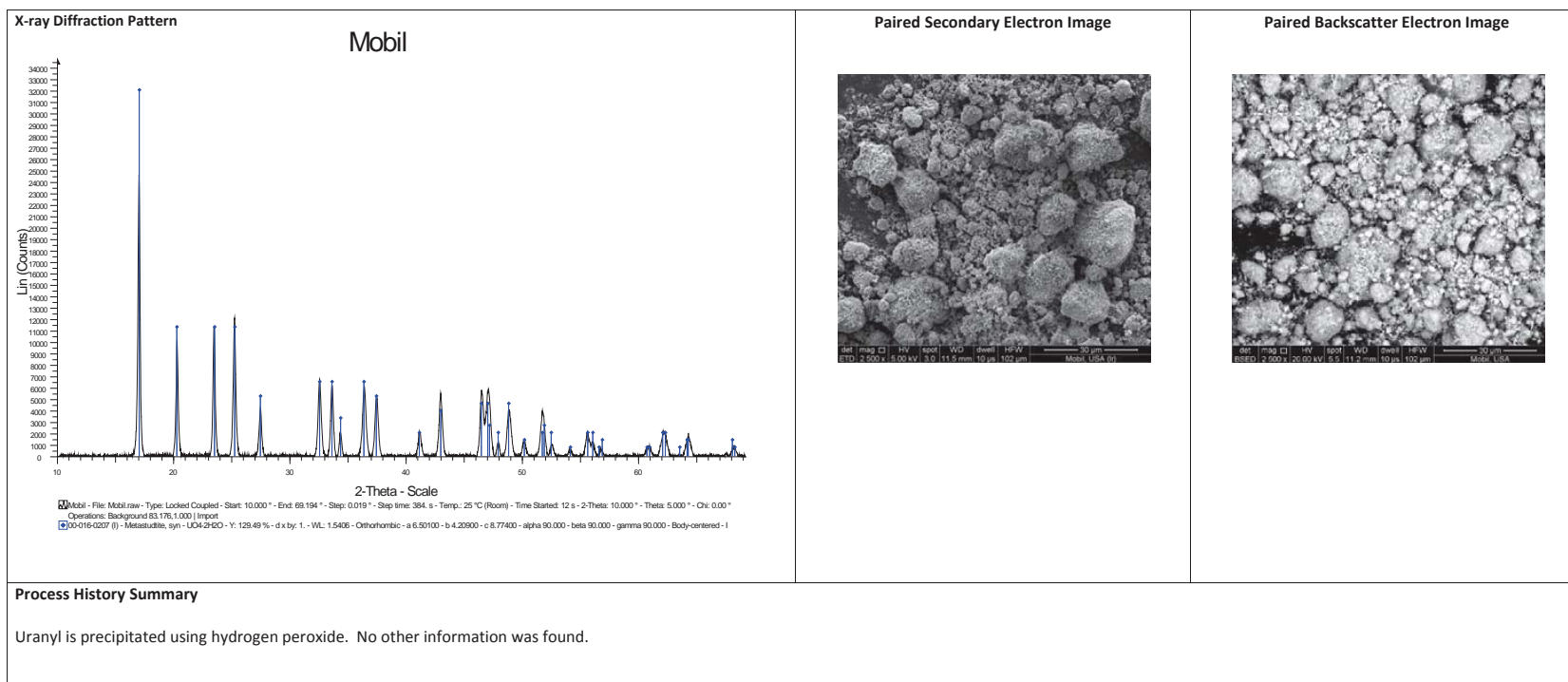
Morphology of uranium ore concentrate from the Irigaray facility in Johnson County, Wyoming, USA



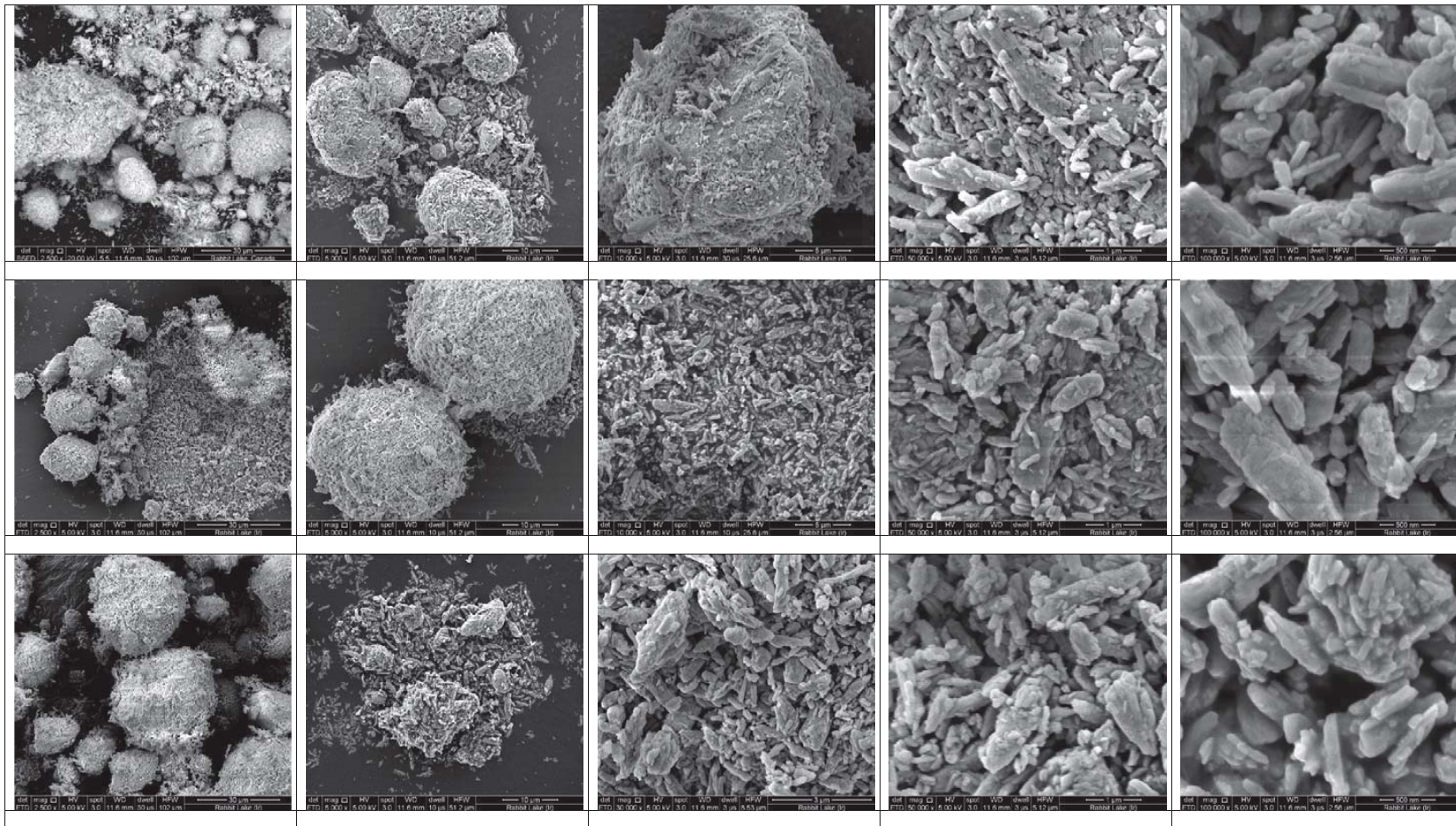


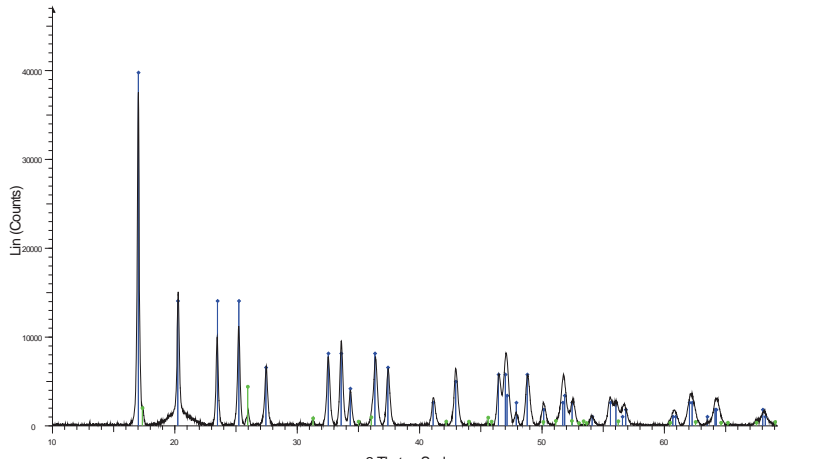

Morphology of uranium ore concentrate from Mobil, USA



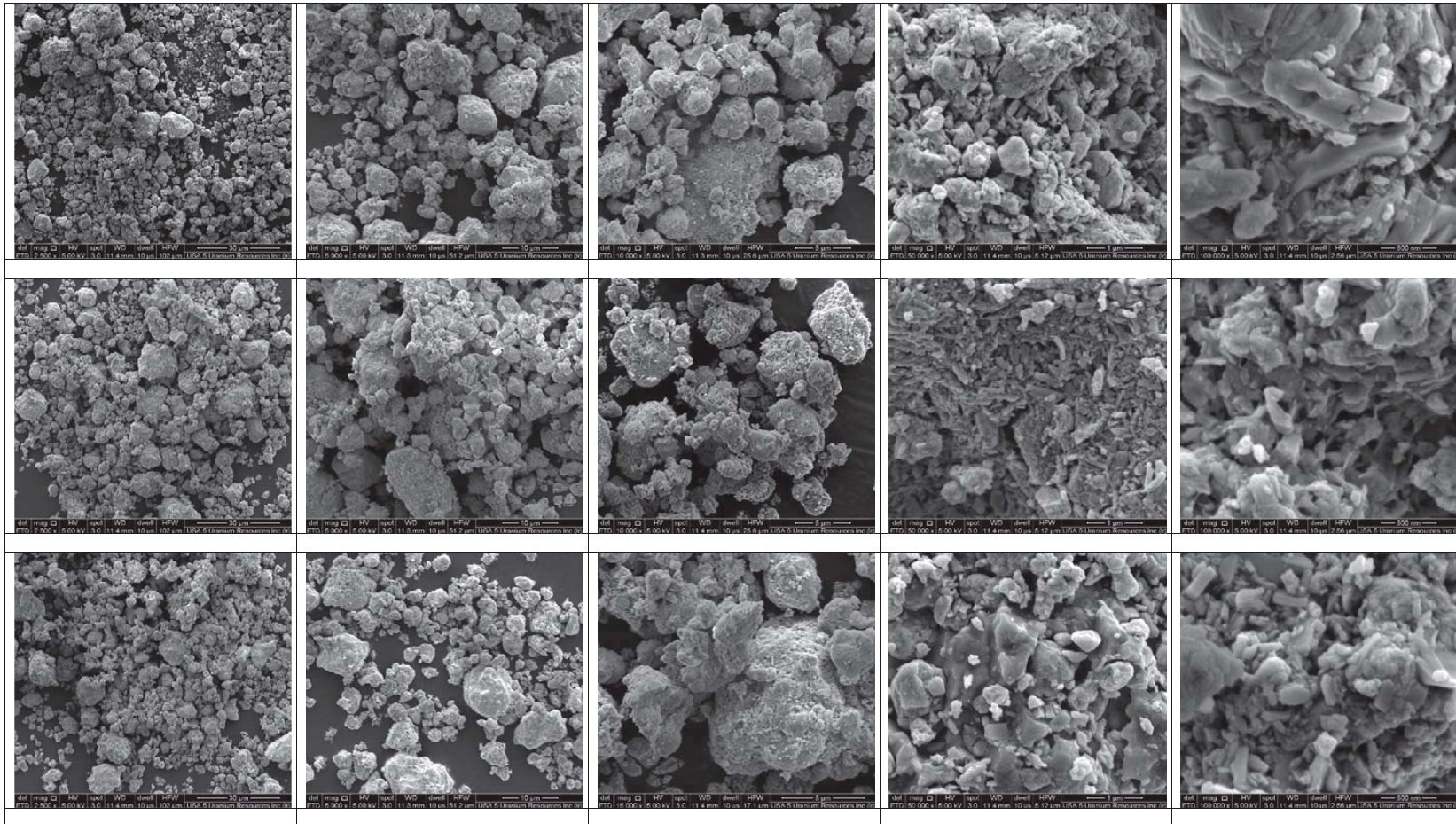


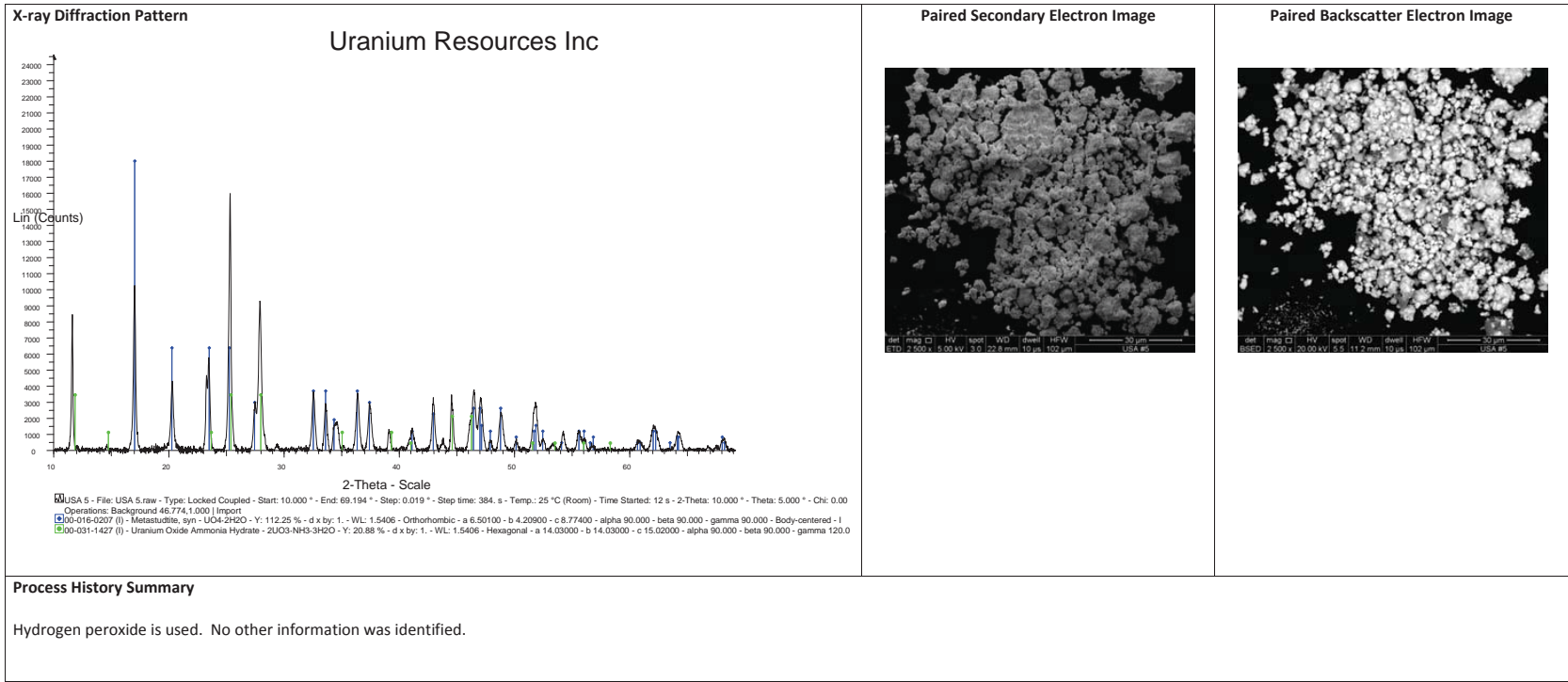
Morphology of uranium ore concentrate from the Rabbit Lake facility in Saskatchewan, Canada



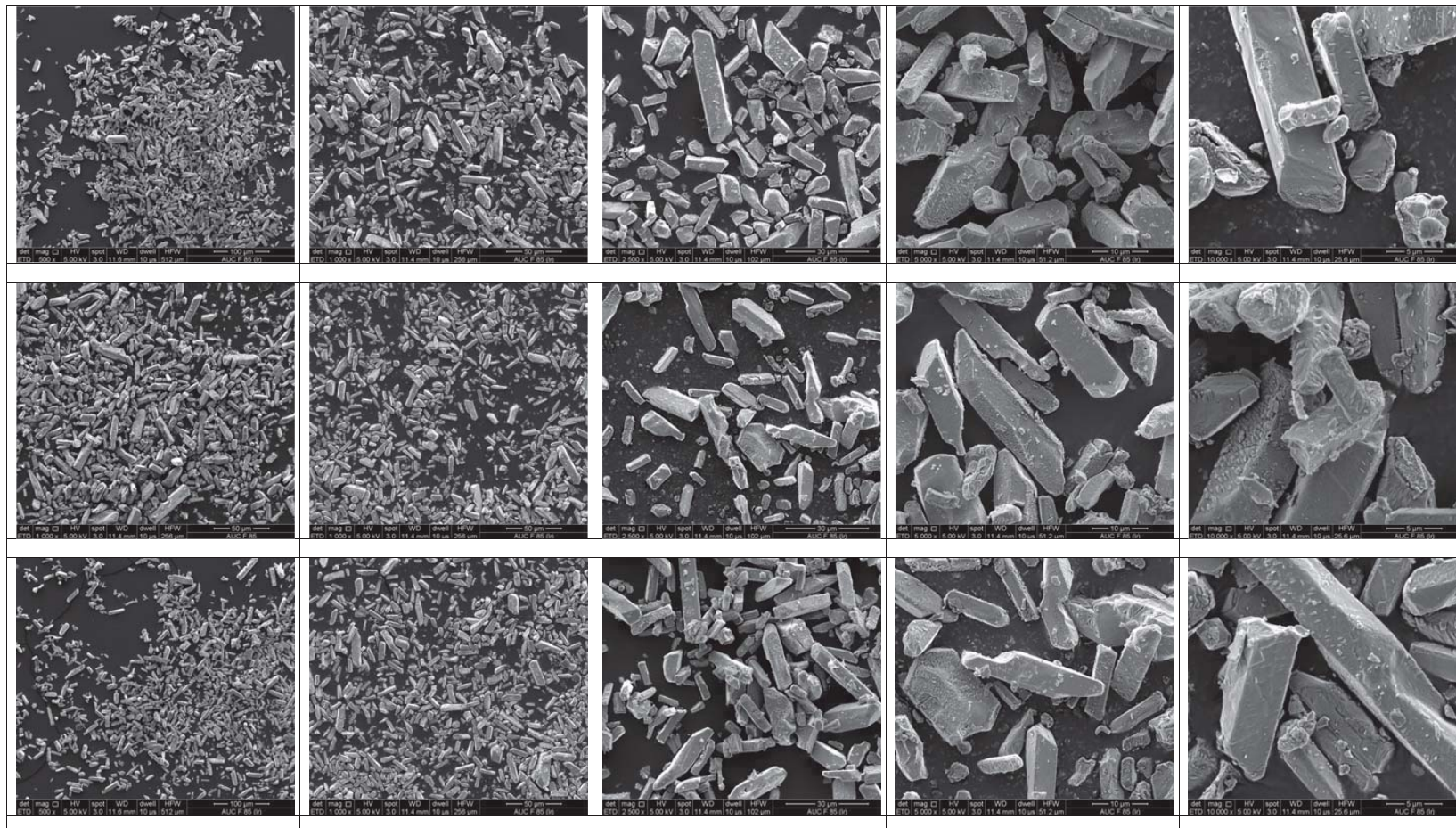
<p>X-ray diffraction pattern</p> <p style="text-align: center;">Rabbit Lake</p>  <p><small>Rabbit Lake - File: Rabbit Lake.raw - Type: Locked Coupled - Start: 10.000 ° - End: 69.194 ° - Step: 0.019 ° - Step time: 384. s - Temp: 25 °C (Room) - Time Started: 12 s - 2-Theta: 10.000 ° - Theta: 5.000 ° Operations: Background 14.454(1.000) Import 00-016-0207 (f) - Misantubite, syn - LiAl₂Si₂O₇ - Y: 105.57 % - d x by: 1. - VL: 1.5406 - Orthorhombic - a 6.50100 - b 4.20900 - c 8.77400 - alpha 90.000 - beta 90.000 - gamma 90.000 - Body-centered - I 00-053-0877 (f) - Uranium Oxide Hydrate - UO₃·0.8H₂O - Y: 11.02 % - d x by: 1. - VL: 1.5406 - Orthorhombic - a 10.23800 - b 6.89860 - c 4.28320 - alpha 90.000 - beta 90.000 - gamma 90.000 - Face-cent</small></p>	<p>Paired Secondary Electron Image</p> <p style="text-align: center;">NOT TAKEN</p>	<p>Paired Backscatter Electron Image</p> 
<p>Process history summary</p> <p>Uranyl is precipitated from a sulfate-based solvent extraction stripping solution using hydrogen peroxide and dried at 110 °C</p>	<p>Energy Dispersive Spectroscopy</p> <p style="text-align: center;">NOT TAKEN</p>	

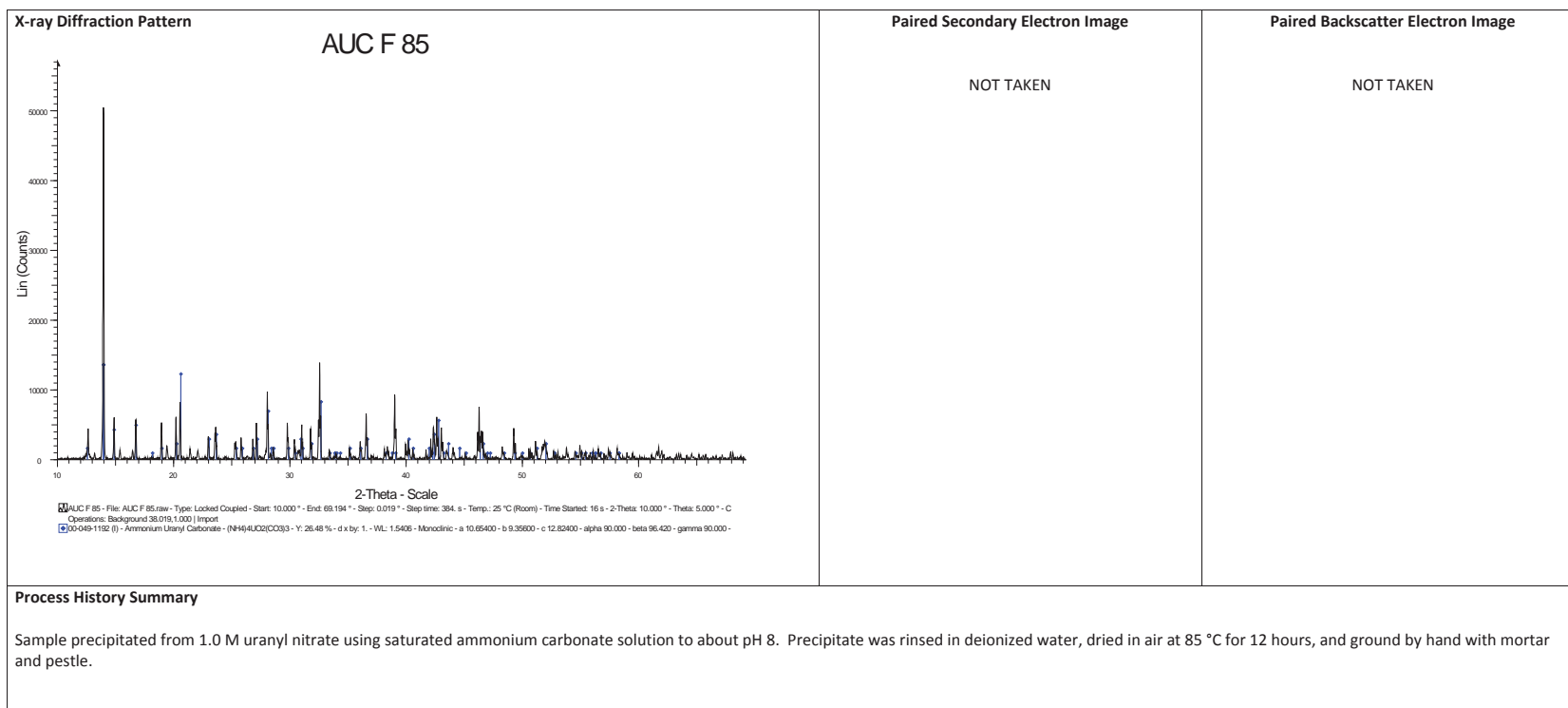
Morphology of uranium ore concentrate from the Uranium Resources Inc. facility in Duval County Texas, USA



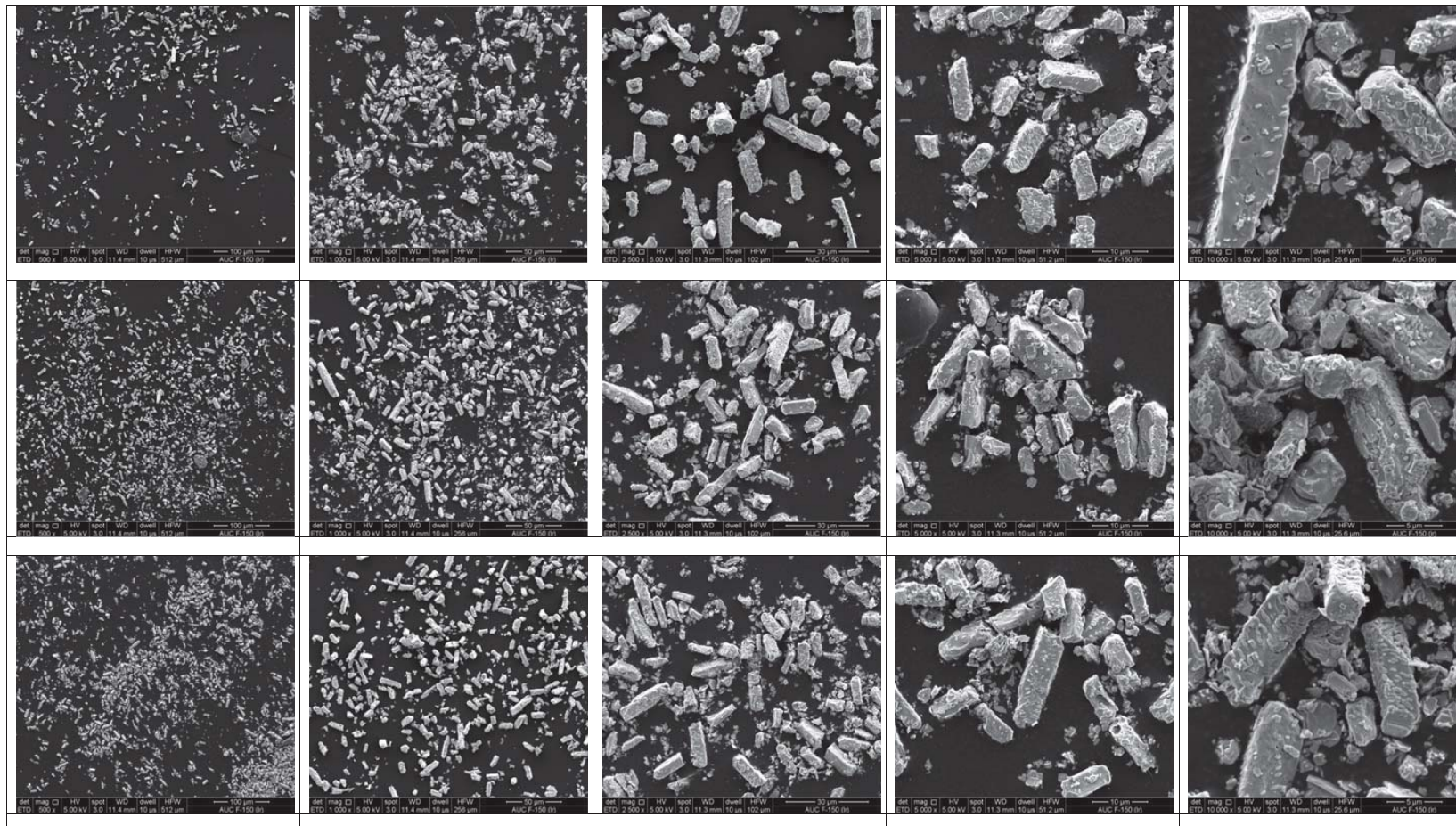


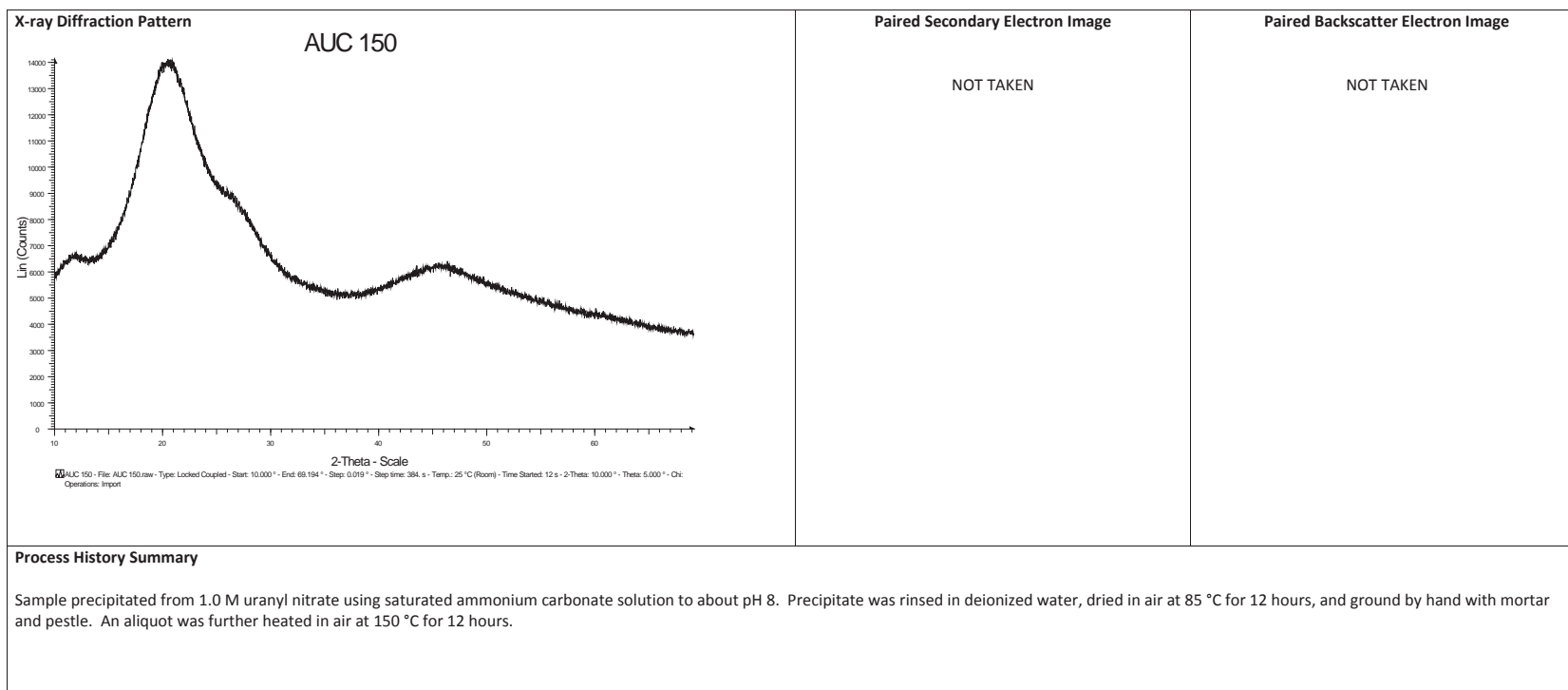
Morphology of the precipitate of uranyl nitrate and ammonium carbonate heated to 85 °C



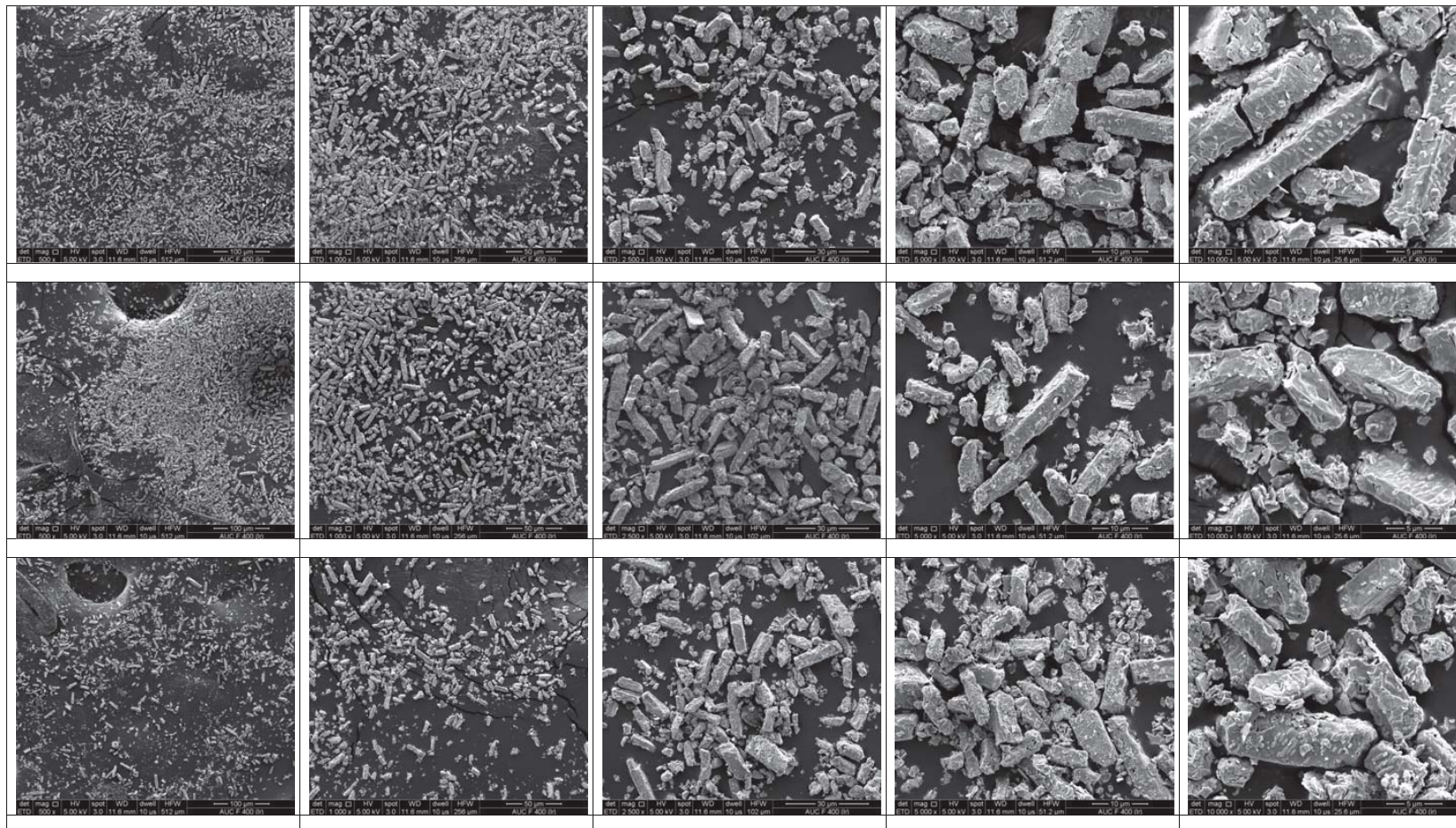


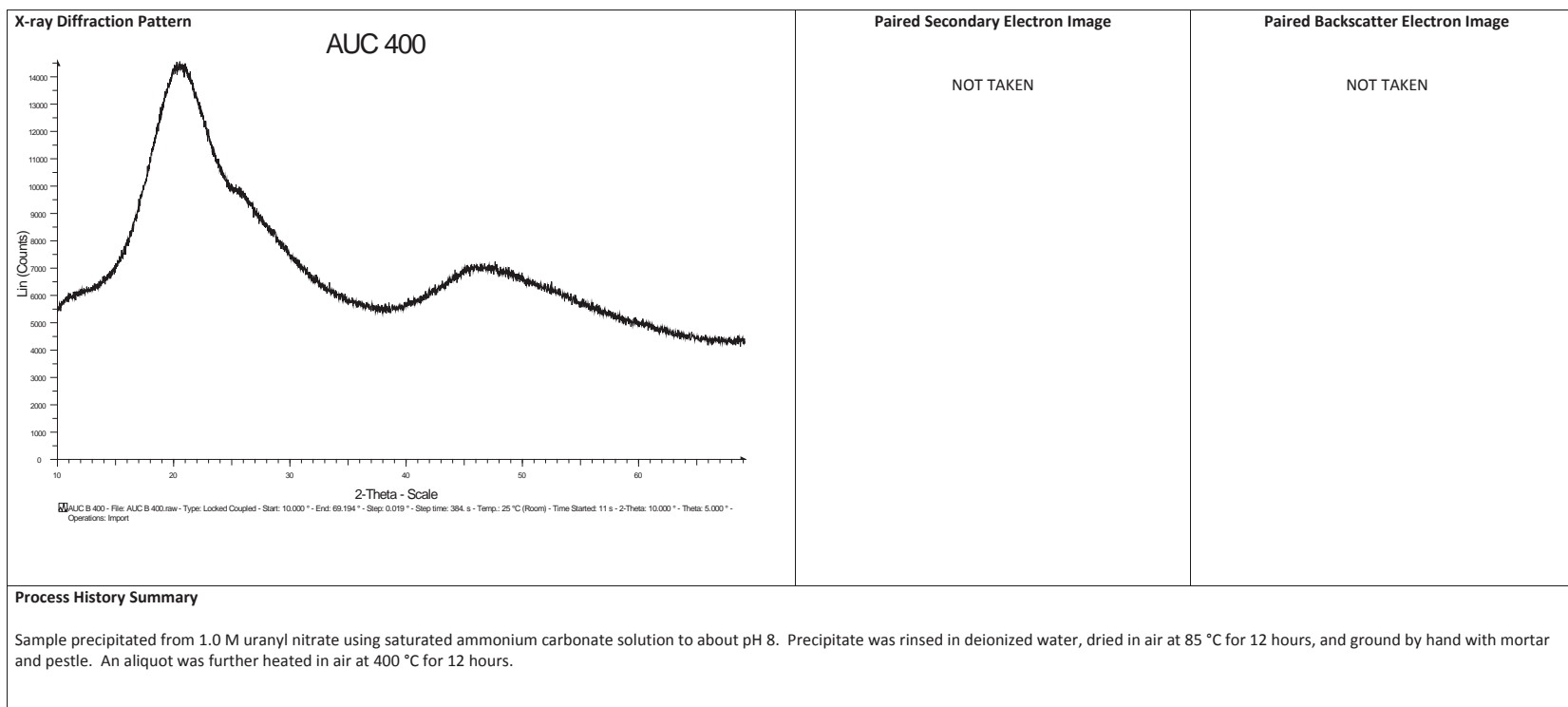
Morphology of the precipitate of uranyl nitrate and ammonium carbonate heated to 150 °C



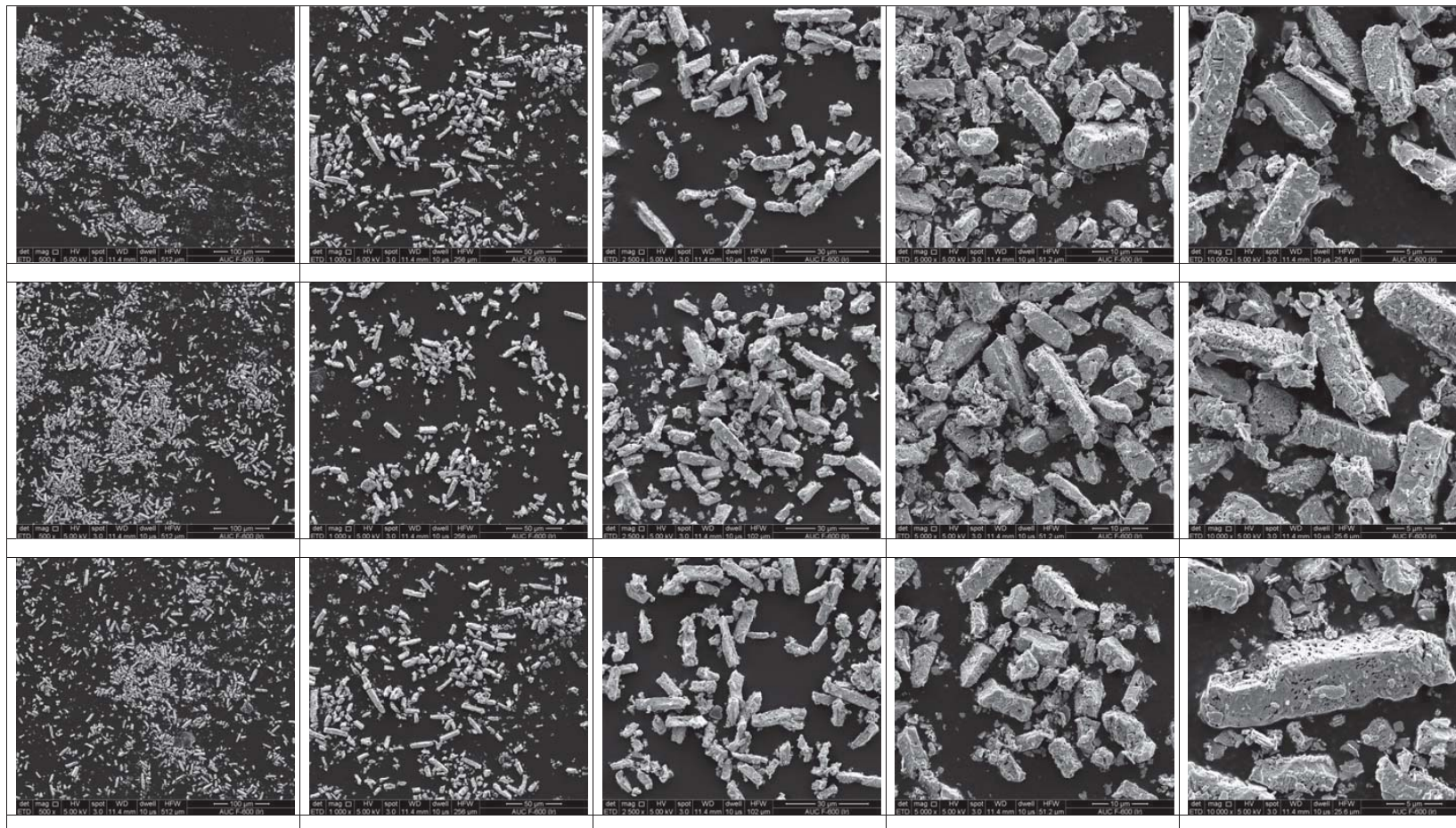


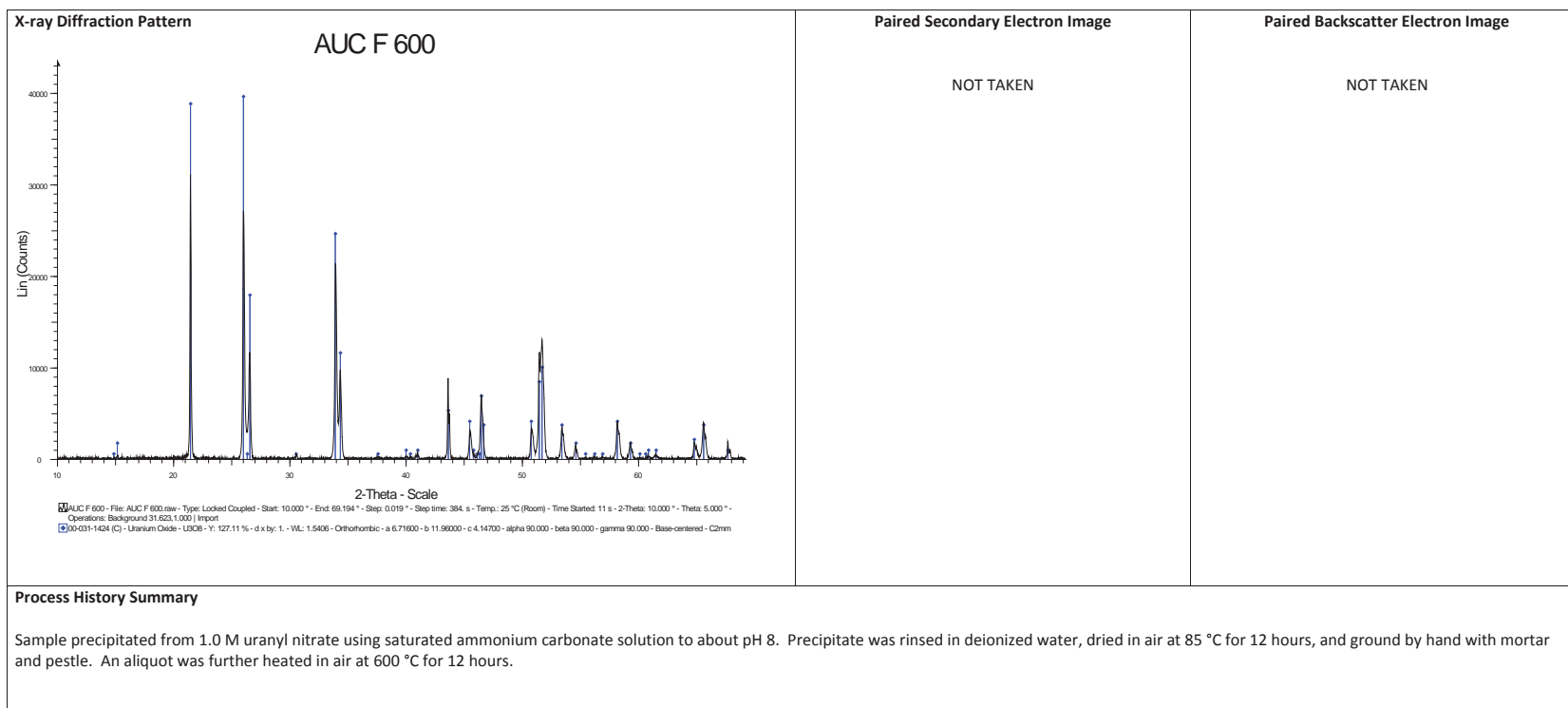
Morphology of the precipitate of uranyl nitrate and ammonium carbonate heated to 400 °C



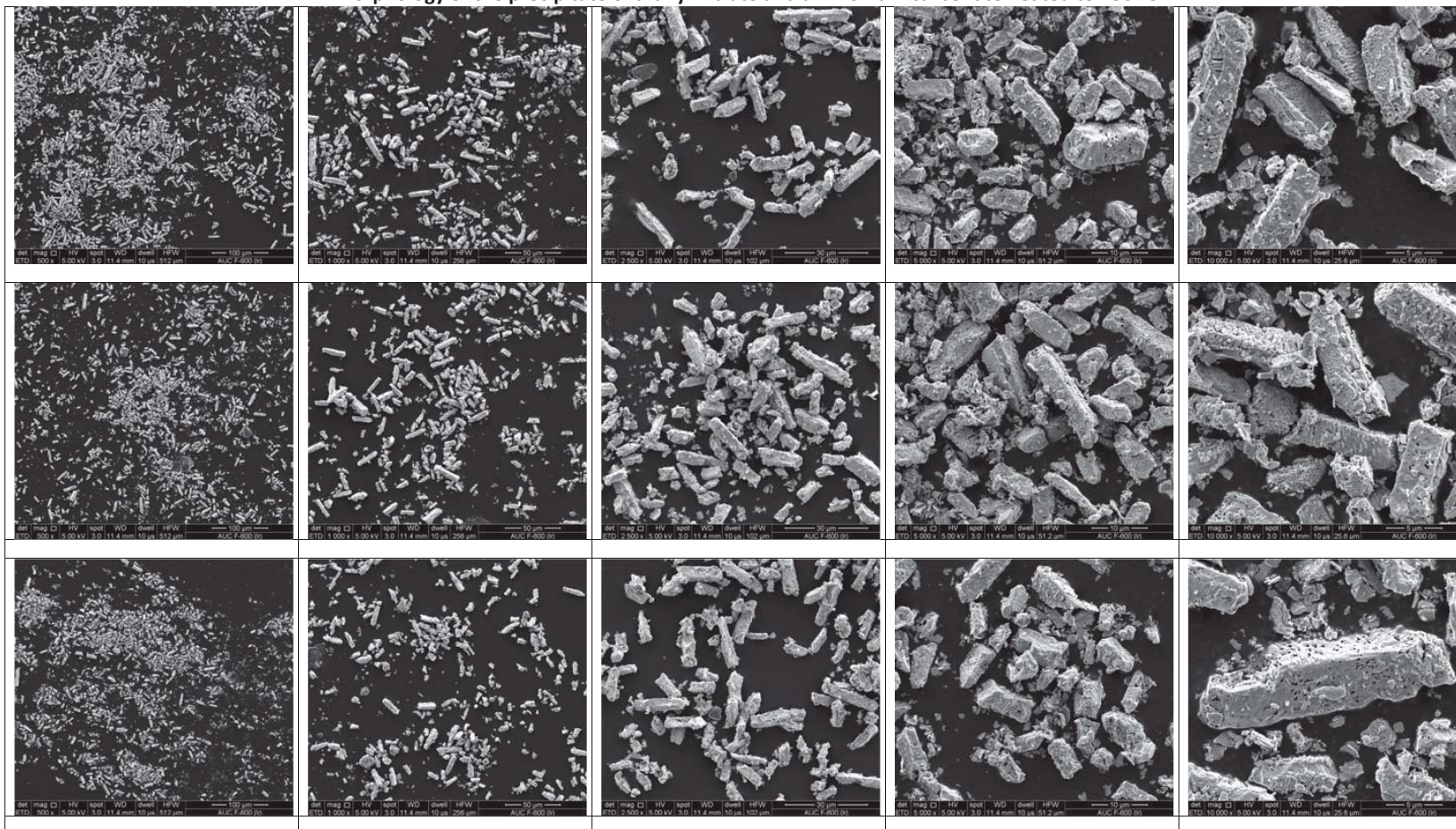


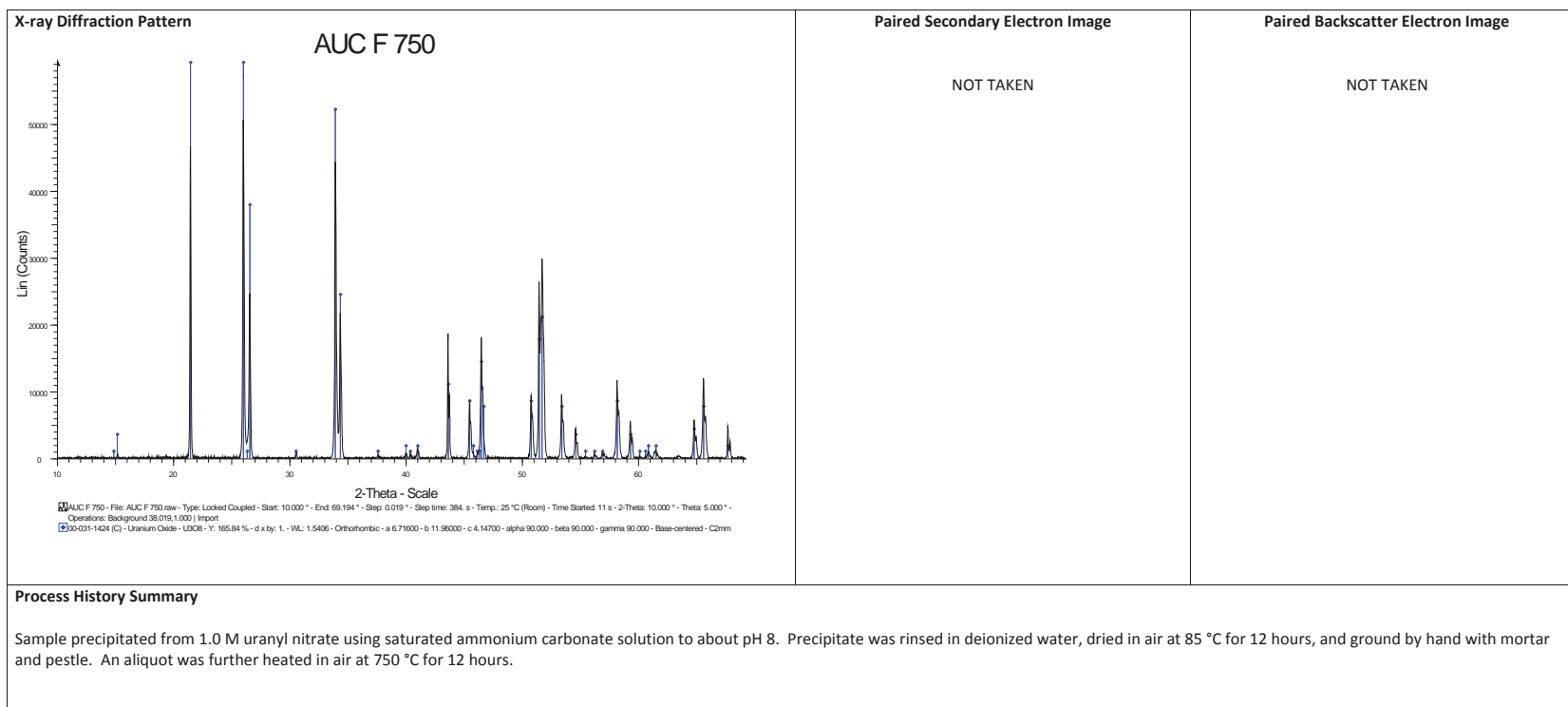
Morphology of the precipitate of uranyl nitrate and ammonium carbonate heated to 600 °C



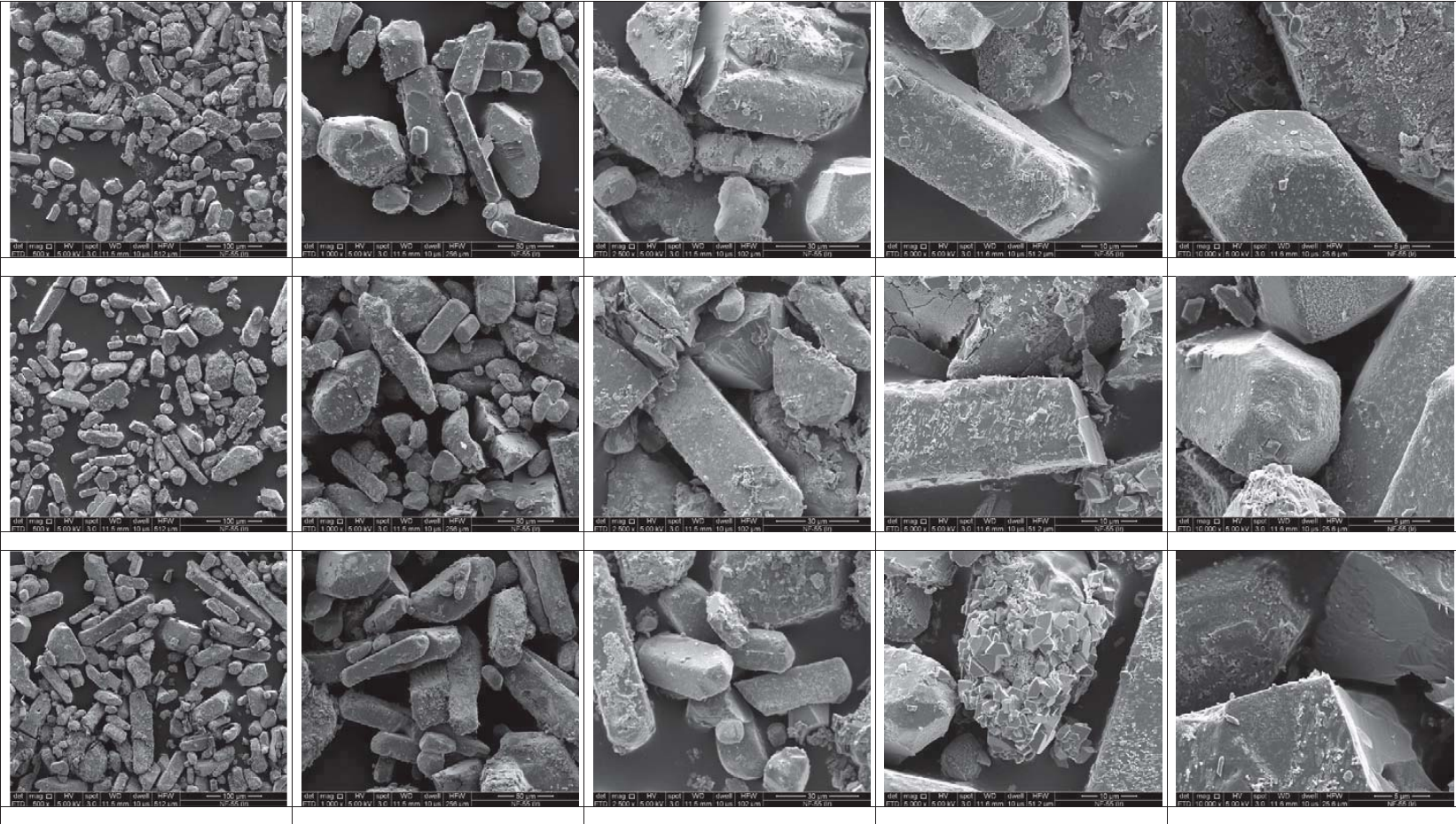


Morphology of the precipitate of uranyl nitrate and ammonium carbonate heated to 750 °C



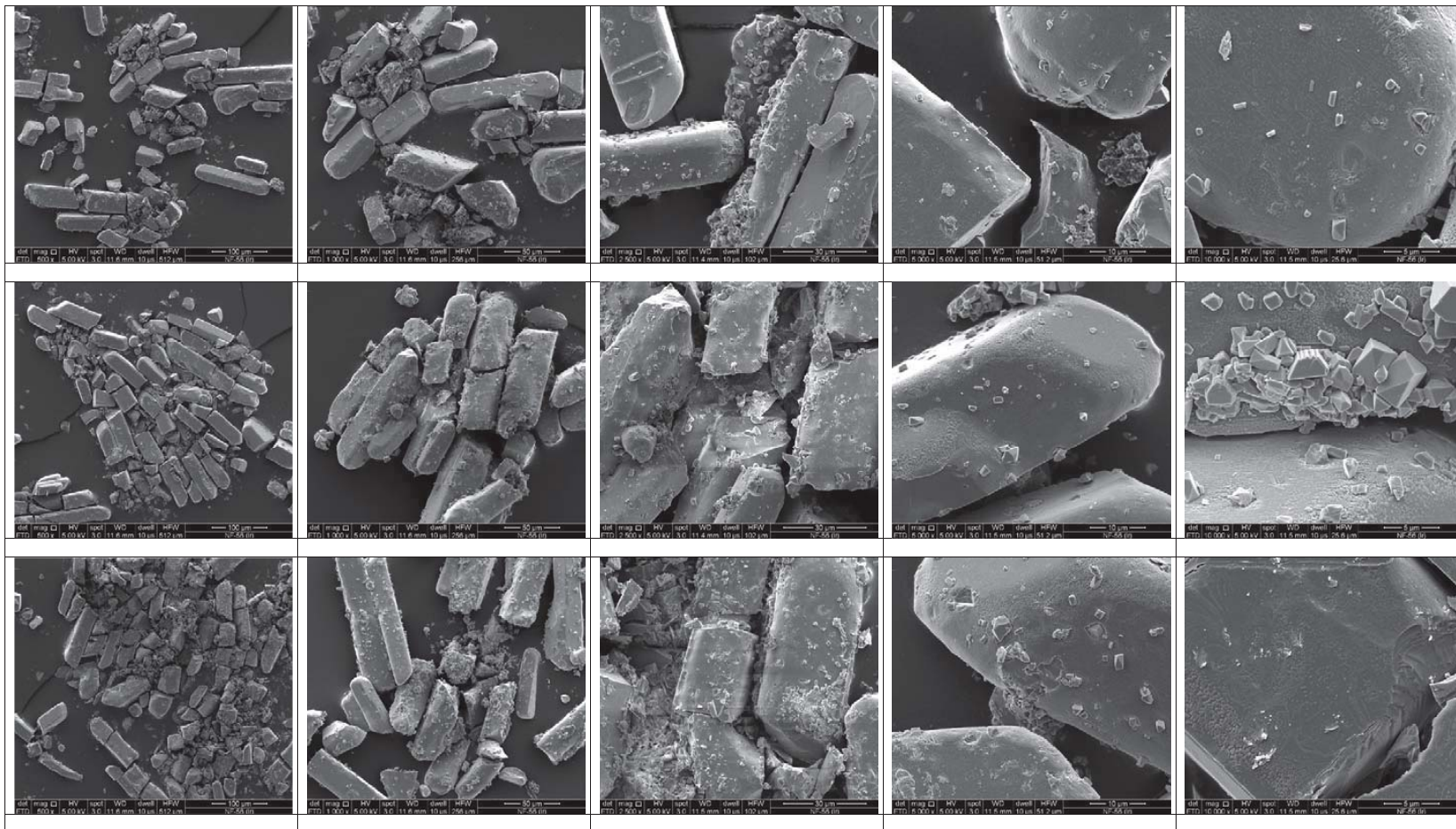


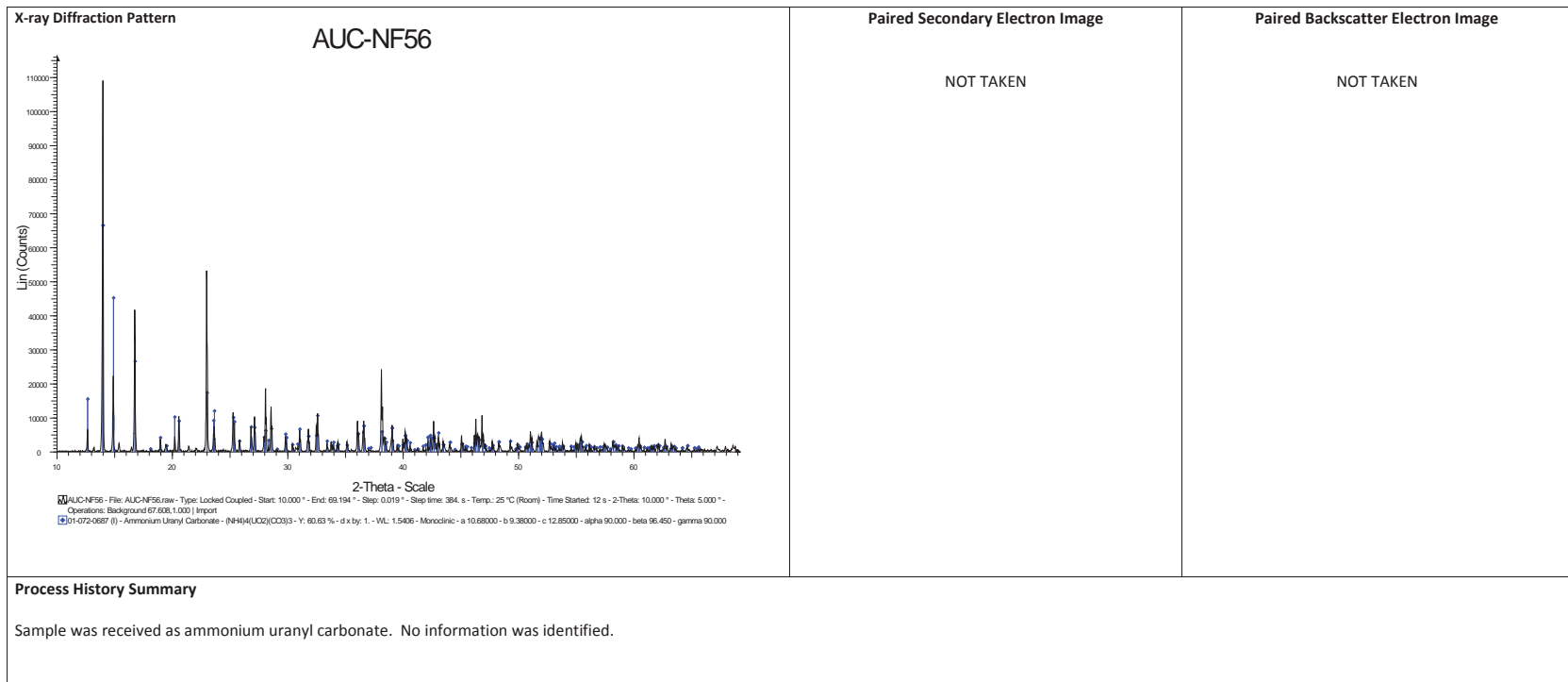
Morphology of Industrial Sample NF-55



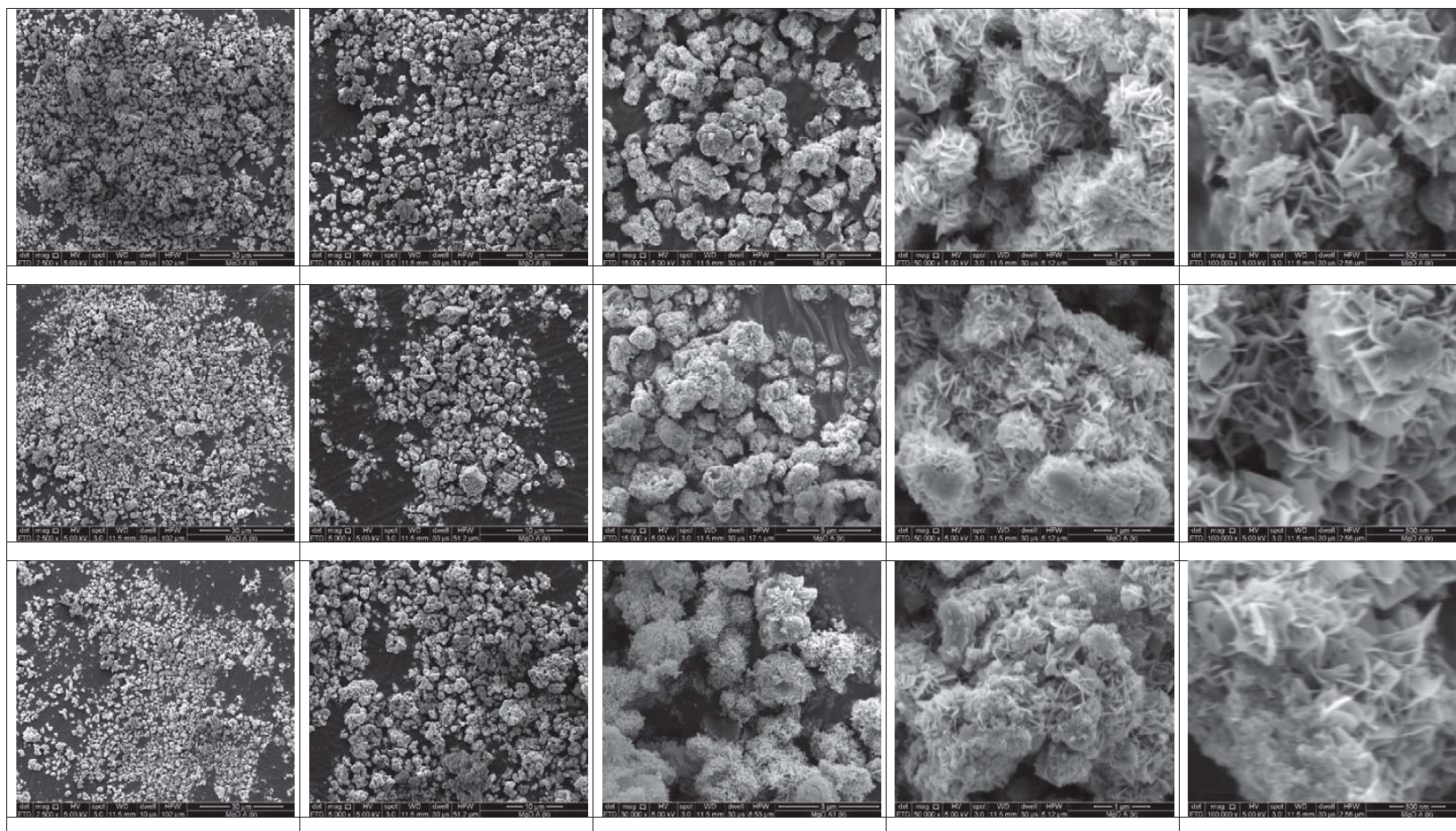
X-ray Diffraction Pattern	Paired Secondary Electron Image	Paired Backscatter Electron Image
<p style="text-align: center;">AUC-NF55</p> <p style="font-size: small;">AUC-NF55 - File: AUC-NF55.raw - Type: Locked Coupled - Start: 10.000 ° - End: 69.194 ° - Step: 0.019 ° - Step time: 384. s - Temp: 25 °C (Room) - Time Started: 11 s - 2-Theta: 10.000 ° - Theta: 5.000 ° - Operations: Background 67.608,1.000 Import [01-072-0687 (f) - Ammonium Uranyl Carbonate - (NH4)4(UO2)(CO3)3 · Y: 109.86 % - d x by: 1, - V/L: 1.5406 - Monodisc - a 10.68000 - b 9.38000 - c 12.85000 - alpha 90.000 - beta 96.450 - gamma 90.000</p>	<p>NOT TAKEN</p>	<p>NOT TAKEN</p>
<p>Process History Summary</p> <p>Sample was received as a uranium uranyl carbonate. No information was identified</p>		

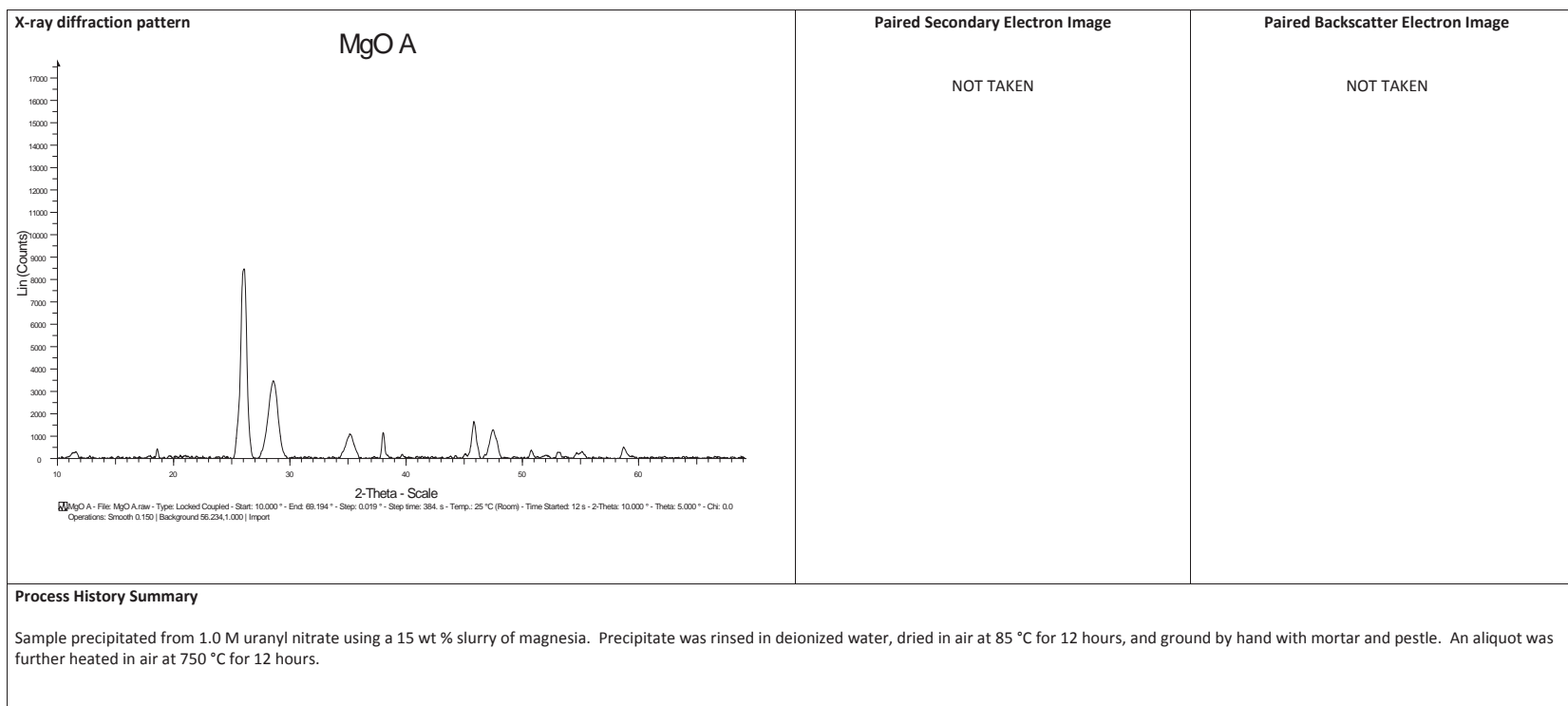
Morphology of Industrial Sample NF-56



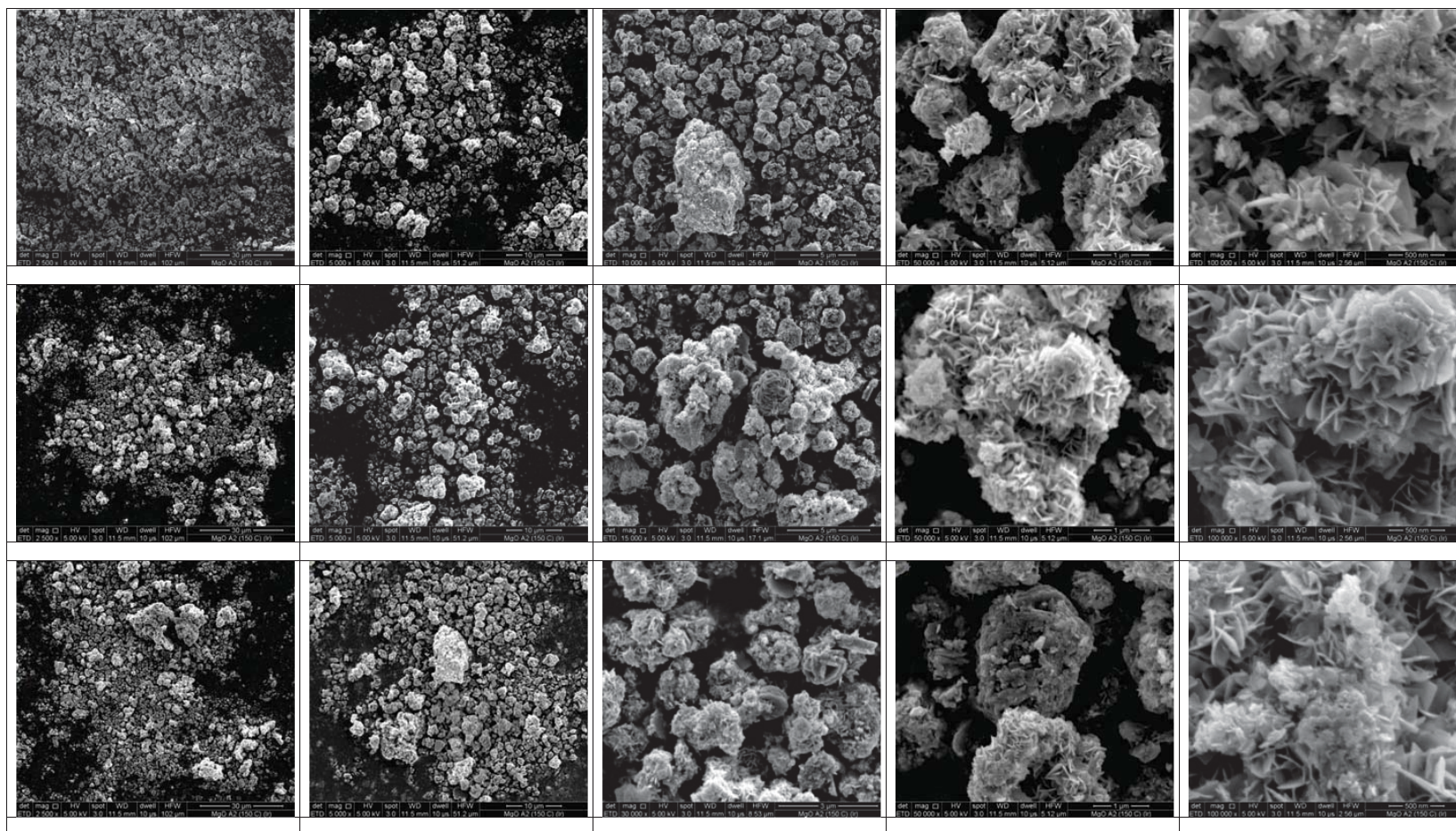


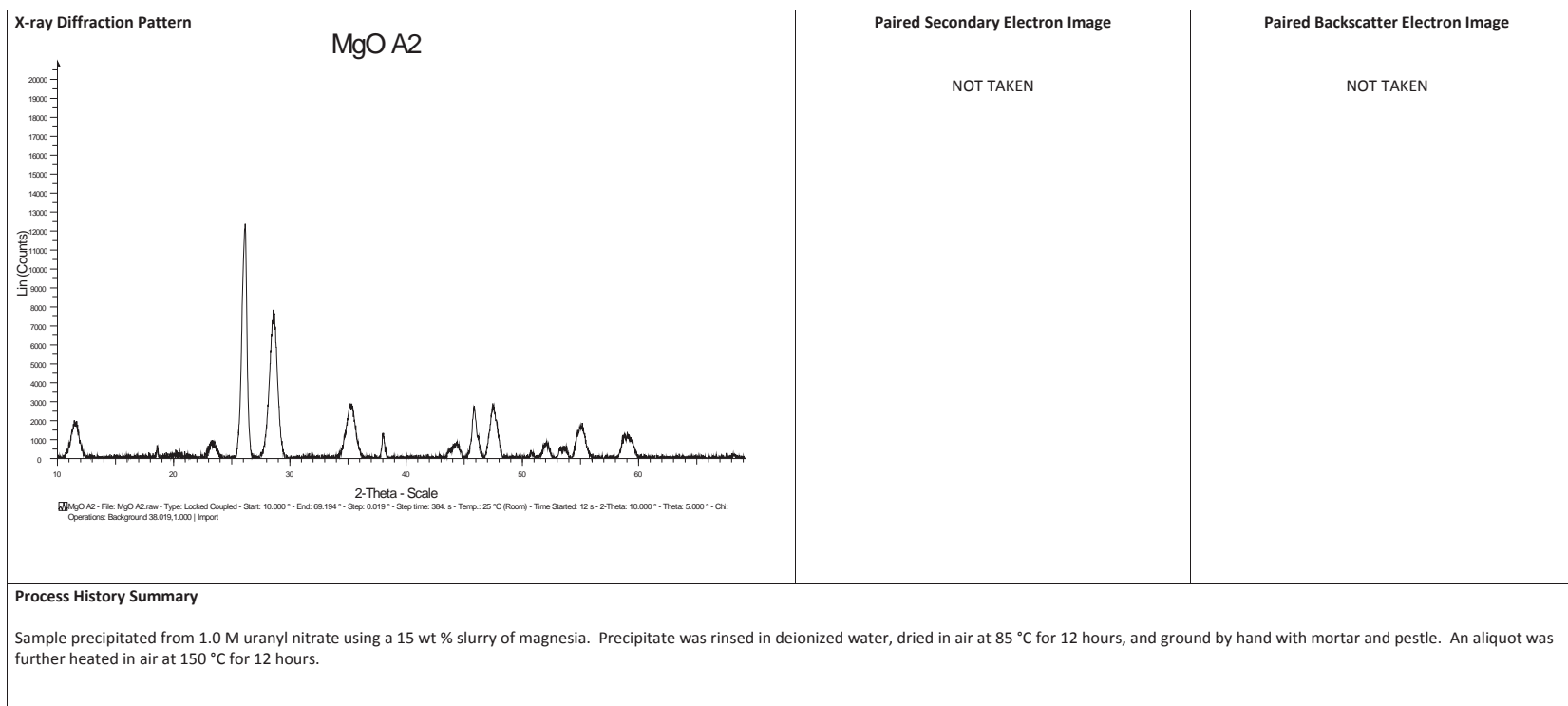
Morphology of the precipitate of uranyl nitrate and magnesia heated to 85 °C



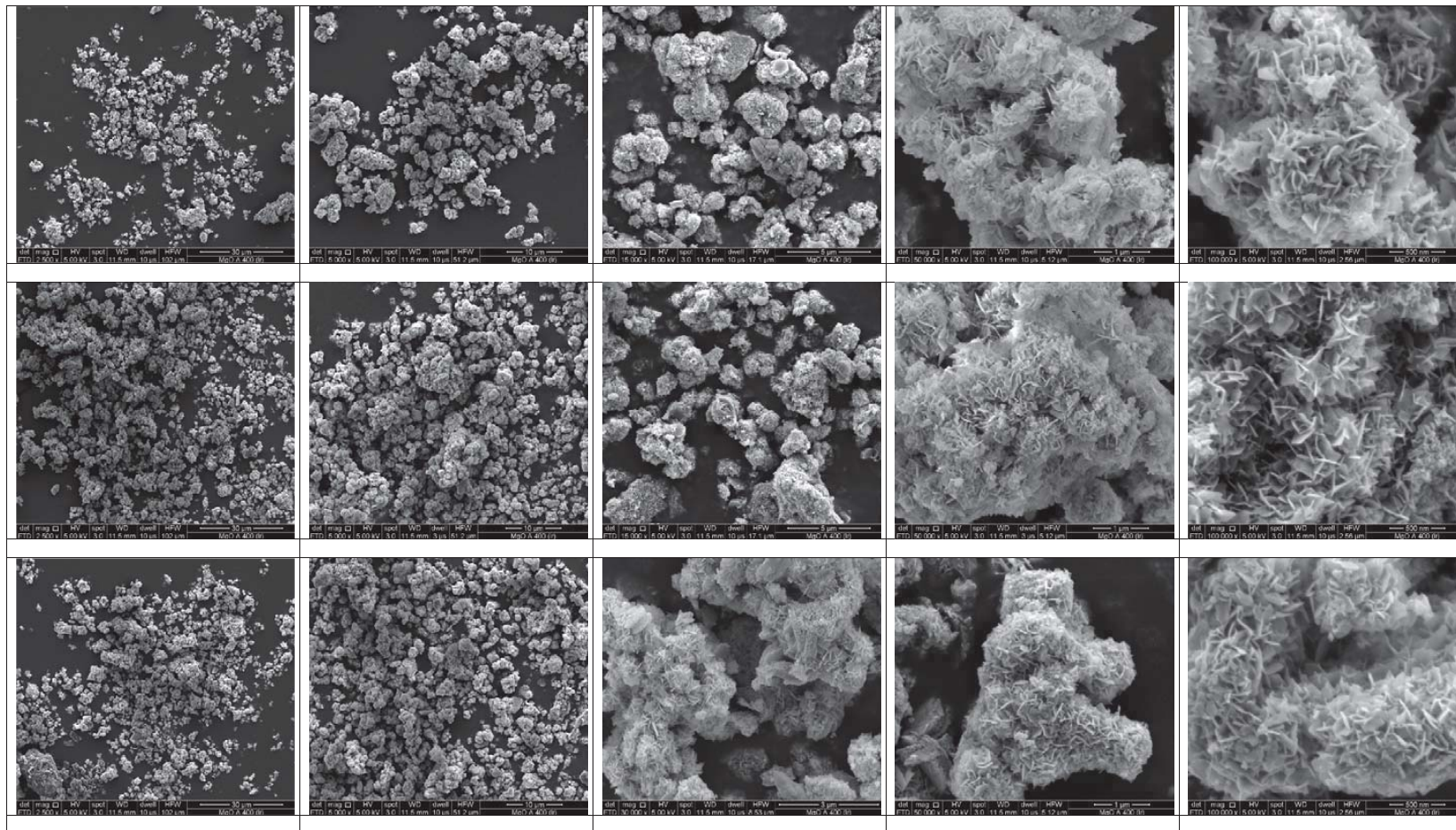


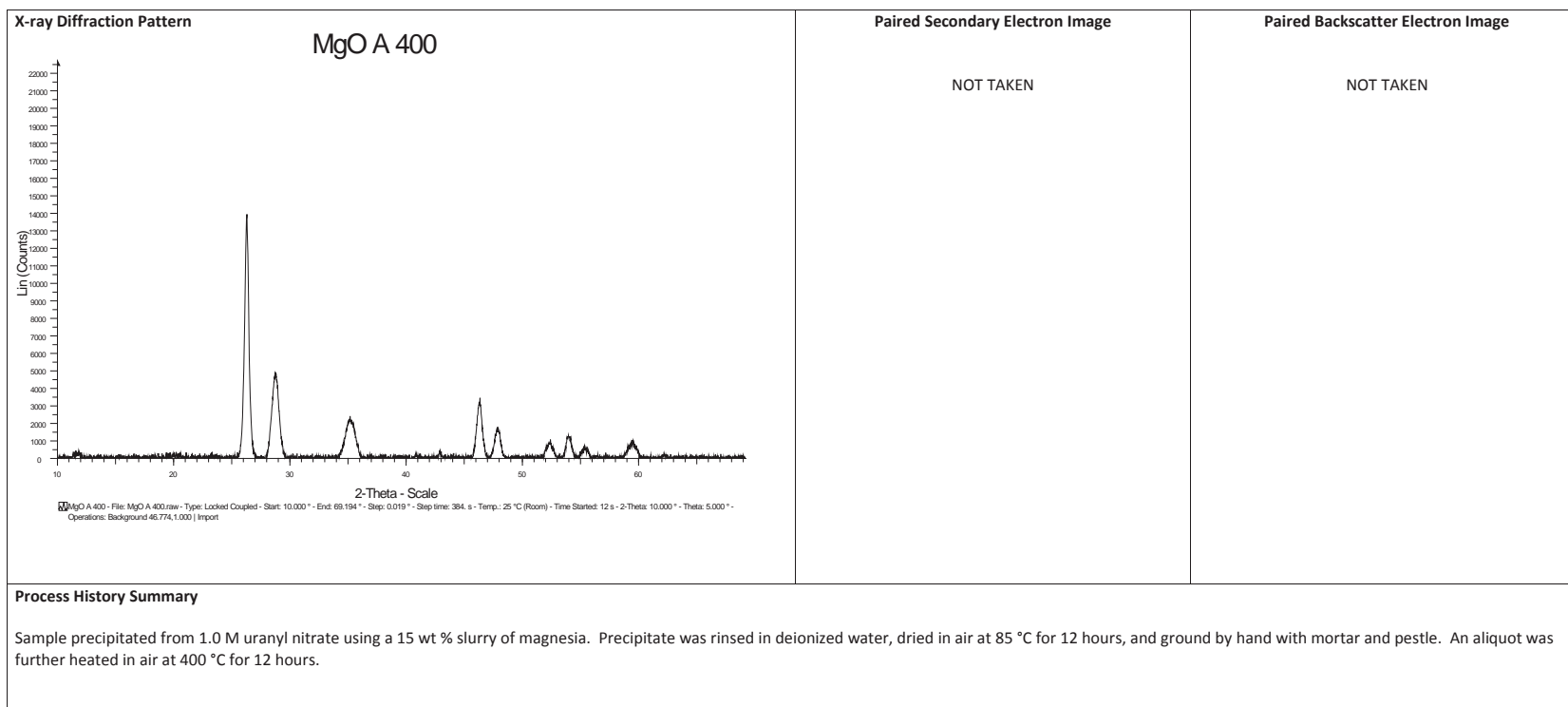
Morphology of the precipitate of uranyl nitrate and magnesia dried to 150 °C



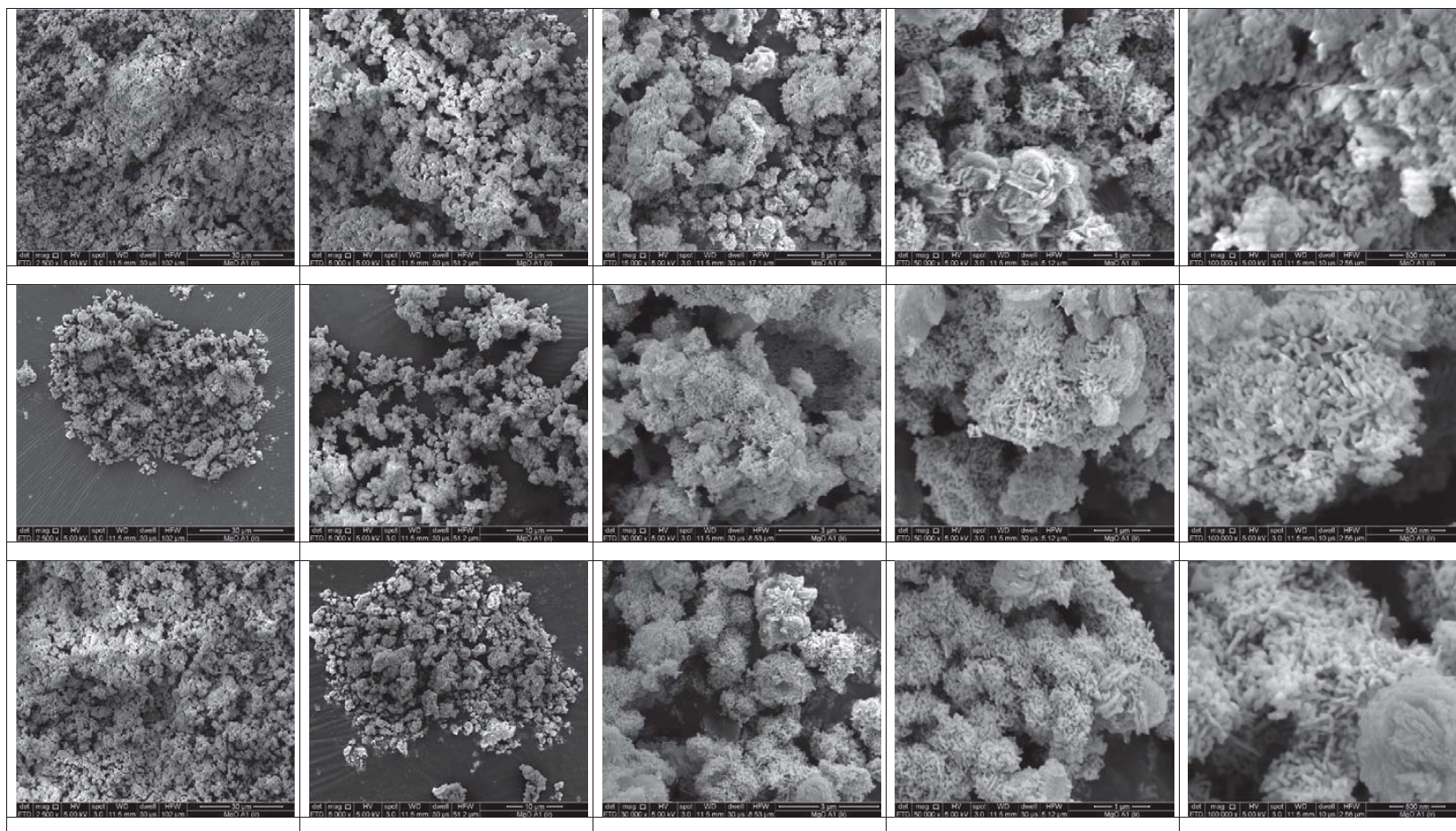


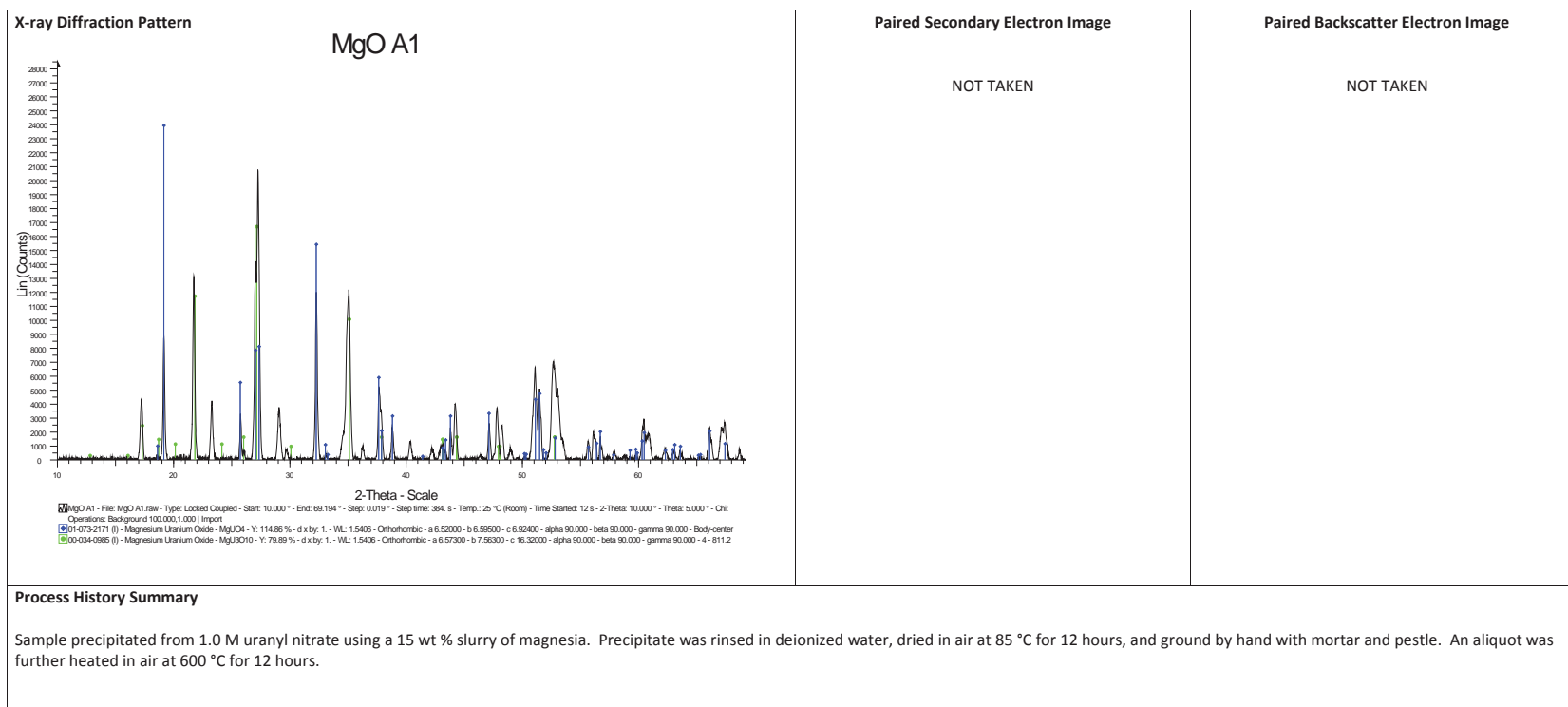
Morphology of the precipitate of uranyl nitrate and magnesia dried to 400 °C



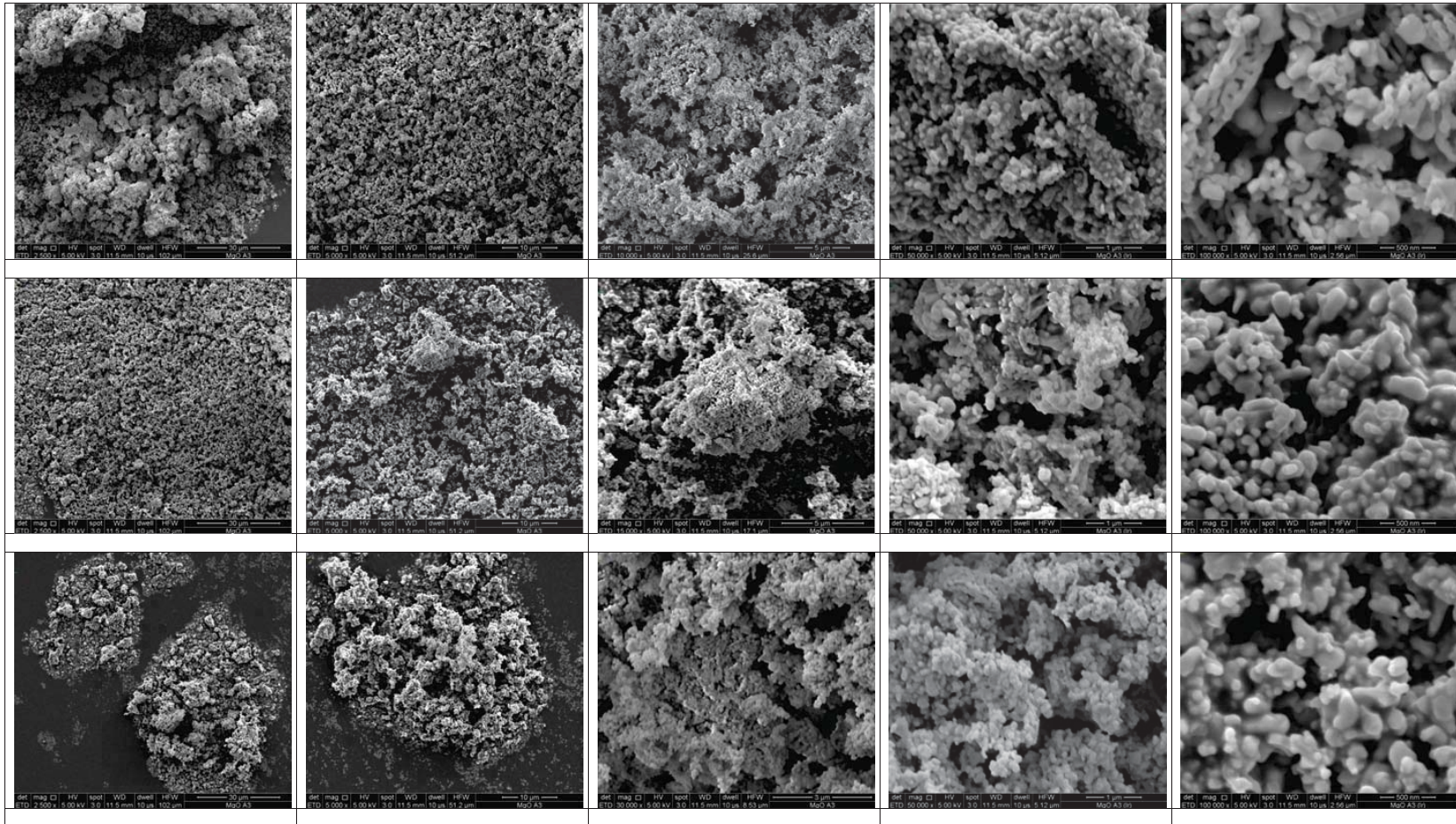


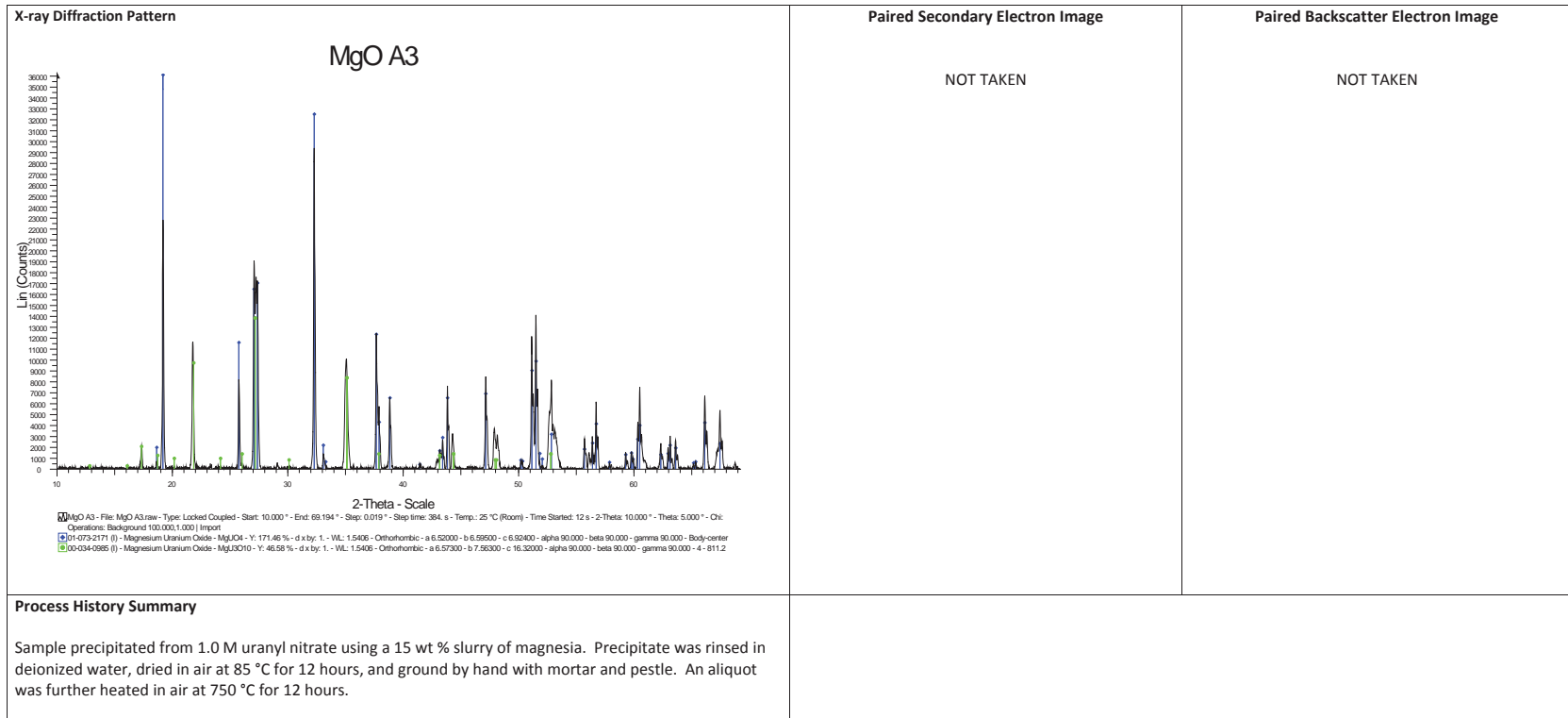
Morphology of the precipitate of uranyl nitrate and magnesia dried to 600 °C



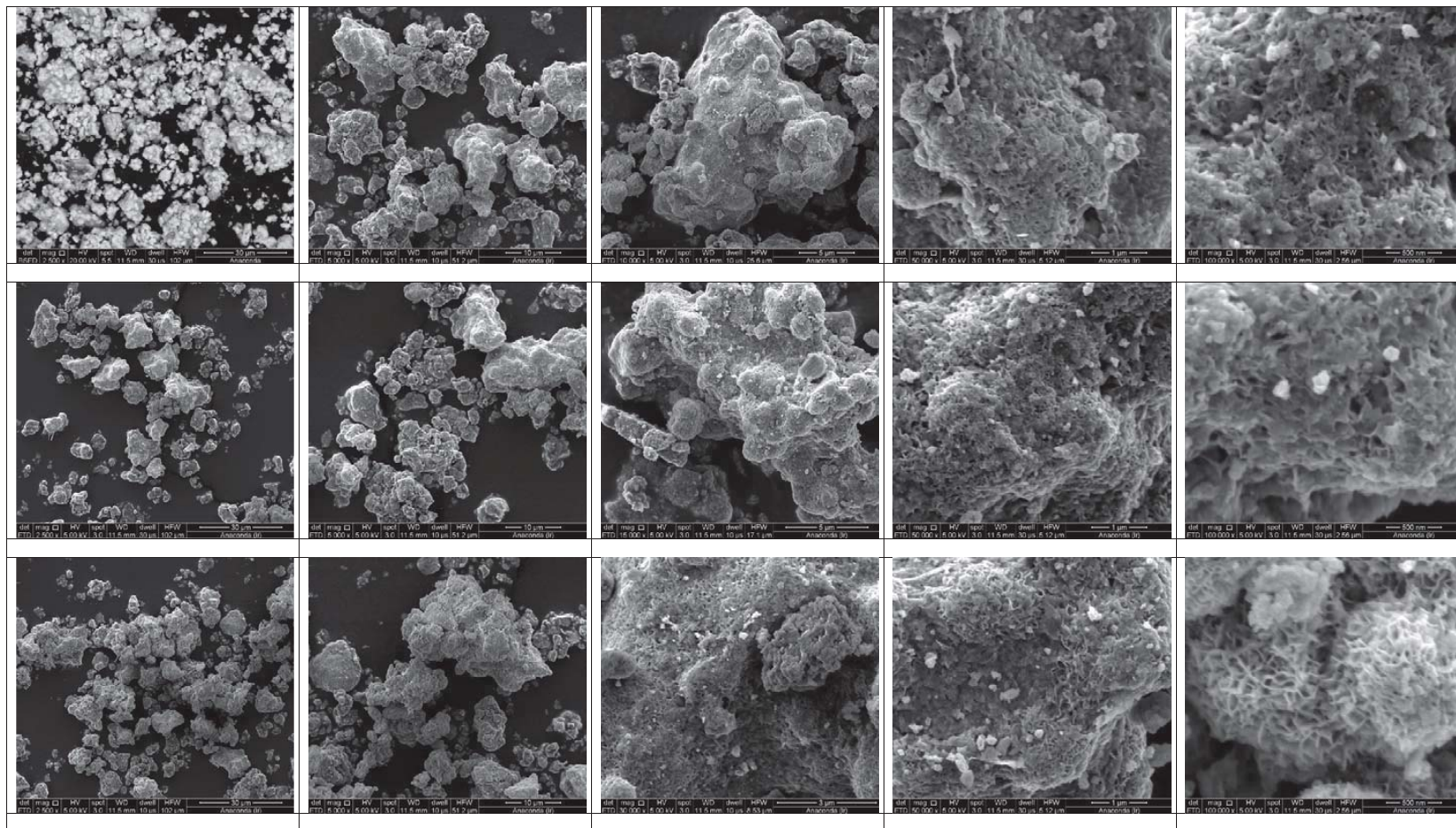


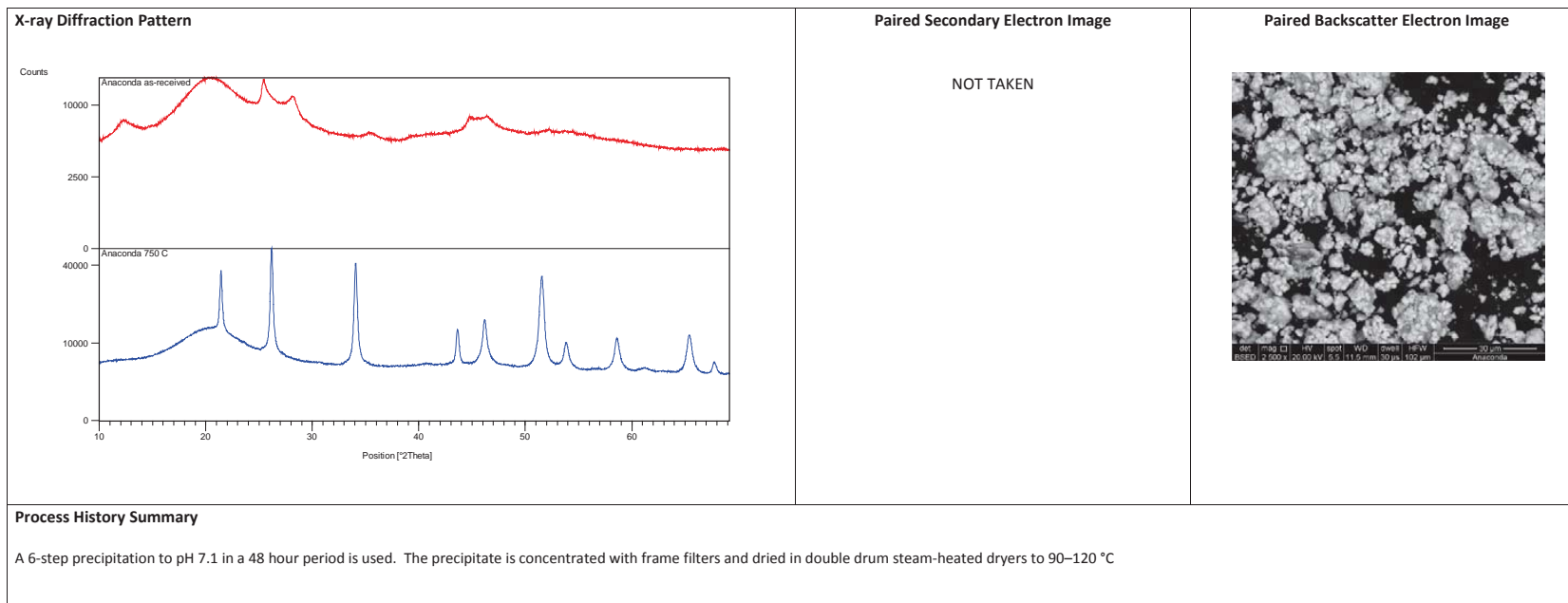
Morphology of the precipitate of uranyl nitrate and magnesia heated to 750 °C



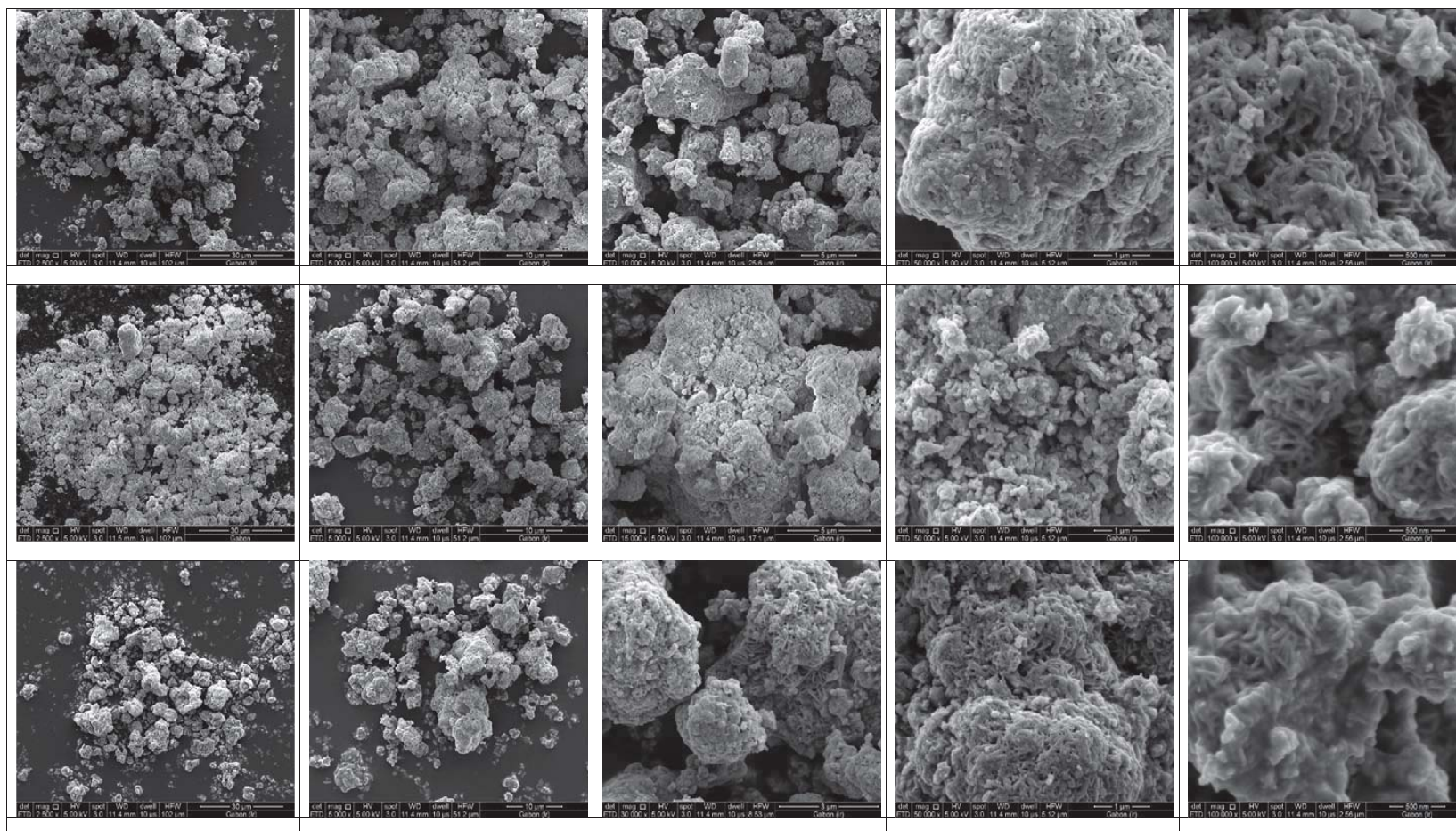


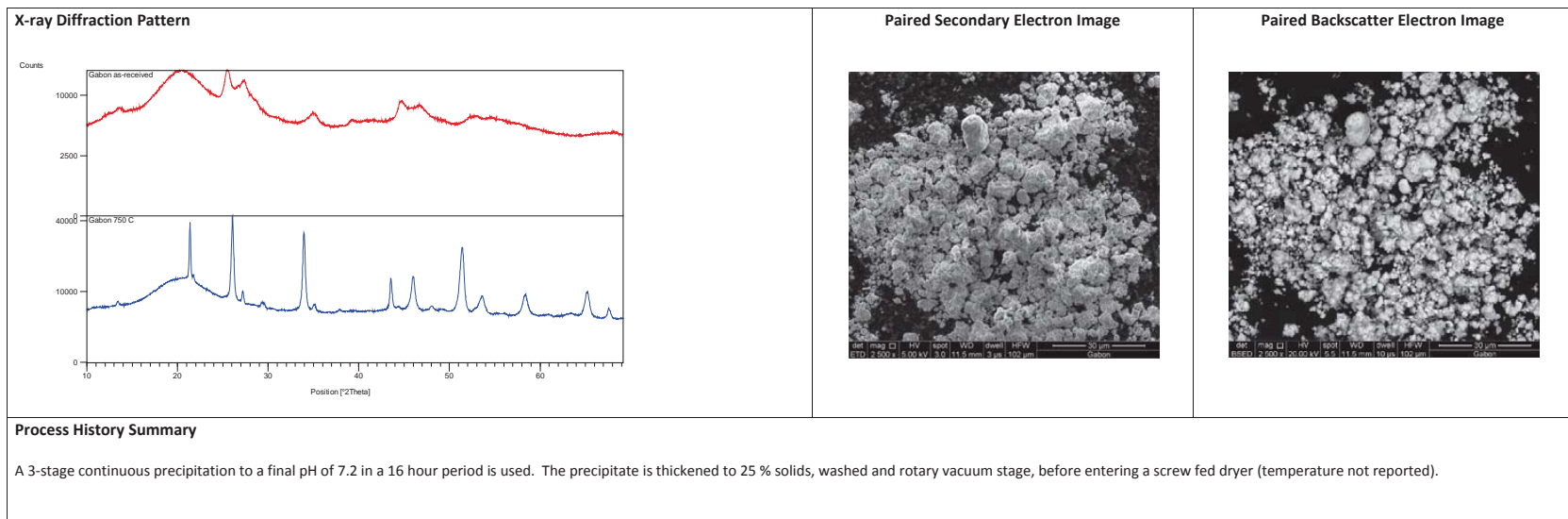
Morphology of uranium ore concentrate from the Anaconda Company Bluewater Plant in Grants, New Mexico



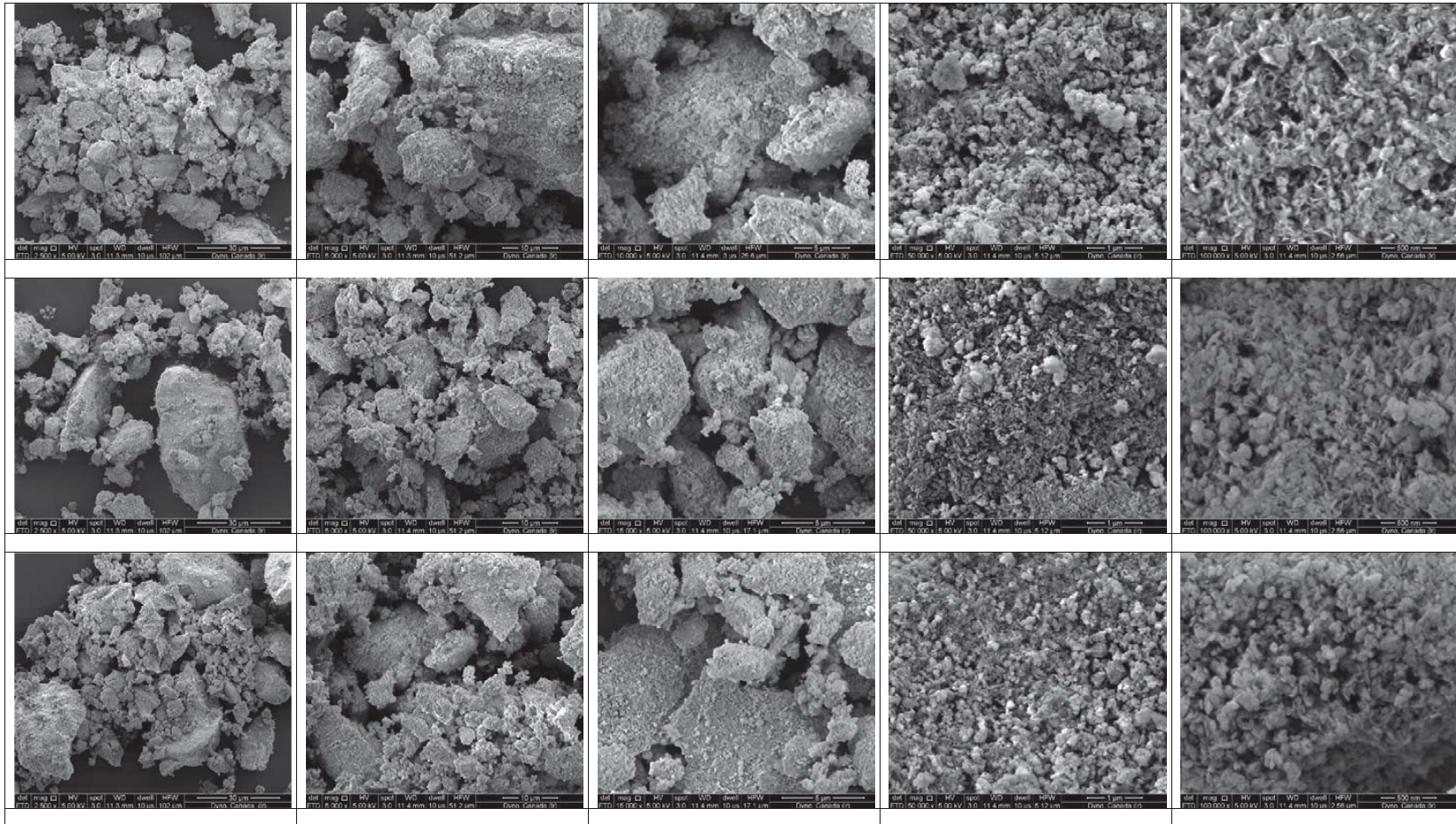


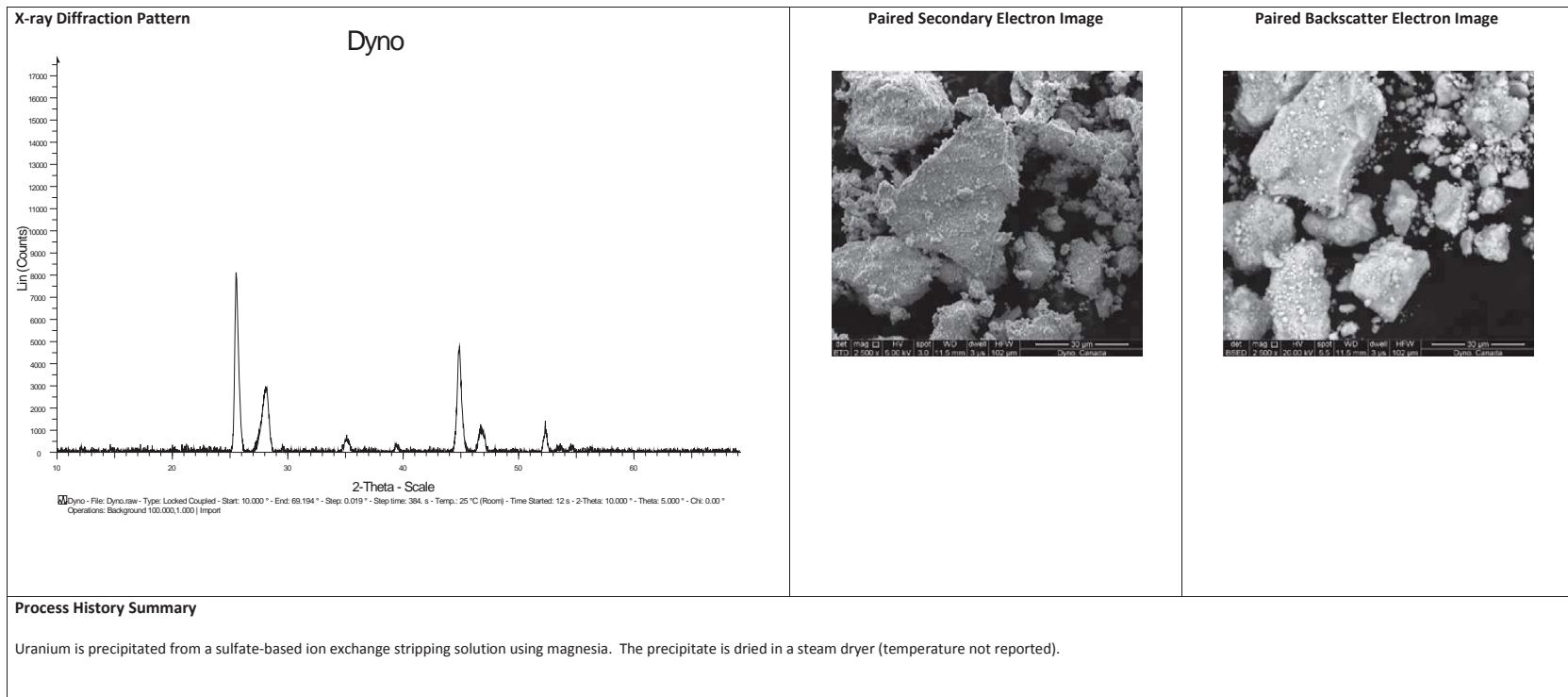
Morphology of uranium ore concentrate from the COMUF facility Mounana, Gabon



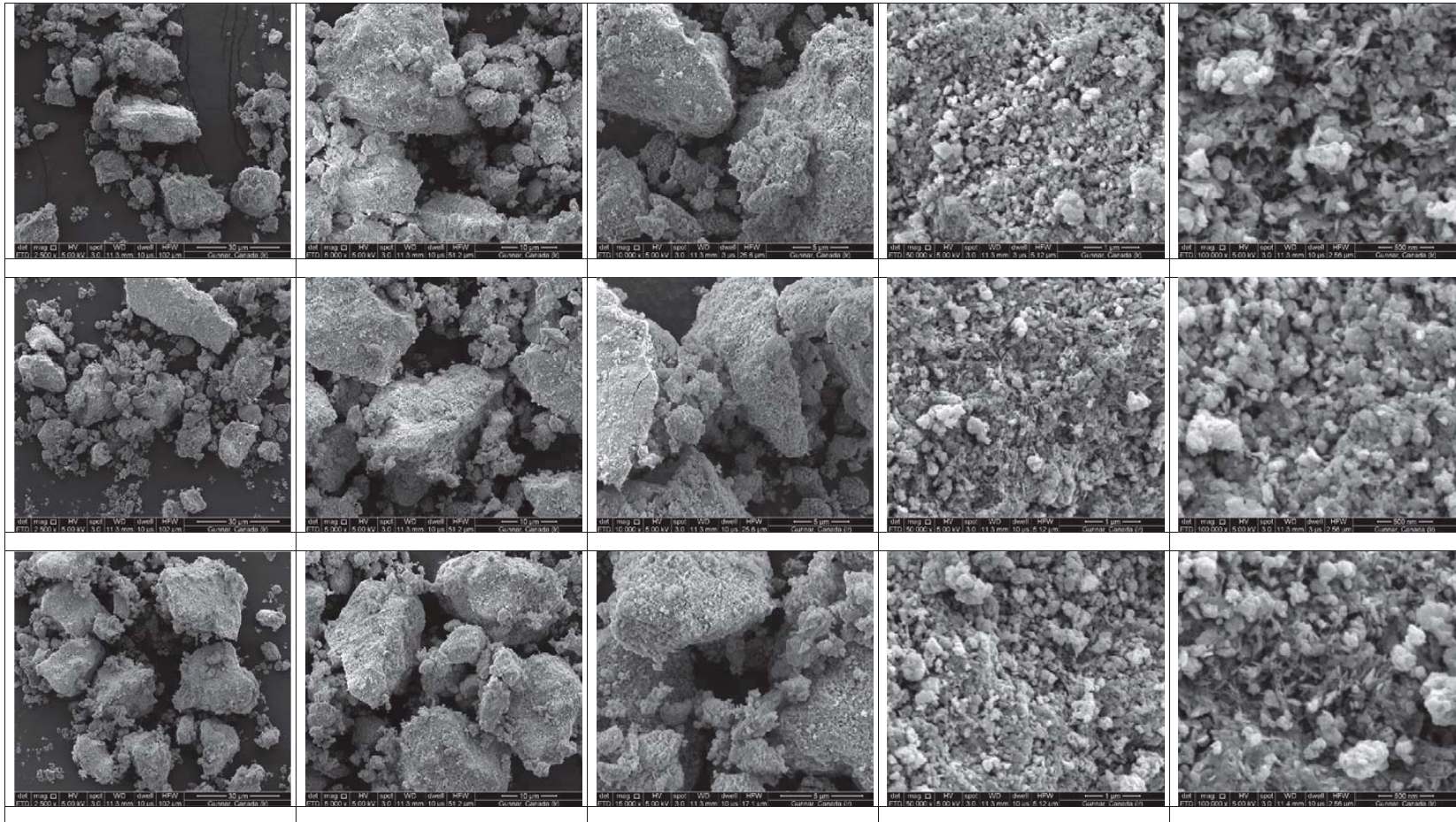


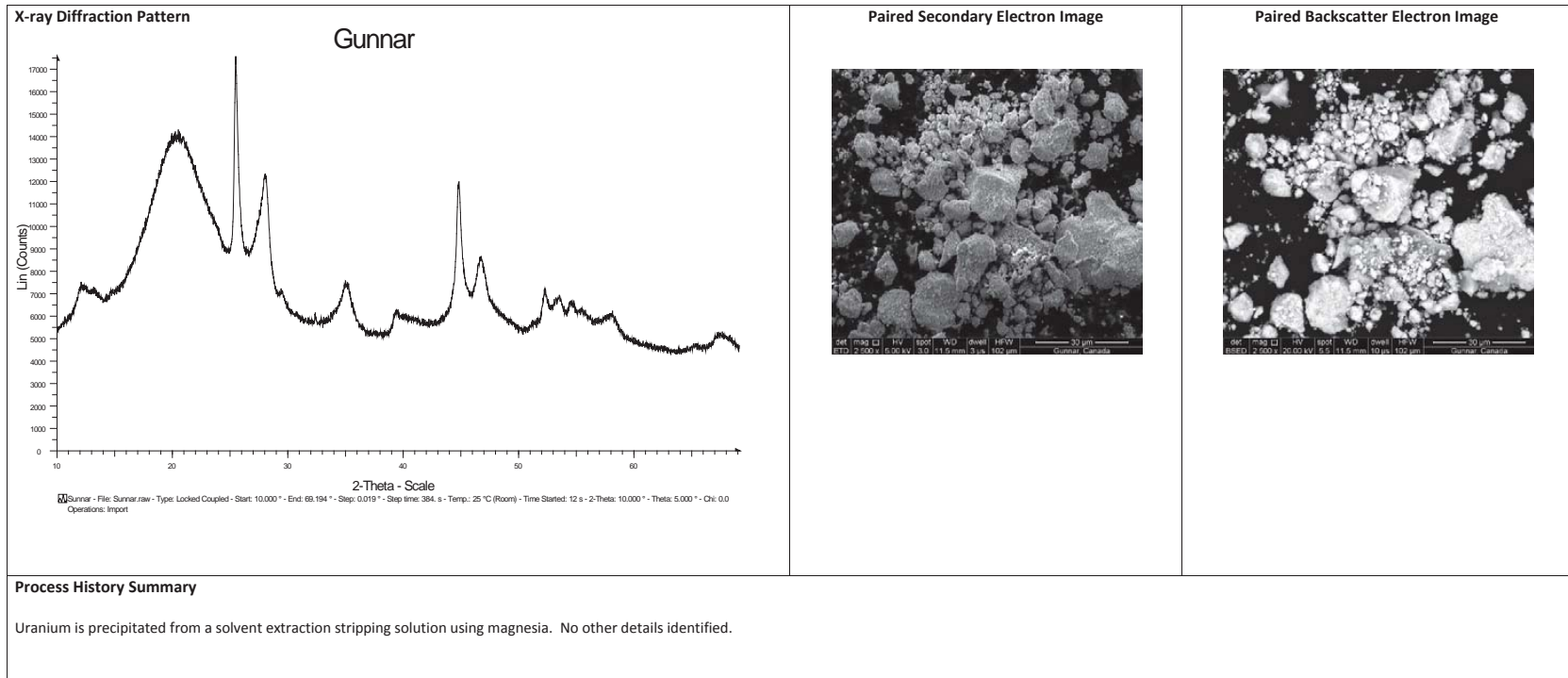
Morphology of uranium ore concentrate from the Dyno facility in Bancroft, Ontario, Canada



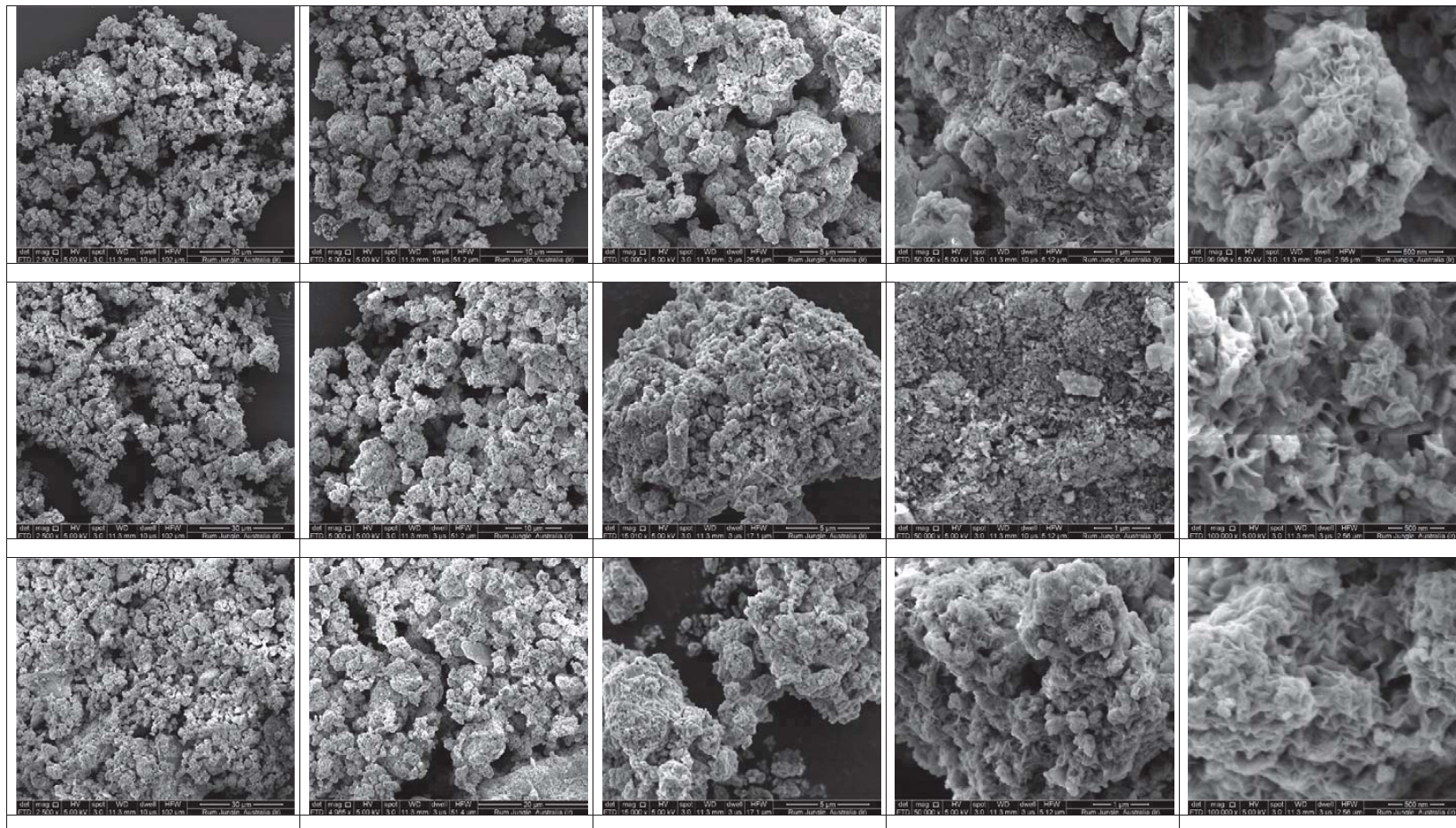


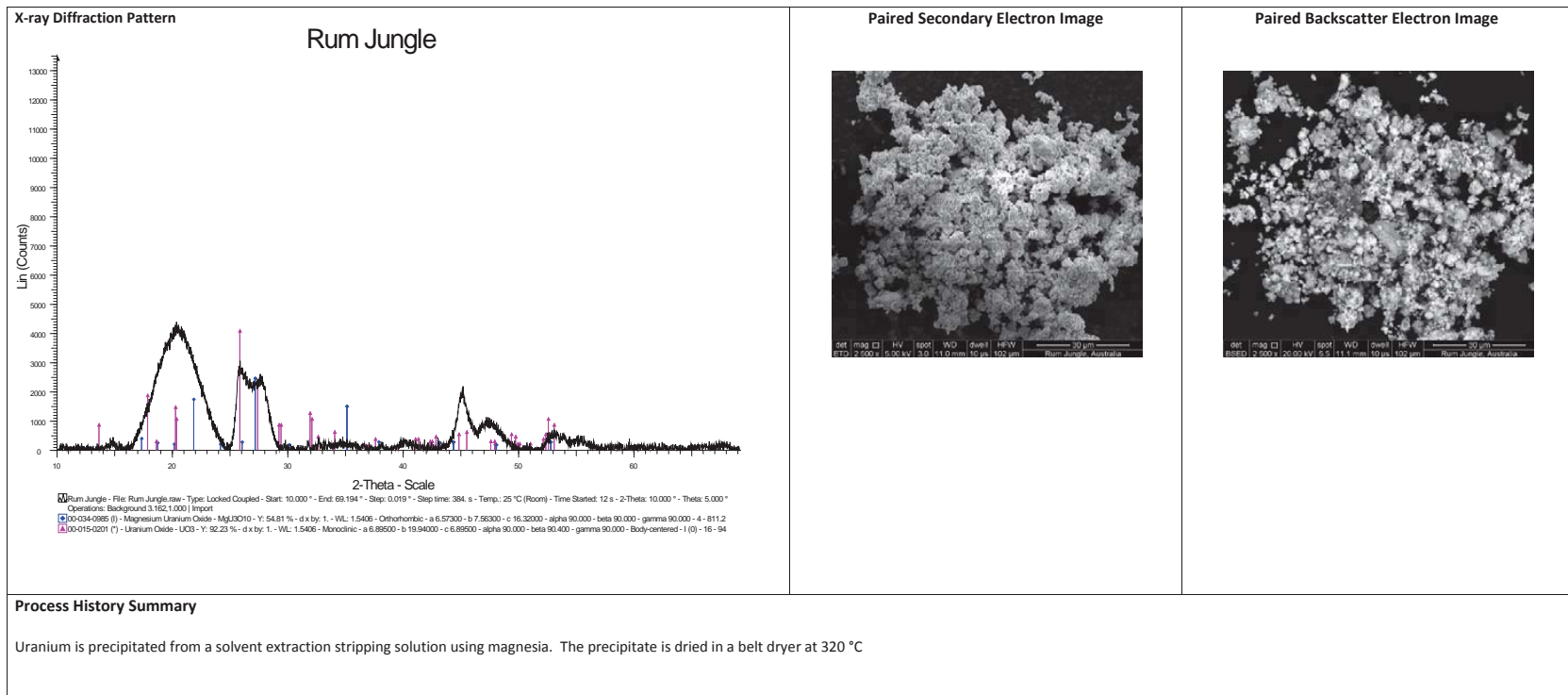
Morphology of uranium ore concentrate from the Gunnar facility in Lake Athabasca, Saskatchewan, Canada



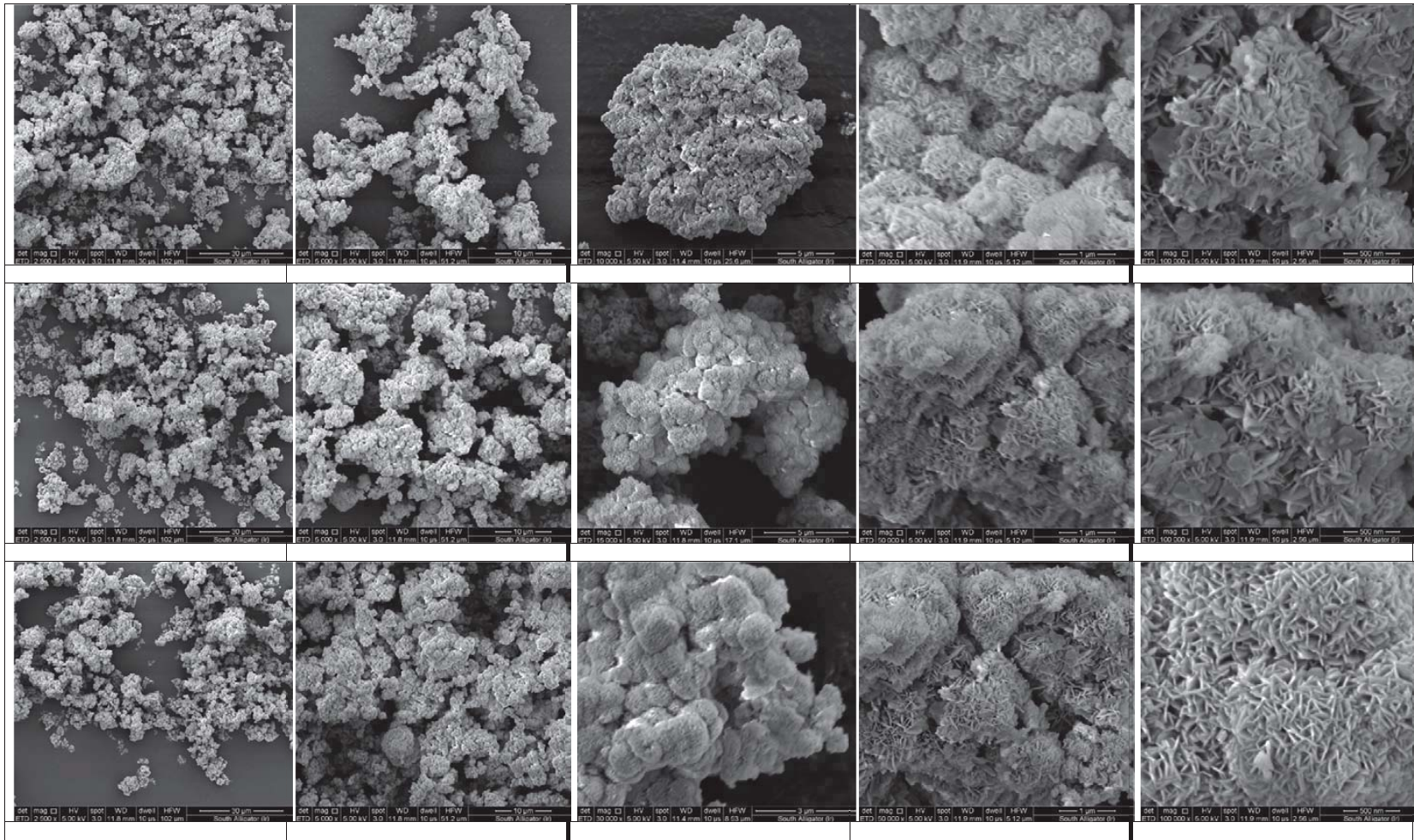


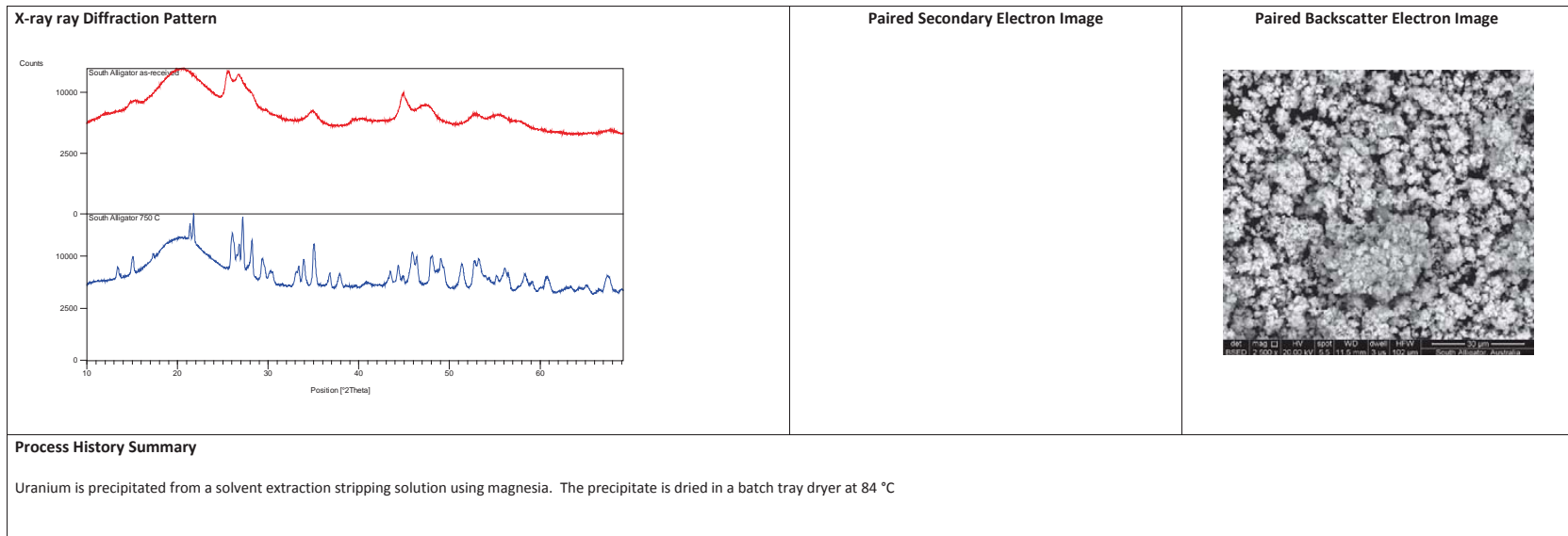
Morphology of uranium ore concentrate from the Rum Jungle facility in Australia



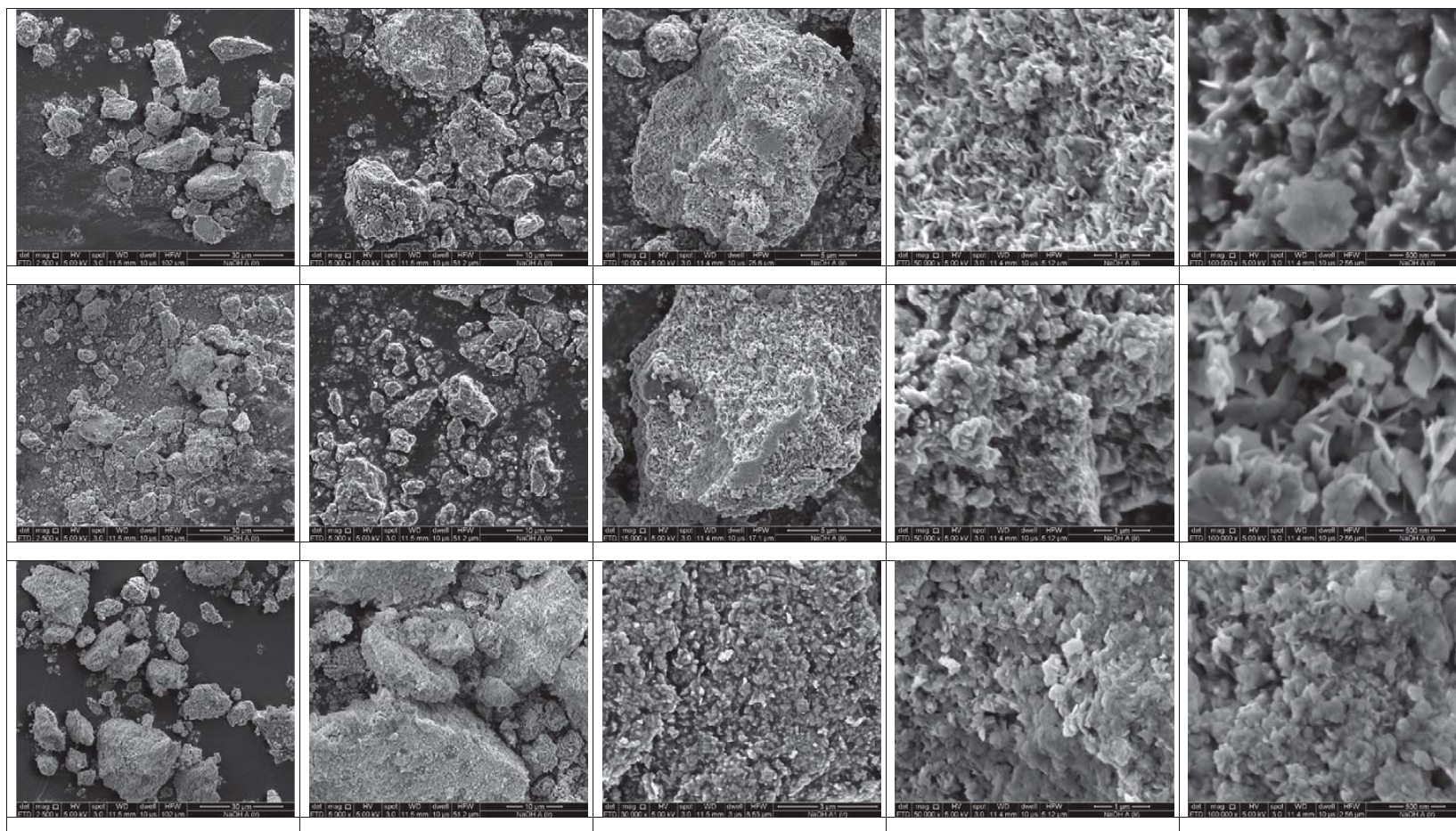


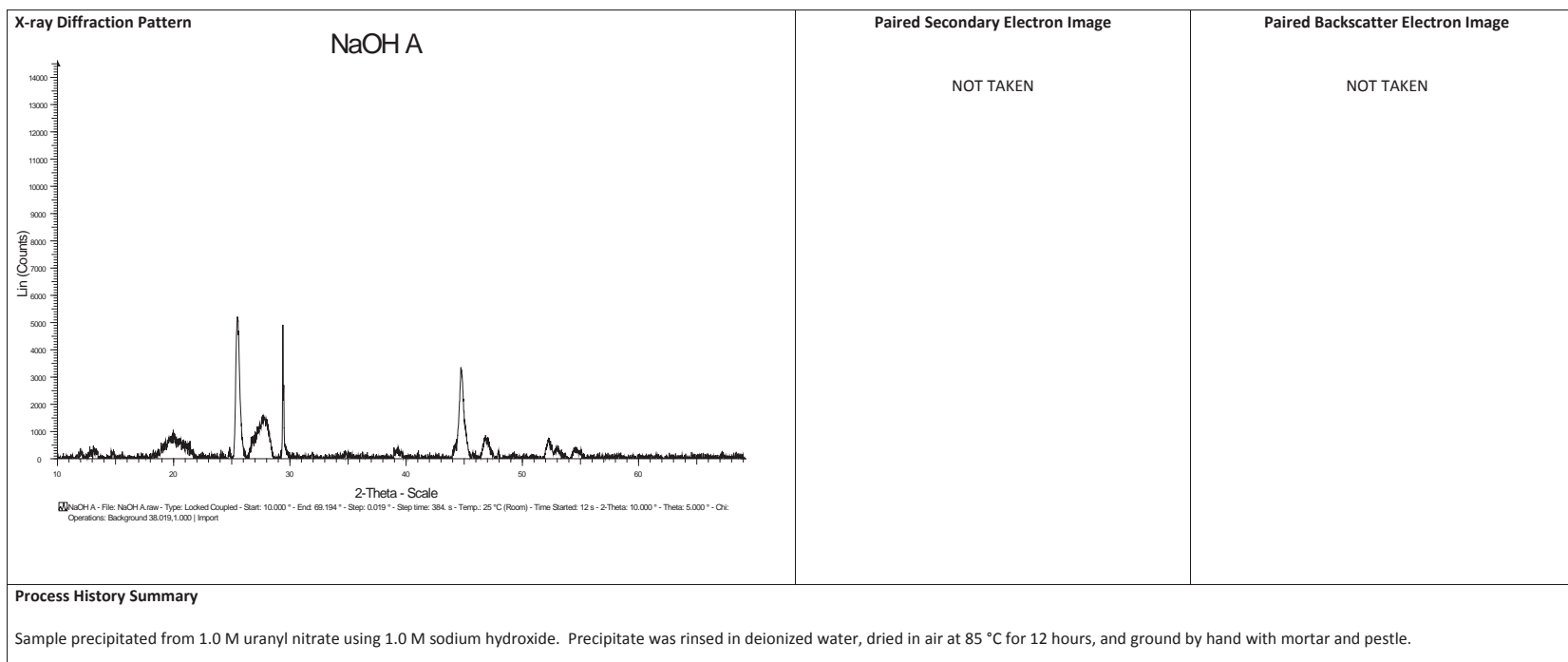
Morphology of uranium ore concentrate from South Alligator, Australia



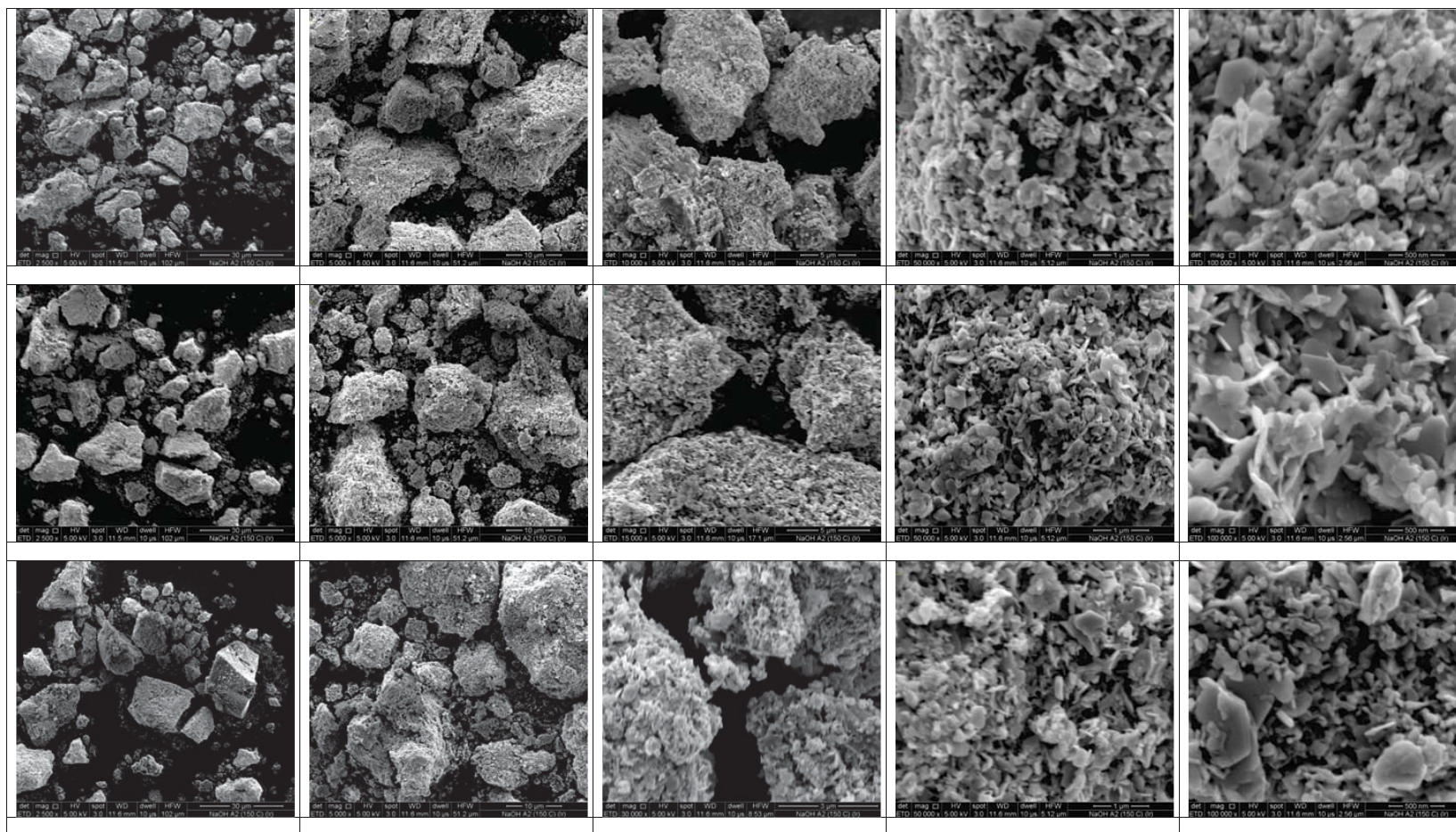


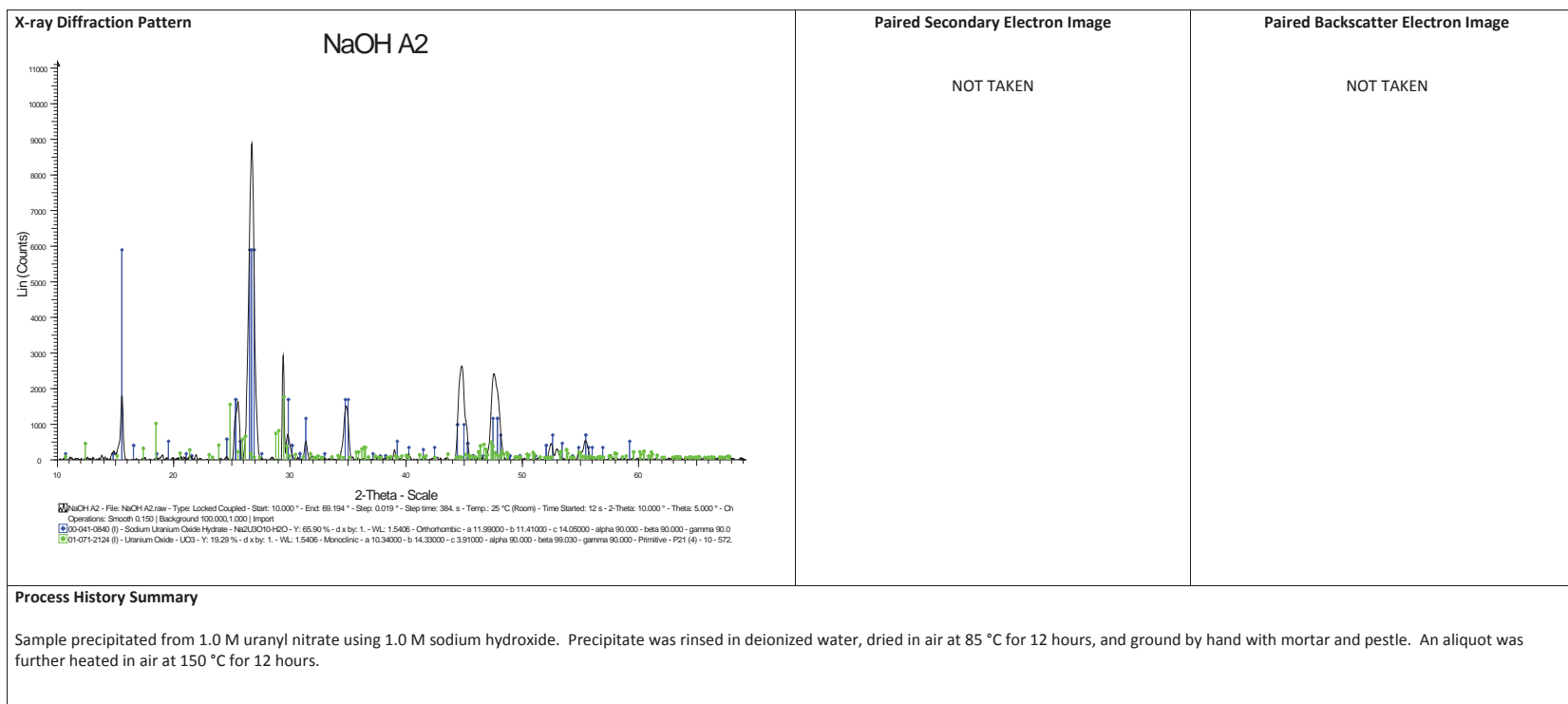
Morphology of the precipitate of uranyl nitrate and sodium hydroxide heated to 85 °C



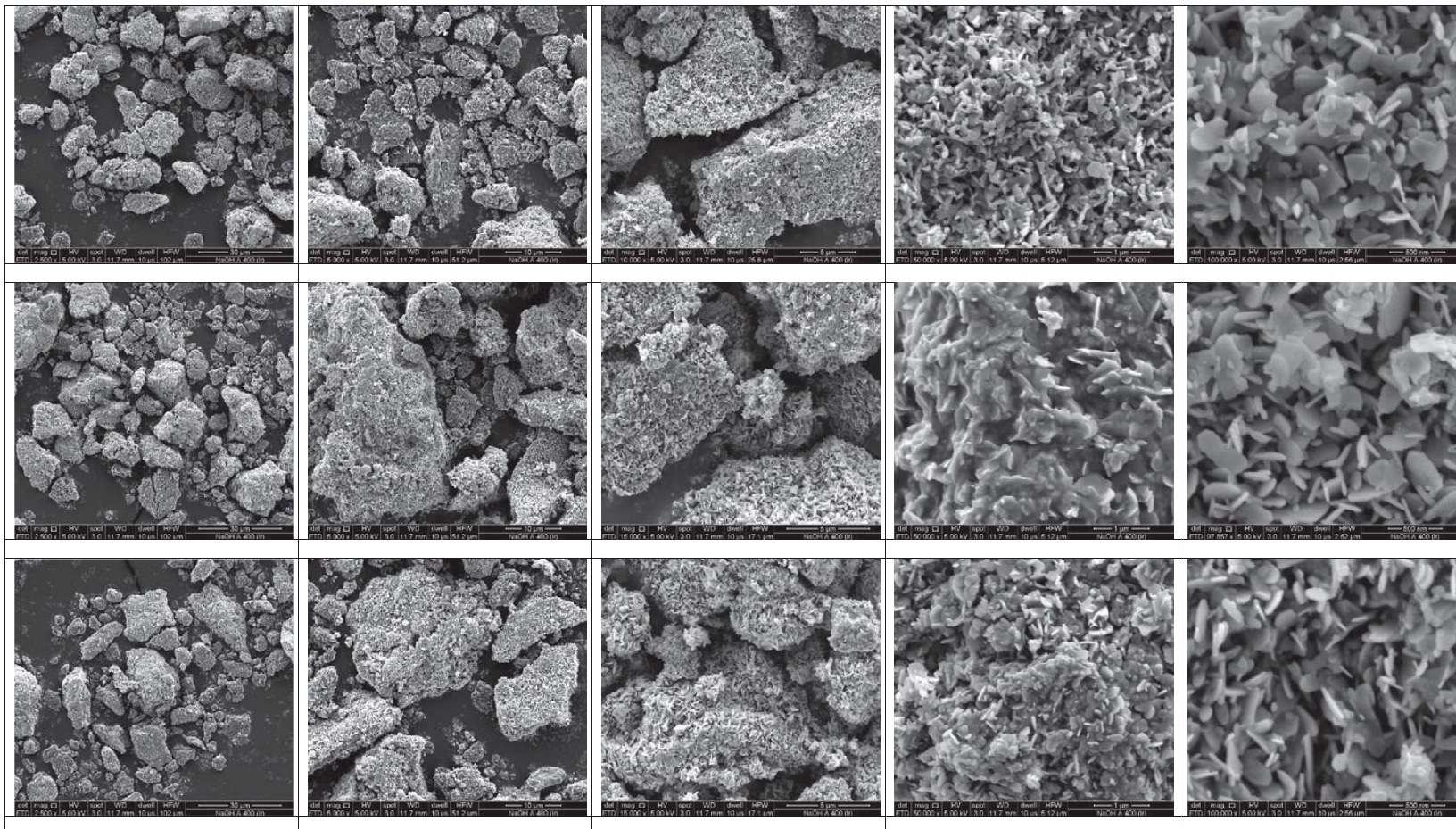


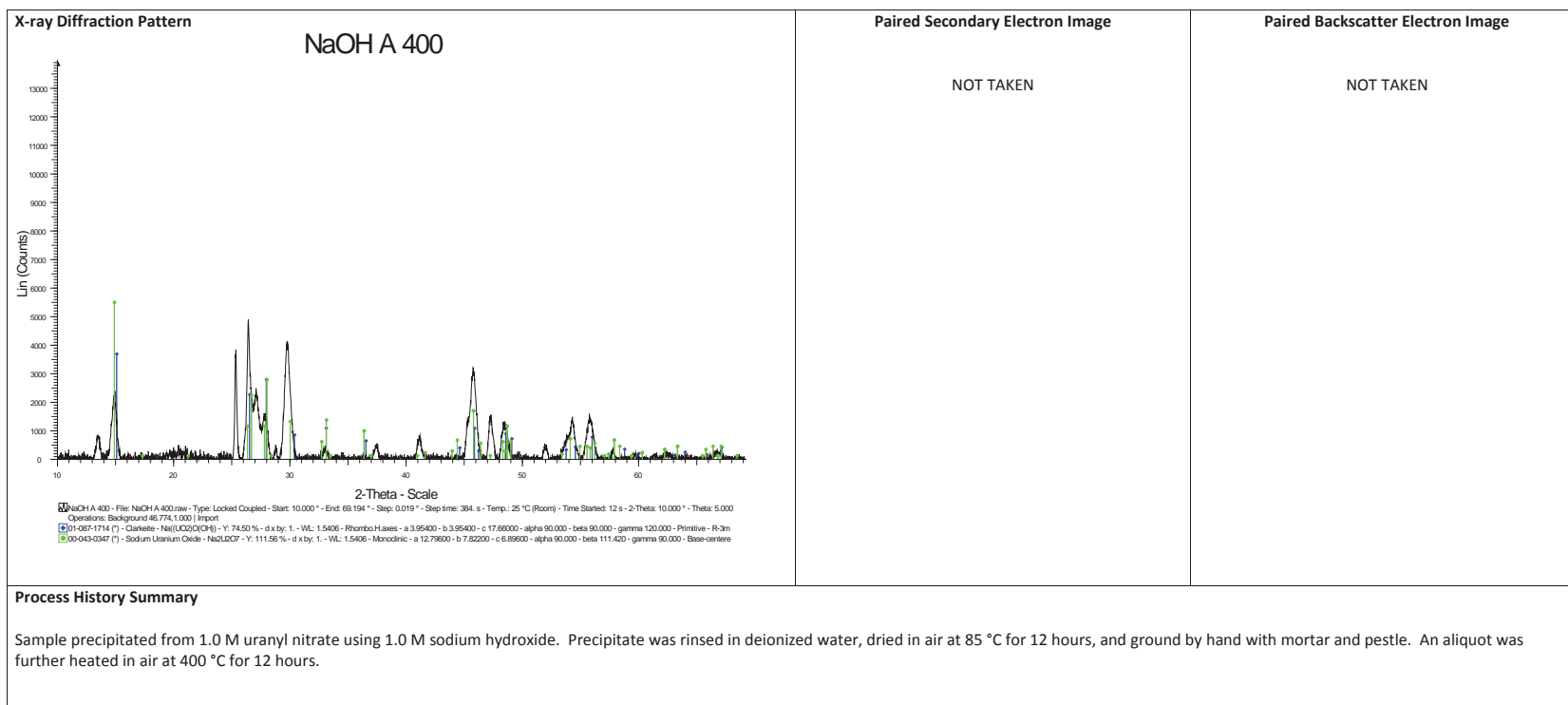
Morphology of the precipitate uranyl nitrate and sodium hydroxide heated to 150 °C



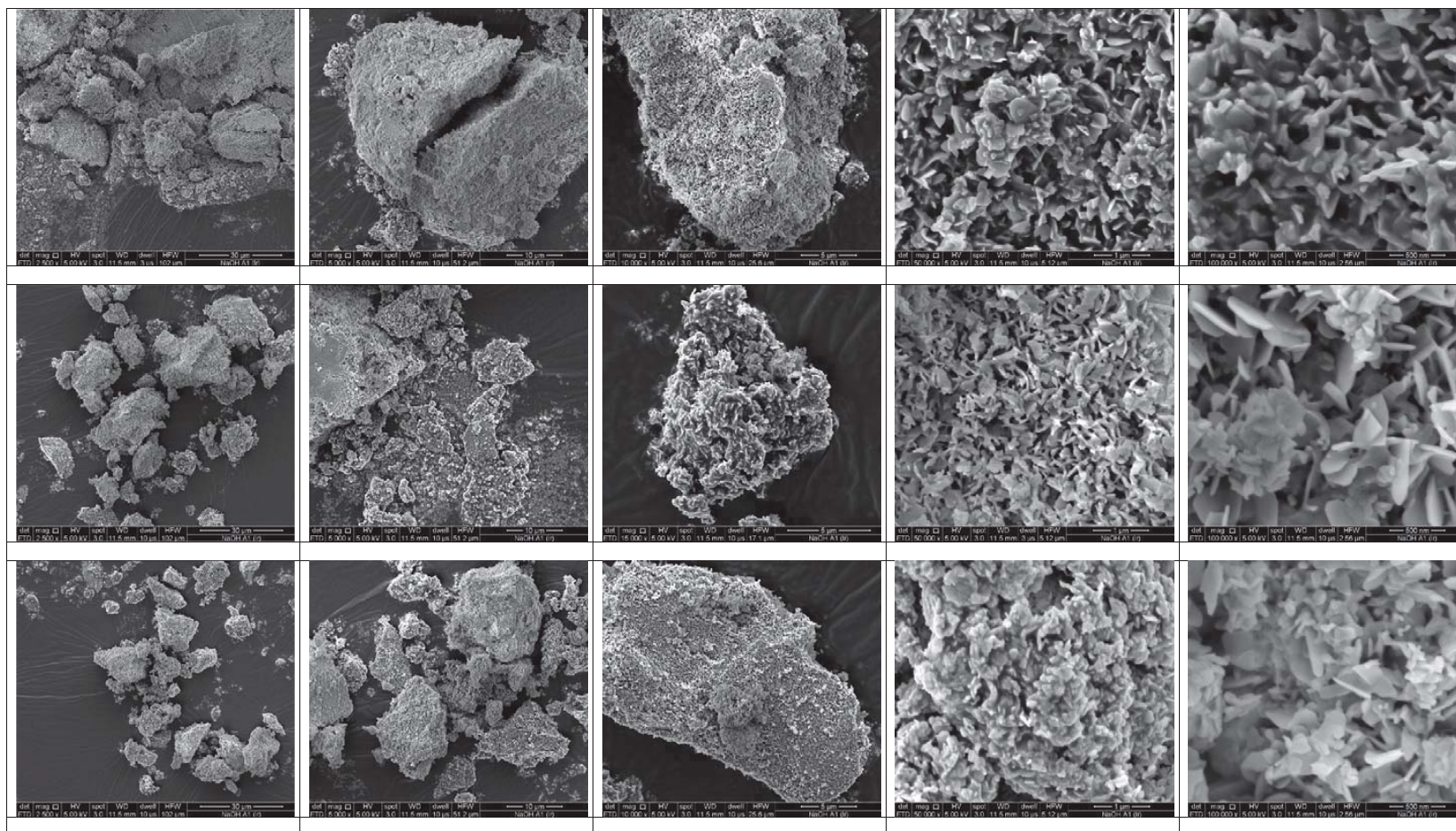


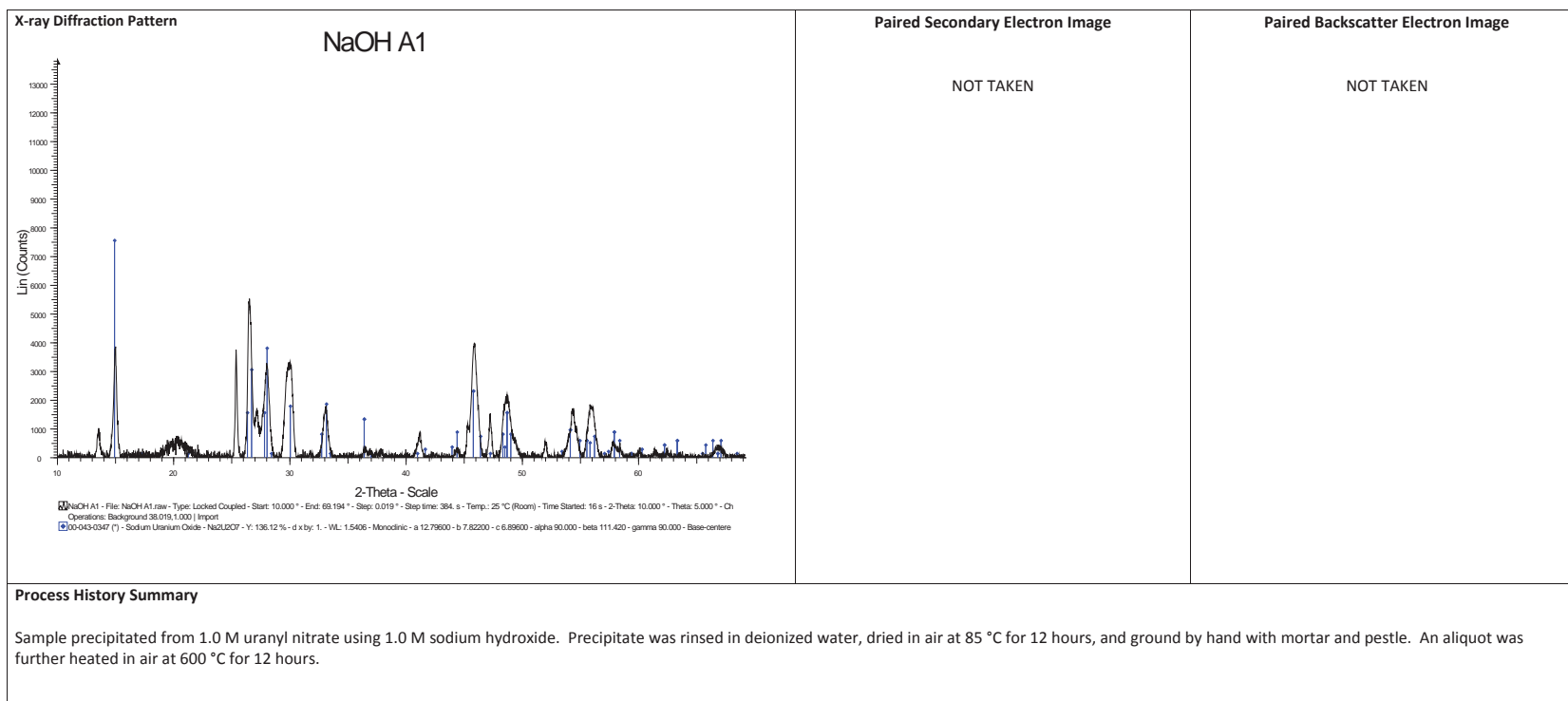
Morphology of the precipitate of uranyl nitrate and sodium hydroxide heated to 400 °C



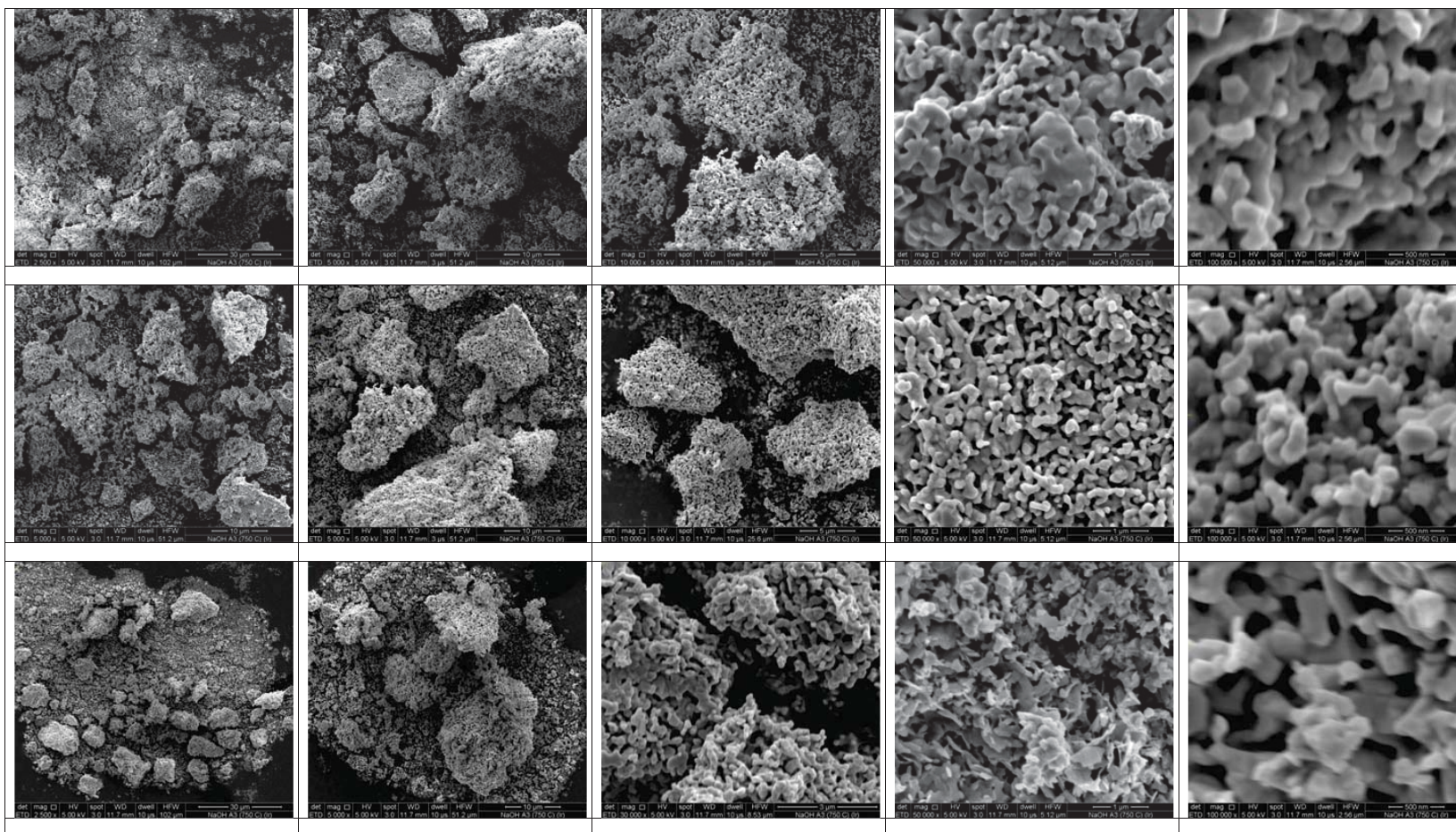


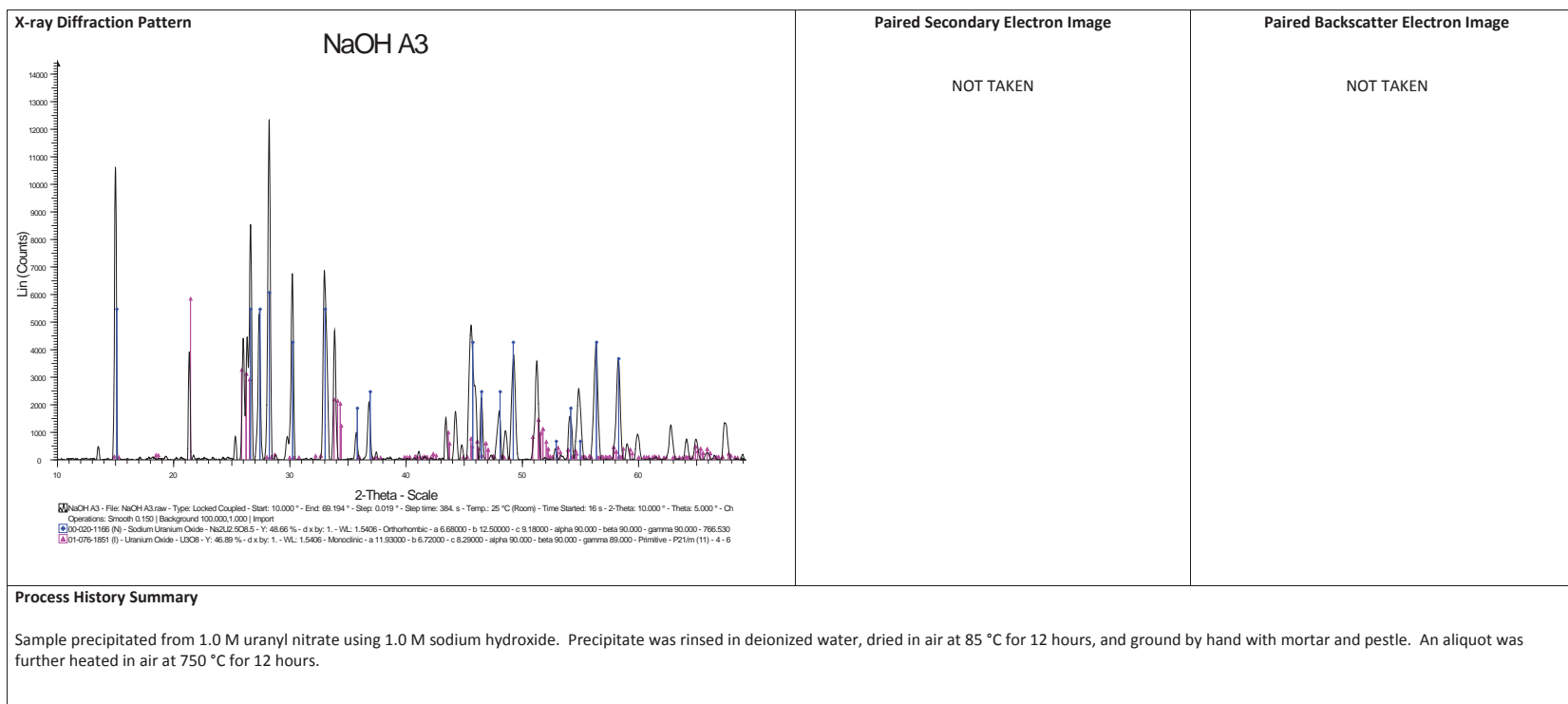
Morphology of the precipitate uranyl nitrate and sodium hydroxide heated to 600 °C



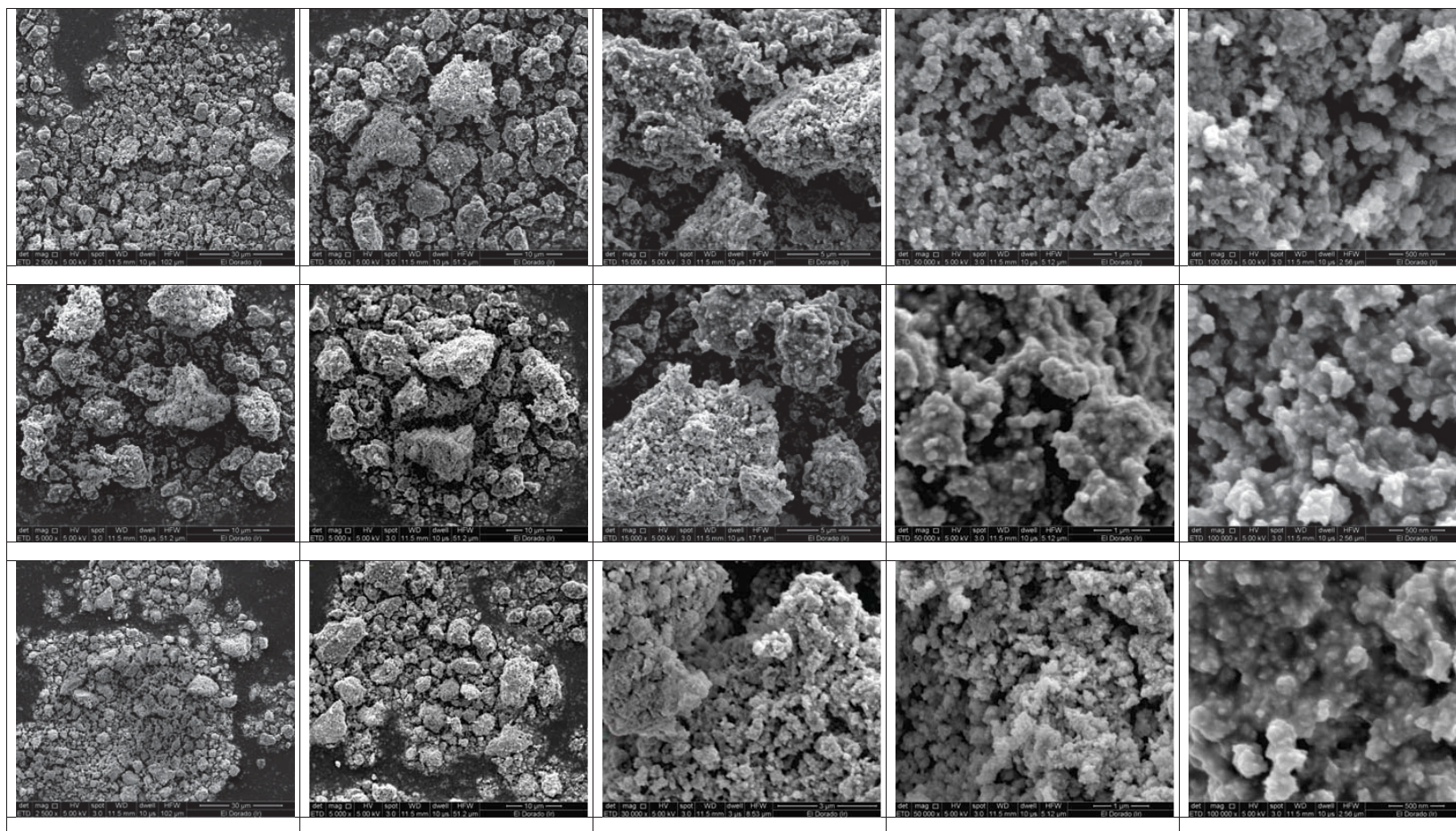


Morphology of the precipitate uranyl nitrate and sodium hydroxide heated to 750 °C

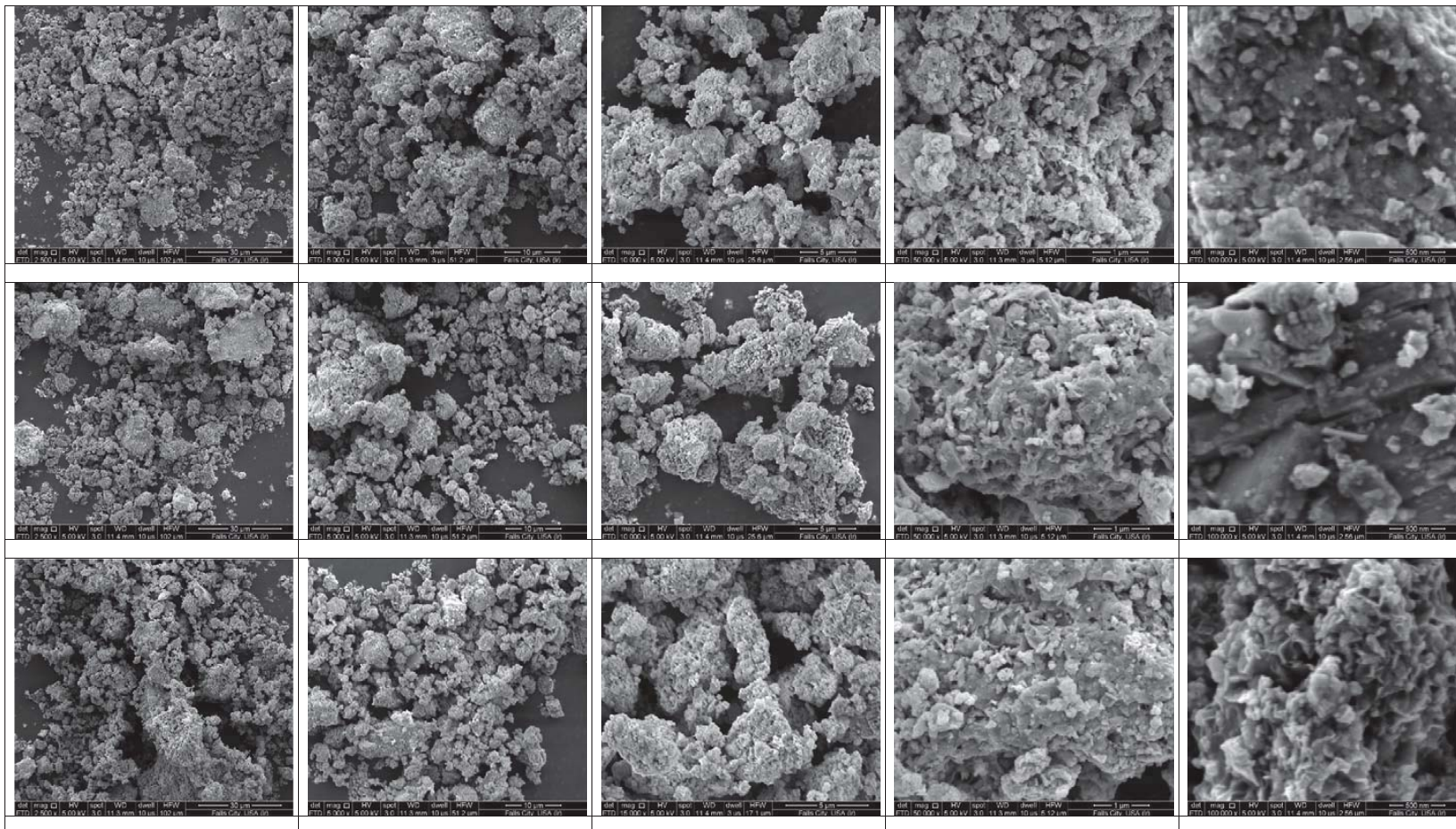


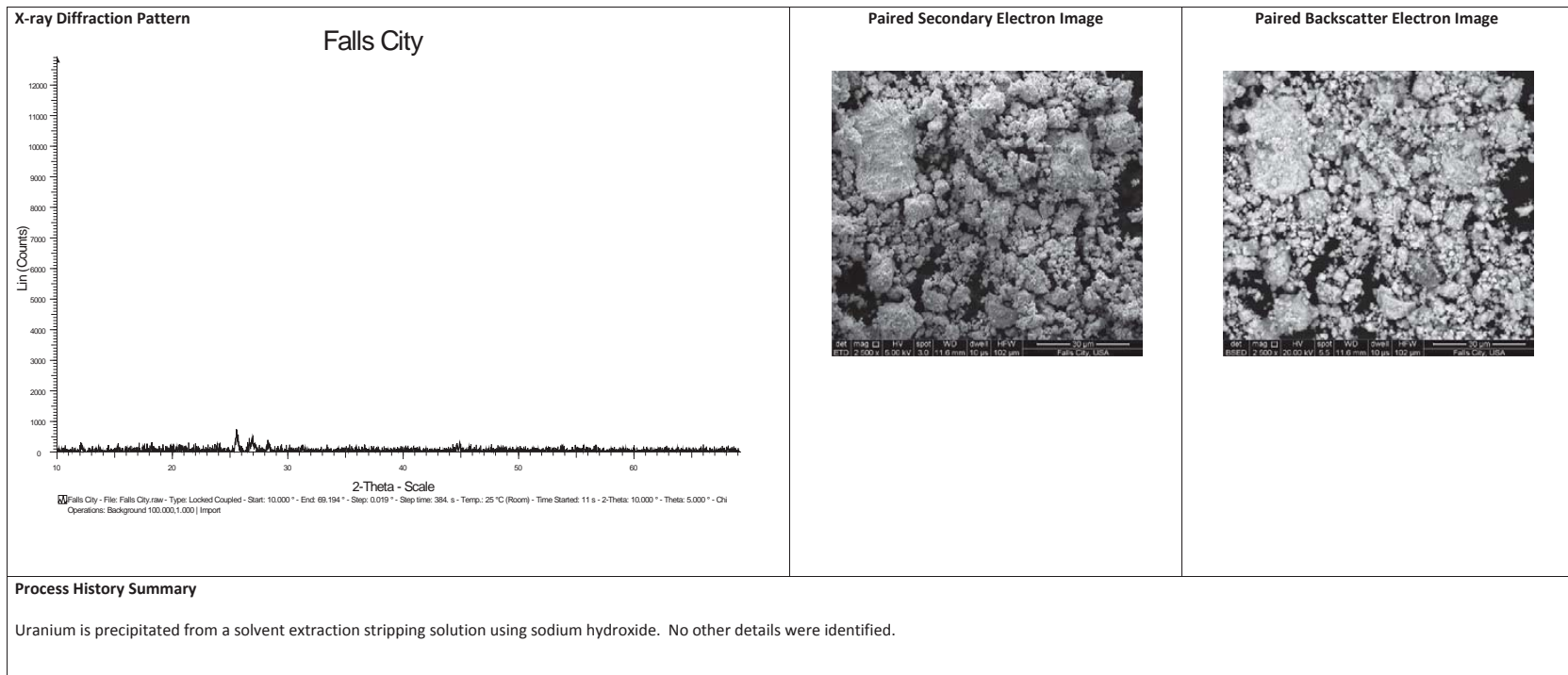


Morphology of uranium ore concentrate from the El Dorado facility in Northwest Territories, Canada

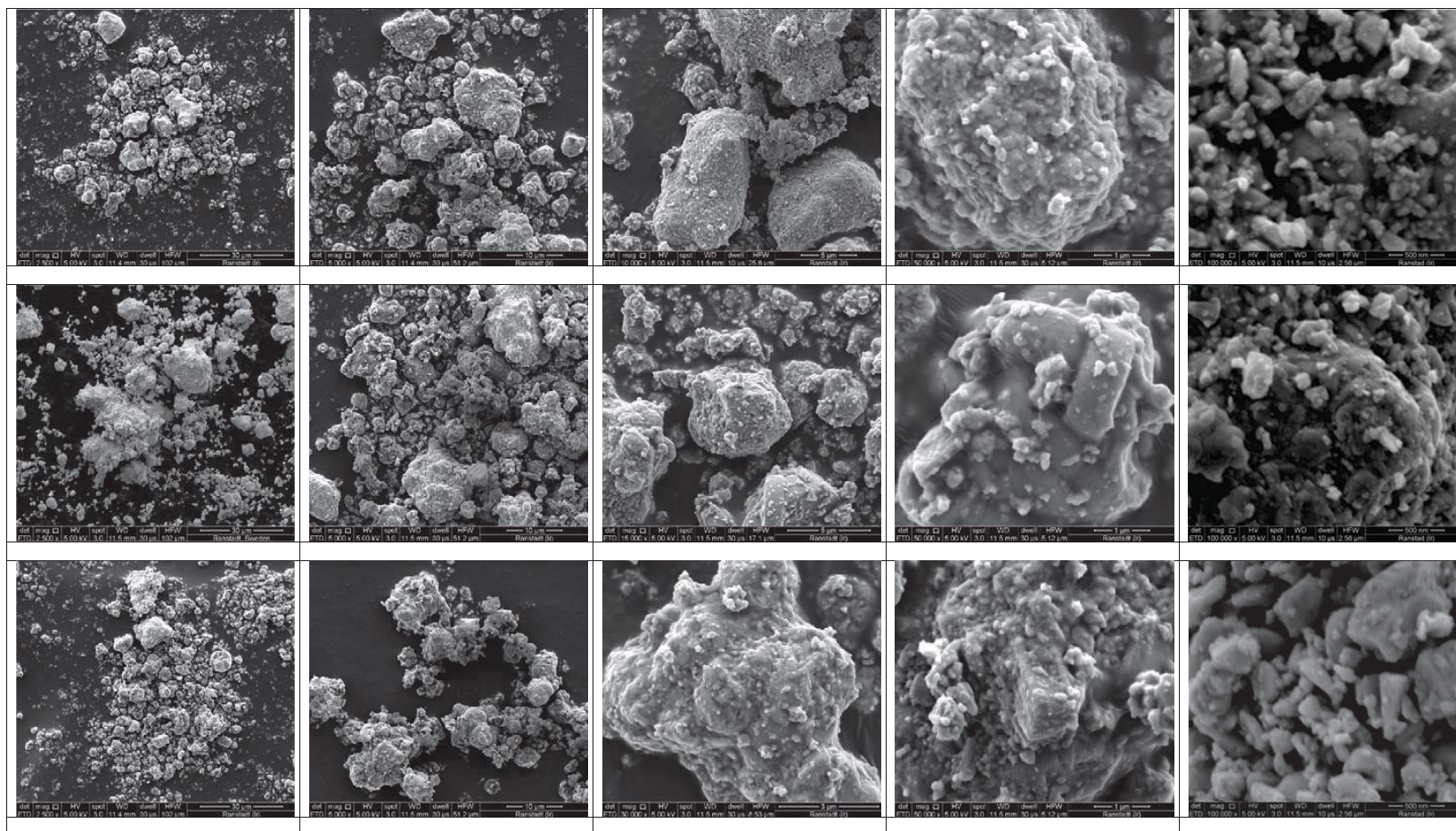


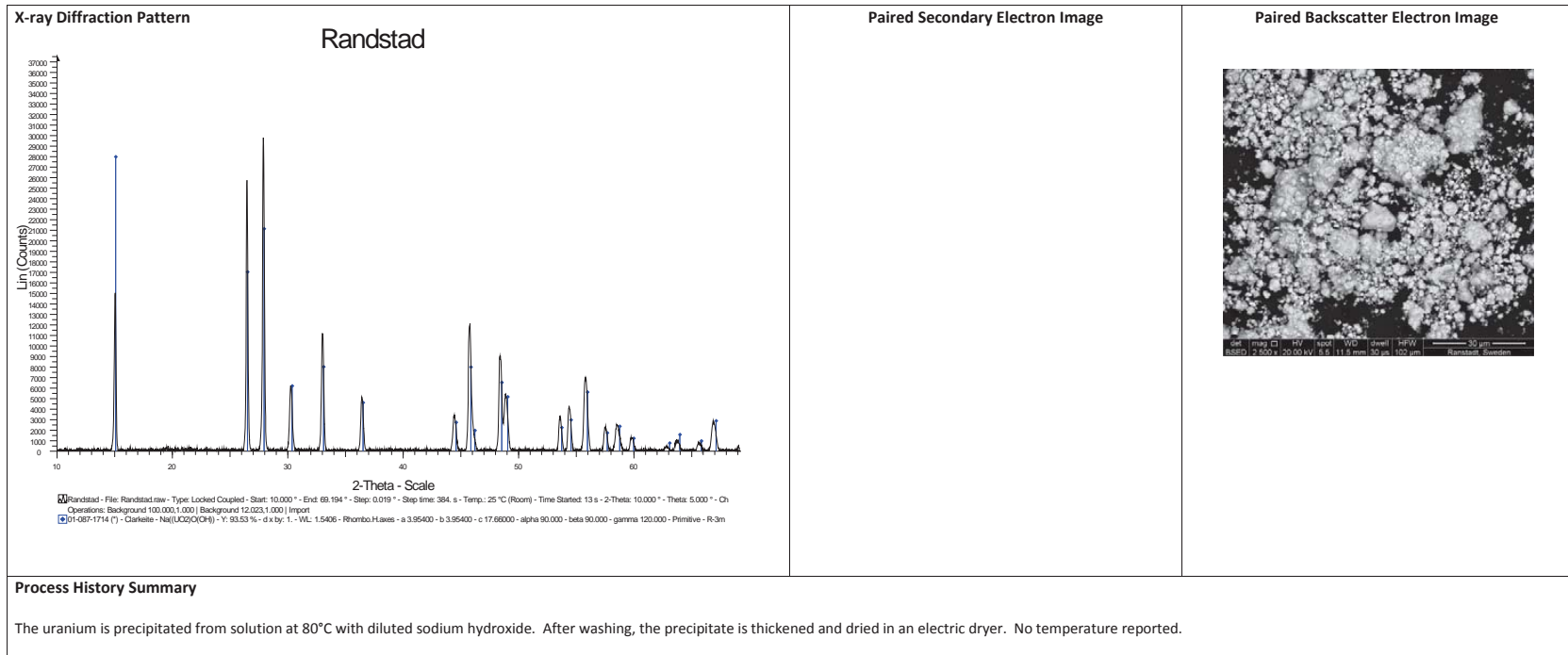
Morphology of uranium ore concentrate from the Sequehanna Western Facility in Falls City, Texas, USA



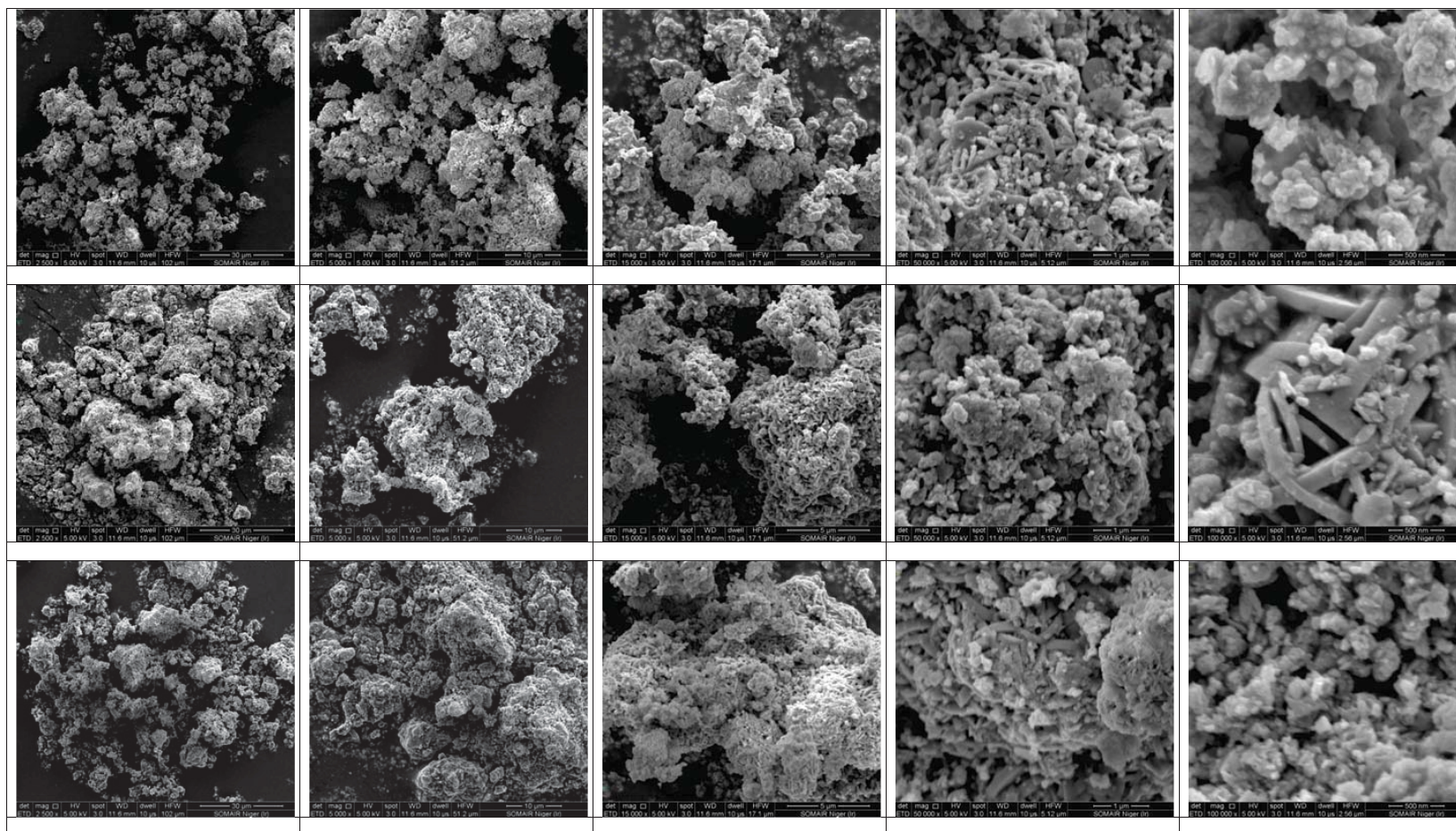


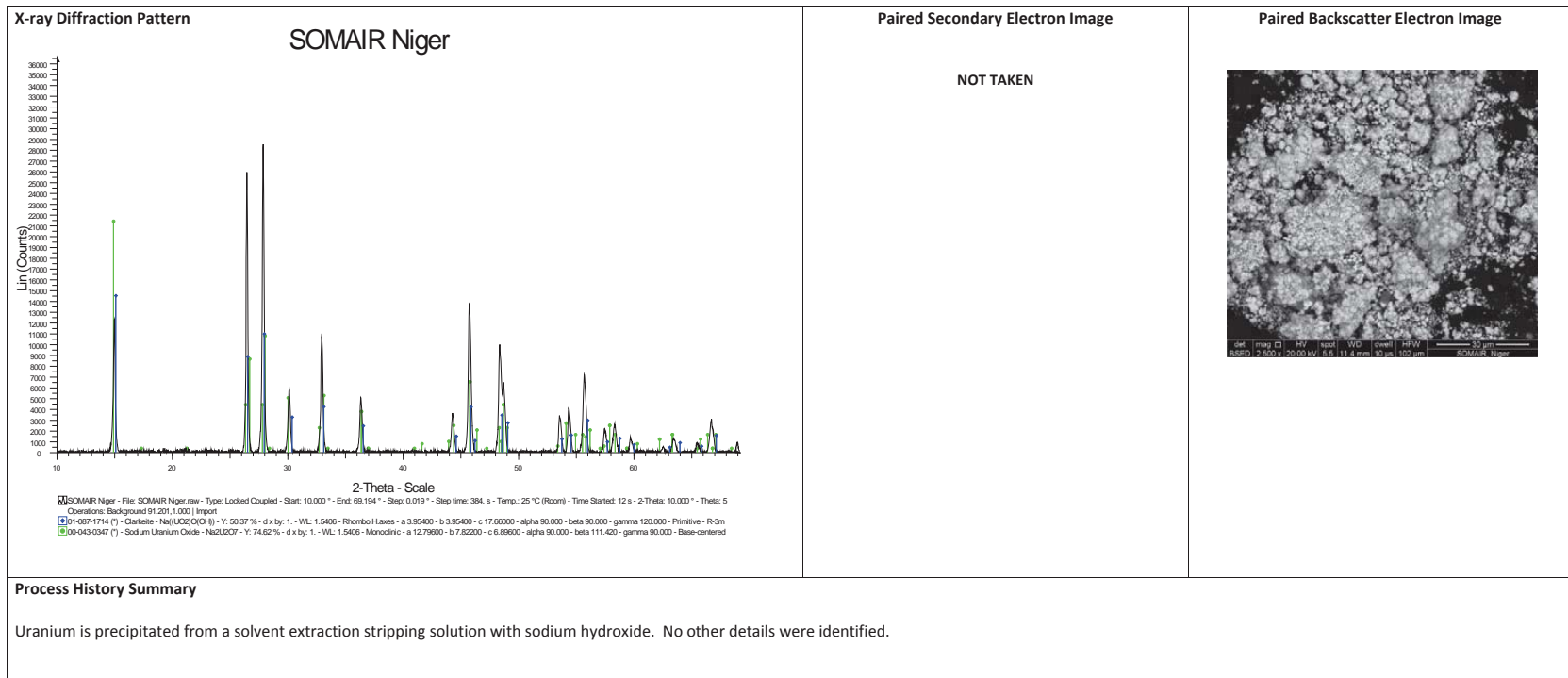
Morphology of uranium ore concentrate from the Ranstad facility in Sweden



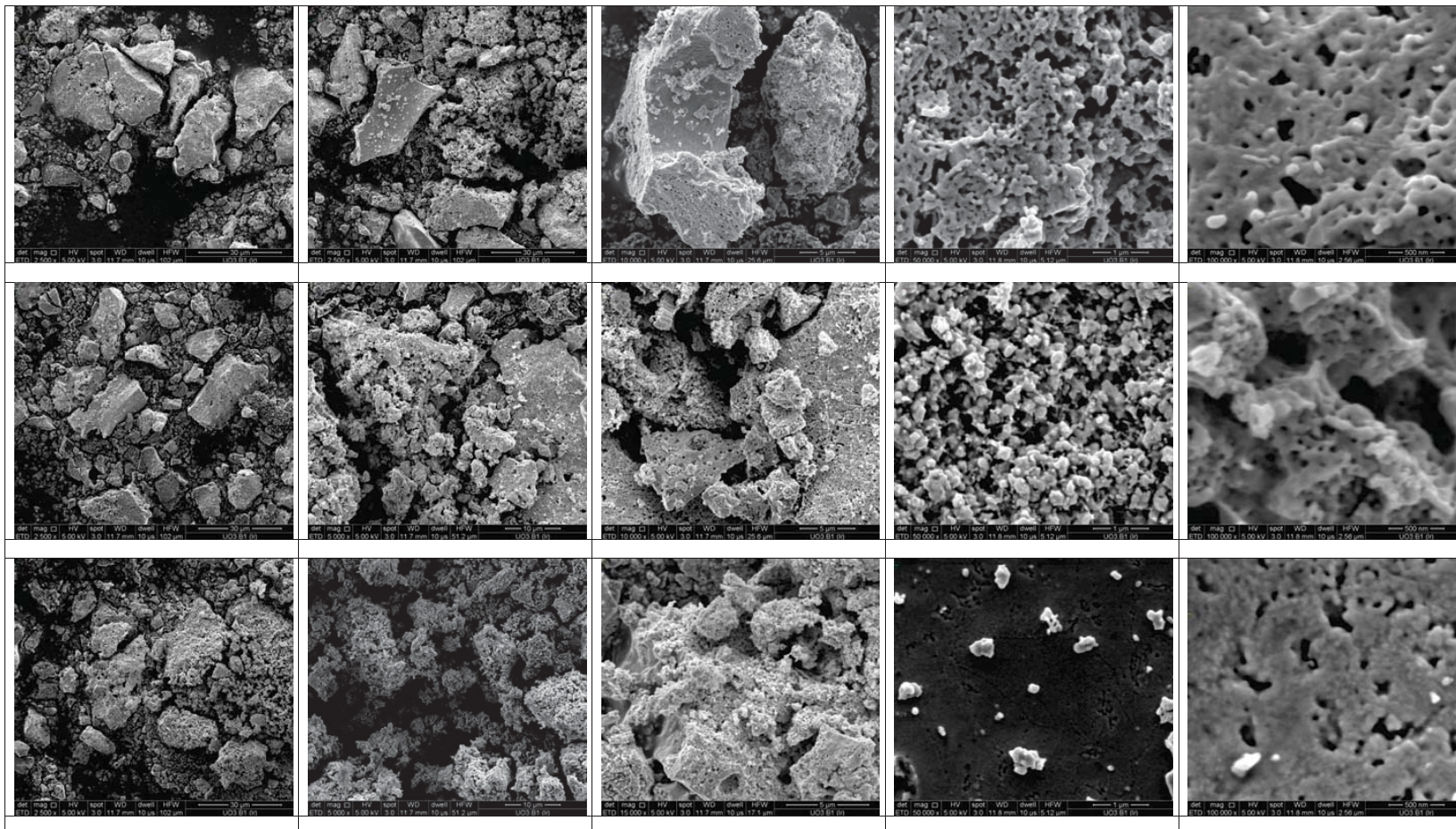


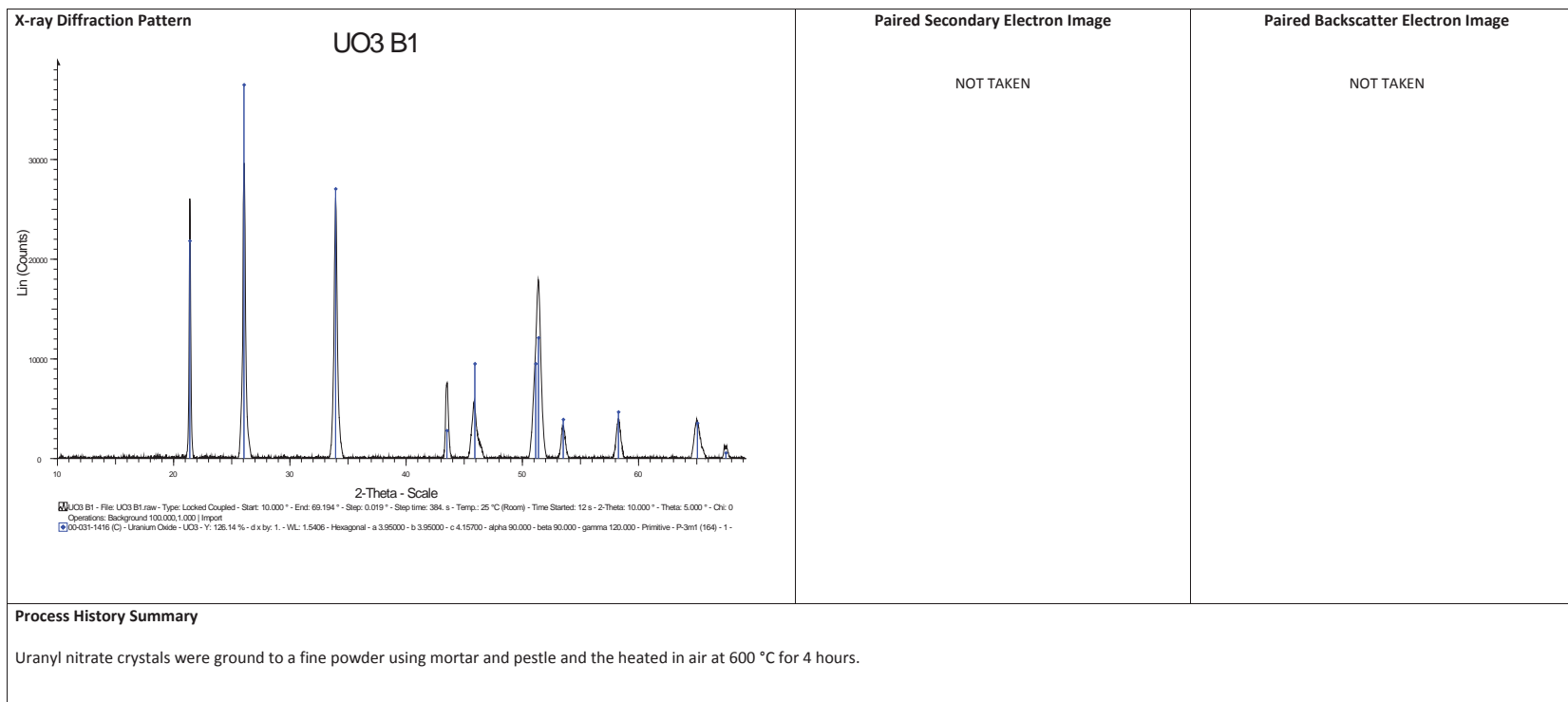
Morphology of uranium ore concentrate from the SOMAIR facility in Niger



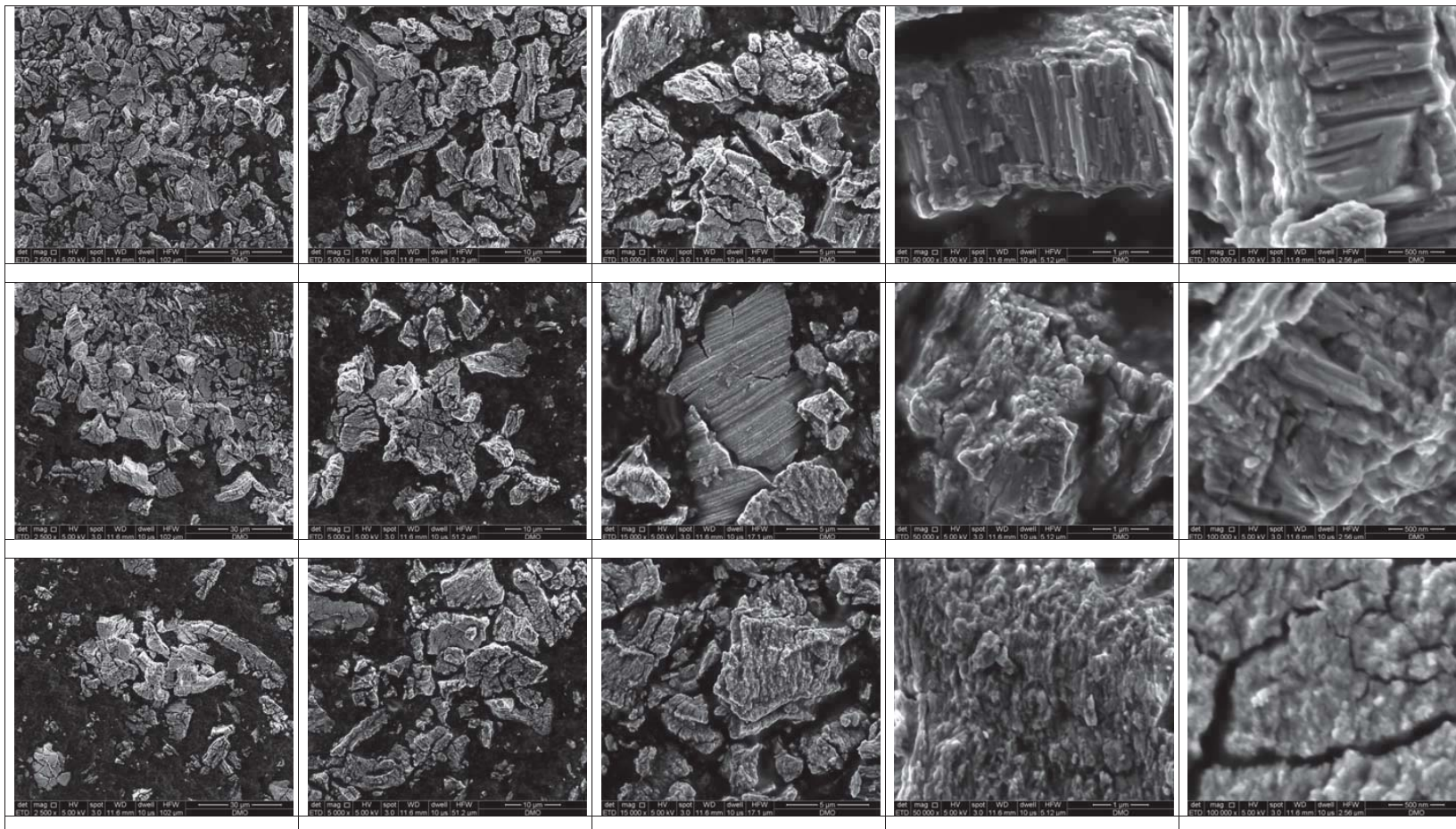


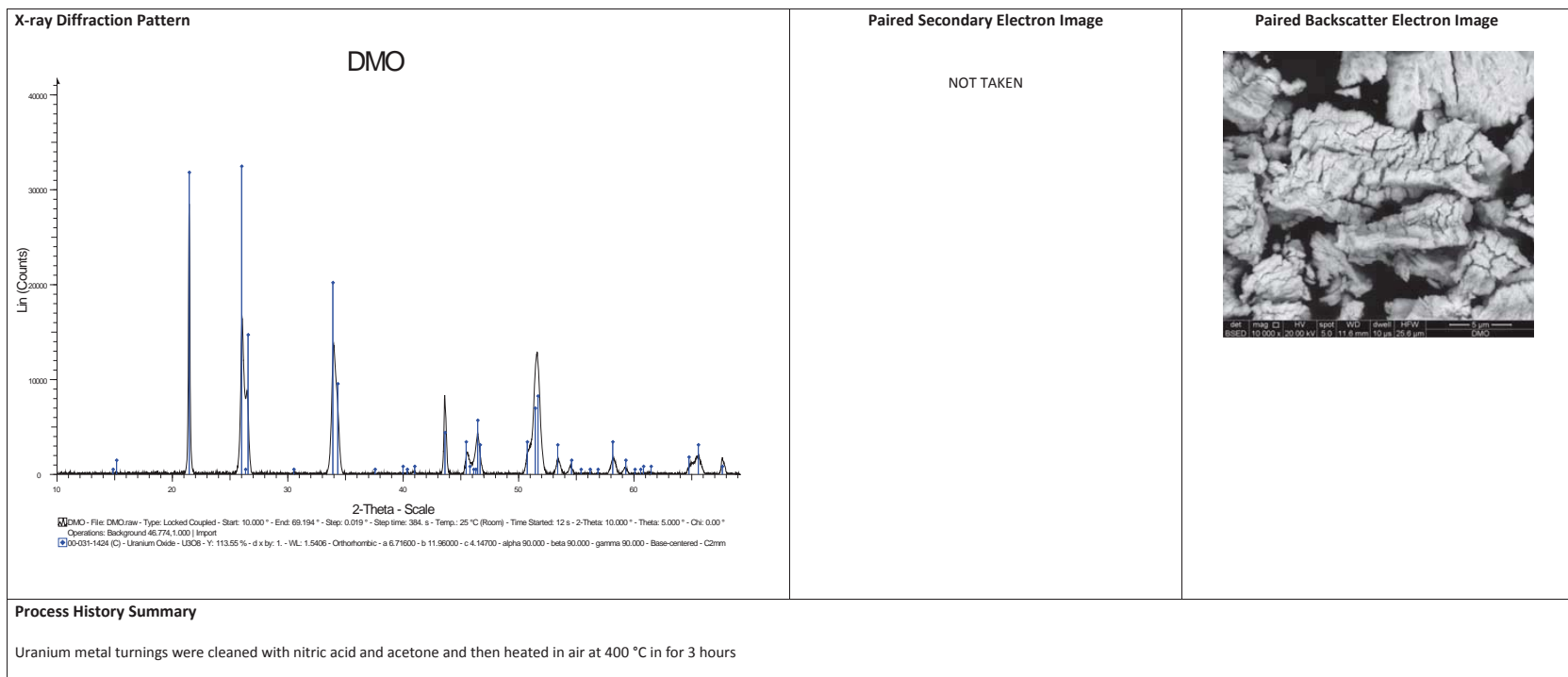
Morphology of uranyl hexanitrate heated to 600 °C for 4 hours



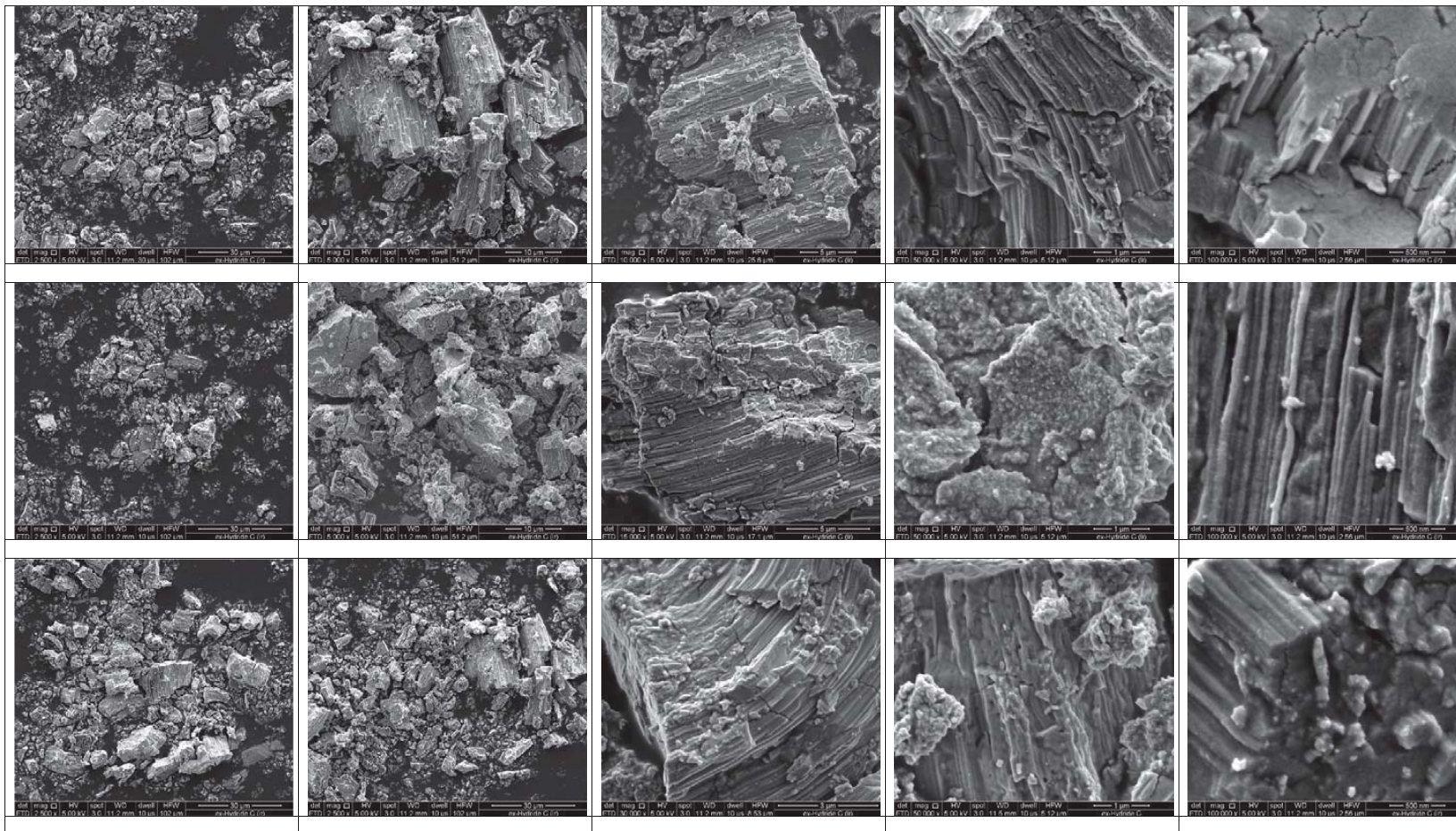


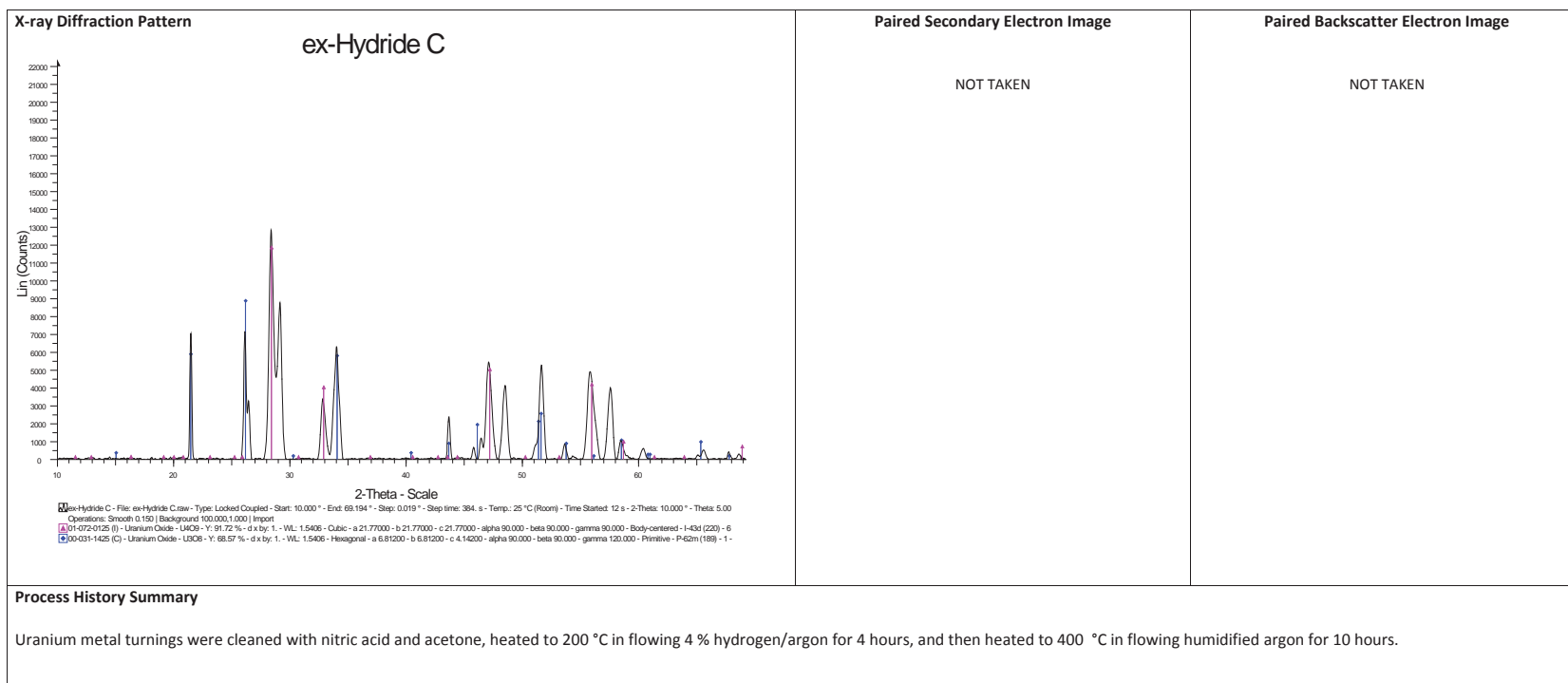
Morphology of uranium metal turnings directly heated to 400 °C



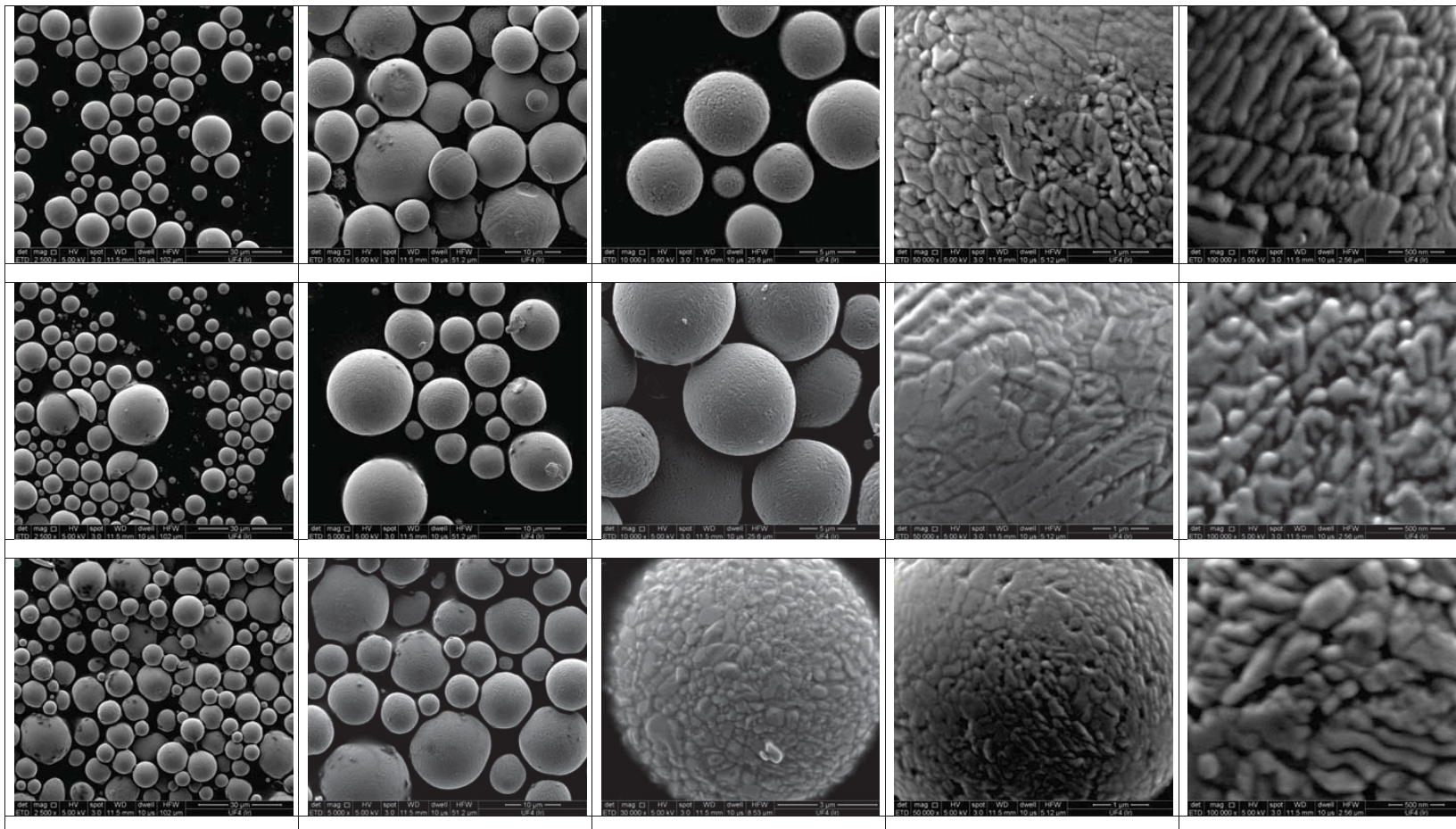


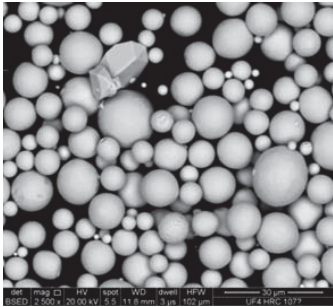
Morphology of uranium hydride heated to 400 °C



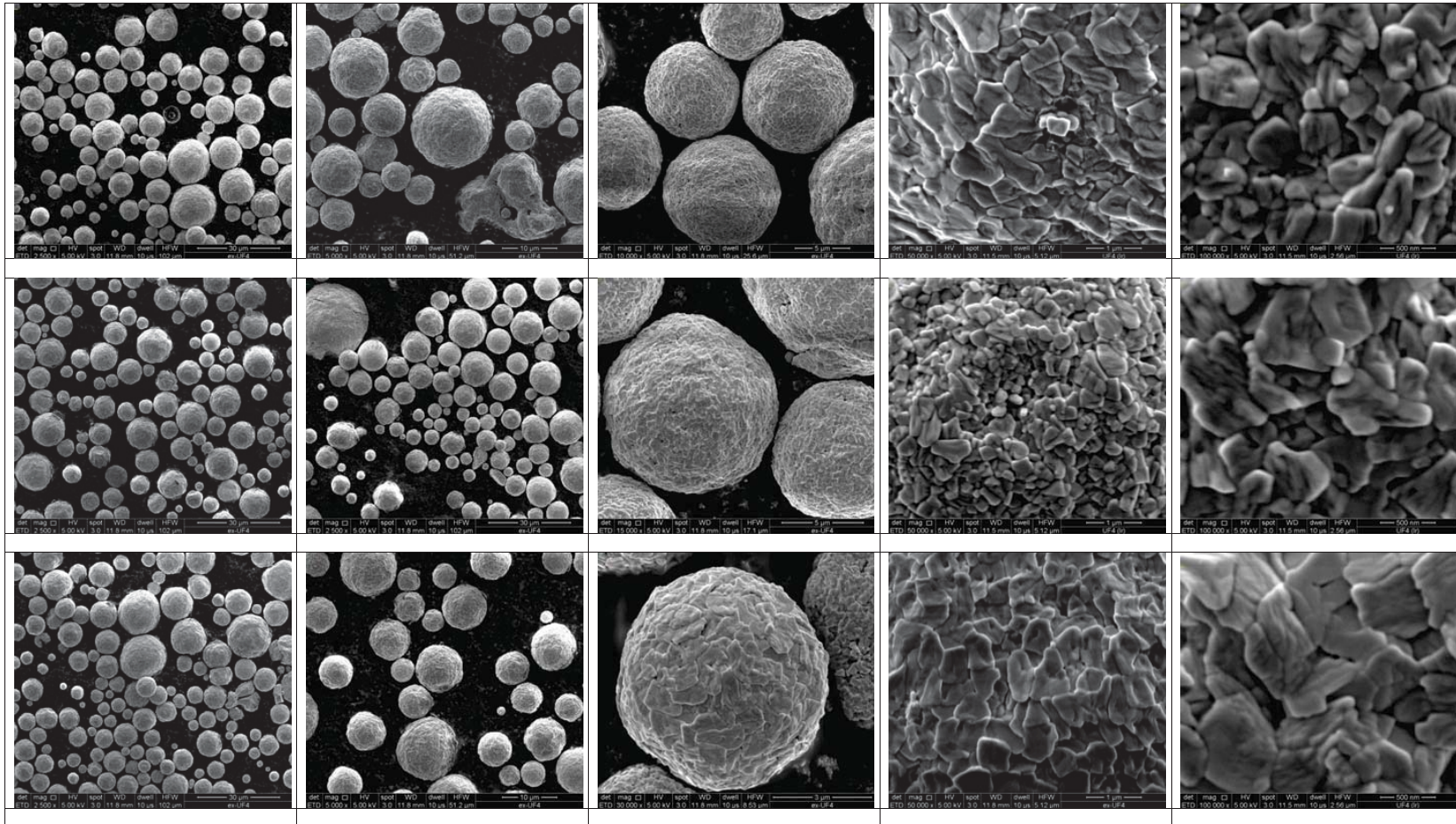


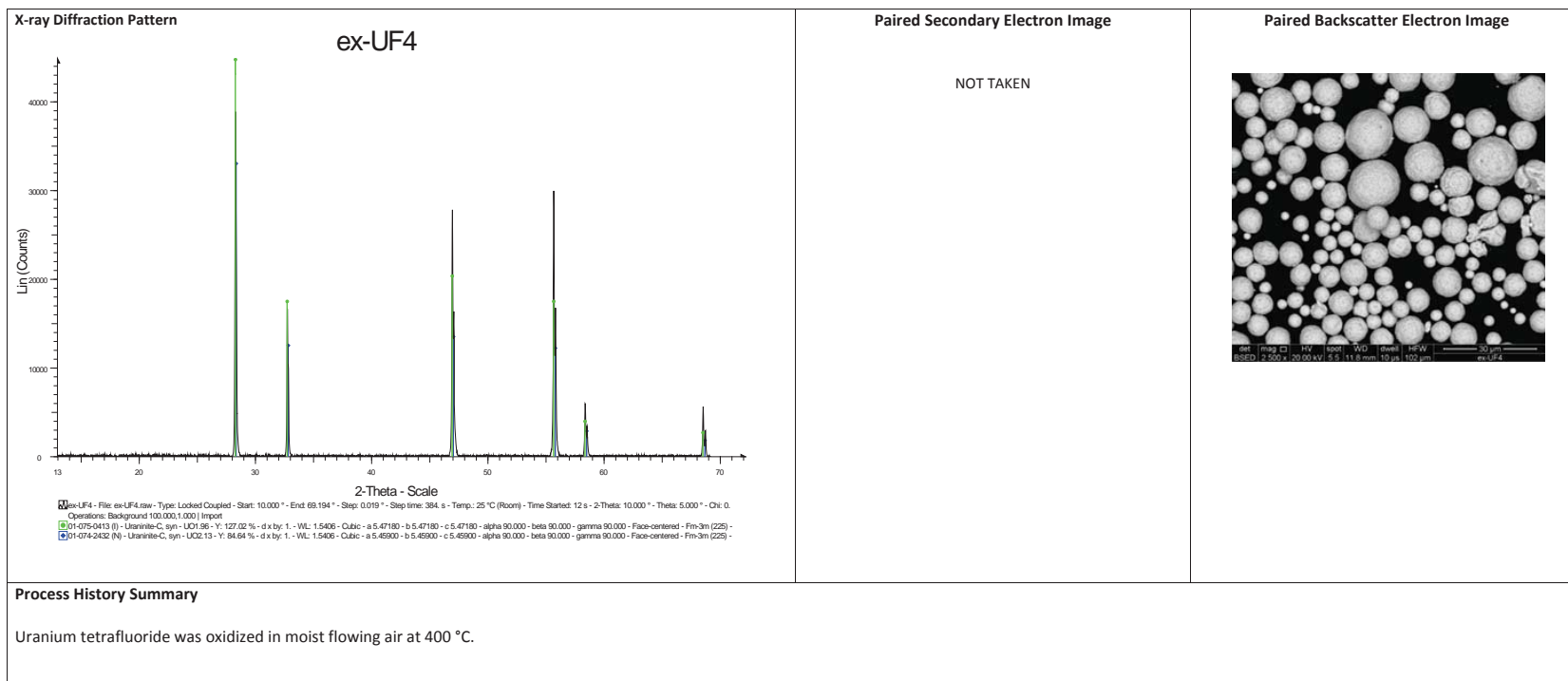
Morphology of purchased uranium tetrafluoride



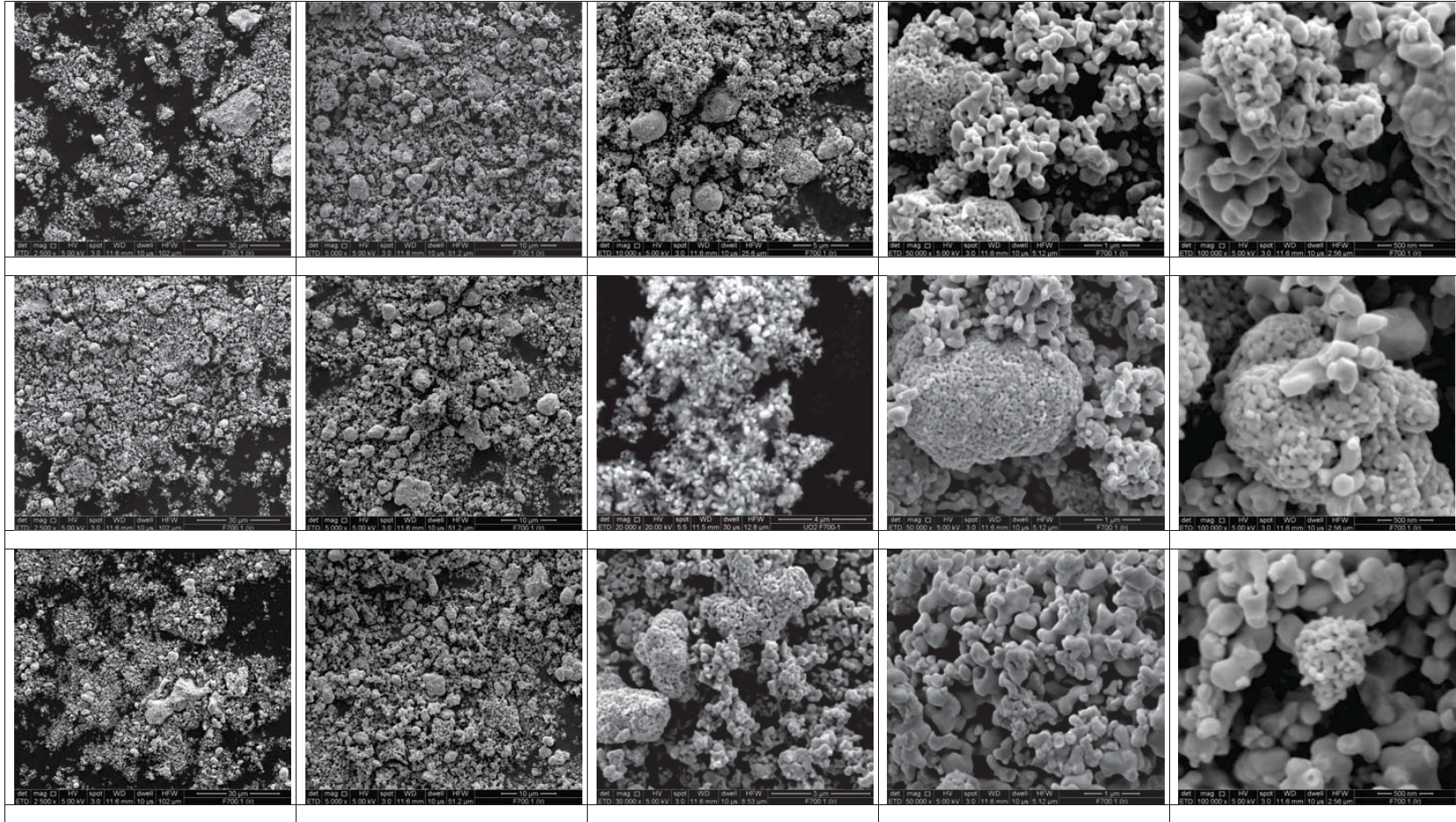
<p>X-ray Diffraction Pattern</p> <p>NOT TAKEN</p>	<p>Paired Secondary Electron Image</p> <p>NOT TAKEN</p>	<p>Paired Backscatter Electron Image</p> 
<p>Process History Summary</p> <p>Uranium tetrafluoride purchased from International Bioanalytical Industries, Inc, Florida</p>		

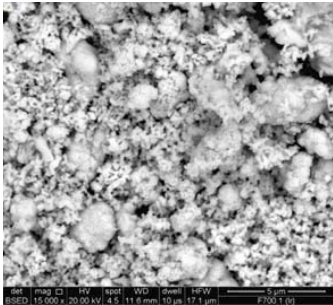
Morphology of uranium tetrafluoride heated in moist air at 400 °C





Morphology of a commercially produced uranium dioxide powder blend



X-ray Diffraction Pattern NOT TAKEN	Paired Secondary Electron Image NOT TAKEN	Paired Backscatter Electron Image  <p>det mag z HV spot WD dwell HV-W 5 µm SEPD 15.000 20.00 kV 4.5 11.6 mm 10 µs 17.4 µm P100 T 01</p>
Process History Summary	Energy Dispersive Spectroscopy NOT TAKEN	

References

- [1] U. S. Joint Working Group of the American Physical Society and the American Association for the Advancement of Science, "Nuclear Forensics: Role, State of the Art, and Program Needs," 2008.
- [2] "Communique of the Washington Nuclear Security Summit." Apr-2010.
- [3] "Communique of the 2012 Seoul Nuclear Security Summit." Mar-2012.
- [4] 111th US Congress, *Nuclear Forensics and Attribution Act*. 2010.
- [5] Committee on Nuclear Forensics; National Research Council, "Nuclear Forensics: A Capability at Risk," National Research Council of the National Academies, Washington, D.C., 2010.
- [6] J. Davis, "The Attribution of WMD Events," *Homelandsecurity.org*, Apr-2003. [Online]. Available: <http://www.homelandsecurity.org/journal/Articles/davis.html>. [Accessed: 06-Sep-2010].
- [7] A. B. Carter, M. M. May, and W. J. Perry, "The day after: action following a nuclear blast in a US city," *The Washington Quarterly*, vol. 30, no. 4, pp. 19–32, 2007.
- [8] M. Miller, "Nuclear Attribution as Deterrence," *The Nonproliferation Revs.*, vol. 14, no. 1, pp. 33–60, Mar. 2007.
- [9] C. Talmadge, "Deterring a Nuclear 9/11," *The Washington Quarterly*, vol. 30, no. 2, pp. 21–34, 2007.
- [10] M. A. Levi, "Deterring State Sponsorship of Nuclear Terrorism," Council on Foreign Relations, CRS No 39, Sep. 2008.
- [11] K. J. Moody, I. D. Hutcheon, and P. M. Grant, *Nuclear Forensic Analysis*. Boca Raton, FL: Taylor & Francis, 2005.
- [12] M. J. Kristo, D. K. Smith, S. Niemeyer, and G. B. Dudder, "Model Action Plan for Nuclear Forensics and Nuclear Attribution," Lawrence Livermore National Laboratory, Livermore, CA, UCRL-TR-202675, 2004.
- [13] K. Mayer, M. Wallenius, and I. Ray, "Nuclear forensics: A methodology providing clues on the origin of illicitly trafficked nuclear materials," *Analyst*, vol. 130, no. 4, p. 433, 2005.
- [14] K. Mayer, M. Wallenius, and T. Fanghänel, "Nuclear forensic science—From cradle to maturity," *Journal of Alloys and Compounds*, vol. 444, pp. 50–56, 2007.
- [15] E. Keegan, S. Richter, I. Kelly, H. Wong, P. Gadd, H. Kuehn, and A. Alonso-Munoz, "The provenance of Australian uranium ore concentrates by elemental and isotopic analysis," *Applied Geochemistry*, vol. 23, no. 4, pp. 765–777, 2008.
- [16] Z. Varga, M. Wallenius, K. Mayer, E. Keegan, and S. Millet, "Application of Lead and Strontium Isotope Ratio Measurements for the Origin Assessment of Uranium Ore Concentrates," *Anal. Chem.*, vol. 81, no. 20, pp. 8327–8334, Oct. 2009.
- [17] M. J. Kristo and S. J. Tumey, "The State of Nuclear Forensics," *Nuclear Instruments and Methods in Physics Research Section B: Beam Interactions with Materials and Atoms*, 2012.

- [18] E. P. Hastings, C. Lewis, J. FitzPatrick, D. Rademacher, and L. Tandon, "Characterization of depleted uranium oxides fabricated using different processing methods," *J Radioanal Nucl Chem*, vol. 276, no. 2, pp. 475–481, May 2008.
- [19] Z. Varga, B. Öztürk, M. Meppen, K. Mayer, M. Wallenius, and C. Apostolidis, "Characterization and classification of uranium ore concentrates (yellow cakes) using infrared spectrometry," *Radiochimica Acta*, p. 110822022707002, Aug. 2011.
- [20] V. A. Orlov, "Illicit Nuclear Trafficking & the new agenda," International Atomic Energy Agency, IAEA Bulletin 46/1, Jun. 2004.
- [21] J. J. Katz, L. R. Morss, N. M. Edelstein, and J. Fuger, *The Chemistry of the Actinide and Transactinide Elements*, 3rd ed. Netherlands: Springer, 2006.
- [22] J. W. Clegg and D. . Foley, *Uranium Ore Processing*. Reading, Massachusetts: Addison-Wesley Publishers Company, Inc, 1958.
- [23] P. D. Wilson, *The Nuclear Fuel Cycle: From Ore to Waste*. Oxford University Press, 1996.
- [24] R. C. Merritt, *The extractive metallurgy of uranium*. US Atomic Energy Commission, 1971.
- [25] J. L. Woolfrey, "The Preparation of UO₂ Powder: Effect of Ammonium Uranate Properties," *Journal of Nuclear Materials*, vol. 74, pp. 123–131, 1978.
- [26] J. Janov, P. G. Alfredson, and V. K. Vilkaitis, "Influence of precipitation conditions on the properties of ammonium diuranate and uranium dioxide powders," Australian Atomic Energy Commission, Lucas Heights, Australia, AAEC/E220, 1971.
- [27] B. N. Murty, P. Balakrishna, R. B. Yadav, and C. Ganguly, "Influence of temperature of precipitation on agglomeration and other powder characteristics of ammonium diuranate," *Powder Technology*, vol. 115, no. 2, pp. 167–183, 2001.
- [28] H. Assmann and M. Becker, "Technology of UO₂ Fuel Fabrication by the AUC Powder Process," *Transactions of the American Nuclear Society*, vol. 31, pp. 147–148, 1979.
- [29] A. Mellah, S. Chegrouche, and M. Barkat, "The precipitation of ammonium uranyl carbonate (AUC): Thermodynamic and kinetic investigations," *Hydrometallurgy*, vol. 85, pp. 163–171, 2007.
- [30] A. E. Cahill and L. E. Burkhart, "Continuous precipitation of uranium with hydrogen peroxide," *Metallurgical and Materials Transactions B*, vol. 21, no. 5, pp. 819–826, 1990.
- [31] K. H. Gayer and L. C. Thompson, "The solubility of uranium peroxide in acidic and basic media at 25 C," *Canadian Journal of Chemistry*, vol. 36, pp. 1649–1652, 1958.
- [32] E. H. P. Cordfunke and B. O. Loopstra, "Sodium uranates: Preparation and thermochemical properties," *Journal of Inorganic and Nuclear Chemistry*, vol. 33, no. 8, pp. 2427–2436, 1971.
- [33] S. E. Ion and R. H. Watson, "20 Years of Production of UO₂ by the Integrated Dry Route-A BNFL Perspective on Dry Conversion," *A Collection of Papers on Engineering Aspects of Fabrication of Ceramics: Ceramic Engineering and Science Proceedings*, vol. 14, no. 11/12, pp. 149–154, 2000.
- [34] G. G. Butler, G. M. Gillies, T. J. Heal, and J. E. Littlechild, "Conversion of uranium hexafluoride to oxides of uranium," U.S. Patent 4,397,82409-Aug-1983.

- [35] J. E. Hart, D. L. Shuck, and W. L. Lyon, "Production of uranium dioxide," U.S. Patent 4,053,559-11-Oct-1977.
- [36] A. G. Dada and W. R. De Hollander, "Process for producing uranium dioxide rich compositions from uranium hexafluoride," U.S. Patent 3,796,672-12-Mar-1974.
- [37] J. E. Littlechild and G. M. Gillies, "Production of uranium dioxide in a rotary kiln," U.S. Patent 3,845,193-29-Oct-1974.
- [38] R. Artaud, "Method of fabrication of uranium oxide by the dry processing route and a device for the practical application of the method," U.S. Patent 4,112,055-05-Sep-1978.
- [39] I. E. Knudsen, N. M. Levitz, and S. Lawroski, "Preliminary Report on Conversion of Uranium Hexafluoride to Uranium Dioxide in a One-step Fluid-bed Process," Argonne National Laboratory, ANL-5023, Aug. 1959.
- [40] I. E. Knudsen, N. M. Levitz, and A. A. Jonke, "Engineering development of fluid-bed fluoride volatility processes, Part 6, Preparation of dense uranium dioxide particles from uranium hexafluoride in a fluidized bed," Argonne National Laboratory, ANL-6902, Dec. 1964.
- [41] I. E. Knudsen, "Production of uranium dioxide," U.S. Patent 4,020,146-26-Apr-1977.
- [42] K. Radford, L. Lyon, and J. Hart, "Fluid Bed Conversion of UF₆ to UO₂," *American Ceramic Society Bulletin*, vol. 58, no. 2, pp. 219–232, 1979.
- [43] N. P. Galkin, U. D. Veryatin, I. F. Yakhonin, A. F. Lugonov, and Y. M. Dymkov, "The conversion of uranium hexafluoride to dioxide," *Atomic Energy*, vol. 52, no. 1, pp. 45–49, 1982.
- [44] J. I. Federer, W. C. Robinson, and F. H. Patterson, "Conversion of UF₆ to UO₂ in a flame reactor," *Nuclear Applications*, vol. 6, no. 4, pp. 298–306, 1969.
- [45] R. L. Heestand and C. F. Leitten, "Thermochemical reduction of uranium hexafluoride for the direct fabrication of uranium dioxide ceramic fuels," *Nuclear Applications*, vol. 1, pp. 584–588, 1965.
- [46] J. W. Valley, H. Taylor Jr, and J. R. O'Neil, *Stable Isotopes in High Temperature Geological Processes*, vol. 16. Mineralogical Society of America, 1986.
- [47] J. Hoefs, *Stable isotope geochemistry*. Springer Verlag, 2009.
- [48] P. Baertschi, "Absolute O-18 content of standard mean ocean water," *Earth and Planetary Science Letters*, vol. 31, no. 3, pp. 341–344, Aug. 1976.
- [49] W. Meier-Augenstein, *Stable Isotope Forensics : An Introduction to the Forensic Application of Stable Isotope Analysis*. Hoboken, NJ: Wiley-Blackwell, 2010.
- [50] "Stable Isotope Primer and Some Hydrological Applications." [Online]. Available: http://serc.carleton.edu/microbelife/research_methods/environ_sampling/stableisotopes.html. [Accessed: 20-Jan-2013].
- [51] J. Goldstein, D. Newbury, D. Joy, C. Lyman, and et al, *Scanning electron microscopy and x-ray microanalysis*, 3rd ed. Kluwer Academic/ Plenum Publishers, 2003.
- [52] J. Atteberry, "HowStuffWorks 'The Key Components of a Scanning Electron Microscope'." [Online]. Available: <http://science.howstuffworks.com/scanning-electron-microscope2.htm>. [Accessed: 18-Nov-2012].
- [53] Phillips, "Scanning Electron Microscopy/Electron Probe X-ray Microanalysis." [Online]. Available:

- <http://www.innovationservices.philips.com/sites/default/files/materials-analysis-sem.pdf>. [Accessed: 18-Nov-2012].
- [54] S. Lowell, J. E. Shields, M. A. Thomas, and M. Thommes, *Characterization of porous solids and powders: surface area, pore size, and density*. Springer, 2006.
- [55] S. Brunauer, P. H. Emmett, and E. Teller, "Adsorption of gases in multimolecular layers," *Journal of the American Chemical Society*, vol. 60, no. 2, pp. 309–319, 1938.
- [56] University of Oxford, "Basic operating principles of the Sorptomatic 1990," *The University of Oxford Surface Analysis Facility Web Site*. [Online]. Available: <http://saf.chem.ox.ac.uk/Instruments/BET/sorpoptprin.html#ads>. [Accessed: 18-Nov-2012].
- [57] C. Suryanarayana and M. Grant Norton, *X-Ray Diffraction: A Practical Approach*. Springer, 1998.
- [58] USGS, "USGS OFR01-041: X-Ray Diffraction Primer." [Online]. Available: <http://pubs.usgs.gov/of/2001/of01-041/htmldocs/xrpd.htm>. [Accessed: 18-Nov-2012].
- [59] D. A. Burns and E. W. Ciurczak, *Handbook of Near-Infrared Analysis*, 3rd Ed. New York, NY: Marcel Dekker, 2007.
- [60] H. Taylor and S. Epstein, "Relationship between O18/O16 ratios in coexisting minerals of igneous and metamorphic rocks. Part 1. Principles and experimental results," *Geol. Soc. Amer. Bull*, vol. 73, pp. 461–480, 1962.
- [61] J. Borthwick and R. S. Harmon, "A note regarding CIFJ as an alternative to BrF5 for oxygen isotope analysis," *Geochimica et Cosmochimica Acta*, vol. 46, pp. 1665–1668, 1982.
- [62] G. Tamborini, D. Phinney, O. Bildstein, and M. Betti, "Oxygen isotopic measurements by secondary ion mass spectrometry in uranium oxide microparticles: A nuclear forensic diagnostic," *Anal. Chem*, vol. 74, no. 23, pp. 6098–6101, 2002.
- [63] M. N. Pons, H. Vivier, K. Belaroui, B. Bernard-Michel, F. Cordier, D. Oulhana, and J. A. Dodds, "Particle morphology: from visualization to measurement," *Powder Technology*, vol. 103, no. 1, pp. 44–57, 1999.
- [64] M. R. Cox and M. Budhu, "A practical approach to grain shape quantification," *Engineering Geology*, 2007.
- [65] X. Arnould, M. Coster, J. L. Chermant, L. Chermant, T. Chartier, and A. Elmoataz, "Segmentation and grain size of ceramics," *Image Anal Stereol*, vol. 20, no. 1, pp. 131–5, 2001.
- [66] W. S. Rasband, *ImageJ*. Bethesda, MD: US National Institutes of Health, 1997.
- [67] R. Porter, C. Ruggiero, D. Hush, N. Harvey, P. Kelly, W. Scoggins, and L. Tandon, "Interactive image quantification tools in nuclear material forensics," *Proceedings of SPIE*, vol. 7877, 2011.
- [68] American Society for Testing and Materials, "Standard Test Method for Determining Average Grain Size ASTM E-112-96." ASTM International, 2004.

- [69] International Standards Organization, "ISO 13322-1 Particle size analysis-Image analysis methods. Part 1: Static image analysis methods." International Standards Organization, 2005.
- [70] H. G. Merkus, *Particle Size Measurements: Fundamentals, Practice, Quality*. Netherlands: Springer, 2009.
- [71] H. Masuda and K. Iino, "Theoretical Study of the Scatter of Experimental Data Due to Particle-Size- Distribution," *J. Chem. Eng., Japan*, vol. 4, pp. 60–70, 1971.
- [72] H. Masuda and K. Gotoh, "Study on the sample size required for the estimation of mean particle diameter," *Advanced Powder Technology*, vol. 10, pp. 159–173, 1999.
- [73] H. Yoshida, T. Igushi, T. Yamamoto, and H. Masuda, "Theoretical calculation of fundamental uncertainty region based on the maximum and/or the minimum size in the preparation of standard reference particles for particle size measurement," *Advanced Powder Technology*, vol. 22, pp. 43–49, 2011.
- [74] M. H. Bharati, J. J. Liu, and J. F. MacGregor, "Image texture analysis: methods and comparisons," *Chemometrics and intelligent laboratory systems*, vol. 72, no. 1, pp. 57–71, 2004.
- [75] M. Tuceryan and A. K. Jain, "Texture analysis," *Handbook of pattern recognition and computer vision*, vol. 2, pp. 207–248, 1993.
- [76] P. Soille, "Morphological texture analysis: an introduction," *Morphology of Condensed Matter*, pp. 215–237, 2002.
- [77] R. M. Haralick, "Statistical and structural approaches to texture," *Proceedings of the IEEE*, vol. 67, no. 5, pp. 786–804, 1979.
- [78] R. W. Connors, M. M. Trivedi, and C. A. Harlow, "Segmentation of a high-resolution urban scene using texture operators," *Computer Vision, Graphics, and Image Processing*, vol. 25, no. 3, pp. 273–310, 1984.
- [79] A. P. Tinke, A. Carnicer, R. Govoreanu, G. Scheltjens, L. Lauwerysen, N. Mertens, K. Vanhoutte, and M. E. Brewster, "Particle shape and orientation in laser diffraction and static image analysis size distribution analysis of micrometer sized rectangular particles," *Powder Technology*, vol. 186, no. 2, pp. 154–167, 2008.
- [80] "Nuclear Safeguards Education Portal | Material Definitions, Part 2." [Online]. Available: <http://nsspi.tamu.edu/nsep/courses/the-nuclear-fuel-cycle/introduction/material-definitions/material-definitions,-part-2>. [Accessed: 31-Dec-2012].
- [81] "Extraction - The Resource News." [Online]. Available: <http://uranium-plutonium.weebly.com/extraction.html>. [Accessed: 31-Dec-2012].
- [82] "Areva and Sogin sign reprocessing contract." [Online]. Available: <http://www.world-nuclear-news.org/newsarticle.aspx?id=13372>. [Accessed: 31-Dec-2012].
- [83] "IAEA: Iran activates second centrifuge - JPost - International." [Online]. Available: <http://www.jpost.com/International/Article.aspx?id=184265>. [Accessed: 31-Dec-2012].

- [84] "Uranium." [Online]. Available: <http://chemistry.about.com/od/periodictableelements/ig/Element-Photo-Gallery.-98/Uranium.htm>. [Accessed: 31-Dec-2012].
- [85] "File:B83 nuclear bomb trainer.jpg - Wikipedia, the free encyclopedia." [Online]. Available: http://en.wikipedia.org/wiki/File:B83_nuclear_bomb_trainer.jpg. [Accessed: 31-Dec-2012].
- [86] "File:Nuclear Power Plant 2.jpg - Wikipedia, the free encyclopedia." [Online]. Available: http://en.wikipedia.org/wiki/File:Nuclear_Power_Plant_2.jpg. [Accessed: 31-Dec-2012].
- [87] R. J. Barnes, M. S. Dhanoa, and S. J. Lister, "Standard Normal Variate Transformation and De-trending of Near-Infrared Diffuse Reflectance Spectra," *Applied Spectroscopy*, vol. 43, no. 5, pp. 772–777, Jul. 1989.
- [88] S. P. Collings, G. Catchpole, and G. Kirchner, "The Crow Butte ISL project- A case history," in *Innovations in uranium exploration, mining and processing techniques, and new exploration target areas*, Vienna, 1994, vol. IAEA-TECDOC-868, pp. 89–117.
- [89] A. B. Carino, "Rabbit Lake operation of Gulf Minerals Canada Limited," *Canadian Institute of Mining and Metallurgy Bulletin*, pp. 162–166, Jun. 1979.
- [90] IAEA, *Uranium Extraction Technology*. Vienna, Austria: International Atomic Energy Agency, 1993.
- [91] C. R. Edwards and A. J. Oliver, "Uranium processing: A review of current methods and technology," *JOM Journal of the Minerals, Metals and Materials Society*, vol. 52, no. 9, pp. 12–20, 2000.
- [92] J. R. Burger, "El Mesquite In Situ Leach Plant Is Mobil's First," *Engineering and Mining Journal*, vol. 182, no. 1, pp. 54–57, 1981.
- [93] Uranium One, "Uranium One - Uranium mining and exploration ::" [Online]. Available: <http://www.uranium1.com/indexu.php?section=uranium%20projects&page=7>. [Accessed: 17-Aug-2011].
- [94] Uranium Resources Inc, "Uranium Resources, Inc.," 2011. [Online]. Available: <http://www.uraniumresources.com/technology/2.htm>. [Accessed: 27-Aug-2011].
- [95] T. C. Vogt, E. T. Strom, P. B. Venuto, J. E. Winget, and M. W. Scoggins, "In-Situ Leaching of Crownpoint, New Mexico, Uranium Ore: Part 6-Section 9 Pilot Test," *Journal of Petroleum Technology*, vol. 36, no. 12, pp. 2243–2254, 1984.
- [96] P. G. Alfredson, "Australian Experience in the Production of Yellowcake and Uranium Fluorides," in *Production of Yellowcake and Uranium Fluorides*, Paris, France, 1980, pp. 149–178.
- [97] P. A. Baily, "Development of the ranger uranium milling operations," in *Uranium '82*, Toronto, Canada, 1982.
- [98] W. Floater, "The acid pressure leaching process for the Key Lake Project, Canada," in *Advances in uranium ore processing and recovery from non-conventional resources*, Vienna, 1985.

- [99] Cameco, "Cameco - Mining - Key Lake - Mining & Milling," 23-Oct-2009. [Online]. Available: http://www.cameco.com/mining/key_lake/mining_and_milling/. [Accessed: 17-Aug-2011].
- [100] M. Neven and L. Gormely, "Design of the Key Lake leaching process," in *Uranium '82*; Toronto, Canada, 1982.
- [101] IAEA, "Table A-1: Classification of commercial uranium extraction flowsheets," in *Uranium Ore Processing: Proceedings of an advisory group meeting November 24-26, 1975, Washington DC*, Vienna: International Atomic Energy Agency, 1976.
- [102] B. Keslar and D. Farbach, "Uranium extraction at Rossing," presented at the Uranium '82 12th Annual Hydrometallurgical Meeting, Toronto, Canada, 1982.
- [103] Rossing, "Rossing Uranium Mine- The production Process - from blasting to shipping -," 2011. [Online]. Available: http://www.rossing.com/uranium_production.htm. [Accessed: 17-Apr-2011].
- [104] S. A. Young, "Production of Uranium Oxide Concentrates by the Nuclear Fuels Corporation of South Africa," in *Production of Yellowcake and Uranium Fluorides*, Paris, France, 1980.
- [105] J. W. Griffith, *The Uranium Industry- Its History, Technology, and Prospects*, Mineral Report 12. Ottawa, Canada: Mineral Resources Division, Department of Energy, Mine and Resources, 1967.
- [106] N. Robb, V. Opratok, and L. S. Price, "Milliken's Two Stage Sulphuric Acid Leaching," *Canadian Institute of Mining and Metallurgy Bulletin*, vol. 56, p. 614, Jun. 1963.
- [107] J. Delavaine, "Uranium milling at COMUF," presented at the Uranium '82 12th Annual hydrometallurgical meeting, Toronto, Canada, 1982.
- [108] N. R. Liest, C. T. Hicke, and J. R. Nelli, "Laboratory and pilot plan evaluation of Dyno uranium concentrate," National Lead Company of Ohio, NLCO-767, Oct. 1958.
- [109] A. Peterson, "Status report from Sweden," in *Processing of low-grade uranium ores*, Vienna, Austria, 1967.
- [110] A. Peterson, "Ranstad- A new uranium processing plant," in *Processing of low-grade uranium ores*, Vienna, Austria, 1967.
- [111] AREVA, "SOMAIR seeking greater competitiveness - AREVA," 2011. [Online]. Available: <http://www.aveva.com/EN/operations-675/somair-seeking-greater-competitiveness.html>. [Accessed: 07-Jul-2011].
- [112] V. Causin, C. Marega, A. Marigo, P. Carresi, V. D. Guardia, and S. Schiavone, "A method based on thermogravimetry/differential scanning calorimetry for the forensic differentiation of latex gloves," *Forensic science international*, vol. 188, no. 1, pp. 57–63, 2009.
- [113] D. M. Hausen, "Characterizing and classifying uranium yellow cakes: A background," *JOM Journal of the Minerals, Metals and Materials Society*, vol. 50, no. 12, pp. 45–47, 1998.
- [114] T. Sato and S. Shiota, "Thermal decomposition of ammonium uranates," *Journal of Thermal Analysis and Calorimetry*, vol. 30, no. 1, pp. 107–120, 1985.

- [115] M. C. Ball, C. R. G. Birkett, D. S. Brown, and M. J. Jaycock, "The thermal decomposition of ammonium diuranate," *Journal of Inorganic and Nuclear Chemistry*, vol. 36, no. 7, pp. 1527–1529, Jul. 1974.
- [116] B. H. Kim, Y. B. Lee, M. A. Prelas, and T. K. Ghosh, "Thermal and X-ray diffraction analysis studies during the decomposition of ammonium uranyl nitrate," *Journal of Radioanalytical and Nuclear Chemistry*, vol. 292, no. 3, pp. 1075–1083, Jan. 2012.
- [117] L. Hälldahl and O. T. Sörensen, "Thermal analysis of the decomposition of ammonium uranyl carbonate (AUC) in different atmospheres," *Thermochimica Acta*, vol. 29, no. 2, pp. 253–259, Apr. 1979.
- [118] L. Hälldahl and M. Nygren, "TG, DSC, X-ray and electron diffraction studies of intermediate phases in the reduction of ammonium uranyl carbonate to UO₂," *Thermochimica Acta*, vol. 72, no. 1–2, pp. 213–218, Jan. 1984.
- [119] H. Lars, "A study of the composition of the amorphous phase formed during decomposition of ammonium uranyl carbonate in various atmospheres," *Thermochimica Acta*, vol. 95, no. 2, pp. 389–394, Nov. 1985.
- [120] T. Sato, "Thermal decomposition of uranium peroxide hydrates," *J. Applied Chem. Biotechnol*, vol. 27, pp. 207–213, 1976.
- [121] A. Rey, I. Casas, J. Giménez, J. Quiñones, and J. de Pablo, "Effect of temperature on studtite stability: Thermogravimetry and differential scanning calorimetry investigations," *Journal of Nuclear Materials*, vol. 385, no. 2, pp. 467–473, 2009.
- [122] V. Baran and M. Tymph, "Thermal Analysis of Sodium Uranates," *Zeitschrift für anorganische und allgemeine Chemie*, vol. 347, no. 3–4, pp. 184–190, 1966.
- [123] E. H. P. Cordfunke and B. O. Loopstra, "Sodium uranates: Preparation and thermochemical properties," *Journal of Inorganic and Nuclear Chemistry*, vol. 33, no. 8, pp. 2427–2436, 1971.
- [124] J. L. Woolfrey, "Surface area changes during the thermal decomposition of ammonium uranate," *Journal of Inorganic and Nuclear Chemistry*, vol. 38, pp. 347–348, 1976.
- [125] J. L. Woolfrey, "The preparation and calcination of ammonium uranates—a literature survey," Australian Atomic Energy Commission, AAEC/TM476, Sep. 1968.
- [126] P. Balakrishna, B. N. Murty, K. P. Chakraborty, R. N. Jayaraj, and C. Ganguly, "Special Features in Powder Preparation, Pressing, and Sintering of Uranium Dioxide," *Mat. & Manufacturing Processes*, vol. 15, no. 5, pp. 679–693, 2000.
- [127] H. Ching-Tsven, "Dry-ADU process for UO₂ production," *Journal of Nuclear Materials*, vol. 199, no. 1, pp. 61–67, 1992.
- [128] H. Doi and T. Ito, "Significance of physical state of starting precipitate in growth of uranium dioxide particles," *Journal of Nuclear Materials*, vol. 11, no. 1, pp. 94–106, 1964.
- [129] E. H. Kim, C. S. Choi, J. H. Park, S. G. Kwon, and I. S. Chang, "A study on morphology and chemical composition of precipitates produced from UO₂(NO₃)₂·(NH₄)₂CO₃ solution," *Journal of Nuclear Materials*, vol. 209, pp. 301–305, 1994.
- [130] M. Lee and C. Wu, "Conversion of UF₆ to UO₂: A quasi-optimization of the ammonium uranyl carbonate process," *Journal of Nuclear Materials*, vol. 185, pp. 190–201, 1991.

- [131] Y.-M. Pan and C.-B. Ma, "The conversion of UO₂ via ammonium uranyl carbonate: Study of precipitation, chemical variation and powder properties," *Journal of Nuclear Materials*, vol. 99, no. 2–3, pp. 135–147, 1981.
- [132] C. S. Choi, J. H. Park, E. H. Kim, H. S. Shin, and I. S. Chang, "The influence of AUC powder characteristics on UO₂ pellets," *Journal of Nuclear Materials*, vol. 153, pp. 148–155, 1988.
- [133] A. Marajofsky, L. Perez, and J. Celora, "On the dependence of characteristics of powders on the AUC process parameters," *Journal of Nuclear Materials*, no. 178, pp. 143–151, 1991.
- [134] Y. W. Lee and M. S. Yang, "Characterization of HWR fuel pellets fabricated using UO₂ powders from different conversion processes," *Journal of Nuclear Materials*, vol. 178, no. 2–3, pp. 217–226, 1991.
- [135] J. C. Clayton and Seymour Aronson, "Some Preparative Methods and Physical Characteristics of Uranium Dioxide Powders," *Journal of Chemical and Engineering Data*, vol. 6, no. 1, pp. 43–51, 1961.
- [136] I. E. Knudsen, "Preparation of ceramic grade UO₂ from UF₆ by direct conversion process," *Transactions of the American Nuclear Society*, vol. 12, no. 2, p. 437, 1969.
- [137] R. Carter and J. T. Semeraz, "Uranium Oxide Production," U.S. Patent 5,723,100.
- [138] W. Roger De Hollander and H. H. Klepfer, "Conversion of uranium hexafluoride to uranium dioxide structures of controlled density and grain size," U.S. Patent 3,786,12015-Jan-1974.
- [139] J. W. Plaue, G. L. Klunder, I. D. Hutcheon, and K. R. Czerwinski, "Near infrared reflectance spectroscopy as a process signature in uranium oxides," *Journal of Radioanalytical and Nuclear Chemistry*, Aug. 2012.
- [140] R. L. Frost, K. L. Erickson, M. O. Adebajo, and M. L. Weier, "Near-infrared spectroscopy of autunites," *Spectrochimica Acta Part A: Molecular and Biomolecular Spectroscopy*, vol. 61, no. 3, pp. 367–372, 2005.
- [141] R. L. Frost, O. Carmody, K. L. Erickson, and M. L. Weier, "Near-infrared spectroscopy to uranyl arsenates of the autunite and metaautunite group," *Spectrochimica Acta Part A: Molecular and Biomolecular Spectroscopy*, vol. 61, no. 8, pp. 1923–1927, Jun. 2005.
- [142] R. L. Frost and J. Čejka, "A Raman spectroscopic study of the uranyl mineral rutherfordine—revisited," *Journal of Raman Spectroscopy*, vol. 40, no. 9, pp. 1096–1103, Sep. 2009.
- [143] R. L. Frost and J. Čejka, "Near-and mid-infrared spectroscopy of the uranyl selenite mineral haynesite (UO₂)₃(SeO₃)₂(OH)₂·5H₂O," *Spectrochimica Acta Part A: Molecular and Biomolecular Spectroscopy*, vol. 71, no. 5, pp. 1959–1963, 2009.
- [144] R. L. Frost, K. L. Erickson, O. Carmody, and M. L. Weier, "Near-infrared spectroscopy of torbernite and metatorbernite," *Spectrochimica Acta Part A: Molecular and Biomolecular Spectroscopy*, vol. 61, no. 4, pp. 749–754, Feb. 2005.
- [145] J. M. Hanchar, "Spectroscopic techniques applied to uranium in minerals," in *Uranium: mineralogy, geochemistry and the environment*, Mineralogical Society of America, 1999.

- [146] J. Workman and L. Weyer, *Practical Guide to Interpretive Near-infrared Spectroscopy*. Taylor & Francis, 2008.
- [147] M. A. Carrell and D. R. Wilder, "Visible and near-infrared absorption of uranium in sodium-silicate glass," *Journal of Nuclear Materials*, vol. 13, no. 2, pp. 142–151, 1964.
- [148] A. F. Eidson, "Infrared analysis of refined uranium ore," *Analytical Chemistry*, vol. 57, no. 11, pp. 2134–2138, Sep. 1985.
- [149] G. L. Klunder, J. W. Plaue, P. Spackman, P. M. Grant, R. Lindvall, and I. D. Hutcheon, "Near Infrared Spectroscopy of Uranium Ore Concentrates," *Applied Spectroscopy*, vol. Submitted, no. Submitted.
- [150] E. I. Andreev, K. V. Glavin, A. V. Ivanov, V. V. Malovik, V. V. Martynov, and V. S. Panov, "Some results uranium dioxide powder structure investigation," *Russ. J. Non-ferrous Metals*, vol. 50, no. 3, pp. 281–285, Jun. 2009.
- [151] R. C. Burk, T. W. Zawadzki, and P. S. Apte, "Particle Size Distribution and Its Relation to Sintering—A Case Study for UO₂ Powders," *Journal of the American Ceramic Society*, vol. 66, no. 11, pp. 815–818, 2006.
- [152] L. Pajo, "UO₂ FUEL PELLETT IMPURITIES, PELLETT SURFACE ROUGHNESS AND n (18 O)/n (16 O) RATIOS, APPLIED TO NUCLEAR FORENSIC SCIENCE."
- [153] L. Pajo, A. Schubert, L. Aldave, L. Koch, Y. K. Bibilashvili, Y. N. Dolgov, and N. A. Chorokhov, "Identification of unknown nuclear fuel by impurities and physical parameters," *Journal of Radioanalytical and Nuclear Chemistry*, vol. 250, no. 1, pp. 79–84, 2001.
- [154] E. H. P. Cordfunke and A. A. Van Der Giessen, "Particle properties and sintering behaviour of uranium dioxide," *Journal of Nuclear Materials*, vol. 24, no. 2, pp. 141–149, 1967.
- [155] H. Assmann, "Überblick über zusammenhänge zwischen lwr-brennstoff-eigenschaften und verfahrensabstufen bei der brennstoffproduktion," *Journal of Nuclear Materials*, vol. 106, no. 1–3, pp. 15–34, 1982.
- [156] H. Assmann, M. Peehs, and H. Roepenack, "Survey of binary oxide fuel manufacturing and quality control," *Journal of Nuclear Materials*, vol. 153, pp. 115–126, 1988.
- [157] D. Bright, "NIST Particle Morphology Glossary." [Online]. Available: <http://www.nist.gov/lispix/doc/particle-form/part-morph-gloss.htm#slide32>. [Accessed: 10-Sep-2011].
- [158] J. Shlens, "A tutorial on principal component analysis," *Systems Neurobiology Laboratory, University of California at San Diego*, 2005.
- [159] E. H. P. Cordfunke and A. Van Der Giessen, "Pseudomorphic decomposition of uranium peroxide into UO₃," *Journal of Inorganic and Nuclear Chemistry*, vol. 25, no. 5, pp. 553–554, 1963.
- [160] R. L. Bates and J. A. Jackson, *Dictionary of geological terms*. The American Geological Insitute, 1984.
- [161] B. I. Omel'yanenko, V. A. Petrov, and V. V. Poluektov, "Behavior of uranium under conditions of interaction of rocks and ores with subsurface water," *Geology of Ore Deposits*, vol. 49, pp. 378–391, Oct. 2007.

- [162] T. Reetz and I. Haase, "On the pseudomorphism in the wet-chemical process of oxide powder preparation," in *High Tech Ceramics*, Milan, Italy, 1987, pp. 481–491.
- [163] C. V. Putnis, "Direct observations of pseudomorphism: compositional and textural evolution at a fluid-solid interface," *American Mineralogist*, vol. 90, pp. 1909–1912, Nov. 2005.
- [164] A. Putnis, "Mineral replacement reactions: from macroscopic observations to microscopic mechanisms," *Mineralogical Magazine*, vol. 66, pp. 689–708, Oct. 2002.
- [165] F. Xia, "Mechanisms and kinetics of pseudomorphic mineral replacement reactions and their applications in materials syntheses.," PhD, University of Adelaide, School of Chemical Engineering, Australia, 2009.
- [166] R. Graziani, G. Bombieri, and E. Forsellini, "Crystal structure of tetra-ammonium uranyl tricarbonatate," *J. Chem. Soc., Dalton Trans.*, no. 19, p. 2059, 1972.
- [167] F. Garrido, R. M. Ibberson, L. Nowicki, and B. T. M. Willis, "Cuboctahedral oxygen clusters in U₃O₇," *Journal of Nuclear Materials*, vol. 322, no. 1, pp. 87–89, Oct. 2003.
- [168] G. Rousseau, L. Desgranges, F. Charlot, N. Millot, J. Ničpce, M. Pijolat, F. Valdivieso, G. Baldinozzi, and J. Béar, "A detailed study of UO₂ to U₃O₈ oxidation phases and the associated rate-limiting steps," *Journal of nuclear materials*, vol. 355, no. 1–3, pp. 10–20, 2006.
- [169] L. Desgranges, G. Baldinozzi, G. Rousseau, J.-C. Nièpce, and G. Calvarin, "Neutron Diffraction Study of the in Situ Oxidation of UO₂," *Inorg. Chem.*, vol. 48, no. 16, pp. 7585–7592, 2009.
- [170] G. Rousseau, L. Desgranges, F. Charlot, N. Millot, J. C. Ničpce, M. Pijolat, F. Valdivieso, G. Baldinozzi, and J. F. Béar, "A detailed study of UO₂ to U₃O₈ oxidation phases and the associated rate-limiting steps," *Journal of Nuclear Materials*, vol. 355, no. 1–3, pp. 10–20, 2006.
- [171] R. Lerch and R. Norman, "Nuclear Fuel Conversion and Fabrication Chemistry," *Radiochimica Acta*, vol. 36, no. 1–2, pp. 75–88, 1984.
- [172] L. Pajo, "Fuel pellet impurities, pellet surface roughness, and O-18/O-16 ratios, applied t nuclear forensic science," University of Helsinki, Finland, 2001.
- [173] M. Kristo, "Nuclear Forensic Signatures in Commercial Nuclear Fuels," Napa Valley, CA, 29-Dec-2009.
- [174] F. Glodeanu, M. Spinzi, and V. Balan, "Correlation between UO₂ powder and pellet quality in PHWR fuel manufacturing," *Journal of Nuclear Materials*, vol. 153, pp. 156–159.
- [175] Gündüz and I. Uslu, "Powder characteristics and microstructure of uranium dioxide and uranium dioxide-gadolinium oxide fuel," *Journal of Nuclear Materials*, vol. 231, no. 1–2, pp. 113–120, 1996.
- [176] S. Allen and K. McConnell, "Uranium Oxide Forensics," University of Nevada, Las Vegas, Aug-2011.
- [177] H. A. Wriedt, "The Al-O (Aluminum-Oxygen) System," *Journal of Phase Equilibria*, vol. 6, no. 6, pp. 548–553, 1985.

- [178] H. He, R. K. Zhu, Z. Qin, P. Keech, Z. Ding, and D. W. Shoesmith, "Determination of Local Corrosion Kinetics on Hyper-Stoichiometric UO_{2+x} by Scanning Electrochemical Microscopy," *J. Electrochem. Soc.*, vol. 156, no. 3, p. C87, 2009.
- [179] K. D. O'Neil, H. He, P. Keech, D. W. Shoesmith, and O. A. Semenikhin, "Anisotropy of local electrical conductivity of hyper-stoichiometric uranium dioxide revealed by current-sensing atomic force microscopy (CS-AFM)," *Electrochemistry Communications*, vol. 10, no. 11, pp. 1805–1808, 2008.
- [180] International Atomic Energy Agency, "Water Resources Programme - Global Network of Isotopes in Precipitation," *Water Resources Programme - Global Network of Isotopes in Precipitation*, 2010. [Online]. Available: http://www-naweb.iaea.org/napc/ih/IHS_resources_gnip.html. [Accessed: 16-Sep-2010].
- [181] G. J. Bowen, "Interpolating the isotopic composition of modern meteoric precipitation," *Water Resources Research*, vol. 39, no. 10, 2003.
- [182] G. J. Bowen and B. Wilkinson, "Spatial distribution of delta O-18 in meteoric precipitation," *Geology*, vol. 30, no. 4, pp. 315–318, 2002.
- [183] L. Pajo, K. Mayer, and L. Koch, "Investigation of the oxygen isotopic composition in oxidic uranium compounds as a new property in nuclear forensic science," *Fresenius' Journal of Analytical Chemistry*, vol. 371, no. 3, pp. 348–352, Oct. 2001.
- [184] M. Fayek, J. Horita, and E. Ripley, "The oxygen isotopic composition of uranium minerals: A review," *Ore Geology Reviews*, 2011.
- [185] M. Fayek and T. K. Kyser, "Low temperature oxygen isotopic fractionation in the uraninite- UO_3 - CO_2 - H_2O system," *Geochimica et cosmochimica acta*, p. 2185, 2000.
- [186] F. J. Johnston, D. A. Hutchison, and J. J. Katz, "Oxygen exchange between uranium oxides and water," *Journal of Inorganic and Nuclear Chemistry*, vol. 7, no. 4, pp. 392–396, Nov. 1958.
- [187] K. Hattori and S. Halas, "Calculation of oxygen isotope fractionation between uranium dioxide, uranium trioxide and water," *Geochimica et cosmochimica acta*, vol. 46, pp. 1863–1868, 1982.
- [188] Y. Zheng, "Calculation of oxygen isotope fractionation in metal oxides," *Geochimica et cosmochimica acta*, vol. 55, pp. 2299–2307, 1991.
- [189] Y. Zheng, "Oxygen Isotope Fractionation in Uranium Oxides," *Nuclear Science and Techniques*, vol. 6, no. 4, pp. 193–197, 1995.
- [190] T. Fang, "Recalculation of oxygen isotope fractionation of uranium trioxide," *Chin. Sci. Bull*, vol. 41, pp. 577–582, 1996.
- [191] M. Dole, "The Relative Atomic Weight of Oxygen in Water and in Air A Discussion of the Atmospheric Distribution of the Oxygen Isotopes and of the Chemical Standard of Atomic Weights," *The Journal of Chemical Physics*, vol. 4, no. 4, pp. 268–275, Apr. 1936.
- [192] M. Robel, I. D. Hutcheon, M. Kristo, and R. Lindvall, "The Uranium Sourcing Database Project: A Comprehensive International Nuclear Forensics Collaboration from Ore to Attribution," Palm Desert, California, 17-Jul-2011.
- [193] M. Robel, M. J. Kristo, and M. A. Heller, "Nuclear forensic inferences using iterative multidimensional statistics," in *Institute of Nuclear Materials Management 50th Annual Meeting Tucson, AZ (July 2007)*, 2009.

- [194] D. A. Northrop and R. N. Clayton, "Oxygen-Isotope Fractionation in Systems Containing Dolomite," *J. Geol.*, vol. 74, pp. 174–196, 1966.
- [195] J. R. O'Neil, "Theoretical and Experimental Aspects of Isotopic Fractionation," *Reviews in Mineralogy and Geochemistry*, vol. 16, pp. 1–40, 1986.
- [196] R. C. Van der Spuy, "Palabora Mining Company Heavy Minerals Plant Uranium from Copper Plant Tailings," in *Uranium '82*; Toronto, Canada, 1982.
- [197] R. C. Van Der Spuy, "The heavy-minerals plant at Palabora Mining Company--a low-grade, high-tonnage gravity concentrator," *Journal of South African Institute of Mining and Metallurgy*, pp. 17–29, Feb. 1982.
- [198] T. T. Bartos and K. M. Ogle, "Water Quality and Environmental Isotopic Analyses of Ground-Water Samples Collected from the Wasatch and Fort Union Formations in Areas of Coal bed Methane Development—Implications to Recharge and Ground- Water Flow, Eastern Powder River Basin, Wyoming," US Dept. of the Interior, US Geological Survey, Cheyenne, Wyoming, 02-4045, 2003.
- [199] G. Gordon and H. Taube, "The exchange reaction between uranyl ion and water in perchloric acid solution," *Journal of Inorganic and Nuclear Chemistry*, vol. 19, no. 1–2, pp. 189–191, 1961.
- [200] "Gordon and Taube - 1961 - The uranium(V)-catalyzed exchange reaction between.pdf." .
- [201] L. G. Mashirov, V. A. Mikhalev, and D. N. Suglobov, "Stoichiometry of uranyl hydrolysis reaction in acidic aqueous solutions from the evidence of oxygen exchange kinetics," *Comptes Rendus Chimie*, vol. 7, no. 12, pp. 1179–1184, Dec. 2004.
- [202] G. Gordon and H. Taube, "Oxygen Tracer Experiments on Oxidation of Aqueous Uranium (IV) with Oxygen-Containing Oxidizing Agents," *Inorganic Chemistry*, vol. 1, no. 1, pp. 69–75, 1962.
- [203] L. Baker, J. G. Schnizlein, and J. D. Bingle, "The ignition of uranium," *Journal of Nuclear Materials*, vol. 20, no. 1, pp. 22–38, 1966.
- [204] "Metdat Home Page." [Online]. Available: <http://www-metdat.llnl.gov/cgi-pub/index.pl>. [Accessed: 06-Jan-2013].
- [205] M. Fayek, L. M. Anovitz, D. R. Cole, and D. A. Bostick, "O and H diffusion in uraninite: Implications for fluid–uraninite interactions, nuclear waste disposal, and nuclear forensics," *Geochimica et Cosmochimica Acta*, vol. 75, no. 13, pp. 3677–3686, Jul. 2011.
- [206] J. Belle, "Oxygen and uranium diffusion in uranium dioxide (a review)," *Journal of Nuclear Materials*, vol. 30, no. 1–2, pp. 3–15, 1969.
- [207] L. Pajo, G. Tamborini, G. Rasmussen, K. Mayer, and L. Koch, "A novel isotope analysis of oxygen in uranium oxides: comparison of secondary ion mass spectrometry, glow discharge mass spectrometry and thermal ionization mass spectrometry," *Spectrochimica Acta Part B: Atomic Spectroscopy*, vol. 56, no. 5, pp. 541–549, May 2001.

VITA

Jonathan William Plaue

Degrees:

Bachelor of Science, Chemical Engineering, 2001
Massachusetts Institute of Technology

Master of Science, Nuclear Engineering, 2003
Massachusetts Institute of Technology

Special Honors and Awards:

John W. Crawford Award for Staff Excellence, Defense Nuclear Facilities Safety Board, 2009

Eagle Scout

Publications:

Plaue, J. W.; Klunder, G. L.; Hutcheon, I. D.; Czerwinski, K. R. Near infrared reflectance spectroscopy as a process signature in uranium oxides. *Journal of Radioanalytical and Nuclear Chemistry* 2012.

Plaue, J.; Gelis, A.; Czerwinski, K. Actinide Third Phase Formation in 1.1 M TBP/Nitric Acid/Alkane Diluent Systems. *Separation Science and Technology* 2006, 41, 2065–2074.

Plaue, J.; Gelis, A.; Czerwinski, K. Plutonium Third Phase Formation in the 30% TBP/Nitric Acid/Hydrogenated Polypropylene Tetramer System. *Solvent Extraction and Ion Exchange* 2006, 24, 271–282.

Plaue, J.; Gelis, A.; Czerwinski, K.; Thiyagarajan, P.; Chiarizia, R. Small-Angle Neutron Scattering Study of Plutonium Third Phase Formation in 30% TBP/HNO₃/Alkane Diluent Systems. *Solvent Extraction and Ion Exchange* 2006, 24, 283–298.

Plaue, J.; Gelis, A.; Czerwinski, K. Insights into third phase formation using neptunium. *Special Publication-Royal of Chemistry* 2006, 305, 503.

Lumetta, G. J.; Industrial, A. C. S. D. of; Chemistry, E.; Chemistry, A. C. S. D. of N.; Technology; Meeting, A. C. S. Separations for the nuclear fuel cycle in the 21st century; American Chemical Society, 2006.

Plaue, J. W.; Czerwinski, K. R. The influence of ozone on ligand-assisted extraction of ²³⁹Pu and ²⁴¹Am from Rocky Flats soil. *Radiochimica Acta* 2003, 91, 309–314.

Plaue, J.; Czerwinski, K. Actinide Speciation in Environmental Remediation. *J. Nucl. Sci. Supp* 2002, 3, 461–465.

Dissertation Title: Forensic Signatures of Chemical Process History in Uranium Oxides

Dissertation Examination Committee:

Chairperson, Kenneth R. Czerwinski, Ph.D.

Committee Member, Ian D. Hutcheon, Ph. D.

Committee Member, Julie M. Gostic, Ph. D.

Graduate Faculty Representative, Gary S. Cerefice, Ph. D.